Optical Spectroscopy of Dynamic Nuclear Spin Polarization in Single InAs Quantum Dots

by

Aaron M. Ross

A dissertation submitted in partial fulfillment
of the requirements for the degree of
Doctor of Philosophy
(Physics)
in The University of Michigan
2019

Doctoral Committee:
Professor Duncan G. Steel, Chair
Assistant Professor Parag Deotare
Professor Mackillo Kira
Professor Theodore B. Norris
Associate Professor Vanessa Sih

Aaron M. Ross

aaross@umich.edu

ORCID iD: 0000-0002-8949-7257

ACKNOWLEDGEMENTS

First off, I would like to thank my advisor Duncan Steel. From my first visit during recruitment weekend until the end of my graduate school career, Duncan has been very welcoming and accommodating, and has always challenged me to view the scientific problems in a positive light. He has molded me into the scientist that I am today, with his demands for precise, rigorous, and logical thought. Many of our insights have been driven by his relentless encouragement to dig deeper into the data to extract as much meaningful information as possible.

My progress in the field of spectroscopy and optics would not have been possible without the concrete foundations set forth by my group mentors, colleagues, and professors. Most importantly, Colin Chow deserves a huge portion of credit and my thanks for his help and guidance during the first few years of my graduate career. Our countless discussions and the joint scientific endeavors we undertook together involving the quantum dot molecule system (a formidable beast that few QD spectroscopists have been willing to approach) will forever shape my future scientific work. Uttam Paudel and Cameron Nelson, my closest contemporaries, also deserve a huge amount of credit for keeping me sane during the last few years of my studies; we bonded in the darkness of the laboratory, and their lightheartedness always brightened my day. My other mentors, John Schaibley and Alex Burgers, laid the groundwork for my future scientific endeavors, passing on their knowledge of lasers, electronics, and optics without losing patience for a newcomer like myself. I have many fond memories of my other labmates, especially Midhat Farooq (a true friend outside of the lab as well) and Adam Katcher.

My time in Ann Arbor was enhanced immensely by my friends and the times we spent together outside of work. The list is too large to write in completion, but I want to especially thank Kian, Alex Golden, Lu Ma, Midhat, Joe, Vanessa, Jared, Adam, Johanna, Catherine, Jess, Natasha, Sam, Erin, Tracy, Byron, Colin, Sebastian, Eric, and Matt.

I especially want to thank my mother Betty, brother Jeremy, and father Chad for the support they have provided me with. My mother Betty is a lifelong inspiration to me, with unwavering resilience when faced with challenge. My brother Jeremy is one of my closest confidants, with whom I share a closely intertwined vision of the world molded and shaped by our shared childhood but enhanced by his experiences abroad.

My life has been changed immeasurably for the better by my partner Veronica, who I was lucky enough to have met near the beginning of my graduate career on a fateful Halloween night. Without her love and support, it's difficult to say that I would have finished this PhD work; through thick and thin, she has always been there for me. She has guided me to become a kinder, more thoughtful person. I love our life together, and can't wait to start a new adventure with her.

Last, I want to acknowledge all of those who have a vision for an equitable future, those who demand that we who have been gifted with good fortune focus our efforts on dramatically transforming our society into one that treats all people with dignity.

TABLE OF CONTENTS

LIST OF TABLES

LIST OF FIGURES

Figure

ABSTRACT

Dynamic nuclear spin polarization is investigated experimentally in the single InAs/GaAs quantum dot system, revealing a strong non-linear feedback mechanism between the spin carriers generated via resonant optical excitation and the nuclear spin ensemble. As measured using resonant Raman scattering, two distinct nuclear spin ensemble configurations are observed that depend strongly on the optical excitation frequency and exhibit hysteresis with respect to the laser frequency scan direction. One regime is characterized by an Overhauser (OH) field that tracks with the excitation frequency, while in the other regime the OH field shifts to avoid a forbidden energy range as the excitation laser is brought into resonance. OH field shifts as large as 794 mT are measured; the fluctuations of the field are also observed as abrupt jumps in Raman scattering energies and CW pump-probe optical response. The resonant Raman scattering technique utilized in this thesis allowed for sub-100 nuclear spin sensitivity, and could be pushed to the single spin sensitivity level with a modest improvement of the scanning etalon spectrometer system.

The nuclear spin environment and its coupling to the quantum dot electron-trion system are also investigated using time-domain techniques including Ramsey fringes (free induction decay) on the electron spin and electro-optic modulator (EOM) pulsed pump-probe experiments. The Ramsey fringes are strongly distorted as a function of rotation pulse delay time, and the qualitative nature of the distortion depends on which electron spin state is probed. Fourier transforms of the Ramsey fringes reveal a broadening of the electron spin frequency distribution beyond what is expected for the quasi-static OH field case. Coherent population trapping of the electron spin state

results in a (19.8 $\pm$ 2.0)% reduction of the OH field distribution width for pumping times of 5 ms and a duty cycle of 70%. EOM-pulsed pump-probe experiments demonstrate DNP-induced non-linear feedback for experimental repetition periods between 100 ns and 3 μs; one possible implication is that the time-averaged electron spin polarization plays a significant role in DNP phenomena in the time-domain. Overall, this thesis presents a comprehensive study of dynamic nuclear spin polarization in the QD electron-trion system in both high-resolution CW and time-domain experiments.

CHAPTER 1

Introduction to quantum information science

1.1 Motivations for developing quantum information systems

Advancements in the development of quantum information technologies promise dramatic societal changes, whether through shifts in the way in which scientific development proceeds via the exponential speed-up of certain classes of computational problems such as quantum chemistry and simulation, the obsolescence of widely-utilized encryption algorithms that underpin secure communications between state governments, financial institutions, and individuals, and enhanced optimization of logistical problems such as airline scheduling and supply chain distribution. For these reasons, a vast amount of experimental and theoretical scientific work has been devoted to understanding the fundamental building blocks (qubits) of these quantum systems. Most researchers in the field of quantum information consider the so-called "quantum revolution" to have been sparked by the seminal work of Richard Feynman in 1981, proposing that computers may be built from single atoms which are enhanced by their emergent quantum properties such as many-body entanglement [4,5]. In that work and related work, Feynman suggested that the only systems that could properly simulate physical and chemical problems efficiently were quantum mechanical computers themselves, and in fact proposed one of the first implementations of the linear photonic quantum computation architecture. Ever since that proposal, quantum physicists have worked towards implementing quantum computers in a variety

of physical architectures that will be summarized later in this chapter, only very recently achieving success in small and moderately-sized systems (up to approximately 50 physical qubits in gate-based systems and 500 qubits in adiabatic systems).

The efficiency gains provided by quantum mechanics in computation, cryptography, and metrology all arise from the many-body entanglement and superposition features that distinguish quantum mechanics from classical mechanics. All quantum technologies take advantage of a general process in which first, the many-body system is prepared in a relatively pure state, which then evolves via the Schrodinger equation; the observables of the system are read out at some later time via electrical and/or optical methods. It is sometimes explained that the advantages of quantum technologies arise due to *constructive and destructive interferences* between the pathways that evolve from initial states to final states; this interference is absent in classical computation. This phenomenon is sometimes referred to as *quantum parallelism*, in which multiple input states are computed "simultaneously" [6].

Inspecting computation more carefully, in classical computation architectures, input bytes constructed from multiple bits are typically stored capacitively in distinct states, ie. in binary notation 1001010 for example. In this example, the byte is 8 bits long, and an 8-bit byte has the ability to store a number as large as $2^8 = 256$. In the classical system, the individual bits are only ever present in the 0 or 1 state during the computation process. Introducing the quantum bit, or the *qubit*, an analogy is made using the two discrete energy levels in a quantum system $\{|0\rangle, |1\rangle\}$. It is known via the Schrodinger equation that this quantum system may evolve into some superposition states, which is generally given by

$$|\psi\rangle_1 = a_{10}\,|0\rangle_1 + a_{11}\,|1\rangle_1 \tag{1.1}$$

where the coefficients a_{ij} in front of the quantum states are complex amplitudes. The postulates underpinning the laws of quantum mechanics dictate that a measurement of the system always results in observing the $|0\rangle$ state with a probability given by $|a_{10}|^2$, or the $|1\rangle$ state with a probability given by $|a_{11}|^2$. The qubit differs from

the classical bit in this sense, that first the outcomes are probabilistic, and second that the amplitudes are complex, meaning that a complex phase exists between the two states. If one scales up the system and works with two qubits, the qubit amplitudes become *entangled* via the interactions between qubits that are absent between classical bits,

$$\begin{aligned} |\psi\rangle_{12} = |\psi\rangle_1 |\psi\rangle_2 = (a_{10}|0\rangle_1 + a_{11}|1\rangle_1) \otimes (a_{20}|0\rangle_2 + a_{21}|1\rangle_2) \\ \xrightarrow{evolution} c_{00}|00\rangle + c_{01}|01\rangle + c_{10}|10\rangle + c_{11}|11\rangle \end{aligned} \tag{1.2}$$

where c_{ij} are the new complex amplitudes in front of the two-qubit basis states which are entangled due to interactions. Thus, complex amplitudes exist which connect the qubit states, and interfere with each other as a function of time due to the Schrodinger equation. This many-body entanglement is what distinguishes quantum information from classical information.

The advantages of quantum computers over their classical counterparts has been referred to specifically as "quantum supremacy" originally by John Preskill [7]; in his words, this supremacy is achieved when one has demonstrated that an algorithm run on a quantum computer solves a problem with a super-polynomial speedup relative to classic computers. The motivation for quantum computation relies on a *postulate* rather than a proof that the set of problems that quantum computers can solve efficiently (bounded-error quantum polynomial time, or BQP) is in fact a proper superset of the class of problems that classical computers solve efficiently (polynomial time, P problems) [8]. No proof exists that BQP is strictly larger than P; however, the possible advantages of the superpolynomial speedups are beneficial enough that researchers of applied quantum mechanics have started the quantum computer development process regardless.

Many important problems are included in the postulated BQP class. The most famous example is Shor's algorithm [9], which is used to determine the prime factors of a number and evaluate discrete logarithms, utilizing a quantum Fourier transform technique. This problem is particularly important in the realm of information security; the RSA cryptography scheme is a public-key system in which a user multiplies

two large prime numbers together and publishes this public key. A private key is generated from these two primes and shared with a desired recipient, who may then decode a message which has been padded with the public key. However, Shor's algorithm leads to an exponential speed-up of the factoring of a number into its primes, allowing a hacker to factor the public key into the two primes and decrypt any intercepted message.

Other superpolynomial speedups (more efficient than classical computation) include the computation of solutions to systems of linear equations, provided that the matrix of coefficients obeys certain properties such as Hermiticity [7]. However, one of the most important applications from a physical science perspective is the simulation of physical and chemical systems. Simulation algorithms such as the phase estimation algorithm [10] rely on correspondences between quantum computer Hamiltonians and the Hamiltonians of systems of interest such as large molecules. It is believed that the quantum simulation algorithms may help lead the way in the bottom-up design of new atom-by-atom constructed materials that may find use in solar energy harvesting, battery technologies, superconducting materials, and many other systems.

Outside of the realm of computation, quantum mechanical effects may also improve encryption protocols [11–13] and metrology techniques [14]. Quantum encryption protocols such as the BB84 protocol utilize the orthogonality of quantum states and the no-cloning theorem to provide provably secure communications between multiple parties [11]. In this protocol, which laid the groundwork for more sophisticated ones to be developed later, the quantum information is stored in both the photon qubit state (polarization typically, but could also include time-bin states) and the basis in which the qubit is measured; a private key is eventually sifted by communicating basis measurements over a public classical channel. Commercial products have been developed around more sophisticated quantum key distribution (QKD) protocols; however, researchers referring to themselves as quantum hackers have notoriously broken the quantum protocols encoded by these physical implementations of QKD [14]. QKD is often times referred to as "provably secure"; however, the actual physical implementations of such systems are not typically taken into account. QKD protocols have been

attacked using methods that take advantage of wavelength-dependent responsivity of single photon detectors, detector blinding attacks, and trojan-horse attacks. Thus, a lesson is learned: physical implementation of quantum information algorithms must be taken into account, and that lesson holds for quantum computation as well.

Quantum metrology also exploits quantum resources such as squeezing and entanglement in order to measure physical quantities such as strain, or electromagnetic fields, beyond the standard quantum limit [14]. In fact, phase squeezing of the optical field generated by a high-power 1064 nm laser will be utilized in the Advanced LIGO experiment (Laser Interferometer Gravitational-Wave Observatory). The most recent generation of this experiment detected the gravitational waves emitted by a black hole merger with strain sensitivity at the level of 10^{-23} $\mathrm{Hz}^{-1/2}$, and the [15]. Other instances of metrology enhancement include beating the standard quantum limit in atomic Ramsey fringe experiments via spin-squeezing, and the implementation of photonic N00N states ($|\psi\rangle \propto |N,0\rangle + |0,N\rangle$) which beat the quantum limit on optical phase measurements in interferometers (similar to LIGO).

The remainder of this chapter will address the quantum computation side of quantum information technologies, exploring especially the candidates for physical implementation of quantum computers, with an emphasis on self-assembled quantum dots.

1.2 Experimental implementations of quantum computation

1.2.1 Requirements for quantum computing

This section will present a brief review of existing quantum computation technologies, starting first with the general criteria required for a functioning computation system. The commonly accepted criteria, at least for the gate-based architectures, is referred to as the DiVincenzo criteria [16]. First and foremost of these criteria is that the qubit system must be well-isolated from the environment, or that the *decoherence time* of the qubit must be long compared to the gate/rotation time; this requirement is sometimes referred to as the "closed box" requirement. Understand-

ing and reducing decoherence is one of the main focuses of this research group; in QDs, decoherence is caused by a combination of nuclear spin ensemble effects, phonon scattering, spin-orbit coupling, and charge fluctuations. Processes which lead to *inhomogeneous broadening*, or ones that cause a drift in the qubit's resonance energy relatively slow compared to the experimental time, or in an ensemble system affect each qubit differently depending on its location, may be dealt with using spin echo and dynamical decoupling techniques. However, the intrinsic transverse relaxation rate which is at best given by $T_2 = 2T_1$, where T_1 is the longitudinal or energy relaxation rate, is typically a fundamental feature of the qubit system, which in QDs is related either to spontaneous emission of the exciton or trion system, or spin-orbit relaxation of the electron spin qubit. This intrinsic decoherence time limits the number of useful gate operations that may take place; in fact, in realistic implementations of quantum computers, quantum error correction and fault-tolerant computing requires that the errors due to decoherence are less than 1%, although some theoretical work predicts much smaller tolerances of 10^{-5} [17].

It is worth noting that, as far as the author is aware, no experimental implementations of a quantum computing system have reached the 10^{-5} error level as of late 2018. Nevertheless, this has not stopped researchers from developing experimental realizations of quantum error corrected systems, especially in superconducting qubit computers [18] and NV-carbon registers in diamond [19, 20]. These error-corrected systems attempt to correct for bit and phase errors in individual qubits by bringing classical error correction into the quantum mechanical framework. Realistic quantum computers will rely on *logical* qubits that consist of multiple (probably at least 7) physical qubits to perform quantum operations indefinitely in the presence of noise. It is also worth noting that a subset of researchers believe that environmental noise may lead to the theoretical infeasability of quantum computing in general. The task is left to the experimentalist and engineers to prove otherwise.

An equally important criterion required for the physical implementation of the quantum computer is *scalability* of the system. This means that the Hilbert space, or the effective logical space of the computer, must grow exponentially without an

exponential rise in the physical resources such as number of qubits, amount of computational time, physical space, or energy costs. This requirement is not just one that relies on quantum mechanics but also engineering. First, the ability to produce many-body entanglement among all qubits in the system must be retained as the system size increases. This scalability discussion requires introducing another criterion, that a quantum computer requires all qubits may be acted upon with a set of *universal gates* that include single-qubit rotations and conditional two-qubit entangling gates. It is sufficient to produce a universal quantum computer if a conditional NOT (CNOT) gate [6] may be produced between any two neighboring qubits in the system, along with single-qubit rotations on each qubit. These gates are produced in a number of ways, depending on the physical implementation of the system, but include laser-induced collective motion of trapped ions, entanglement of photonic modes at beamsplitters, Rydberg dipole blockade in optical lattices of Rydberg/neutral atoms, and the always-on exchange interactions between nuclear spins in molecular liquids and also vertically-stacked quantum dot molecules [17].

While it has been shown in a variety of physical implementations that single and two-qubit gates are possible, retaining high fidelity of these gates has proved to be difficult as system size increases. For example, in the NMR system, the interactions which are always-on between neighboring nuclear spins (the qubits) become more difficult to manage as the molecular size increases, requiring more complicated pulse sequences to effect single and two-qubit gates. In optical lattice and trapped ion systems, interactions that go beyond nearest neighbor effects must be accounted for. The systems which have proved to be scalable in the medium-term (approximately 50 qubits) include the trapped ion systems and superconducting qubits, systems that allow for controllable decoupling of the qubits from one another after an entangling interaction. These two systems have achieved moderate commercial success, resulting in investments from companies such as Google and the creation of start-ups including D-Wave and IonQ.

Two other important requirements for quantum computation include the ability to *initialize* the quantum state of the system and *measure* the final state of the system

using a protocol that scales polynomially with the number of qubits in the system. Initialization of the system in a pure quantum state may result in a final quantum state that can be measured, as compared to thermalized states, in for example liquid-state NMR systems, which results in very low signal to noise ratio measurements. Initialization in the neutral atom and trapped ion systems often proceeds via Zeeman slowing and optical pumping; liquid-state NMR systems now utilize algorithimic cooling, while solid-state NMR systems utilize dynamic nuclear spin polarization techniques which can lead to as high as 99% state initialization fidelity. The measurement protocols proceed via fluorescence techniques in trapped ion and neutral atom systems where the qubits are spatially separated by tens of nanometers and the readout signals can be isolated easily from one another. However, readout schemes are often times destructive, always collapsing the wavefunction of the many-body entangled system, requiring re-initialization and re-entanglement, contributing to the required computational resources of the computational scheme. Quantum non-demolition techniques have been developed, in which the quantum state of the system returns to its pre-measurement state after the measurement period; this work was awarded with the Nobel Prize in 2012.

Specific implementations of quantum computation systems are discussed in the next section, with a detailed discussion of how self-assembled QDs may be incorporated into these systems.

1.2.2 Implementations of quantum computing

The first successful implementation of primitive quantum computation was in *nuclear magnetic resonance* (NMR) systems, and the architecture executed there has laid the groundwork for nearly all other quantum computation systems to follow (in the gate-based systems). The nuclear spins of molecules in the liquid state form have exceptionally long decoherence times due to their isolation from the environment, with coherence times on the order of thousands of seconds [21]. However, initialization techniques had not been developed in the liquid-state during the early instances

of the NMR systems; therefore, techniques were developed to extract signals in the bulk systems from ensemble measurements with small thermal equilibrium population differences on the order of 10^{-6} [22]. NMR techniques benefit from at least half a century of CW and pulsed RF control of nuclear spins. The resonances of each nuclear spin species are split by a strong magnetic field on the order of multiple Tesla. Individual nuclei of a given nuclear species are additionally split by the local chemical shift environment; depending on the symmetry of the molecule, these local chemical shifts may lead to degeneracy-breaking of the energy levels of every nuclear spin in the molecule, allowing the spectroscopist to address each nuclear spin individually. A resonant radio-frequency (RF) magnetic field which is orthogonal to the strong external magnetic is pulsed to drive transitions between different nuclear spin states for an individual nucleus, and CNOT gates between nuclei are generated by a combination of RF pulses combined with relying on, for instance, scalar coupling between nuclei [23].

The pulsed rotation framework laid the groundwork for quantum computational schemes in trapped ion systems, as well as gate-defined and self-assembled QDs. Early experimental work demonstrated execution of the less-studied Deutsch-Josza algorithm on a carbon-13 labelled chloroform molecule [24] involving two nuclear spins, and Shor's algorithm involving seven qubits to factor the number $15 = 3 \times 5$ using the custom-developed molecule perflorobutadienyl iron complex [25]. Unfortunately, it was eventually shown that the ensemble averaging technique does not scale polynomially with a higher number of qubits; solid-state NMR techniques involving large gradient high magnetic fields and dynamic nuclear spin polarization to enhance initial state purity are actively being developed to achieve a scalable NMR quantum computer.

An improvement was made in a number of aspects by the utilization of trapped ions for quantum computation. A scheme based off of confining ions to a Penning trap and addressing them using lasers was proposed by Cirac and Zoller [26], and experimentally demonstrated by David Wineland and coworkers using Be^{+9} ions. Strikingly, these Be^{+9} ions exhibit coherence times between Zeeman levels exceeding 10 minutes,

providing a very promising platform for quantum manipulation. The qubits are typically taken as two sub-levels of a Zeeman-split angular momentum manifold which is split by an external magnetic field. Single qubit operations were achieved by utilizing the optically-induced AC Stark shift, and multiple qubit gates can be generated by the quantized collective motion of the lattice which is induced by Coulomb repulsion. Single atom optical pumping can lead to effectively 100% initialization fidelity into a magnetic sub-level, and measurement fidelities using fluorescence techniques are similarly high. Readout of individual qubits is made convenient by the spatial separation of the qubits in linear Penning traps, allowing for a multi-plexed readout method which is absent from other quantum computation systems. This experimental implementation has been particularly successful; two recent studies demonstrated quantum simulators involving 53 $^{171}Yb^{+}$ qubits in one case [27] and 51 cold neutral ^{87}Rb atoms excited into their Rydberg states. Both cases exhibited phase transitions, observations of which have already contributed insights to the problem of quantum magnetism. Both trapped ion and neutral atom systems are already being commercialized, and improvements are promised by the utilization of on-chip atom trapping incorporating nanometer-sized gate electrodes. It is not obvious that there are any fundamental physical limitations to restrict the growth and advancement of these systems.

Another system of interest that has achieved both considerable scientific and commercial success is the superconducting qubit system [28]. The superconducting qubit, while taking on many forms, basically consists of a superconducting LC circuit, typically fabricated from Al microwave striplines and resonators. When the circuit is cooled down below 50 mK (requiring dilution cryostats), the circuit becomes superconducting. In addition, these circuits include a Josephson junction, which is a superconductor-insulator-superconductor device through which Cooper pairs (two electrons bound together by a phonon) can flow without an applied voltage across the device. The important feature of the junction is that the device is dissipationless and has a non-linear inductance. The introduction of this junction into the circuit may result in three different types of qubits, the charge, flux, and phase qubits [28],

which were expanded into more complex qubit types in order to deal with decoherence caused by stray capacitances. In the first device used as a primitive qubit [29], a single Cooper pair box was demonstrated in which the qubit consisted of the two lowest energy states of the system which differed by a single Cooper pair excitation. In some ways, these qubit systems are most analogously related to the self-assembled quantum dot system in the sense that they are *artificial atoms*; their Hamiltonians (resonance energies and couplings) can be tuned across a broad range by adjusting the macroscopic inductances and capacitances of the system. Quantum computation involving superconducting qubits is rapidly evolving. This experimental implementation was used to realize quantum error correction involving a single transmon qubit in a 3D circuit architecture, joining liquid-state NMR [30] and trapped ion systems [31] in that achievement, and in fact was the first system to demonstrate an actual increase in coherence time of the quantum-error-corrected system compared to the bare physical qubit [18].

One current controversy in the field of quantum computation involves *adiabatic quantum computation*, sometimes referred to as quantum annealing. Systems have been developed by the company D-Wave Systems which supposedly incorporate hundreds of nearest-neighbor coupled superconducting qubits. It was proposed around the same time as the first experimental demonstration of the Cooper pair box qubit that a new architecture of quantum computation could be utilized in which adiabatic tuning of the resonance energies of the coupled qubits would lead to many-body entanglement via level crossings, and in fact could generate a CNOT gate [32]. Equivalence between this model of quantum computation and the circuit model involving pulsed gates was proven rigorously [33, 34]. An indirect demonstration of quantum entanglement was shown in a system with 108 qubits via comparison to optimized classical algorithms [35], and a quantum spin glass was supposedly simulated in a 512 qubit simulator [36]. The question of whether many-body entanglement exists in this system still stands, and actually anticipates a bigger problem with future implementations of quantum computation: how does one check the results of a quantum computation when no efficient classical algorithm exists to do so? This is an especially

important question when claims are made that the adiabatic quantum computation architecture can be used to solve NP-hard (non-deterministic polynomial) combinatorial minimization problems [37], a set of problems that may be larger than the BQP class. This result would have ground-breaking consequences for real world problems in the fields of bioinformatics, computational chemistry, artificial intelligence, circuit design, and likely many other equivalent problems which have not yet been formulated.

Another unique quantum information processing framework that may end up benefiting from the incorporation of self-assembled QDs is *linear photonic quantum computation*. A surprising result was demonstrated theroetically [38] that universal quantum computation could efficiently be performed using only beam splitters, optical phase shifters, single photon sources, single-photon detectors. Before that enlightening result, it was assumed that photonic systems were limited by the requirement for non-linear interactions between the qubits; photons do not directly interact with one another in the vacuum. Such a non-linear interaction may be mediated by strong light-matter interactions, and this is an active field of research that heavily involves QD-light interactions. The lack of photon interactions with other photonic qubits may be interpreted as a positive feature of the system; the photonic qubits are more resilient against certain types of noise that are present in matter-based quantum computation implementations. In the linear photonic system, the photonic qubit is realized by a single photon which can be found in two optical modes, for example polarization, spatial mode, or time-binning. In fact, there are certain implementations which utilize multiple modes for a single photon to yield higher dimensional Hilbert spaces while reducing the total number of required physical resources [39]. In general, gates acting on the photonic qubits proceed via phase shifting and beam splitters, the former which may for example rotate the polarization arbitrarily using waveplates and the latter which may be utilized for CNOT gates in combination with post-selection and heralding techniques. For qubits which are path-encoded, arbitrary phase shifts between the paths may be generated using resistive elements which heat waveguides, thereby changing the refractive index locally in one path of the arm of

a waveguide interferometer [40]. Most linear photonic systems are engineered using silicon CMOS technologies; this technology is the main semiconductor fabrication technique for most classical processors today, eliminating a full generation of technology development that will have to be developed for some of the other quantum computation technologies such as trapped ions and NMR systems. Additionally, some estimates say that a useful photonic quantum computer with computational power exceeding that of a classical computer will require between 10^{15} and 10^{17} components (beamsplitters, phase shifters, detectors); the CMOS (complementary metal-oxide semiconductor) fabrication technology is currently the only path forward [41]. Nevertheless, some photonic devices that are analogous to the D-Wave adiabatic quantum computing systems have already been developed, and are referred to as photonic recurrent Ising samplers [42–44]. Similar to the superconducting qubit systems, the photonic sampler determines the ground state of the 2D Ising problem, a problem that can be mapped onto NP-hard combinatorics problems. These are not universal quantum computers, but prove that the photonic framework is already useful for computational speedups.

The biggest hurdle to developing a useful linear photonic quantum computer is the search for a photon source that yields single, bi- and tri- photon sources [41]. This search has been especially hampered by the need for incorporation into existing CMOS technology. Quantum-correlated photonic states are required as inputs to photonic quantum computing systems; phenomena such as the Hong-Ou-Mandel (HOM) effect also depend on utilizing indistinguishable photons, or photons that have identical spectral, polarization and spatial mode properties. The earliest implementations relied on attenuation of the coherent states generated by a laser; this approach fails fundamentally in generating a quantum Fock state, since attenuation of a coherent state still results in a coherent state [45]. Spontaneous parametric down-conversion is often used, in which a strong pump field is focused into a periodically-poled Lithium Niobate crystal or a microresonator ring [46], yielding a strong optical non-linearity which results in the generation of pairs of entangled photons [47]. This photon pair generation can be enhanced by the incorporation of high Q-factor cavities, yielding

greatly enhanced photon pair generation rates. However, this method also suffers from the generation of higher photon number pairs, contributing to reductions in entanglement fidelity. This problem could be solved by the utilization of photon-number-resolving detectors which could be utilized for the heralding of a truly single photon state, but high detection efficiency detectors with this feature are highly elusive. Self-assembled quantum dots provide a solution to this problem, as discussed in the next section.

1.3 Utilizing quantum dots for quantum information

Self-assembled quantum dots (QDs), the subject of this thesis, are often times referred to as "artificial atoms", with optical resonance energies which can be tuned through various fabrication processes by changing the QD size, alloying with host materials, strain, and doping. These fabrication processes will be covered in more detail in the next Chapter. What is the point in studying self-assembled QDs for the purposes of quantum information when so many other candidate systems are already available? QDs composed of InAs and GaAs can be addressed optically using either narrow bandwidth CW lasers to drive resonant excitation of optical transitions, or using pulsed lasers to drive higher-order nonlinear processes discussed further below; the QD resonant energies can be tuned to fall within the Ti:Saph range, the most widely used broadband tunable laser technology. QDs may also be grown using existing semiconductor fabrication technologies such as molecular beam epitaxy which is commonly used to fabricate quantum well lasers, although not as commonly used as CMOS fabrication tech. From the perspective of photonic quantum technologies, single QDs are truly exceptional; resonant excitation of a QD in a microcavity system (on-chip) can result in exceptionally pure single photons. QDs embedded in an electrically-biased nano-pillar structure were recently demonstrated to exceed all other systems in quality, exhibiting photon indistinguishability of 0.9956 ± 0.0045, with a photon extraction of 65% and brightness of 0.154, 20 times brighter than any other source with a similar indistinguishability [48]. This level of single photon pu-

rity was previously thought to be unattainable, and will fundamentally change the nature of linear photonic quantum computing. A recent review of various QD-based single photon sources demonstrates very high brightnesses and indistinguishabilities for a wide range of QD architectures, including tapered nanowires, nano-trumpets, micropillars, and photonic crystal cavities [49]. Bi-photons may also be produced by resonant excitation of the two-photon transition to the bi-exciton, which leads to a cascade process yielding a polarization-entangled photon pair [50]. Although the bi-exciton emission cascade suffers from degeneracy-breaking due to the electron-hole exchange, this fine structure splitting can be completely eliminated by the utilization of in-plane piezo-strain of the QD [51,52]. As single and bi-photon sources, QDs may also be grown using different materials and techniques in order to bring their optical resonance energies closer to atomic sources such as Rb and Yb ions [53–55]; thus, quantum information may be transmitted between hybrid quantum systems using photonic teleportation techniques [56].

Researchers studying QDs have made considerable inroads in terms of satisfying the DiVincenzo criteria addressed in Section 1.2.1. First, the system has multiple well-defined qubits; in this thesis, the electron spin ground state of the trion system is utilized by breaking the degeneracy using an external magnetic field. Although the decoherence time T_2^* due to inhomogeneous broadening of a single electron spin measured over a large number of experimental shots is on the order of a few nanoseconds, the intrinsic decoherence time T_2 has been measured using spin echo techniques to exceed a microsecond. The main source of inhomogeneous broadening and spectral wandering is due to the interactions between the confined electron and the constituent nuclear spins in the QD; a fluctuating effective magnetic field called the Overhauser field acts on the electron with a standard deviation between 10-40 mT [57]. This field has been studied extensively throughout this thesis; mitigating decoherence and broadening caused by this field is one of the primarily goals of researchers attempting to bring the QD electron spin qubit into the realm of useful quantum computing. In terms of pure state initialization, the QD system is also exceptional: under the application of an in-plane magnetic field, the QD electron ground state may be

initialized with fidelity exceeding 98% with a few nanoseconds via resonant optical excitation [58], bringing it on the same level as trapped ions and with initialization fidelities far exceeding that of the NMR systems. However, as will be seen in this thesis, resonant excitation of the electron-trion transitions can lead to the generation of high nuclear spin polarization in the QD, which results in non-linear feedback between the electron and nuclei. This feedback process must be addressed if resonant excitation is to be utilized. Interestingly, the nuclear spin polarization may also provide an interesting quantum resource known as a quantum memory; this feature has yet to be explored in the InAs/GaAs QD system and would require that many-body nuclear spin coherence is retained in the presence of quantum operations acting on the electron spin.

Another exceptional feature of the optically-addressable QD electron-trion system is that gate operations may be performed utilizing ultrafast optical pulses, with pulse widths on the order of 2 ps [59–61], resulting in geometric phase rotations of the electron spin and rotations about the optical axis using two-photon detuned Raman pulses. In combination with an external magnetic field, the entire Hilbert space of the single electron spin qubit may be utilized; additionally, the number of gate operations that may be performed in the decoherence time is equal to approximately 1 $\mu s/2$ ps = 500,000. This number exceeds results for most other qubit systems, promising that complex quantum operations may be performed. However, the scalability of the QD electron-trion system is quite challenging. Current state-of-the-art fabrication processes do not allow for precise placement of QDs with equal resonance energies and morphology and with high optical quality (narrow linewidths). Many studies have focused on vertically-stacked quantum dot molecules (QDMs) in which the electrons which reside in separate QDs are coupled via the Coulomb exchange interaction [62, 63]. A similar framework utilized in developing NMR pulse sequences may be used to determine complex optical pulse sequences which generate CNOT gates between the two electrons; however, generating the pulse sequences in the lab is an experimentally demanding task [64]. Initialization of the states of the QDM requires four resonant CW lasers [62, 63]. It is not obvious that the number of physi-

cal resources required to initialize, control, and measure the electron spins in coupled QDs are manageable given current optical technologies. Nevertheless, it is worth attempting to scale up these systems due to the easy incorporation into the solid state, extremely fast gate operation times, and exquisite quantum optical properties. In general, QDs are extremely promising systems for the future of quantum information science, especially in the arena of photonic quantum computation.

CHAPTER 2

Self-assembled InAs QDs: sample structure, optical and electronic properties

2.1 Introduction

This chapter covers the background required for understanding some of the optical and electronic properties of self-assembled InAs quantum dots (QDs). The first section details the self-assembly fabrication process, through which QDs are grown using molecular beam epitaxy; the details of the periodic layered sample under investigation in this thesis are given. Then a thorough exposition of the band structure of GaAs and InAs is given, with an emphasis on the optical selection rules that arise due to the symmetry properties of the zincblende band structure. The next section covers the physics of the trion state and some of the effects of quantum confinement. Then the Zeeman Hamiltonian is introduced, and the selection rules in the presence of an in-plane magnetic field are derived, along with some special cases including heavy-hole light-hole mixing and perturbatively small fields transverse to the external field. The electric field structure used to deterministically bias the QD with electrons is laid out, and the on-chip DBR cavity structure which enhances the brightness of the QD is detailed.

2.2 Self-assembly process of InAs/GaAs quantum dots

The quantum dots investigated in this thesis are grown using molecular beam

epitaxy (MBE), a thin film deposition technique used to produce extremely high purity single crystal layers. An ultra-high vacuum chamber contains a set of shuttered crucibles containing elements such as In, Ga and As. The crucibles are heated and an atomic jet deposits the material atom-by-atom on to the substrate, in this case a GaAs wafer, resulting in a deposition rate of approximately one monolayer per second [65]. Although the technique was originally used to fabricate structures based off of high-purity semiconductor monolayers, nanostructure growth methods were discovered using the Stranski-Krastanov (SK) growth technique [66,67]. In this process, In and As are deposited onto the GaAs wafer. The sample is heated up to approximately 500° C, and the adatoms that have absorbed onto the GaAs wafer surface diffuse, forming a thin monolayer of crystalline InAs. However, the lattice mismatch between GaAs and InAs is equal to around 7%; thus, elastic energy builds up at the interface between the GaAs wafer and InAs crystal. This growth is at first coherent, in that the In and As ionically bond to the GaAs surface, but the crystal interface is strained. This first layer is referred to as the InAs wetting layer, and is utilized in photoluminescence experiments to optically inject carriers into the QD.

As the strain in the layer increases, InAs islands begin to percolate, reducing the overall free energy of the system due to strain. These islands are referred to as quantum dots (QDs); the bandgap offset between the GaAs and InAs semicondutors leads to electron and hole confinement in the QD. A cross-sectional scanning tunneling microscopy image and transmission electron microscopy image of a typical InAs QD system are displayed in Figure 2.1. Because the lattice mismatch between the two materials is relatively small, no dislocations or defects are generated at the interfaces, and therefore QDs grown via the SK method tend to have high optical quality (lack of photoblinking due to charge traps commonly observed in colloidal QDs [68]). A modification of the process known as the "Indium flush" technique is used to remove the tops of the InAs quantum dots, resulting in a strong blue shift of the optical resonance energy due to tighter carrier confinement [69]. The indium flush technique also results in a narrowed inhomogeneous distribution of QD energies due to a homogenizing of QD heights. The QD optical energies now fall within the 920-980 nm

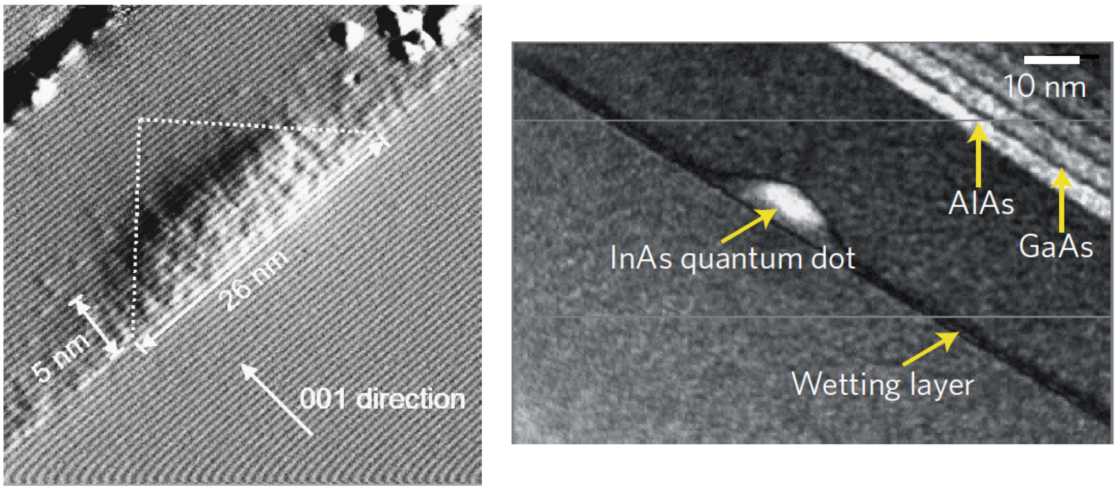

Figure 2.1: Electron microscopy images of typical InAs quantum dots. Left: Cross-sectional scanning tunneling microscopy image of QD with 26 nm base and 5 nm height grown along the (001) direction of the GaAs wafer, taking the shape of a truncated pyramid. Individual crystal layers are evident here. Image taken from [2]. Right: Transmission electron microscopy image of another InAs QD, with the InAs layer evident below the QD. Taken from [3].

range, easily accessible by Ti:Saph tunable lasers, although often times overlapping with water absorption lines.

The SK growth method has great advantages to other QD fabrication methods such as colloidal techniques; since the growth method is in the class of MBE techniques, it allows for simple incorporation of QDs into more complex electric field structures such as Schottky diodes, and superlattice optical structures such as distributed Bragg reflector cavities (DBRs), discussed in more detail later in this chapter (Section 2.7). Even further, complex QD structures such as vertically-stacked QDMs may easily be fabricated, allowing for studies of multi-electron QD systems [62, 63]. The sample under study (R150424F) in this thesis consists of InAs quantum dots embedded in a diode heterostructure (Figure 2.2), and was designed and fabricated by Allan Bracker and Daniel Gammon at the Naval Research Laboratory. The QDs are approximately 2.5 nm in height. The heterostructure is grown on a 500 μm n-doped GaAs wafer (Si, $\geq 1 \times 10^{18}/cm^3$), and consists of a distributed Bragg reflector

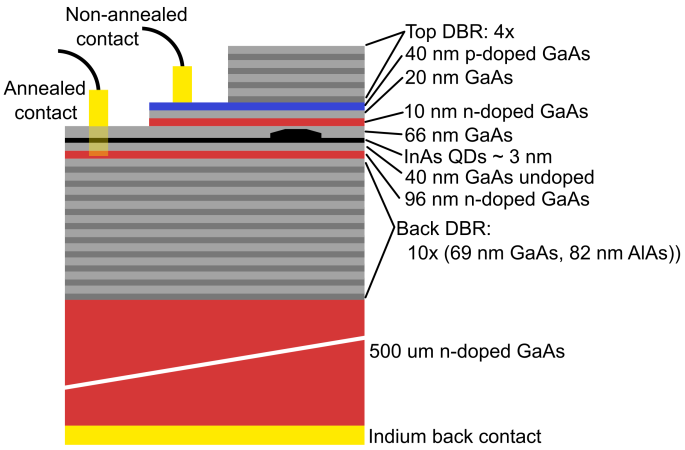

Figure 2.2: Sample diagram schematic. See text for details.

(DBR) mirror (10 periods of 69 nm GaAs and 82 nm AlAs), 96 nm of n-doped GaAs ($\sim 2\times10^{18}/cm^3$), 40 nm of undoped GaAs, the QD layer, 66 nm of undoped GaAs, 10 nm of n-doped GaAs ($\sim 1.5\times10^{18}/cm^3$), 20 nm of undoped GaAs, 40 nm of p-doped GaAs (Be, $\sim 3\times10^{19}/cm^3$), and a top DBR consisting of 4 periods of GaAs and AlAs with the same thicknesses as the bottom DBR. Two indium electrical contacts are used to apply a bias to DC Stark shift the QD energy levels into the $1e^-$ stability range (see Chapter 3 for details on the DC Stark shift). The contacts are made following wet etching to two different layers. The lower contact is made to the 96 nm n-doped GaAs layer below the QDs and is annealed, while the top contact is non-annealed and is connected to the 40 nm p-doped GaAs layer beneath the top DBR. The top and bottom DBR layers are not affected by the electric field produced across the diode structure; as a result, the sample does not suffer from charge fluctuations in the DBR layers.

2.3 Semiconductor band-structure and optical selection rules in the bulk

The semiconductor crystal environment consists of a highly-ordered periodic array of atoms bound together by, in the case of zincblende crystals, ionic bonding. The electronic and optical properties of the crystal arise from the interactions of the outer

valence electrons of the crystal atoms with the weak periodic electrostatic potential due to each ionic lattice site, since the inner shell electrons are screened effectively by the outer electronic shells [70]. The inner electronic shells, or core electrons, are mostly localized around the nucleus, and occupy filled orbitals [71]. Thus, the properties of the electronic system may be derived by taking into account the periodic nature of the ordered crystalline structure, allowing for the utilization of group theoretic methods to analyze the translational symmetries of the crystal lattice. Bloch's theorem showed that electronic wavefunction in the periodic crystal lattice structure inherits the periodicity of the lattice structure; therefore, the same symmetry methods used to analyze the crystal lattice structure can be used to construct the electronic wavefunctions in the bulk crystal.

More specifically, to arrive at the electronic wavefunction in the semiconductor structure, one solves the Schrodinger equation

$$\left[-\frac{\hbar^2}{2m}\nabla^2 + V(\vec{r})\right]\psi_{nk}(\vec{r}) = E_{nk}\psi_{nk}(\vec{r}) \tag{2.1}$$

where $V(\vec{r}), E_{nk}$ are the periodic electrostatic potential of the crystal lattice, and the energy associated with the eigenstate ψ_{nk}. The solutions to this equation for an infinite period crystal lattice are given by

$$\psi_{nk}(\vec{r}) = \frac{1}{\sqrt{V}}e^{i\vec{k}\cdot\vec{r}}u_{nk}(\vec{r}) \tag{2.2}$$

where V is the crystal volume, k is the reciprocal lattice vector for the given eigenstate, and u_{nk} is known as the Bloch function, which is periodic for a given reciprocal lattice vector, obeying the periodicity condition $u_{nk}(\boldsymbol{r} + \boldsymbol{R}) = u_{nk}(\boldsymbol{r})$, where $\boldsymbol{R}$ is a vector associated with the translation symmetry of the crystal. Thus, the electronic wavefunctions in a purely bulk crystal are of the form of plane waves multiplied by a periodic wavefunction that inherits the crystal periodicity. When the crystal is large (Avogadro's number of atoms can effectively be considered infinite with respect to the electronic wavefunction), the resulting energy levels calculated via solving the Schrodinger equation using a variety of different methods [71] form

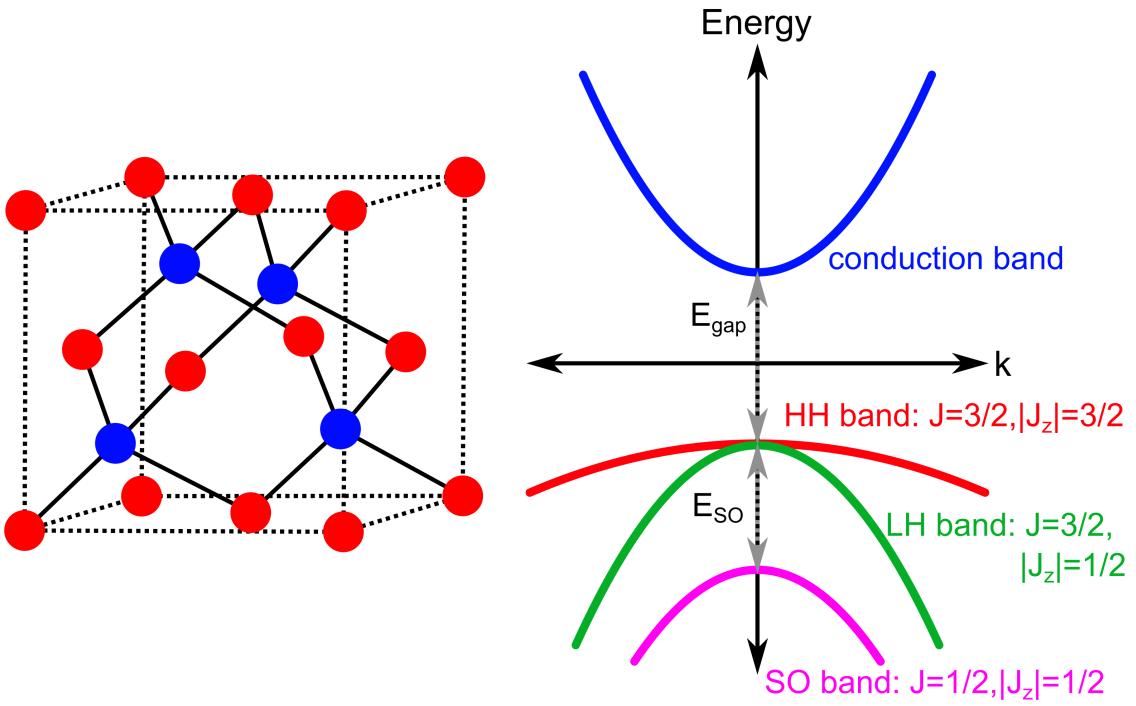

Figure 2.3: Crystal structure for zincblende materials (GaAs, InAs) and resulting band diagram. Left: crystal structure. Dashed lines indicate the extent of a full unit cell of the zincblende structure, solid lines indicate ionic bonds between atoms, and red and blue atoms are the In(Ga) and As atoms, although the crystal structure is invariant upon switching cations and anions. Right: Resulting one-dimensional band diagram in the vicinity of the Γ point (energy versus crystal wavevector k) for the zincblende crystal structure. Conduction (electron) band is indicated in blue, heavy-hole (HH) band indicated in red, light-hole (LH) band indicated in green, and split-off (SO) band indicated in purple. Non-parabolicity due to interactions between the LH and SO bands is neglected here [1].

allowed energy bands. Each band carries with it a given symmetry related to the atomic spatial symmetry, ie. s-like, p-like, and so on.

In semiconductor materials, the resulting allowed bands with different spatial symmetries are separated by a large band gap, which may be driven optically when the band minima and maxima overlap in momentum (k) space. Other theses written by students from this group have gone into considerable detail into the symmetry properties of crystal structures as related to the electronic wavefunctions [62, 65]. This thesis will only briefly review the band structure for zincblende materials (GaAs,

InAs), reporting the resulting valence and conduction band wavefunctions.

The resulting band structure for InAs/GaAs arrived at using the $\boldsymbol{k}\cdot\boldsymbol{p}$ method [71] leads to a conduction band with s-type symmetry (two times Kramer degenerate), and three (two times Kramer degenerate) valence bands with p-type symmetry (Figure 2.3). The valence bands are split into three bands, the heavy-hole, light-hole and split-off bands. The valence band states, which are hereby referred to as hole states, are eigenstates of the total Hamiltonian which includes the periodic electrostatic potential of the crystal lattice and the spin orbit coupling, which is given by $H_{SO} = \lambda \hat{L}\cdot\hat{S}$, where $\hat{L}, \hat{S}$ are the orbital angular momentum and spin. Thus, the hole eigenfunctions are eigenstates of the total angular momentum $\hat{J} = \hat{L} + \hat{S}$ and its projection along the $\hat{z}$ direction. The resulting Bloch wavefunctions for the electron (J=0) and holes (J=1) are found to be equal to

$$\begin{aligned}
|\frac{1}{2},+\frac{1}{2}\rangle_e &= |S\rangle\,|\uparrow\rangle \\
|\frac{1}{2},-\frac{1}{2}\rangle_e &= |S\rangle\,|\downarrow\rangle \\
|\frac{3}{2},+\frac{3}{2}\rangle_h &= -\frac{1}{\sqrt{2}}\,|X+iY\rangle\,|\uparrow\rangle \\
|\frac{3}{2},+\frac{1}{2}\rangle_h &= \frac{1}{\sqrt{3}}\left[-\frac{1}{\sqrt{2}}\,|X+iY\rangle\,|\downarrow\rangle + \sqrt{2}\,|Z\rangle\,|\uparrow\rangle\right] \\
|\frac{3}{2},-\frac{1}{2}\rangle_h &= \frac{1}{\sqrt{3}}\left[\frac{1}{\sqrt{2}}\,|X-iY\rangle\,|\uparrow\rangle + \sqrt{2}\,|Z\rangle\,|\downarrow\rangle\right] \\
|\frac{3}{2},-\frac{3}{2}\rangle_h &= \frac{1}{\sqrt{2}}\,|X-iY\rangle\,|\downarrow\rangle
\end{aligned} \tag{2.3}$$

where the first two lines are the conduction band electrons, with spatial wavefunctions of s-type $|S\rangle$, and the last four lines are the two lowest energy valence bands $|J, J_z\rangle$, the heavy ($J_z = \pm\frac{3}{2}$) and light ($J_z = \pm\frac{1}{2}$) holes, and their spatial wavefunctions $|X, Y, Z\rangle$ are p-type [1]. The split-off band, with $J = \frac{1}{2}$, is separated from the heavy and light hole bands by the spin-orbit interaction, leading to an energy splitting of 380 and 341 meV for InAs and GaAs, respectively [71]; thus, the SO band is neglected here. The nature of the spatial wavefunction for the conduction and valence bands are especially relevant for the determination of optical selection rules, which allow for optical excitation of the valence-conduction band transition, leaving behind

an unoccupied hole in the valence band while simultaneously promoting an electron to the conduction band. The spatial wavefunctions are also essential in determining the nature of how the electron and hole carriers interact with the constituent nuclear spin ensemble present in the bulk and QD systems, resulting in dramatically different interaction strengths for electrons and holes to the nuclear spins [1].

The light-matter interaction in semiconductors can be treated perturbatively in the dipole limit, allowing one to calculate selection rules and oscillator strengths for transitions between the valence band and the conduction band. The interaction Hamiltonian is taken to be equal to $\mathrm{V}_{opt} = -\boldsymbol{\mu} \cdot \boldsymbol{E} = e\boldsymbol{r} \cdot \boldsymbol{E}$, where μ is the optical dipole after an electron-hole pair (exciton) is produced. The polarization selection rules may now be determined by calculating the matrix elements of the interaction potential described above, ie. $-\langle c|\boldsymbol{\mu} \cdot \boldsymbol{E}|v\rangle$, where $|c, v\rangle$ are the conduction and valence band states, respectively. A semi-classical approach is taken in which the semiconductor system is treated quantum mechanically while the light field is treated classically, taking the optical electric field equal to $\boldsymbol{E}(t) = \boldsymbol{E}\cos(kz - \omega t)$, a traveling wave propagating along the QD growth direction $\hat{z}$. The easiest way of determining the selection rules for the dipole interaction is to re-write the dipole interaction in terms of complex spherical vectors (Chapter 16, [45]), allowing for the subsequent utilization of the Wigner-Eckart theorem:

$$\begin{aligned} \boldsymbol{A} &= \sum_{q=-1,0,+1} (-1)^q A_q \hat{\epsilon}_{-q} \\ \boldsymbol{A} \cdot \boldsymbol{B} &= \sum_{q=-1,0,+1} (-1)^q A_q B_{-q} \end{aligned} \tag{2.4}$$

where the vector components in Cartesian and spherical coordinates are related by

$$A_{+1} = -\frac{A_x + iA_y}{\sqrt{2}}, A_{-1} = \frac{A_x - iA_y}{\sqrt{2}}, A_0 = E_z \tag{2.5}$$

Compare these coefficients to the complex spherical unit vectors:

$$\hat{\epsilon}_{+1} = -\frac{\hat{x} + i\hat{y}}{\sqrt{2}}, \hat{\epsilon}_{-1} = \frac{\hat{x} - i\hat{y}}{\sqrt{2}}, \hat{\epsilon}_0 = \hat{z} \tag{2.6}$$

These unit vectors correspond to circularly-polarized light, ie. that $\sigma_{\pm} \rightarrow \mp\hat{\epsilon}_{\pm}$. Thus, a slight confusion may occur here: the coefficents in front of the $\hat{\epsilon}_{\pm}$ unit vectors in the spherical expansion of the electric field (Equation 2.4) correspond to the electric field vectors $\sigma_{\mp}$.

The dipole interaction is then written in the following form

$$-\boldsymbol{\mu} \cdot \boldsymbol{E} = er \sum_{q=-1,0,+1} (-1)^q C_q^{(1)} E_{-q} = er(-C_{-1}^{(1)} E_{+1} + C_0^{(1)} E_0 - C_{+1}^{(1)} E_{-1}) \tag{2.7}$$

where $C_m^{(1)} = \left(\frac{4\pi}{3}\right) Y_{1,m}$ and $\mathrm{Y}_{l,m}$ are the spherical harmonics. The Wigner-Eckart theorem can then be utilized to evaluate the dipole matrix elements [45]. The theorem states that

$$\langle n'j'm_j'|rC_q^{(1)}|njm_j\rangle = \langle n'j'||rC^{(1)}||nj\rangle \langle j1, m_j q|j'm_j'\rangle \tag{2.8}$$

where the second braket on the right hand side of the equation is the Clebsch-Gordon coefficient, and the first braket is the reduced dipole matrix element. The result is that the Clebsch-Gordon coefficient is only non-zero if $m_j' = q + m_j$ and $|j - 1| \leq j' \leq j + 1$, or effectively that the sum of the angular momentum associated with the unit vector ϵ_q and the initial state is equal to the final angular momentum.

Without yet defining the trion (negatively-charged exciton) states, the matrix elements may be calculated between the HH and LH valence bands and the conduction band. One example calculation is shown below for calculating the selection rule associated with the $|\frac{1}{2}, +\frac{1}{2}\rangle_e \rightarrow |\frac{3}{2}, +\frac{3}{2}\rangle_h$ transition. Plugging in the dipole interaction written using the spherical vectors, the matrix element is calculated below

$$
\begin{aligned}
-\langle \frac{3}{2},+\frac{3}{2}|_h \, \boldsymbol{\mu}\cdot\boldsymbol{E} \, |\frac{1}{2},+\frac{1}{2}\rangle_e &= er\,\langle \frac{3}{2},+\frac{3}{2}|_h \left(-C^{(1)}_{-1}E_{+1}+C^{(1)}_{0}E_{0}-C^{(1)}_{+1}E_{-1}\right)|\frac{1}{2},+\frac{1}{2}\rangle_e \\
&= -er\,\langle \frac{3}{2},+\frac{3}{2}|_h \, C^{(1)}_{+1}\,|\frac{1}{2},+\frac{1}{2}\rangle_e \, E_{-1}
\end{aligned}
\tag{2.9}
$$

which corresponds to a σ_+-polarized selection rule. The remaining selection rules are recorded in Table 2.1, as reproduced from Chapter 2 of [1].

		conduction	
Band	valence	$\|\frac{1}{2},+\frac{1}{2}\rangle_e$	$\|\frac{1}{2},-\frac{1}{2}\rangle_e$
HH	$\|\frac{3}{2},+\frac{3}{2}\rangle_h$	$-\sqrt{\frac{1}{2}}(\hat{x}+i\hat{y})$	0
	$\|\frac{3}{2},-\frac{3}{2}\rangle_h$	0	$\sqrt{\frac{1}{2}}(\hat{x}-i\hat{y})$
LH	$\|\frac{3}{2},+\frac{1}{2}\rangle_h$	$\sqrt{\frac{2}{3}}\hat{z}$	$-\sqrt{\frac{1}{6}}(\hat{x}+i\hat{y})$
	$\|\frac{3}{2},-\frac{1}{2}\rangle_h$	$\sqrt{\frac{1}{6}}(\hat{x}-i\hat{y})$	$\sqrt{\frac{2}{3}}\hat{z}$

Table 2.1: Optical selection rules for transitions between valence bands (heavy- and light-holes) and the electron conduction band, as reproduced from [1].

Thus, the optical selection rules in the bulk zincblende (GaAs, InAs) semiconductor at zero magnetic field have been derived, and will later be used to derive the selection rules in the presence of a magnetic field (parallel to the growth axis, perpendicular to the growth axis, and arbitarily) as well as heavy-hole light-hole mixing (HHLH mixing).

2.4 Excitons, trions and quantum confinement

When an electron is promoted via optical excitation from one of the valence bands to the conduction band at the band maxima/minima, or the Γ point ($k \sim 0$), one must take into account the Coulomb interaction between the excited carriers. Taking into account the Coulomb interaction results in a quasi-particle state known as an exciton which is neutrally charged and has a lower energy than the bandgap of the bulk

semiconductor. Especially relevant to the quantum dot system is the three-particle state, or the trion, in which an electron is bound to an optically-generated exciton. The Hamiltonian for the general multi-particle state in the bulk semiconductor is given by

$$H\psi_{quasi} = \left[-\sum_{electrons} \frac{\hbar^2}{2m^*_{e,i}} \nabla^2_{e,i} - \sum_{holes} \frac{\hbar^2}{2m^*_{h,i}} \nabla^2_{h,i} - \sum_{i \neq j} \frac{e_i e_j}{4\pi\epsilon |r_i - r_j|^2} \right] \psi_{quasi} = E\psi_{quasi} \tag{2.10}$$

where $m^*_{e,i}, m^*_{h,i}$ are the effective masses of the electrons and holes that are determined by the curvature of the bands at the gamma point, and the third term is the Coulomb interaction which is summed up over all particles, and ψ_{quasi} is the multi-particle quasi-particle state. The resulting eigenfunctions of the Hamiltonian written above are bound states of the multi-particle system with energies slightly below the bandgap of the bulk semiconductor; the two-particle problem is equivalent to the positron problem which can be solved for using the same methods as solving the hydrogen atom problem. The excitonic binding energies in GaAs, for instance, is equal to 4.9 meV, compared to the bandgap of 1.519 eV [71]. As in the case of the hydrogen atom, one can calculate the Bohr radius of the electron wavefunction, which is found to be equal to 11.2 nm for GaAs, considerably larger than the crystal lattice constant of 5.653 Å; thus, the exciton in GaAs is considered a Wannier-Mott exciton, since the excitonic wavefunction extends over a large number of crystal lattice sites. The binding energy for the trion was calculated in the bulk, but is found to be negligibly small [72], but was later shown to be considerably enhanced ten fold in the presence of quantum confinement in a 2D semiconductor [73], allowing for experimental observation.

As discussed in Section 2.2 of this chapter, the lattice mismatch between GaAs, the host environment material, and InAs, the QD material, leads to strained island growth, which is referred to as a quantum dot (QD). QDs under investigation in this thesis have typical heights of 2.5 nm and base diameters of around 20 nm; thus, the dimensions of the InAs QDs are on the order of or smaller than the Bohr radius of

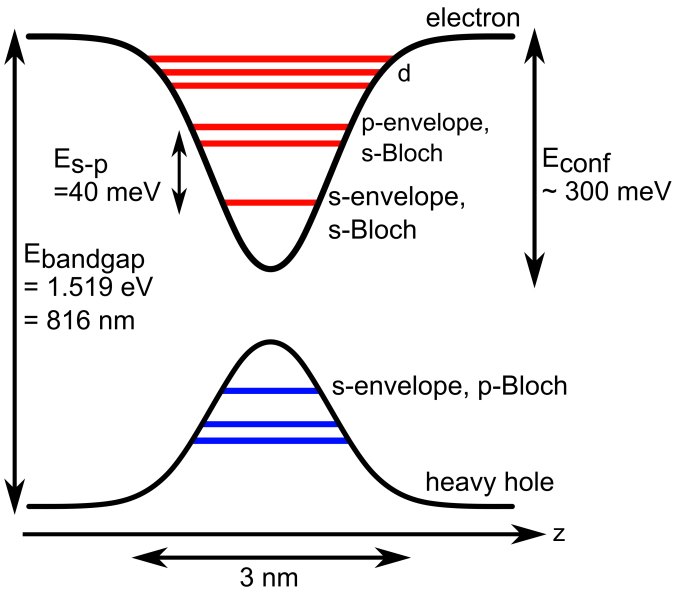

Figure 2.4: Energy level diagram for the confined InAs/GaAs QD system as a function of distance along the growth direction $\hat{z}$. The electron(hole) energy levels are indicated in red(blue), with corresponding spatial symmetries indicated next to each energy level. The lowest energy ground states for the electrons have s-envelope and s-Bloch symmetry, compared to the hole wavefunction which has an s-envelope and p-Bloch symmetry.

the exciton. It is therefore expected that quantum confinement due to the differences in the bandgaps of the two materials should lead to a strong modification of the optical properties of the confined excitons. This topic has been considered thoroughly in other sources, and will not be covered in depth in this thesis [62, 74–76]. The confinement potential may be treated using variational perturbation theory methods, replacing the continuum of band states with discrete states that inherit the spatial symmetry of the Bloch wavefunctions from the bulk. More simplistically, one may consider the finite box model commonly treated in quantum mechanics textbooks [77] that has approximate solutions of bound states with a cosine dependence for even parity within the bounds of the QD and decaying exponentials outside of the QD. In the semiconductor system, the wavefunctions of the electron and holes are now the same Bloch amplitude functions inherited from the bulk multiplied by an envelope function, which many more sophisticated variational approaches take to be a Gaussian. Ad-

ditionally, it should be noted that the electron and hole wavefunctions are distorted significantly in the growth direction as compared to the in-plane directions due to substantially higher confinement the former direction (reduced height compared to base diameter).

More importantly, the tight quantum confinement of the exciton and trions to the QD leads to a strong Coulomb blockade process, in which the energy required to generate new carriers in the QD is shifted from the exciton/trion energy due to the Coulomb and exchange interactions. For instance, if an exciton $|\uparrow\Downarrow\rangle$ is present in the QD, the exchange interaction requires that only the exciton with spin configuration $|\downarrow\Uparrow\rangle$ may be generated with the same envelope functions. The separation in energy between the s- and p-envelope wavefunctions in the conduction band is typically on the order of 40 meV [78] as measured via PL excitation for InAs/GaAs QDs. Additionally, the introduction of another electron, leading to the formation of a negatively-charged trion, is typically red-shifted from the exciton by approximately 7 meV [78], allowing for easy spectroscopic distinction between excitons and trions. This Coulomb blockade process allows for the optical excitation of a single exciton/trion in the QD, laying the groundwork for optical studies of fundamental processes related to quantized two-level systems. More quantitatively, the energy levels for the InAs/GaAs QD are displayed in Figure 2.4, with corresponding confinement, band-gap, and s-p splittings. Sophisticated calculations were performed by Colin Chow [62] using the finite-difference-time-domain (FDTD) method to calculate envelope functions for electrons and holes in arbitary geometry QD systems, including vertically stacked quantum dot molecules (QDMs).

Another important ramification of the QD quantum confinement is the change in oscillator strength between the bulk exciton versus the QD [68]. The absorption strength for resonant excitation, as related to the oscillator strength of the exciton proportional to $|\langle\psi_f|\boldsymbol{\mu}\cdot\boldsymbol{E}|\psi_i\rangle|^2$, which is nearly equal to the dipole matrix element calculated in Section 2.3 above. However, in the presence of quantum confinement, the matrix element now includes a contribution due to the overlap of the envelope functions, or

$$\langle f|\boldsymbol{\mu}\cdot\boldsymbol{E}|i\rangle = \langle u_f|\boldsymbol{\mu}\cdot\boldsymbol{E}|u_i\rangle\,\langle\phi_e|\phi_h\rangle \tag{2.11}$$

where the first term in the product is the bulk dipole matrix element term, and the second term is overlap between the electron and hole wavefunctions [68], which is integrated over the entire volume of the QD. Thus, the envelope functions, which are concentrated significantly in the QD as compared to the bulk (which technically has no envelope function for a perfectly periodic crystal), lead to an enhancement in the oscillator strength. In fact, the ratio of the oscillator strength in the QD system versus the bulk may be determined in this simplified regime for a spherical QD, and is given by [68]

$$\frac{f_{QD}}{f_{bulk}} = \frac{a_B^3}{R^3} \tag{2.12}$$

where a_B is the Bohr radius of the exciton and R is the radius of the QD core. Thus, the oscillator strength is enhanced when the Bohr radius is larger than the radius of the QD; in the QDs under study in this thesis, a comparable figure is the ratio of the QD height (2.5-3 nm) to the Bohr radius ($\sim$11 nm), indicating a strong enhancement due to confinement.

Another consequence of the result given above is that if the envelope functions $|\phi\rangle$ are orthonormal functions and the particles are assumed to be non-interacting (no Coulomb or exchange interactions), then only transitions between equal parity envelope states are allowed [68]. Of course, it has already been shown that the interactions are important to explain the fundamental optical properties of excitons and trions in the QD. Additionally, QDs which are embedded in a host environment or an electric field structure (Section 2.6) exhibit a spatial separation between the electron and hole envelope functions, leading to reduced overlap and lower oscillator strength [79–81].

Finally, the electron and heavy-hole trion states (neglecting the light-hole contributions for now) in the confined QD system under investigation in this thesis are defined in the following way:

$$
\begin{aligned}
|\pm\frac{1}{2}\rangle_e &= \chi_{s,c}(r_e)\,|\frac{1}{2},\pm\frac{1}{2}\rangle_e\,, \\
|\pm\frac{3}{2}\rangle_t &= \chi_{s,hh}(r_h)\,|\frac{3}{2},\pm\frac{3}{2}\rangle_h \\
&\quad\otimes \chi_{s,c}(r_{e1})\chi_{s,c}(r_{e2})\left[|\frac{1}{2},+\frac{1}{2}\rangle_{e,1}|\frac{1}{2},-\frac{1}{2}\rangle_{e,2} - |\frac{1}{2},-\frac{1}{2}\rangle_{e,1}|\frac{1}{2},+\frac{1}{2}\rangle_{e,2}\right]
\end{aligned}
\tag{2.13}
$$

where $\chi_{s,c}$ is the amplitude corresponding to the s-envelope, conduction band electron state, and $\chi_{s,hh}$ is the amplitude corresponding to the s-envelope, heavy-hole state. The electronic term in the trion wavefunction is in the spin-singlet state; the spin-triplet state (with $m_z = 0$) has a higher energy due to the exchange splitting, which has not been considered here but is experimentally resolvable under certain conditions [82].

2.5 Reduction of QD symmetries via external magnetic fields and heavy-hole light-hole mixing

The degeneracy of the confined QD electron and hole states may be broken by the application of an external magnetic field, resulting in a Zeeman splitting. Although it has already been demonstrated above that the two optical transitions corresponding to the $|\frac{1}{2},+\frac{1}{2}\rangle_e \rightarrow |\frac{3}{2},+\frac{3}{2}\rangle_h$ may be addressed individually via polarization selection rules, the application of an external magnetic field will split both the electron and hole states, leading to a splitting of the electron-trion optical transitions which may be addressed individually using narrowband CW lasers. The optical behavior of the QD system in a magnetic field differs dramatically from the zero field case, providing a rich testbed for the investigation of spin physics that will be investigated thoroughly in this thesis.

The Zeeman Hamiltonian is written in the following form

$$
H_{\text{Zeeman}} = \mu_B \sum_{i=x,y,z} \left(g_{e,i}\hat{S}_{e,i} - g_{h,i}\hat{J}_{h,i} \right) \cdot \boldsymbol{B}_i \tag{2.14}
$$

where $g_{e,i}, g_{h,i}$ are the electron and hole g-factors, which differ considerably from

the bare electron g-factor due to quantum confinement effects [68]. Higher-order Zeeman terms proportional to $J_{h,i}^3$ are neglected here, which can be justified by examining the Luttinger-Kohn Hamiltonian, revealing that the terms proportional to $J_{h,i}$ have significantly larger coefficients [76, 82, 83]. This neglect of the cubic term is equivalent to neglecting the contribution of light-hole terms.

For an arbitrary magnetic field, this Hamiltonian is given in matrix form by

$$H_{\text{Zeeman}} = \begin{array}{c} \\ \frac{\mu_B}{2} \end{array} \begin{array}{c} \begin{array}{cccc} |+\frac{1}{2}\rangle_e & |-\frac{1}{2}\rangle_e & |+\frac{3}{2}\rangle_h & |-\frac{3}{2}\rangle_h \end{array} \\ \begin{pmatrix} g_{e,z}B_z & +g_{e,x}B_x - ig_{e,y}B_y & 0 & 0 \\ +g_{e,x}B_x + ig_{e,y}B_y & -g_{e,z}B_z & 0 & 0 \\ 0 & 0 & -g_{h,z}B_z & -g_{h,x}B_x + ig_{h,y}B_y \\ 0 & 0 & -g_{h,x}B_x - ig_{h,y}B_y & +g_{h,z}B_z \end{pmatrix} \end{array} \tag{2.15}$$

When an external magnetic field is applied along the QD growth direction $\hat{z}$ (Faraday geometry), both the electron and trion states are split, with an energy level splitting of $\mu_B g_{(e/h),z} B_z$, but no mixing occurs between the spin states, which can be understood as no new symmetries being broken (Figure 2.5). When an external magnetic field is applied in the sample plane ($\hat{x}$ or $\hat{y}$), the spin states become mixed. This mixing can be understood in two possible ways: first, if the Hamiltonian is not re-diagonalized and an appropriate time-domain experiment is utilized, the spin states $|\pm\frac{1}{2}\rangle$ will precess in an orthogonal magnetic field $\boldsymbol{B}_\perp = B_x\hat{x} + B_y\hat{y}$ [84]. More appropriately for a CW experiment, the Hamiltonian can be re-diagonalized and the new eigenstates are probed with modified selection rules, as explained further below.

Under the application of only a Voigt geometry ($\boldsymbol{B} = B_x\hat{x}$) magnetic field, the resulting eigenstates and eigenenergies are given in Table 2.2

where the new eigenstates which will be used throughout this thesis have been defined. Since the eigenstates in the Voigt geometry are superposition states of the zero field eigenstates, the selection rules also need to be re-calculated. The polariza-

Voigt geometry ($\boldsymbol{B} = B_x\hat{x}$)	
Energy	Eigenstate
$-\frac{1}{2}\mu_B g_{e,x} B_x$	$\lvert x-\rangle = \frac{1}{\sqrt{2}}\left[-\lvert+\frac{1}{2}\rangle_e + \lvert-\frac{1}{2}\rangle_e\right]$
$+\frac{1}{2}\mu_B g_{e,x} B_x$	$\lvert x+\rangle = \frac{1}{\sqrt{2}}\left[\lvert+\frac{1}{2}\rangle_e + \lvert-\frac{1}{2}\rangle_e\right]$
$+\frac{1}{2}\mu_B g_{h,x} B_x$	$\lvert T-\rangle = \frac{1}{\sqrt{2}}\left[-\lvert+\frac{3}{2}\rangle_h + \lvert-\frac{3}{2}\rangle_h\right]$
$-\frac{1}{2}\mu_B g_{h,x} B_x$	$\lvert T+\rangle = \frac{1}{\sqrt{2}}\left[\lvert+\frac{3}{2}\rangle_h + \lvert-\frac{3}{2}\rangle_h\right]$

Table 2.2: Eigenstates and energies of the electron and trion states in the Voigt geometry (magnetic field along the $\hat{x}$ direction.)

tion selection rules listed in Table 2.1 may be used to determine the selection rules in the Voigt geometry. The resulting Hamiltonian $H_{\text{Voigt}} = H_{Zeeman} + H_{dipole}$ is equal to

$$H_{\text{Voigt}} = \begin{array}{c} \\ \lvert x+\rangle \\ \lvert x-\rangle \\ \lvert T+\rangle \\ \lvert T-\rangle \end{array} \begin{array}{c} \begin{array}{cccc} \lvert x+\rangle & \lvert x-\rangle & \lvert T+\rangle & \lvert T-\rangle \end{array} \\ \begin{pmatrix} +\frac{1}{2}\mu_B g_{e,x} B_x & 0 & \frac{i}{\sqrt{2}}\mu E_y(t) & -\frac{1}{\sqrt{2}}\mu E_x(t) \\ 0 & -\frac{1}{2}\mu_B g_{e,x} B_x & -\frac{1}{\sqrt{2}}\mu E_x(t) & \frac{i}{\sqrt{2}}\mu E_y(t) \\ -\frac{i}{\sqrt{2}}\mu E_y^*(t) & -\frac{1}{\sqrt{2}}\mu E_x^*(t) & \omega_0 - \frac{1}{2}\mu_B g_{h,x} B_x & 0 \\ -\frac{1}{\sqrt{2}}\mu E_x^*(t) & -\frac{i}{\sqrt{2}}\mu E_y^*(t) & 0 & \omega_0 + \frac{1}{2}\mu_B g_{h,x} B_x \end{pmatrix} \end{array} \tag{2.16}$$

where μ is the dipole moment for the electron-trion transition, assumed to be equal for all transitions, and $E_{x,y}(t)$ are the time-dependent optical fields. The selection rules and energy level diagram are schematically illustrated in Figure 2.5. Thus, four optical transitions are now observed in the Voigt geometry which are horizontally and vertically polarized. The new cross-transitions which couple, for instance, the $|T+\rangle$ state to the $|x-\rangle$ state, allow for novel optical phenomena including optical pumping [58], electromagnetically-induced transparency due to coherent population trapping [85], and two-photon detuned Raman pulse electron spin state rotations [59, 61, 86, 87], all of which are discussed and utilized throughout this thesis.

The coupling of the electron and trion states to the QD constituent nuclear spin environment will not be discussed in detail in this chapter, since multiple chapters in this thesis are devoted solely to that topic (Chapters 5 and 4). However, it is worth briefly discussing how the eigenstates, eigenenergies, and selection rules change in the presence of nuclear spin polarization in the QD. It is understood that the constituent nuclear spin ensemble of the QD may generate an internal magnetic field $\boldsymbol{B}_{OH}$ called the Overhauser field (OH) acting on the electron and trion states which can be created using optical orientation techniques [1, 57]. From the perspective of the physics as related to the Hamiltonian, the OH field may act as a quasi-static magnetic field term which points randomly and isotropically with an assumed Gaussian probability distribution (Chapter 7). Making these assumptions, it is assumed here that the external magnetic field is in the Voigt configuration and is considerably larger than the OH field fluctuations; thus, the x-component of the OH field is neglected. Additionally, the coupling of the nuclear spin polarization to the hole spins is considerably weaker than to the electrons; one calculation states that the coupling to the hole is only 10% the electron coupling [88]. Thus, the OH field shift on the hole spin is neglected in this treatment.

In the presence of fluctuating OH fields, the Zeeman Hamiltonian for the electronic subspace is equal to

$$H_{\text{Zeeman,e}} = \frac{1}{2} \begin{array}{c} \begin{array}{cc} \left|+\frac{1}{2}\right\rangle_e & \left|-\frac{1}{2}\right\rangle_e \end{array} \\ \begin{pmatrix} \Delta_z^{OH} & \Delta_x - i\Delta_y^{OH} \\ \Delta_x + i\Delta_y^{OH} & -\Delta_z^{OH} \end{pmatrix} \end{array} \tag{2.17}$$

where the $\Delta_{(z,y)}^{OH} = \mu_B g_{e,(z,y)} B_{(z,y)}^{OH}, \Delta_x = \mu_B g_{e,x} B_x$. This Hamiltonian is diagonalized, and only the first-order terms Δ_y/Δ_x and Δ_z/Δ_x are kept. The resulting energies and eigenstates are listed below in Table 2.3

where $|\uparrow / \downarrow\rangle$ is used for short-hand for the zero field electron spin eigenstates. As a check, in the limit of a very strong Voigt geometry field compared to the fluctuating OH fields ($\frac{\Delta_{y,z}}{\Delta_x} \ll 1$), the new eigenstates $|x' \pm\rangle$ return to the Voigt geometry

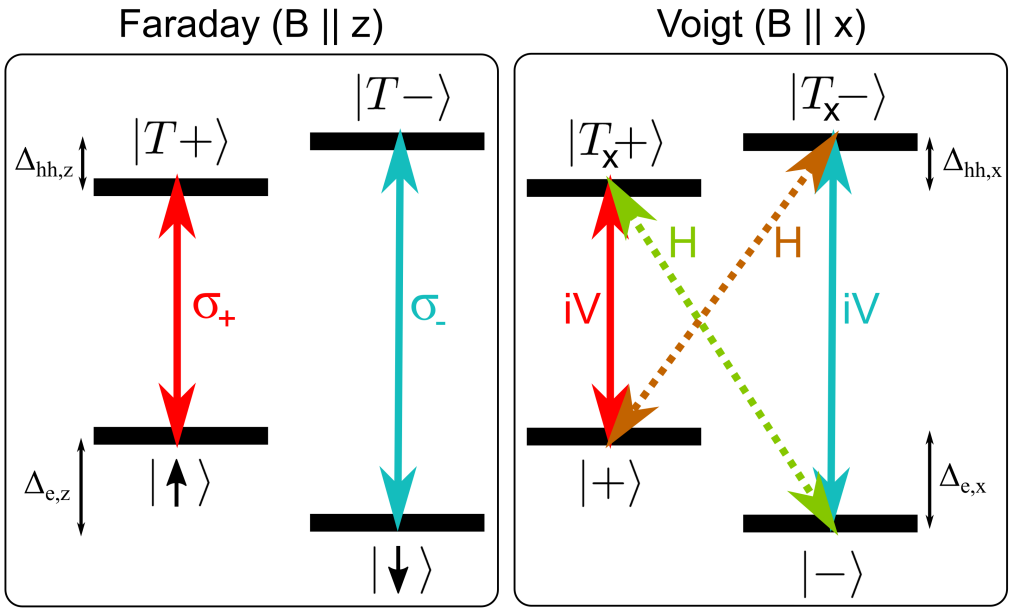

Figure 2.5: Selection rules and energy level diagram for the Faraday and Voigt geometries.

Strong Voigt geometry field plus perpendicular fluctuating fields

Energy	Eigenstate
$-\frac{1}{2}\sqrt{\Delta_x^2+\Delta_y^2+\Delta_z^2}$	$\lvert x'-\rangle = \frac{1}{\sqrt{2(1-\frac{\Delta_z}{\Delta_x})}}\left[(-1+\frac{\Delta_z}{\Delta_x}-i\frac{\Delta_y}{\Delta_x})\lvert\uparrow\rangle+\lvert\downarrow\rangle\right]$
$+\frac{1}{2}\sqrt{\Delta_x^2+\Delta_y^2+\Delta_z^2}$	$\lvert x'+\rangle = \frac{1}{\sqrt{2(1+\frac{\Delta_z}{\Delta_x})}}\left[(+1+\frac{\Delta_z}{\Delta_x}+i\frac{\Delta_y}{\Delta_x})\lvert\uparrow\rangle+\lvert\downarrow\rangle\right]$

Table 2.3: Eigenstates and energies of the electron subspace in the presence of a strong Voigt geometry field and weak perpendicular fields $\boldsymbol{B} = B_y\hat{y} + B_z\hat{z}$.

eigenstates. These new eigenstates are no longer equal superpositions of the zero field electron spin eigenstates, but are unequal admixtures that depend on the exact ratios of the fluctuating perpendicular fields to the external Voigt geometry field. The new energies of these eigenstates are just the vector lengths of the total magnetic field, which fluctuate on timescales on the order of 1 ms with typical distribution widths of between 20-40 mT [89]. An important consequence of the new admixture eigenstates is that the polarization selection rules also fluctuate with the magnetic field. For instance, the new optical selection rule connecting the $|x'+\rangle$ state to the $|T_x+\rangle$ state

is calculated below:

$$\begin{aligned}\mu \langle T_x + |\boldsymbol{E}|x'+\rangle &= \frac{\mu}{\sqrt{2}(1+\frac{\Delta_z}{\Delta_x})}\left[(\langle T+| + \langle T-|)\boldsymbol{E}((1-\frac{\Delta_z}{\Delta_x} - i\frac{\Delta_y}{\Delta_x})\,|\uparrow\rangle + |\downarrow\rangle)\right] \\ &= \frac{\mu E}{2\sqrt{2}(1+\frac{\Delta_z}{\Delta_x})}\left[(-\frac{\Delta_z}{\Delta_x} - i\frac{\Delta_y}{\Delta_x})\hat{x} - i(2+\frac{\Delta_z}{\Delta_x} + i\frac{\Delta_y}{\Delta_x})\hat{y}\right]\end{aligned} \tag{2.18}$$

Thus, the formerly vertically-polarized transition has become elliptically polarized due to the fluctuating OH field components which are perpendicular to the external Voigt geometry field. This deterioration of the optical selection rules has important consequences for both optical spectroscopy as well as photonic-based quantum information technologies such as quantum key distribution (QKD) and quantum teleportation [11, 47, 90]. The selection rules derived here describe not only the polarization of the resonant excitation selection rules, but also the polarization of the scattered/emitted QD photons. If these photons are utilized for quantum teleportation, which requires that the photonic degrees of freedom including polarization and frequency are indistinguishable either between optical excitation shots or between QDs, then variations in optical polarization and frequency due to fluctuating nuclear fields will reduce the fidelity of such protocols. Additionally, increasing the external Voigt geometry magnetic field in order to reduce the percentage fluctuations of the total field compared to the x-component (Δ_z/Δ_x) does not necessarily increase the indistinguishability of the scattered photons since electronic spin-orbit coupling leads to an electron spin lifetime which is proportional to B^{-5}, thereby reducing the allowed time-of-flight of a scattered photon before the energy and polarization of the next photon fluctuates [91]. More significantly, a *net* nuclear spin polarization may be generated optically in a direction orthogonal to the external Voigt field. In such a scenario, this perpendicular field can be measured via either resonant excitation or non-resonant PL excitation, allowing for the vectorial reconstruction of the OH field present in a QD [92].

Another form of symmetry breaking which may occur in the strained QD system

is heavy-hole light-hole mixing (HHLH mixing). In the presence of in-built strain, which is at the heart of self-assembly of InAs/GaAs QDs when grown via the Stranski-Krastanov method, the heavy-hole and light-hole bands become mixed and the degeneracy between the bands is broken (∼10 meV) [93–96]. The symmetry breaking occurs when the QD becomes anisotropic in the x-y plane, i.e. that the dimensions of the QD are different in the $\hat{x}$ direction versus $\hat{y}$. Thus, the crystal structure symmetry is reduced from D_{2d} to C_{2v} locally [97]. In the case of HHLH mixing, the new mixed hole states become

$$|\psi_h^{\pm}\rangle = |\frac{3}{2}, \pm\frac{3}{2}\rangle_h - \frac{\gamma^{\pm}}{\Delta E_{l-h}} |\frac{3}{2}, \mp\frac{1}{2}\rangle_h \tag{2.19}$$

where $\gamma^{\pm} = \gamma e^{\pm 2i\theta}$, $\gamma = \langle\psi_{lh}|\frac{d}{dx} + i\frac{d}{dy}|\psi_{hh}\rangle$, and ΔE_{l-h} is the heavy-light hole band energy splitting [96]. Therefore, the extent to which the light-hole is admixed into the new hole state becomes greater as the HH-LH band splitting becomes smaller and the mixing integral becomes larger. Going back to the zero field band states, the selection rules associated with the $|\uparrow\rangle$ transitions are derived below:

$$\begin{aligned}
\langle\psi_h^{+}|\mu E|\uparrow\rangle &= \langle +\frac{3}{2}|_h \mu E| + \frac{1}{2}\rangle_e - \frac{\gamma^{+}}{\Delta E_{l-h}} \langle -\frac{1}{2}|_h \mu E| + \frac{1}{2}\rangle_e \\
&= \mu E \left[\hat{x}(-\frac{1}{\sqrt{2}} - \frac{\gamma^{+}}{\sqrt{6}\Delta E_{l-h}}) + i\hat{y}(-\frac{1}{\sqrt{2}} + \frac{\gamma^{+}}{\sqrt{6}\Delta E_{l-h}})\right], \\
\langle\psi_h^{-}|\mu E|\uparrow\rangle &= \langle -\frac{3}{2}|_h \mu E| - \frac{1}{2}\rangle_e - \frac{\gamma^{-}}{\Delta E_{l-h}} \langle +\frac{1}{2}|_h \mu E| + \frac{1}{2}\rangle_e \\
&= -\frac{\mu_z E_z \gamma^{-}}{\Delta E_{l-h}} \sqrt{\frac{2}{3}} \hat{z}
\end{aligned} \tag{2.20}$$

There are at least two consequences of the symmetry-breaking HHLH mixing. First, the formerly circularly-polarized electron-trion transitions become elliptically polarized. The second optical selection rule calculation connecting the $|\psi_h^{-}\rangle$ state to the $|\uparrow\rangle$ electron is now non-zero, compared to the HHLH mixing-free case in which there are no cross-transitions. This result is especially important with implications for optical pumping; the first demonstration of resonant electron spin optical pumping

was performed at both zero magnetic field and Faraday geometry in a QD with strong HHLH mixing [98]. In that experiment, the weak spontaneous emission channel that opens up on the cross-transition leads to optical pumping into the $|\downarrow\rangle$ state. It is noted that this optical selection rule corresponds to a dipole which is polarized along the z-axis; resonant optical excitation would require an optical electric field with a component along the propagation direction. It is known [99, 100] that for beams with finite spatial extent (ie. Gaussian), that in the paraxial limit a circularly-polarized beam is required to have a z-component given by $\frac{-i}{k}\left(\frac{\partial E_0}{\partial x} - i\frac{\partial E_0}{\partial y}\right)$, where $E_0(x, y)$ is the spatial profile of the electric field. In addition, HHLH mixing plays a very significant role in DNP processes, and may be detected in a QD by careful examination of the polarization selection rules under resonant excitation.

2.6 Electric field structure

The QDs under investigation in this thesis are embedded in a larger semiconductor structure which allows for electric biasing of the structure, resulting in an electric field pointing along the growth axis. The significance of the electric field in the context of the DC Stark shift will be discussed more thoroughly in the next chapter. The biasing structure, which schematically is of the form of a diode with a n-i-QD-i-n-i-p structure, allows for the deterministic charging of the embedded QDs, where n,i,p refers to n-(i-,p-) doped GaAs (Section 2.2). The sample may be qualitatively analyzed as a n-i-p diode, since the first n-i-n section of the diode does not contribute to the overall built-in electric field, only acting to increase the effective diode thickness. When the sample is unbiased, ie. no voltage is applied across the annealed and non-annealed contacts of the sample (Figure 2.2), an in-built electric field exists across the sample due to the differing Fermi levels (relative to the bands in the respective layers, but not globally across the structure since the system is in thermal equilibrium) in the n-GaAs and p-GaAs layers (Figure 2.6). In the n-GaAs reservoir, the Fermi level (highest energy state of electrons in that reservoir) is closer to the conduction band, compared to the p-GaAs layer where the doping leads to the Fermi level being closer

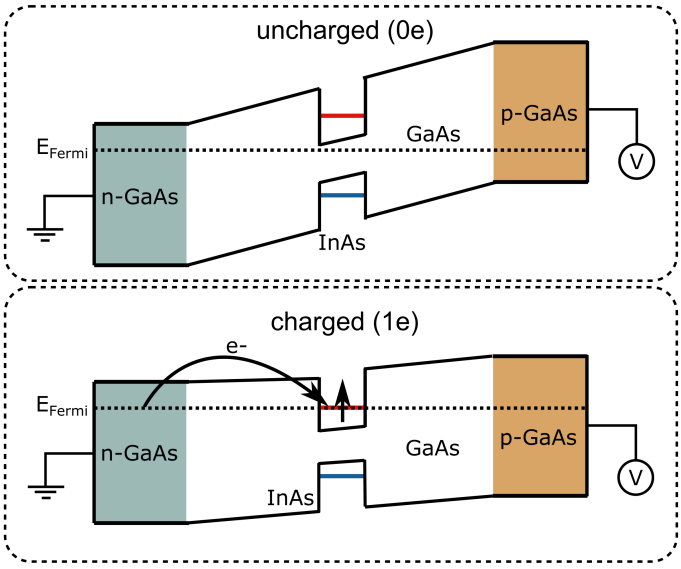

Figure 2.6: Schematic of diode biasing of the QD, leading to deterministic charging. The diode structure is simplified into a n-i-QD-i-p structure without neglecting the qualitative physical behavior of the QD diode system.

to the valence band.

At this point, depending on the doping levels of the two reservoirs and the location of the QD layer relative to them (distance along the growth axis), the discrete energy levels of the QD due to quantum confinement are likely tuned out of resonance with the Fermi level (top panel of Figure 2.6). If the n-GaAs reservoir is grounded and the p-GaAs reservoir is connected to a positive (forward) bias, injection of electrons into the p-GaAs lowers the conduction band relative to the Fermi level, which may bring the QD discrete energy level into resonance with the Fermi reservoirs. When this condition is satisfied, electrons actively tunnel back and forth between the n-GaAs reservoir and the QD; this regime is hereby referred to as the *co-tunneling*, since the resonant enhancement between the Fermi level and the QD level leads to tunneling over the slight energy barrier arising from the slope of the conduction band as a function of position along the growth direction [62].

The stability ranges for each charge configuration (0e, 1e, 2e, et cetera) have complicated dependences on the exact structure of the diode, QD confinement energies, and the exchange interactions between confined carriers, and have been studied ex-

tensively elsewhere [62, 101]. It is observed both experimentally and theoretically that charge stability regimes occur for which a given charge configuration is more energetically favorable than another; at low biases in this structure, the 0e and exciton configurations are stable, switching abruptly to stable 1e and trion configurations at higher biases. This bias dependence is investigated in the next Chapter using bias-dependent photoluminescence.

2.7 DBR cavity

A novel feature of this sample as compared to other samples studied by previous researchers in this group is the incorporation of a distributed Bragg reflector cavity (DBR) surrounding the QD layer. Dielectric mirrors which depend on the phenomena of multi-wave interference may be fabricated out of sub-wavelength layers of semiconductor materials [100]. A single mirror may be fabricated out of a large number of alternating layers of two materials with differing indices of refraction such as GaAs and AlAs (or Si and SiO_2). However, one may fabricate an on-chip optical cavity system by the utilization of two DBR mirrors, and the parameters of the associated reflectivity/transmission resonance may be tuned by adjusting the number of alternating DBR layers and the percentage difference in the two indices of refraction. These periodic systems may be treated formally in many ways, including similar band gap-style methods as used to analyze electronic wavefunctions in periodic crystal structures, resulting in forbidden frequency ranges over which the mirrors/cavities are high quality reflectors [100].

In this sample, the back DBR mirror consists of 10 pairs of a 69 nm layer of GaAs and and 82 nm layer of AlAs, while the front mirror consists of 4 pairs of the same alternating layers. The cavity resonances associated with two different DBR samples from the same wafer were measured by scanning a narrow bandwidth laser (MSquared Solstis) across a broad range of wavelengths (10100-11600 cm^{-1}, or 990-862 nm) while measuring the reflectivity (and transmission for one sample which was polished on the backside to reduce scattering) on an APD and the input power

before the cryostat and dividing the two (Figure 2.7, reflectivity/transmission axis has arbitrary units due to lack of absolute calibration). In the first sample (left panel), as the laser is scanned around 10390 cm^{-1}, the reflectivity drops dramatically and the transmission increases, and the reflectivity/transmission profiles have Lorentzian-like (Airy functions, technically) lineshapes. The reflectivity and transmission curves in the left panel are taken at room temperature, indicating that the optical response is due to the DBR cavity structure rather than any QD optical response. The Q-factor, defined here as $Q = \frac{f_c}{f_{FWHM}}$ is equal to approximately 100, indicating a strong enhancement of the internal electric field in the cavity compared to samples without DBR cavities.

The second sample (right panel of Figure 2.7) is a reflectivity scan of the sample under study for the remainder of this thesis at both room temperature (black) and 5.5 K (red) over a broader range than the previous scan. Two new features are observed: first, the reflectivity starts to drop at higher wavenumbers, likely due to resonant absorption in the InAs wetting layer and the bulk GaAs. Second, the reflectivity resonance shifts to higher energies when the sample is cooled to 5.5 K, which is likely due to the modification of the index of refraction of the involved semiconductors at lower temperatures, while retaining a high Q-factor [102].

The DBR cavity utilized in this sample benefits optical spectroscopy in a number of ways. First, the internal optical electric field is enhanced in the cavity when the laser frequency is in the vicinity of the cavity resonance. The exact factor of electric field enhancement may be determined using the transfer matrix formalism; experimental measurements of Rabi oscillations indicates an approximately 9x enhancement in the DBR cavity compared to samples without a cavity. Thus, experiments which require high optical input powers such as detuned Raman rotations benefit from such an enhancement. Second, scattered photon rates in the reflection geometry increase dramatically in this system due to a higher back mirror reflectivity compared to the front mirror. The exact physics of this enhancement are not analyzed here, but are generally understood to arise from a modification of the scattering response as a function of angle away from the growth axis, focusing the scattering into a tighter

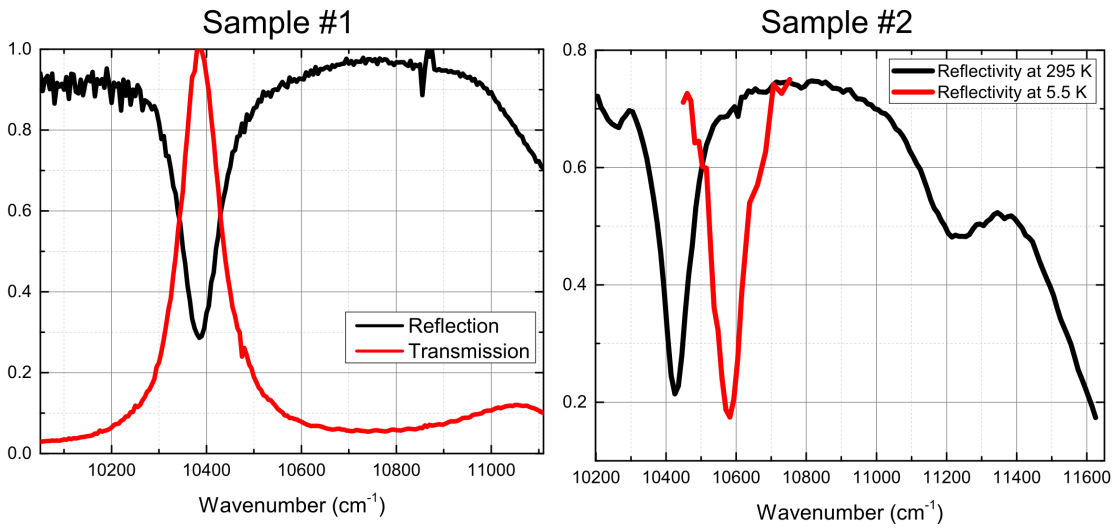

Figure 2.7: QD DBR cavity reflectivity and transmission. Left: sample #1 (not the main study of this thesis) reflectivity (black) and transmission (red) normalized by input power at room temperature. Right: sample #2 reflectivity at room temperature (black) and 5.5 K (red).

cone which is collected with higher efficiency [103].

2.8 Chapter summary

In this chapter, some fundamental aspects of the InAs/GaAs semiconductor QD system were introduced, including the optical and electronic properties. Calculations of the optical selection rules were carried out in the cases zero magnetic field and the Voigt (in-plane) magnetic field configuration, as well as example calculations in the presence of perturbatively small multi-component magnetic fields and heavy-hole light-hole mixing. A very brief overview of the electric field structure and DBR cavity structures are given. The next chapter will discuss in great detail continuous wave (CW) spectroscopy of the QD system, in which more complete details about the DC Stark shift due to the electric field biasing is investigated.

CHAPTER 3

Continuous wave (CW) optical spectroscopy of single InAs QDs

3.1 Introduction

Continuous wave (CW) spectroscopy is utilized for the investigation of QD optical properties due to the narrow linewidths of the lowest energy exciton/trion transitions, typically on the order of 2 μeV in InAs at 5 K. High-resolution CW Ti:Saph lasers routinely yield sub 50 kHz-linewidth outputs, which can be tuned over a broad wavelength range between 700-1000 nm, allowing for both initial QD characterization using off-resonant photoluminescence (PL) measurements as well as on-resonant excitation resulting in absorption, fluorescence, and scattering. This chapter will explain the details of the CW spectroscopy techniques utilized in this thesis. First, the PL technique is introduced, in the context of the DC Stark shift and magnetic field tuning. Then the density matrix and Maxwell-Bloch equations are introduced, which allows for modeling and fitting of optical spectra measured using resonant excitation. The bias-modulation lock-in amplification technique is then discussed, which is the workhorse of high-resolution QD experiments performed in this research group. The strength of the technique is demonstrated by its resolution enhancement over non-resonant PL measurements. Broadband high-resolution DC Stark shift experiments are performed that demonstrate statistical correlation between the linear and quadratic Stark shift terms. Then, two fluorescence and scattering techniques are introduced: resonance fluorescence and Raman scattering, which allow for a direct measurement of scattered photons, resulting in lineshapes that are free of reflectivity interference issues that

obscure quantitative spectroscopic results in modulation spectroscopy. Finally, the concept of optical pumping is introduced, and two beam experiments are discussed in the context of coherent population trapping of the electron spin states.

3.2 Photoluminescence (PL) measurements

As discussed in Chapter 2, self-assembled InAs QDs are optically active due to the direct bandgap of InAs/GaAs inherited from the bulk system that becomes quantized under the strong quantum confinement. The new optical spectra of the confined and strained QD system differ significantly from the bulk GaAs/InAs system in energy, polarization, and oscillator strength. The first tool that is typically utilized in studying the QD system is *photoluminescence* (PL). A typical CW PL experiment is performed via optical excitation of carriers (electrons and holes) either above the band-gap of the host material ($E_{GaAs} = 1.519$ eV (816 nm)), or into the *wetting layer* of the QD system. The wetting layer is a unique feature of the SK-grown QD system; as observed using cross-sectional STM techniques (Figure 2.1), the coherent growth of the QD system on GaAs results in a monolayer to few monolayer-thick InAs layer below the QD which can effectively be treated like a quantum well in its optical properties. Because the quantum well structure only exhibits quantum confinement of carriers in the growth direction, a continuum of states exists (albeit with a density of states that differs from the bulk [104]) that may be optically excited (Figure 3.1). Typical energy splittings of around 150 meV are observed between the wetting layer absorption and exciton/trion recombination in the QD [105, 106]. When PL experiments are performed via excitation into either the bulk or wetting layer, the carriers rapidly non-radiatively decay via electron/hole-phonon scattering within tens of picoseconds [107], a relatively short time compared to typical radiative recombination times for the excitons of between 400 ps and 1.5 ns [108]. This non-radiative relaxation occurs due to multiple LO scattering events [107].

Although the wetting layer provides a continuum of states for optical excitation, the QD energy levels are discrete due to zero-dimensional confinement; recombination

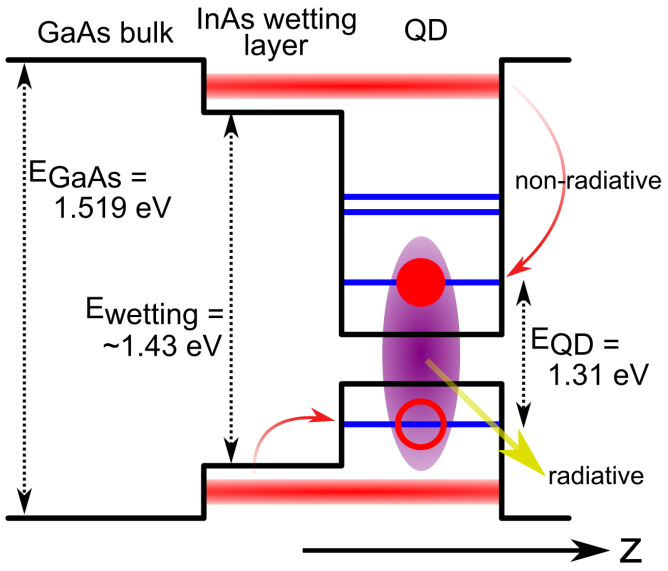

Figure 3.1: Processes leading to photoluminescence (PL).

of the confined exciton/trion leads to narrow linewidth emission lines, which in the absence of inhomogeneous broadening due to environmental charge fluctuations and nuclear spin broadening, leads to spontaneous emission limited linewidths. These linewidths are not significantly broadened by optical injection into the wetting layer at reasonable PL pump powers (below the regime in which biexciton creation starts), although single-photon time-correlation experiments show that the photon indistinguishability does improve using resonant excitation as compared to wetting layer injection. This improvement is due to a reduction in "timing jitter" of the emission of the photon under resonant excitation due to the elimination of the non-radiative relaxation processes [109, 110]. Thus, the PL scheme is a relatively simple experimental protocol which does not require precise knowledge of the absorption/emission spectrum of the discrete energies of the QD.

A typical PL experiment is performed at low temperature (2-10 K) using optical powers in the range of 1-100 μW depending on the presence of a DBR cavity structure; the PL spectra demonstrated in this thesis utilize a pump wavelength of ~893 nm (1.388 eV), which is below the band-gap of GaAs and approximately in resonance with the wetting layer transitions (provided by either an MSquared Solstis laser or

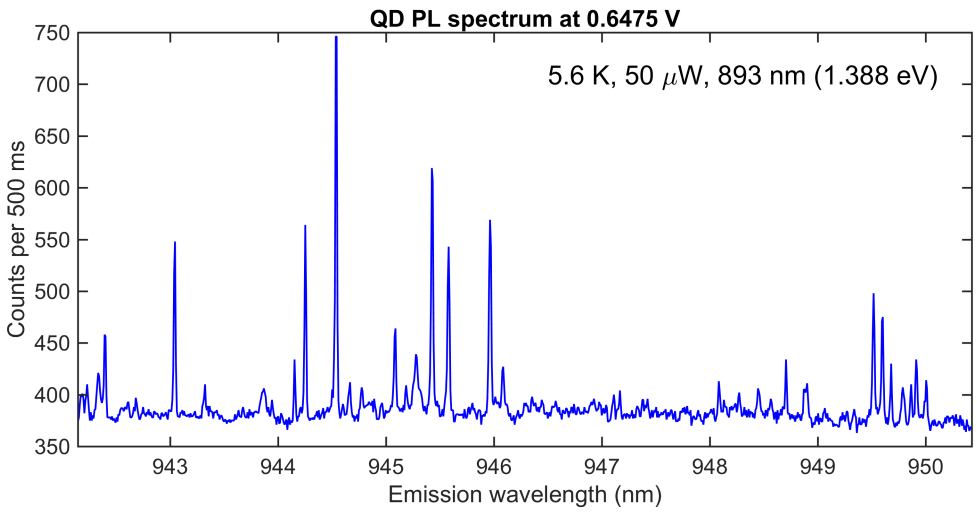

Figure 3.2: Single photoluminescence (PL) spectrum taken in the trion stability range. PL counts are integrated for 500 ms under excitation from 50 μW of 893 nm narrow bandwidth laser light.

Coherent MBR). The pumping beam is intensity-noise stabilized by a noise eater, collimated, and focused down onto the sample by a 0.68 NA aspherical lens, resulting in an optical beam spot at the QD layer of approximately 1 μm. The PL spectrum is then collected in either the reflection or transmission geometry depending on the nature of the sample structure, and the excitation beam is filtered by a long-pass spectral filter; the emission is sent to a grating spectrometer (Jobin Yvon 640 (640 mm focal length), 1800 lines/mm, blazed between 450 and 850 nm, 11 cm wide) and dispersed on a thermo-cooled high-sensitivity CCD (Andor Newton DU920), resulting in a linear dispersion at the CCD image plane of approximately 0.008 nm/pixel, or 11 μeV resolution. A single PL spectrum is plotted in Figure 3.2 where the sample bias (discussed in more detail later in this section) is fixed in the trion stability range. Sharp and bright emission peaks are observed over at least a spectral range of 942-951 nm; many of the peaks have widths which are limited by the spectrometer dispersion, indicating that narrow emission lines can be generated by recombination of optical carriers generated in the wetting layer. More importantly, PL can be used as a relatively high-resolution spectroscopy technique for determining the energy levels associated with confined QDs.

Examining the single spectrum from Figure 3.2, multiple lines are observed; a single spectrum does not allow for the unique determination of the energy levels of a single QD, since multiple QDs are within the excitation spot due to relatively high QD growth density. Additionally, there is very considerable inhomogeneity of the PL emission lines relative to the homogeneous linewidth for a single QD. This inhomogeneity problem plagues the QD system from a technological perspective, inhibiting easy incorporation QDs into photonic nodes due to photon distinguishability. However, their inhomogeneity actually provides a useful spectroscopic advantage; in samples with moderate QD areal densities, spectral inhomogeneity allows for the separation of emission lines spectral in both PL and resonant excitation, ensuring that one can excite a single quantum emitter.

The electric field bias structure (Section 2.6) may be utilized to produce bias-dependent PL maps which may allow for the determination of single QD energy level structures. Two features of self-assembled QDs become apparent under the application of a DC electric field along the growth axis. First, as described above, the QDs are highly inhomogeneous; thus, the accompanying Stark shifts associated with each QD are different. Second, charge stability regimes as introduced in Section 2.6 of the last chapter become obvious when PL lines are observed to turn off completely at certain electric bias values that are common to many lines in a single PL bias map. At the bias points where the PL lines disappear, a new charge configuration has become the lowest energy state of the system, whether in the excited state or ground state (these bias values do not always overlap entirely, leading either to bias regions with multiple charge states available or no charge states at all). These phenomena, both the DC Stark shift and the charge stability ranges are demonstrated in Figure 3.3. Lower biases between 0 and approximately 0.5 V correspond to neutral exciton states, which are DC Stark shifted over a wide emission energy range (as large as 90 GHz in this sample) before abruptly turning off. At higher bias between 0.5 and 0.7 V, the single electron becomes the energetically favorable ground state; the energy shift as a function of bias voltage becomes smaller, indicating a smaller permanent dipole moment of the trion state compared to to the exciton. There are

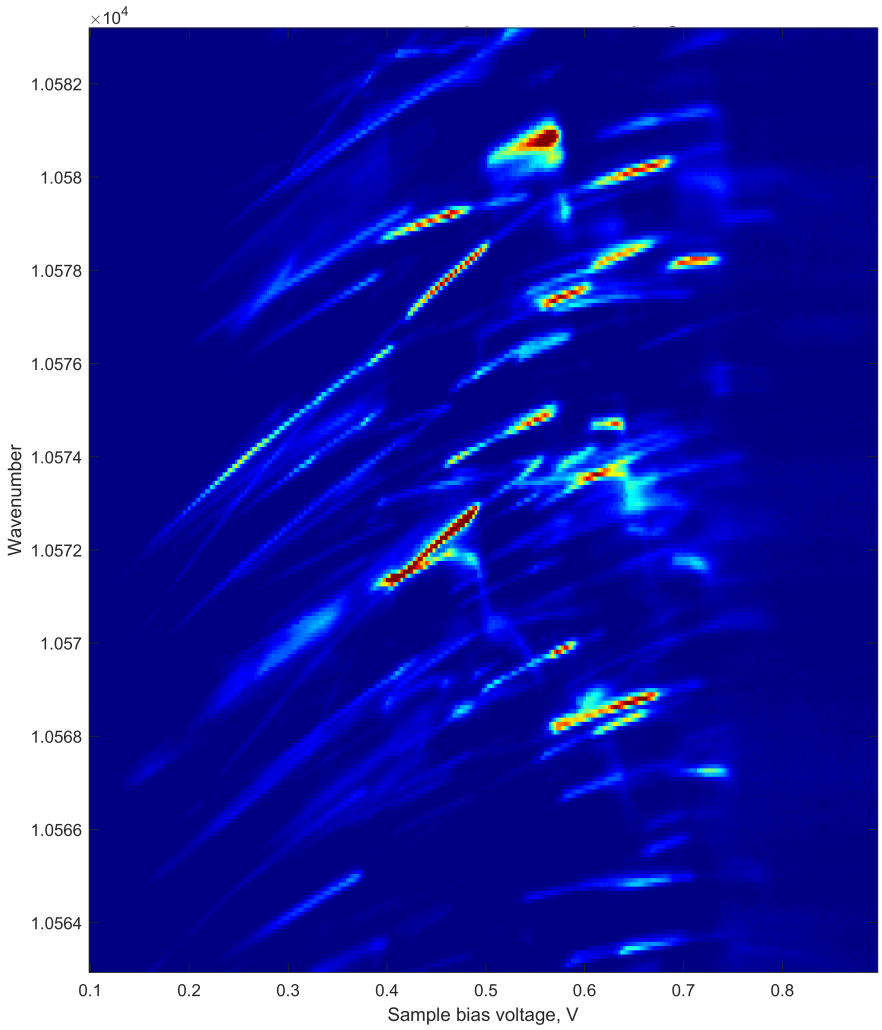

Figure 3.3: PL bias map. Bottom axis is the sample bias voltage (volts), and each vertical slice of the map is a single PL spectrum.

noticeably more complicated features that likely arise from defective QDs that are highly anisotropic, affected by trapped charge carriers at interfaces, or exhibit fine structure. However, the fine structure due to the electron-hole exchange which arises strongly in the exciton compared to the trion is typically too small to be easily measured in PL measurements, resulting in a doublet feature with splittings smaller than the spectrometer resolution (11 μeV). The electron-hole exchange arises due to the Coulomb attraction between the electron and hole and the requirement that the total multi-particle wavefunction is antisymmetric since the particles are fermions [76]. The interaction has been studied extensively in the bulk, quantum wells, and QDs.

The interaction can be split up into two regimes, the short-range and long-range interactions, where the short-range is only taken over the unit cell and the long-range interaction is calculated over the unit cells that fall within the Bohr radius of the exciton/trion [111–115]. The interaction is referred to as an exchange interaction because the Hamiltonian may take the form of $H_{e-h} = -\sum_{x,y,z}(aJ_{h,i}S_{e,i} + bJ^3_{h,i}S_{e,i})$. In summary, the short-range interaction splits the bright, for example $|\uparrow\Downarrow\rangle$, and dark, for example $|\uparrow\Uparrow\rangle$, excitons energetically, and the long-range interaction splits the bright exciton energy levels.

Going into more detail on the physics of the quantum-confined DC Stark effect, the energy shift on the exciton/trion confined to the QD is given by $\Delta E = -pF+\beta F^2$, where p is the permanent dipole moment of the charge system, β is the polarizability of the electron and holes (a second-order perturbation theory effect [116]), and $F = -(V_{bi} - V)/t$ is the electric field across the ninip diode,V_{bi} is the built-in field due to doping of the n- and p-GaAs layers, t is the thickness of material between the first n and final p layers, and V is the bias voltage [117–120]. When the energy level shifts on the states are small compared to the exciton/trion binding energies, the Hamiltonian can be treated perturbatively, resulting in a mixing of states that have differing wavefunction parity. However, a unique effect in the QD system result from confinement: the system differs dramatically from the Coulomb-bound exciton/trion state due to the QD confinement potential, hence the *quantum-confined* nature of the Stark effect here. This confinement in turn affects the permanent dipole moment and polarizability of the wavefunctions. In fact, this quantum confinement is strong enough that the electrons and holes (in the absence of an electric field) are spatially-separated in the QD, with the holes occupying the base of the structure and the electron occupying the apex of the cone/pyramid [120], resulting in a permanent dipole moment that leads to a large DC Stark shift but may also reduce the oscillator strength.

The DC Stark shift is utilized throughout this thesis as a very powerful tool for tuning the QD in and out of resonance with the laser, which is useful for bias-modulation spectroscopy (Section 3.4) and background subtraction in resonance fluorescence mea-

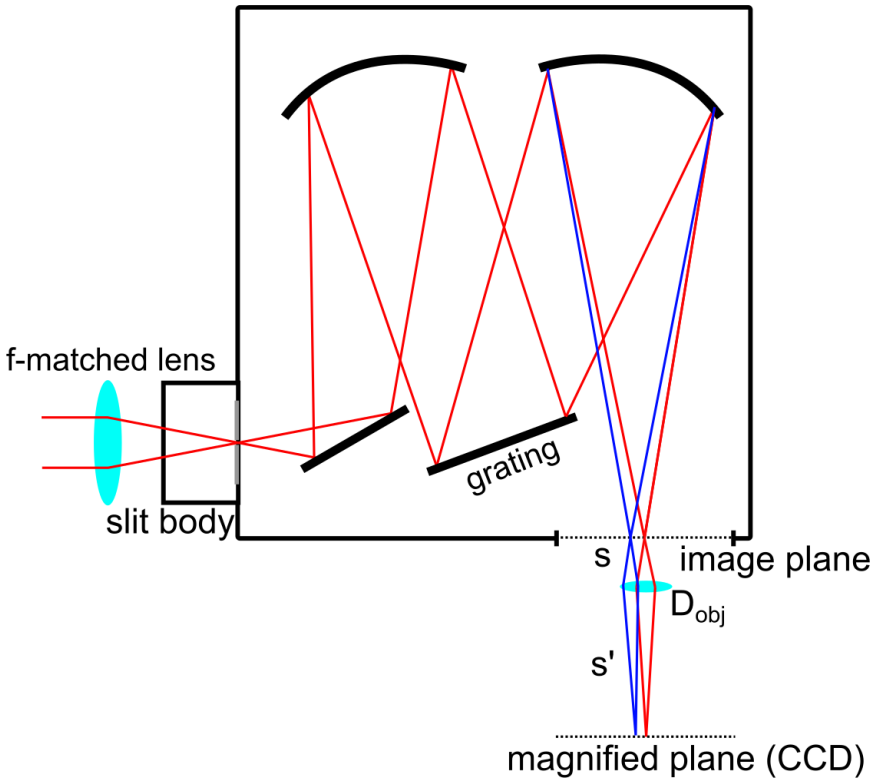

Figure 3.4: Spectrometer magnification scheme, with details written below.

surements (Section 3.5). A statistical analysis of the DC Stark shifts of 97 QDs as measured using broadband high-resolution modulation spectroscopy will be presented in Section 3.4.

If the goal of the PL experiments is to determine the line centers of each PL line with high precision, the spectrometer can improved dramatically, at the cost of examining a narrower spectral region of the PL and with increased optical complexity. The optical schematic for the improved spectrometer is displayed in Figure 3.4. In this configuration, the emission from the QD is sent into a lens which is f-matched to the spectrometer, and the light is focused down onto the slit. The diverging light is reflected off a mirror directed towards curved mirrors; if the spectrometer is mode-matched correctly, the light should be collimated after hitting the first curved mirror. The light is then diffracted off of the grating, which determines the *angular* dispersion of the spectrometer, with a higher angular dispersion for a greater number of lines

per millimeter. The light is then refocused by a second curved mirror onto where the CCD (image plane) would typically sit. Instead, the CCD is removed and an objective lens is introduced with some diameter D_{obj} at a distance s from the image plane, the spectrum will be magnified and focused at some distance s' from the objective, and the magnification of the spectrum is given by s'/s. To be clear, the spectrometer benefits from an increase in the *linear* dispersion, not the angular dispersion; the overall linewidths of the emission lines are determined by the angular dispersion of the grating. There are a number of practical concerns here made in choosing the optics; the diameter of the objective limits the amount of light reaching the CCD in the magnified plane. Additionally, a tighter objective (higher NA) will result in a greater magnification, but the distance s' increases, and may become unfeasibly large in the lab. Higher magnification objectives are more sensitive to vibrations, resulting in noise on the magnified image at the new CCD plane. One must also take care to use objective lenses that do not introduce considerable spherical abberrations, which will abberrate the resulting spectrum. Magnifications of between 15x and 25x were achieved in the lab.

What is the point of this magnification? If one wishes to determine the line centers with greater precision, the QD emission line of choice may be expanded over a large number of pixels on the CCD image plane. Thus, one may then utilize either derivative methods or lineshape fitting to determine the lineshape center with higher certainty. A comparison of the standard spectrometer setup (left) and the magnified PL (right) are displayed in Figure 3.5. The figure on the left has been digitally cropped over a narrower range of energies in the PL spectrum than normal, but the figure on the right is not cropped: the spectrum shown filled the CCD. Differences in intensity and a fine structure in the DC Stark shift are observed in the figure on the right more easily than the left, allowing for higher resolution studies than normally accessible. Although a pressure-tuned etalon was eventually utilized for the Raman scattering experiments used to study small DNP-induced shifts for a number of reasons discussed in Chapter 5, this method may provide useful for studying large DNP shifts, Stark shift effects, and coupled QD effects without having to resort to

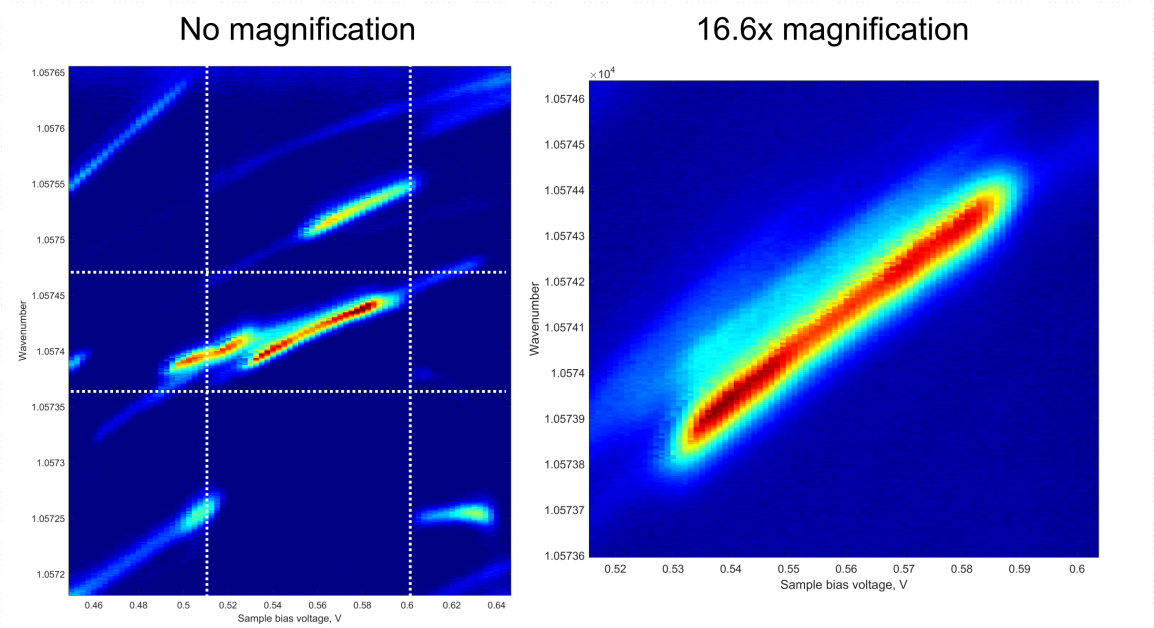

Figure 3.5: Comparison of PL taken using standard spectrometer configuration to the magnified configuration. Left: standard spectrometer configuration. White dashed lines indicate region over which spectrum on the right is taken. Right: CCD removed, objective inserted after CCD plane, spectrum imaged onto CCD, resulting in 16.6x magnification of spectrum. The QD feature observed in the left figure at slightly higher energies at the low bias end not observed in the figure on the right is emission from a different QD that is out of the field of view.

resonant excitation experiments.

Last, the non-resonant PL method was utilized to perform early characterization of the QD under application of a Voigt (in-plane) magnetic field. In this configuration, the PL beam is linearly-polarized at 45° relative to the vertical QD axis; after the low-pass filter which eliminates the excitation beam in the collection path, polarization analyzer optics may also be used to analyze the polarization of the QD emission. A large body of literature has been devoted to the examination of PL line shifts under circularly-polarized excitation, which through various mechanisms generated nuclear spin polarization as measured through the PL, examined in Chapter 4. This nuclear spin polarization effect is avoided by the utilization of the linearly-polarized pump. PL of the QD studied in the Raman scattering chapter at magnetic fields ranging from 0 to 3 T are shown in Figure 3.6. As the magnetic field is increased, the single line observed

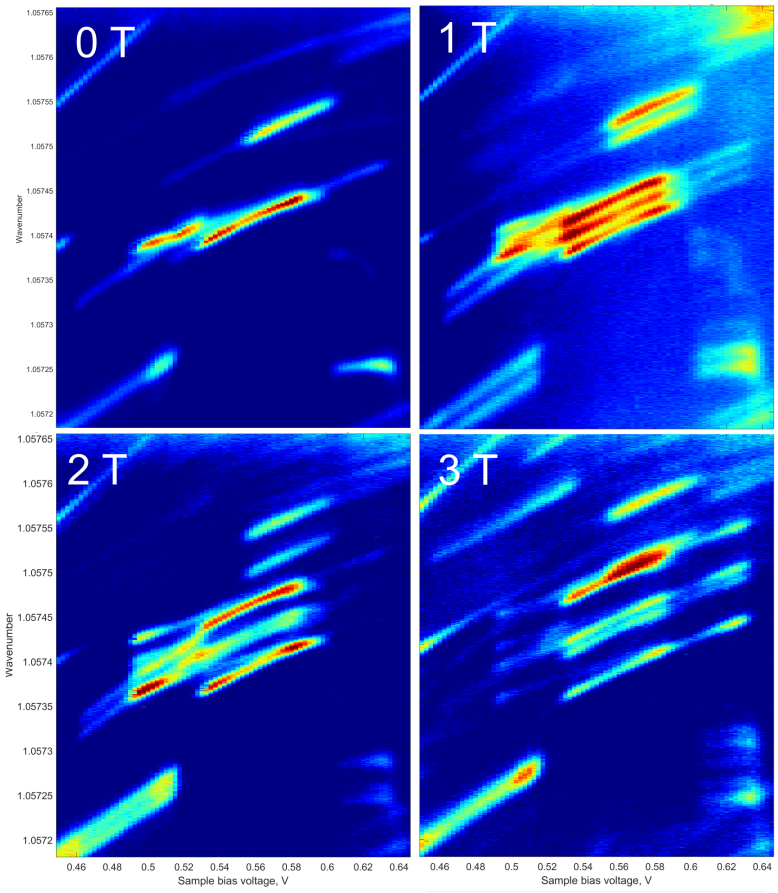

Figure 3.6: Comparison of PL taken at increasing Voigt geometry magnetic fields from 0 to 3 T (indicated in the top left corner of each panel). The sample bias range and emission energy range are the same for each of the four panels.

from bias ranges 0.52 to 0.6 V splits into four lines at 3 T, and further polarization analysis shows that the transitions are linearly-polarized; therefore identifying the resonance as corresponding to a trion. This simple experiment allows one to easily distinguish between excitons and trions, since excitons will only split into a doublet.

3.3 Density matrix formalism for optical absorption, fluorescence and scattering

One may utilize high-resolution CW spectroscopy to resonantly drive the optical transitions between the ground states (either the crystal ground state or the electron

spin state) and the excited states (exciton or trion). The light-matter interaction and subsequent evolution of the QD system is governed fundamentally by the Schrodinger equation, $i\hbar\frac{d}{dt}\left|\psi(t)\right\rangle = \hat{H}\left|\psi(t)\right\rangle$; a change is imparted on the state vector of the QD system by the interaction of the QD dipole with the optical electromagnetic field. A polarization is generated via the QD dipole, which imparts a change in the optical field, and is subsequently detected either via interference techniques such as homodyning or direct detection of the field scattered by the QD. In this thesis, a semi-classical approach is taken regarding the QD-light interaction, in which the QD system is quantized but the field is, for the most part, taken as classical (except in the discussion of Raman and Rayleigh scattering). In the semi-classical approach, the most convenient method for understanding the optical spectra under resonant excitation is the *density matrix* formalism. This approach is taken because it allows for the easy incorporation of decay and dephasing terms due to, for instance, spontaneous emission and pure dephasing (from collisions or electron-phonon scattering, for example).

More specifically, the density matrix is defined here as $\hat{\rho}(t) = \left|\psi(t)\right\rangle\left\langle\psi(t)\right|$, which is a matrix operator that is $n \times n$, where n is the size of the span of the Hilbert space of the QD-light system, with matrix elements given by $\langle n|\rho(t)|m\rangle = a_n(t)a_m^*(t)$, where the coefficients are the amplitudes of the wavefunction of the system, ie. $\left|\psi(t)\right\rangle = \sum a_n(t)\left|n\right\rangle$ (note the time-independent eigenstates in the Schrodinger picture). Expectation values of Hermitean operators (the measurables of the system) are given by $\langle\hat{A}\rangle = \langle\psi(t)|\hat{A}|\psi(t)\rangle = \sum_{nm}\rho_{nm}A_{mn} = Tr\left[\rho(t)A\right]$.

Most importantly, the unitary evolution of the density matrix is given by

$$i\hbar\frac{d\rho}{dt} = [H, \rho] \tag{3.1}$$

where H is the full Hamiltonian which includes both the QD bare Hamiltonian and the light-matter interaction. Although this thesis is not primarily concerned with the physics of the basic two-level system, which can be found for instance in the zero-field trion case (approximately, neglecting heavy-light hole mixing and fluctuating

Overhauser fields), it is instructive to understand that particular case. After utilizing the rotating wave approximation through which terms that oscillate at $\omega + \omega_0$, or approximately twice the natural frequency of the two-level system are tossed aside, the Hamiltonian for the system is given by [45]

$$\hat{H}(t) = \frac{\hbar}{2}\begin{bmatrix} -\omega_0 & \Omega_0^*(t)e^{i\omega t} \\ \Omega_0(t)e^{-i\omega t} & \omega_0 \end{bmatrix} \tag{3.2}$$

where ω_0 is the natural frequency of the two-level system, ω is the driving (laser) frequency, and $\Omega_0 = -\mu_{21} \cdot \epsilon E_0(t)/\hbar$ is the Rabi frequency. Thus, the equations of motion can be derived by plugging in the Hamiltonian to Equation 3.1, with the ρ_{ii} terms corresponding to the population in the $|i\rangle$ state and ρ_{ij} corresponding to the coherences between the eigenstates. However, in order for these density matrix elements to be useful, one must find a way to relate them back to the optical response of the system. There are a multitude of ways to accomplish this, and a few will be discussed in this thesis.

The first method is called the Maxwell-Bloch equations [45], which relates the density matrix elements calculated using Equation 3.1 to the polarization term that is plugged into Maxwell's equations. Neglecting transverse beam effects and working in the plane wave limit, the wave equation is given by

$$\frac{\partial^2 \boldsymbol{E}}{\partial Z^2} - \frac{1}{c^2}\frac{\partial^2 \boldsymbol{E}}{\partial t^2} = \frac{1}{c^2\epsilon_0}\frac{\partial^2 \boldsymbol{P}}{\partial t^2} \tag{3.3}$$

where $\boldsymbol{P}$ is the polarization that results from the QD system. This result is relatively general; however, for simplicity and illustration, one may treat an optical field transmitted through a medium consisting of two-level systems, resulting in an expression for the expectation value of the polarization given by

$$\langle P(z,t)\rangle = \mathcal{N}\left[\mu_{21}\langle\rho_{12}\rangle e^{-i(kz-\omega t)} + \mu_{12}\langle\rho_{21}\rangle e^{+i(kz-\omega t)}\right] \tag{3.4}$$

where the coherence terms are averaged over their inhomogeneous distributions

(velocities, charge and magnetic field fluctuations). Thus, it is seen immediately that the coherence generated in the two-level system between the ground and excited states by the optical excitation leads to a polarization term which can interfere with the driving field, resulting in changes in reflectivity and transmission of the driving field. Subsequently, further approximation may be made by assuming the slowly varying amplitude and phase approximation, which says that the electric field amplitudes vary slowly in the medium, which physically corresponds to a medium with index of refraction relatively close to 1 and without much absorption. This is somewhat unrealistic when considering the GaAs/InAs QD system, with bulk index of refraction of around 3.5 in the 900-1000 nm range, and QDs which are highly absorptive. However, the consequent result of the calculation is still illustrative of basic light-matter interactions.

The result of the ensuing calculation after making the approximation is that [45]

$$\frac{\partial E}{\partial z} = \frac{i\mathcal{N}k\mu_{12}}{\epsilon_0}\left\langle \rho_{12}(z)\right\rangle \tag{3.5}$$

with $\mathcal{N}$ equal to the emitter density. Thus, the change in the optical electric field is related to the density matrix coherence term. It is important to note that the density matrix coherence term is complex, and that this leads to both absorption (decay of the field) and refraction (phase changes in the field).

A few more steps are required to utilize the Maxwell-Bloch equations. First, radiative relaxation and pure dephasing of the two-level system must be taken into account. The spontaneous emission of the two-level system may be approached via the Weisskopf-Wigner approximation [45], which results in a decay of the excited state population down into the ground state on timescales that are determined in atomic systems by the fine structure constant, reduced dipole matrix elements connecting the two states by the optical field, and the natural frequency of the two-level system. However, this radiative decay is approached in the solid-state typically by taking a phenomenological decay approach. Without additional dephasing, this radiative decay causes a dephasing of the two-level coherence at half the rate of the population

decay. Pure dephasing (transverse relaxation), or decay of the coherences without population decay (longitudinal relaxation), may occur in the solid-state due to interactions with the lattice and the nuclei associated with each lattice site, whether through electron/hole-phonon scattering or nuclear spin flips.

In summary, the relaxation and decay in the two-level system resulting in non-unitary evolution of the density matrix elements is taken into account by additional terms

$$\text{relaxation terms} = \mathcal{L} = \begin{bmatrix} \gamma_2 & -\frac{\gamma_2}{2} - \Gamma \\ -\frac{\gamma_2}{2} - \Gamma & -\gamma_2 \end{bmatrix} \tag{3.6}$$

where γ_2 is the radiative relaxation rate due to spontaneous emission, and Γ is the pure dephasing rate.

One last step is typically utilized to eliminate the oscillating time dependences of the density matrix elements under continuous wave excitation. A unitary transformation of the wavefunction, and therefore the density matrix elements, may be utilized without changing the fundamental physics of the problem. If the state amplitudes in the Schrodinger picture $\vec{a}(t)$ are transformed by $\vec{a}(t) = \hat{U}(t)\vec{c}(t)$, then the transformed Hamiltonian for the equations for motion of the $\vec{c}(t)$ amplitudes is given by

$$H_{trans} = \hat{U}^\dagger \hat{H} \hat{U} - i\hbar \hat{U}^\dagger \frac{\partial \hat{U}}{\partial t} \tag{3.7}$$

which can then be plugged in to the density matrix equations of motion. For the two-level system, the state vectors can be transformed using the field interaction representation [45], given by $|\psi(t)\rangle = c_1(t)e^{i\omega t/2}|1\rangle + c_2(t)e^{-i\omega t/2}|2\rangle$, which results in the following transformed Hamiltonian

$$\hat{H}_{trans}(t) = \frac{\hbar}{2} \begin{bmatrix} -\delta & \Omega_0^*(t) \\ \Omega_0(t) & \delta \end{bmatrix} \tag{3.8}$$

where $\delta = \omega_0 - \omega$ is the detuning. Now, one can solve for the density matrix coherence terms in the steady-state by setting the time-derivatives of the density matrix elements equal to zero. The coherence term for the two-level system is given by

$$\tilde{\rho}_{12} = \frac{i\chi\gamma - \chi\delta}{\gamma^2 + \delta^2 + 4\frac{\gamma}{\gamma_2}\chi^2} \tag{3.9}$$

where $\chi = \Omega_0/2$, $\gamma = \gamma_2/2 + \Gamma$. This is a very important result that contains commonly observed features in optical spectroscopy. First, the response is a complex Lorentzian, with a width that is given by $\sqrt{\gamma^2 + 4\chi^2\gamma/\gamma_2}$; the width is given by the spontaneous emission width, pure dephasing, and power broadening. Second, the optical response has a real and imaginary part; plugging this response into Equation 3.5 shows that the absorption is an even Lorentzian (peaked at $\delta = 0$) and the phase accumulated by the electric field is a dispersive, odd Lorentzian (zero at $\delta = 0$). In the QD system, the response is more complicated due to the effects of driving a single quantum emitter rather than the bulk response, and the interference of fields reflected off of interfaces will also play a role that is addressed using the *source-field* formalism (Section 3.4). However, a direct reflectivity measurement (which can be related to absorption under careful consideration of losses in the experimental system) for a single QD is typically given by the even Lorentzian term, with an example displayed in Figure 3.7, resulting in a 0.45% reflectivity change induced by a single quantum emitter.

More realistically, the electron-trion system is a four-level system in which, under the application of an external in-plane field, there are four optical transitions coupling the ground states to the excited states. The density matrix equations may be used to reproduce novel optical phenomena such as optical pumping, coherent population trapping, and Rayleigh and Raman scattering, as demonstrated in the next sections, with a Hamiltonian given by Equation 2.16.

3.4 Bias-modulated lock-in measurements of differential reflectivity

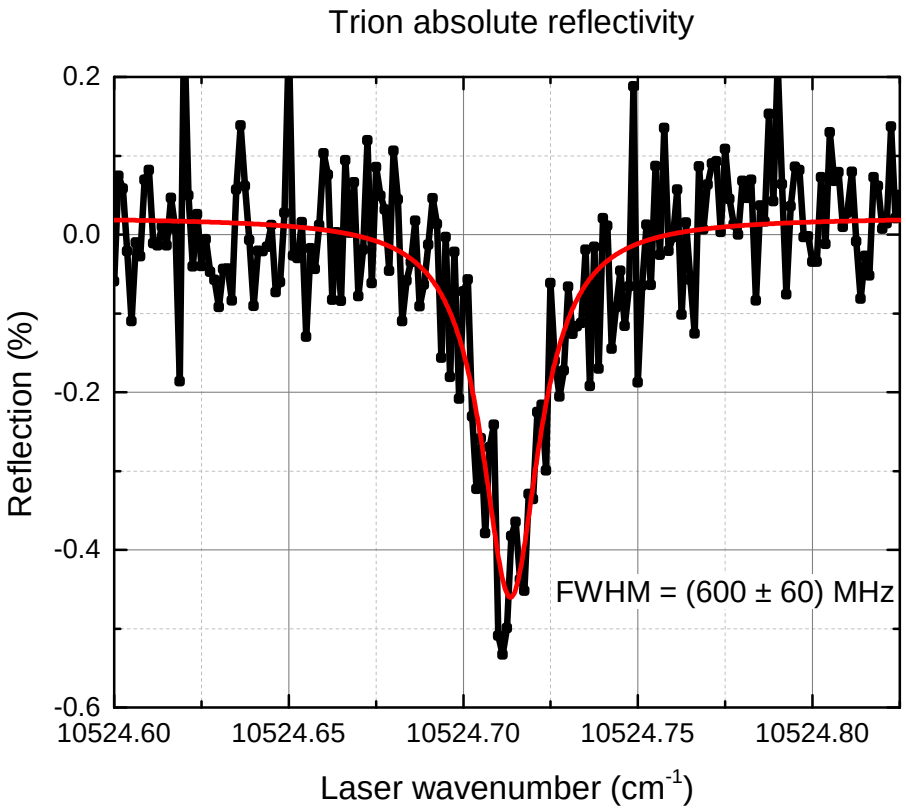

Figure 3.7: Trion absolute reflectivity measured by scanning a CW laser across the optical resonance at zero magnetic field. The reflectivity is measured by measuring the reflected optical power after the field interacts with the QD at an avalanche photodiode. The background is subtracted by DC Stark shifting the trion resonance away from the laser by a large bias shift of 500 mV.

While it is possible to measure the optical response of the single QDs when they are embedded in optical field-enhancing structures such as on-chip DBR cavities, the optical response typically leads to less than 1% modulation of the reflected and transmitted driving fields. At this level, experimental errors including high frequency noise due to fluctuating light backgrounds, low frequency optical power drift may entirely wash out the QD response as measured in a direct reflectivity/absorption measurement. The signal to noise ratio of the optical experiment may be improved dramatically by the utilization of *modulation spectroscopy* techniques. A typical experiment in the solid state environment consists of two fields, one or both of which is

amplitude or frequency modulated using a device such as an acousto-optic modulator. The response of an optically active sample can be detected more easily by demodulating the optical signal at a photodiode using a lock-in amplifier that is synchronized to the amplitude/frequency modulation of the driving fields. However, the situation is improved considerably in terms of technical considerations in the QD system due to the presence of the electric biasing structure (ninip diode). In this case, instead of modulating the optical fields, the QD optical resonance itself is modulated in and out of resonance with the optical field. As shown in Section 3.2, the DC Stark effect allows one to shift the optical resonance of the trion system by the application of an electric field along the growth axis. As it will be shown below, the DC Stark shifts are large enough that the QD may tuned entirely out of resonance, leading to large modulation depths of the reflectivity signal. The signal to noise ratio is then determined by the amount of background noise that is band-passed by the lock-in amplifer at the modulation frequency that is used to bias-modulate the sample.

More specifically, it was shown in the previous section that the absorption of the driving field for the emitter is given by a Lorentzian $A = \frac{\alpha\chi\gamma}{\gamma^2+(\omega_0+\Delta_S-\omega)^2}$, where Δ_S is the Stark shift of the resonance and α is the maximum absorption on resonance. Thus, changing the bias on the sample changes the absorption, and when the shift is much larger than the trion linewidth, the absorption is effectively turned off. It can be shown that the electric field generated by the QD optical polarization interferes with the driving field at the detector. Assuming that the QD transition is driven with a square wave bias between on resonance and far off resonance, the field at the square-law detector is given by

$$\begin{aligned} \text{Signal} &= |E_{inc} - E_{QD} f_{mod}(t)|^2 \\ &\sim E_{inc}E_{inc}^* + E_{QD}E_{QD}^* \sin^2(2\pi f t) - 2Re[E_{inc}E_{QD}] \sin(2\pi f t) \end{aligned} \tag{3.10}$$

where f_{mod} is the square wave modulation, out of which only the principal component has been chosen from the Fourier transform. Then, the lock-in amplifier demodulates the time-dependent signal incident on the photodetector, eliminating the

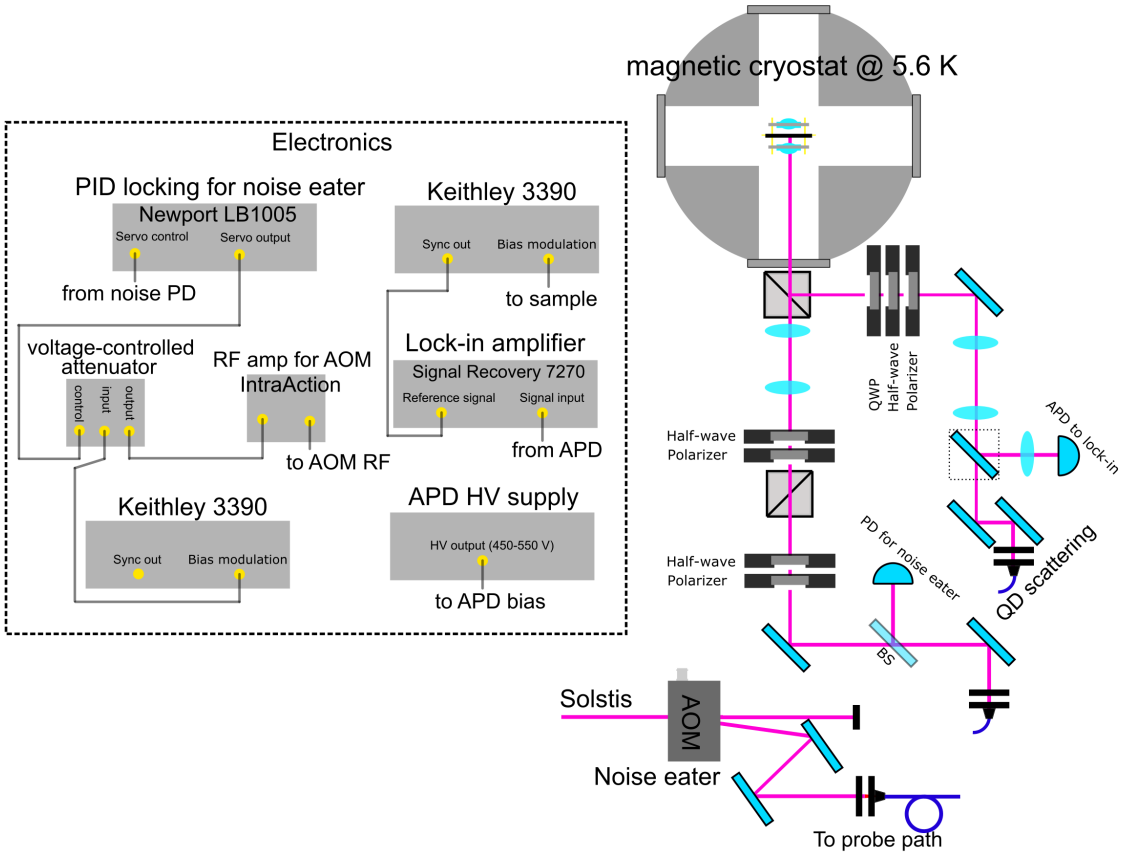

Figure 3.8: Experimental setup for measuring sample-modulation lock-in differential reflectivity. Details are in the text below.

contribution from the DC incident field and the QD term which oscillates at twice the modulation frequency and is also small compared to the homodyned $E_{inc}E_{QD}$ term. The lock-in amplifier bandpasses a narrow frequency range around the modulation frequency, thus filtering out noise contributions from other frequency ranges, and the signal is effectively amplified by the homodyning from the incident field.

The experimental configuration for measuring the sample modulation lock-in differential reflectivity is shown in Figure 3.8. First, a high-resolution CW laser such as the MSquared Solstis or Coherent MBR is sent through an AOM (IntraAction AOM-40N), and the diffracted 1st order beam is coupled into a fiber. The noise in the fiber path, which travels across the lab to the magnetic cryostat setup, is compensated for by the noise eater setup, which consists of a pick-off BS and photodiode

(Thorlabs DET36A) after the fiber output. The current from the photodiode is either amplified via a transimpedance amplifier (SR570 current pre-amplifier) or yields a voltage when sent through a 10kΩ shunt resistor, and used as the servo input for the PID controller (Newport LB1005). A voltage setpoint is chosen that corresponds to a certain optical power at the servo PD, and the servo voltage is sent to a voltage-controlled attenuator, which decreases/increases the 50 MHz AOM driving RF when the power fluctuates at the servo PD, thereby tuning the power diffracted into the 1st order beam. For narrow bandwidth scans over 30 GHz, the high frequency noise and slow drift are reduced down to less than 1% of the unlocked variations. The noise eating is also useful for broadband laser scans, reducing the power drift down to around 10% over a scan range of 100 cm^{-1}, with the frequency-dependent power "drift" caused by the wavelength-dependent reflectivity of the pick-off BS. The probe beam is sent through a polarizer and half-wave plate, which allows for tuning of the optical power by the addition of another polarizer afterward. Then another half-wave plate is introduced and typically rotated to set the incident linear polarization to 45° relative to the vertical laboratory axis. The probe is sent through a 90R/10T BS and focused down onto the sample by a 0.68 NA aspherical lens held in place by a sample-mounted lens holder. The reflected light is collected on the same lens, reflected on the 90R/10T BS towards polarization analyzers, collimated, and directed to either the spectrometer, avalanche photodiode (Hamamatsu 8890-15 APD), or single-mode for further spectral filtering.

A typical trion differential reflectivity lineshape when the laser is scanned across the resonance is displayed in Figure 3.9. The reflectivity dip is sharply peaked with a maximum dR/R signal of -0.16% which varies from dot to dot and ranges from around 0.05% to 1.5% in this DBR-enhanced sample, but the lineshape is non-Lorentzian. In fact, this is a commonly observed feature, and the exact nature of the reflectivity lineshape depends on how deeply the QD is embedded in the sample, the number and thicknesses of interfaces in the DBR sample, and the aligment into the system, and the lineshapes may vary even within a sample due to varying thickness across a sample. It is shown below that the lineshapes that result from driving an embedded

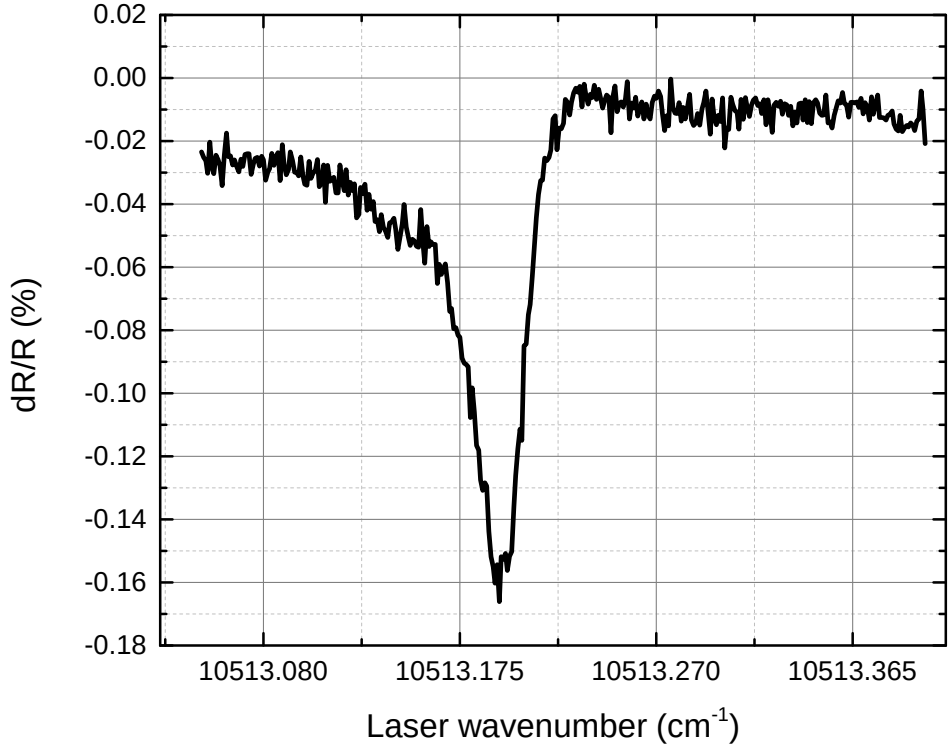

Figure 3.9: Differential reflectivity laser scan of a trion at zero magnetic field.

two-level system are actually given by an admixture of the dispersive and absorptive lineshapes that arise from the complex Lorentzian.

The *source-field* approach may be used to more accurately understand the electric field that is produced by the QD dipole moment under excitation by a quantum field [45]. In that approach, the Heisenberg picture is adopted in which the time-dependence of the problem is associated with the operators rather than the state amplitudes. It can be shown that the source field generated by the QD dipole can be given by the expectation value of the atomic lowering operator $\hat{\sigma}_-$, with the source field given by

$$E_S^+(R,t) = -\frac{\omega^2 \mu_{12} \sin\theta}{4\pi\epsilon_0 c^2 R}\hat{\sigma}_-(t - R/c) \tag{3.11}$$

where θ is the spherical coordinate angle dropping away from the propagation

vector, and R is the distance from the emitter to the detection point. The source field may then be interfered (homodyned) with the driving field, which may have reflected off of multiple surfaces, acquiring a fixed phase that differs from the phase difference that would have occurred if the field interacted with the atom (QD) in free space.

It can be shown further that for a two-level system that the source field is given by [45]

$$E_S^+ = \frac{i\alpha \langle E^+(0) \rangle e^{i\phi}}{\gamma + i\delta} \sin\theta\hat{\theta} \tag{3.12}$$

where α are the lumped constants associated with the transition strength, $\langle E^+(0) \rangle = E_0$ is the incident field strength, and the constant phase difference accumulated between the incident field and the source field due to reflections from interfaces of the incident field is held in the complex phase factor $e^{i\phi}$. Now, the square-law detector measures the squared sum of the two fields, given by (only choosing to measure the z-component which is along the dipole axis)

$$\begin{aligned} I_{detector} &= |E + E_S^+|^2 = |E_0 + \alpha E_0 \frac{i}{\gamma + i\delta} \sin^2\theta e^{i\phi}|^2 \\ &= |E_0|^2 \left[1 - 2\alpha \left[\sin\phi \frac{\gamma}{\gamma^2 + \delta^2} - \cos\phi \frac{\delta}{\gamma^2 + \delta^2}\right]\right] \end{aligned} \tag{3.13}$$

where the first term is just the incident field intensity, and the second term is the admixture of the even Lorentzian and dispersive Lorentzians, where the admixture depends on the fixed phase angle between the incident field and the source field. Although no attempt is made here to determine that phase, it has been shown that the measured reflectivity and transmission at a detector when homodyned with the incident field can range from an even Lorentzian (peaked at $\delta = 0$) to a dispersive function with admixtures in between. This explains the anomalous optical response displayed in Figure 3.9 for the two-level system without relying on more complicated Fano couplings to continuum states [121].

The utilization of the MSquared Solstis CW laser allows the spectroscopist to perform high-resolution CW laser scans over very wide spectral ranges (theoretically

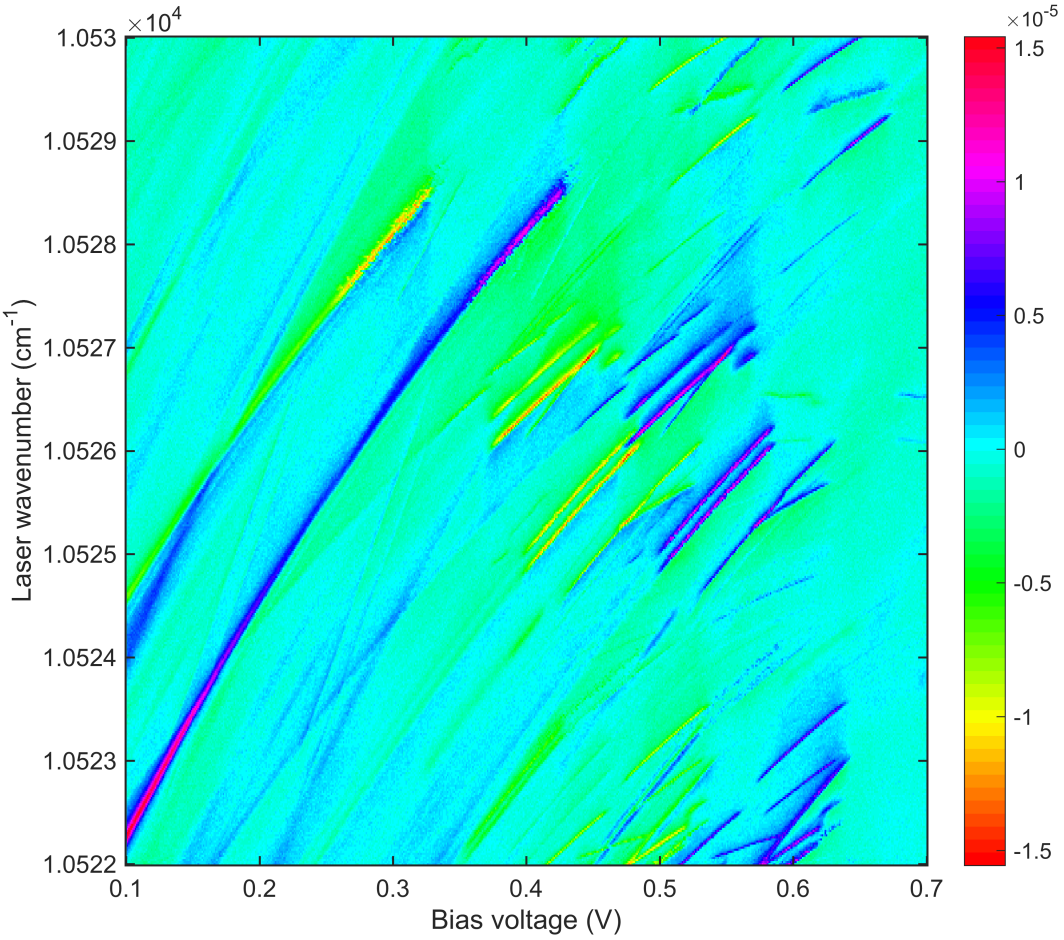

Figure 3.10: Modulated reflectivity bias mapping measured at zero magnetic field.

from 700-1000 nm). In this manner, the laser was used in this work to find active trions over 50 cm^{-1} scanning ranges by producing resonant excitation bias maps (Figures 3.10 and 3.12). In these experiments, the sample is bias-modulated with 100 mV peak-to-peak amplitude. The laser is held fixed a given wavenumber, and the bias is scanned, sometimes bringing a QD transition into resonance with the laser, leading to a modulated reflectivity signal. The laser is then stepped by a small amount ($\sim$ 150 MHz for coarse scans), and the bias is scanned again, iterating to produce a map. These modulated reflectivity maps reveal that the QD actively reflects light with narrow linewidths (typically around 500 MHz) and that the absorption transition energies can be tuned using the DC Stark shift. In Figure 3.10, starting from low

biases, bright absorption lines are observed to be blue shifted with increasing bias voltage. From at least 0.1 to 0.4 V, a bright feature is observed which is tuned over a huge spectral range from 10522 to 10528 cm^{-1} (180 GHz). This feature likely corresponds to a rare positively charged trion, which are likely due to morphological anomalies in this sample and are unintended. A point worth noting is that this method produces artifacts of multiple absorption lines (explained using Figure 3.11). This can be understood because the bias modulation operates by scanning the DC bias, ie. the voltage is given by $V_{dc} \pm V_{p-p}/2$; thus, the QD transitions are brought into resonance with the laser twice over a given bias scan, and the DC bias value at which the transition would be in resonance (with no modulation) with the laser is the average of the two biases, given by V_0 in the figure. Additionally, one peak is negative and the other is positive: the lock-in is phased with the reference from the bias modulation such that the higher bias value yields a positive peak when the LOW portion of the bias modulation brings the QD in resonance; thus, the negative peak is when the transition is brought into resonance on the HIGH portion of the bias modulation square wave. In the figure, the purple curve on the left is where the modulated reflectivity resonance would be observed for infinitesimally small peak-to-peak bias modulation.

These absorption bias maps allow one to determine DC Stark shifts precisely, to find QDs which lack fine structure which is typically indicative of morphological anomalies such as in-plane distortion, and to separate the exciton species from the trions. Charge stability transitions are observed at the bias is tuned higher; for instance, at approximately 0.4 V, the positive trion abrupt turns off, and the next charge states become the new lowest energy configuration. These new lines have different Stark shifts, and show considerable fine structure, indicating that they are excitonic doublets which are split by the electron-hole exchange [82]. The exciton identification is corroborated by rotating the half-wave plate before the cryostat and showing that the selection rules are linear, rather than circular for the zero-field trion states. At higher bias starting around 0.57 V_{dc}, new reflectivity lines with lower Stark shifts appear. This region corresponds to the negatively-charged exciton, or trion

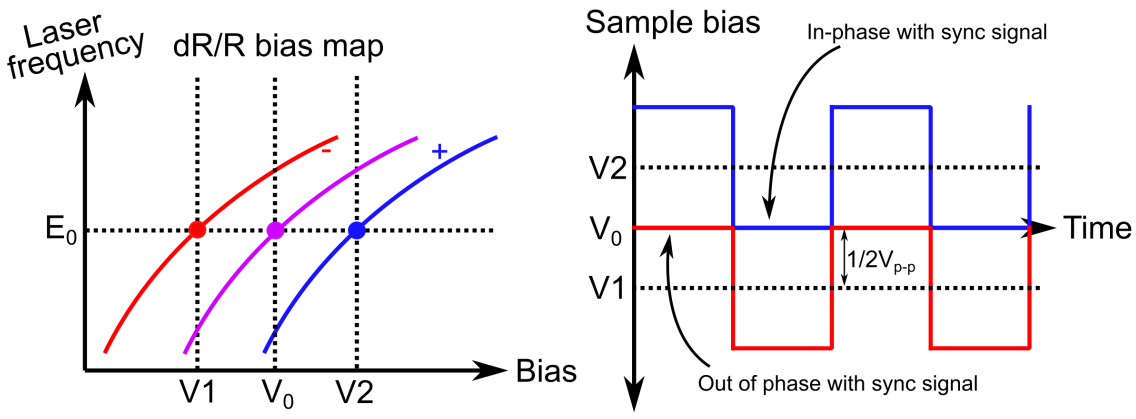

Figure 3.11: Schematic explanation of lock-in negative and positive signals. Left: schematic of modulated reflectivity bias map. Signals are negative on the red line and positive on the blue Stark-shifted line. The purple line is where the resonance is expected to lie for infinitesimally small peak-to-peak amplitudes. Right: Sample bias time-dependence. The lock-in was auto-phased so that the signal is positive on resonance when the bias is set to V2. Thus, when the QD is brought into resonance at the low bias range, ie. when V1+$V_{p-p}/2$ = V2-$V_{p-p}/2$, the sample bias is π out of phase with the sync reference, resulting in a negative signal.

state that is investigated for the remainder of this thesis. These trions exist over a shorter bias range than either the exciton or positive trion, with the next charge states broadening due to stronger coupling to continuum states (not pictured).

One exemplary trion modulated reflectivity bias map is displayed in Figure 3.12. The trion reflectivity signal turns on abruptly at low bias values of 0.61 V, and is Stark tuned over a spectral range of 18.9 GHz over a 70 mV bias shift, retaining a very narrow lineshape across the entire range, and turning off again at approximately 0.68 V. One key indicator that this lineshape corresponds to a trion is the lack of any fine structure, eliminated by the pairing of the electrons in the excited state, leading to a strong reduction in the electron-hole exchange. Additionally, trion lines are circularly polarized (in the absence of strong HHLH mixing), showing very little variation in reflectivity as the half-wave plate is rotated. The absorption map technique demonstrated here allows for high-resolution studies of DC Stark shifts and fine structure physics with much higher resolution (50 kHz) than PL techniques (2.6 GHz

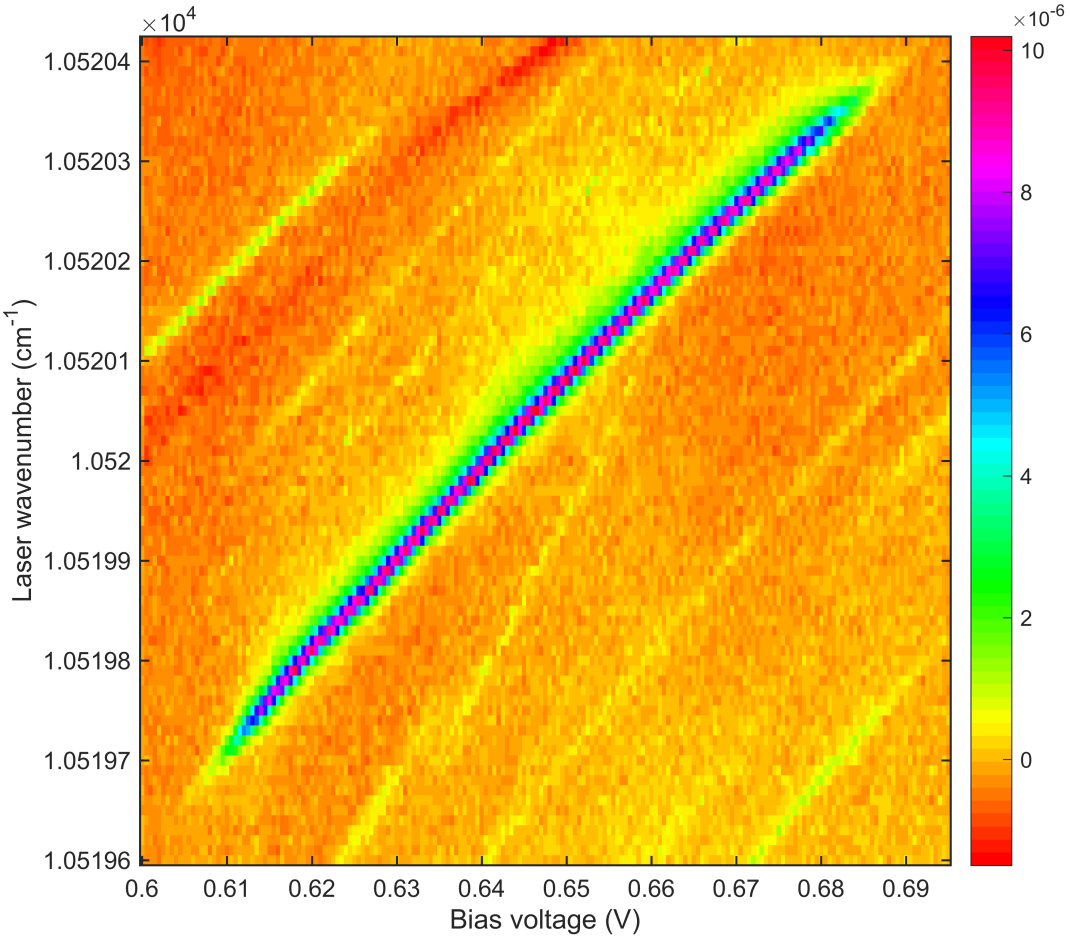

Figure 3.12: High resolution modulated reflectivity bias mapping of a trion at zero magnetic field.

for a grating with 1800 lines/mm); the map demonstrated in Figure 3.12 utilizes a laser step size of 60 MHz.

The differential reflectivity technique was utilized to perform a statistical study on the DC Stark Shifts of 97 trions with high spectral and bias resolution. Multiple high resolution maps were acquired over the trion stability range from approximately 0.5 to 0.7 V, over laser wavenumbers ranging from 10463 to 10553 cm^{-1} (2.7 THz); this wide bandwidth combined with high resolution was previously unattainable without manually stitching together 1 cm^{-1} (30 GHz) maps, allowing for convenient statistical studies over a large number of QDs. Each trion resonance was isolated in post-

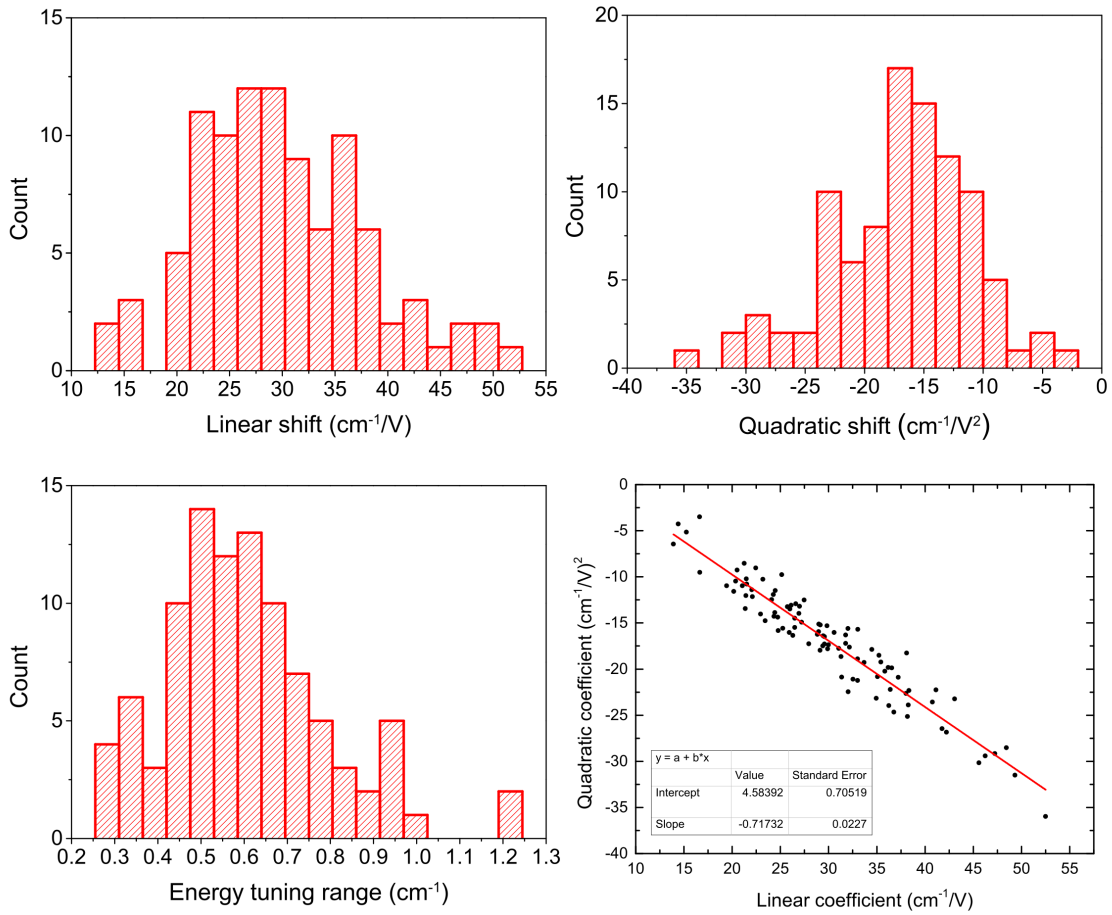

Figure 3.13: Histograms of quantum-confined Stark effect linear and quadratic coefficients (with respect to voltage, not electric field), energy tuning range, and scatter plot of quadratic versus linear coefficients (with linear fit) for 97 trions.

processing and the resonance bias dependence was fit with a quadratic curve $E = E_0 + bV + cV^2$; the batch processing was assisted by undergraduate research assistant Michelle Ripari. Histograms of the linear and quadratic coefficients, and the energy tuning range (highest wavenumber - lowest wavenumber for a given trion) and plotted in Figure 3.13. The averages and standard deviations for the three histograms are equal to (30.0 $\pm$ 8.0) cm^{-1}/V (linear), (-16.9 $\pm$ 6.0) cm^{-1}/V^2 (quadratic), and (0.604 $\pm$ 0.194) cm^{-1} (energy range). No correlation is measured between the Stark shift constants and the central wavenumber for each trion (not displayed here). However, a strong linear relationship between the quadratic coefficient and the linear coefficient for each trion quantum-confined Stark shift is observed (bottom right panel of Figure

3.13), with the fit given by c = a_1b + a_0 = (-0.717 ± 0.023 cm^{-1}/V)b + (4.58 ± 0.71 cm^{-1}/V^2). This correlation implies that there is a connection between the built-in dipole moment of the trion and the polarizability of the charge carriers, which is likely connected to the quantum-confined aspect of the Stark shift measured here. At zero applied electric field, the spatial extent of the electron and hole separation leads to the built-in permanent dipole moment, which depends on the confinement structure of the QD and the in-built electric field of the nip diode. As the electric field is increased, the spatial separation of the charges increases, but is confined to the QD (when the field is small compared to the field required to ionize (tunnel) the charges out of the QD), leading to a larger Stark shift. However, the wavefunctions of the electron and hole confined to the QD are also warped with increasing bias, and this warping effect is related to the confinement potential. No attempts are made in this thesis to model this effect in order to determine a connection between the linear and quadratic terms, but existing literature may provide clues for the connection [120].

However, the relationship between the polarizability and permanent dipole moment is determined below. The Stark shift in terms of the electric field across the diode is given by E-E_f = -pF + βF^2, where p is the permanent dipole moment and β is the polarizability [117]. However, the experiment performed here tunes the bias rather than the electric field. Plugging in the relationship between the electric field and bias results in

$$\begin{aligned} E_{Stark} &= E_f - pF + \beta F^2 = E_f + p\frac{V_{bi} - V}{t} + \beta\frac{(V_{bi} - V)^2}{t^2} \\ &= \left(E_f + \frac{pV_{bi}}{t} + \frac{\beta V_{bi}^2}{t^2}\right) - V\left(\frac{p}{t} + \frac{2V_{bi}\beta}{t^2}\right) + \frac{\beta}{t^2}V^2 = E_0 + bV + cV^2 \end{aligned} \tag{3.14}$$

where V_{bi} is the built-in voltage from the nip diode, and t is the thickness of the diode, which are constants across all QDs in the sample. These coefficients are now compared to the linear relationship measured experimentally between the quadratic and linear coefficients, resulting in

$$\beta = \frac{-a_1 t}{1 + 2a_1 V_{bi}} p + a_0 \frac{t^2}{1 + 2a_1 V_{bi}} \tag{3.15}$$

showing that the polarizability of the QD trion can be related linearly to the built-in permanent dipole moment of the trion. Thus, the high-resolution DC Stark shift differential reflectivity technique has revealed a connection between the linear and quadratic DC Stark shift terms that is, as far as the author is aware, unreported in the literature. Further theoretical analysis of the QD morphology may reveal this connection more deeply.

3.5 Scattering experiments: resonance fluorescence and Raman scattering

The light-matter interaction in the QD system is strongly enhanced as compared to both atomic systems and bulk semiconductors due to the confinement of the exciton/trion to the QD, as well as due to the on-chip DBR cavity field enhancement. This strong interaction, combined with state-of-the-art single photon detecting nanowires, allows one to measure single photon scattering, referred to as *resonance fluorescence* (generically referring to all scattering and fluorescence processes in the QD system). Instead of utilizing the sample modulation technique to measure reflectivity signals which are distorted by homodyne interference with the driving field, the excitation laser is rejected either through frequency-filtering (in the case of Raman scattering) or through polarization rejection (Rayleigh scattering). The remaining optical field after rejection of the excitation beam is the source field covered in the previous section, which directly corresponds to the QD polarization, and must be treated as a quantum field. Studies of two-level systems and their interactions with light revealed time-dependent Rabi oscillations of the scattering intensity that level off at long times compared to the spontaneous emission time, and anti-bunching in the scattered single photons [110, 122, 123], indicating the quantum nature of the field scattered by the QD. These quantum fields differ in significant ways from the coherent states generated by a laser; the field scattered by the QD is a Fock state, or number state, which may

be prepared in the single photon state with high fidelity, a feature that is not simply attained by attenuating the coherent state produced by a laser. Furthermore, in the lambda system present in the QD trion system under certain excitation conditions, it has been demonstrated theoretically and experimentally that the polarization and energy of the photon is entangled with the electron spin state, allowing for quantum teleportation schemes between distant QD nodes [124–129]. Another scattering feature that has not received as much attention in the QD system is Raman scattering, which is scattered at energies given by $E_{laser} \pm \Delta_e$, where Δ_e is the ground state splitting. As will be shown later in this section, Raman scattering allows the spectroscopist to measure ground state (electron spin) splitting which a resolution that is given by the laser linewidth and the ground state decoherence time, which is often times orders of magnitude longer than the lifetime-broadened width of the trion resonance. Additionally, Raman scattered photons allow for tuning of the scattered single photons when the ground state splitting can be tuned via the application of an external magnetic field, allowing for incorporation of the QD into a quantum network where the optical receivers may have disparate resonance energies. Resonant Raman scattering is the workhorse technique used throughout this thesis for understanding the role that the nuclear spin polarization plays on shifting the electron spin state splitting.

The resonance fluorescence experiments are performed in the following manner. The probe beam is prepared in the same manner as described in Figure 3.8 before the cryostat. When the beam passes through the high NA aspherical lens before the sample, careful inspection of the s- and p-polarized components of the optical field at the high curvature lens interface reveal significant spatial mode abberrations and spatial dependence of the polarization within the transverse extent of the Gaussian beam [130, 131]. In fact, the polarization is rotated as a function of the azimuthal angle θ around the beam propagation direction such that a cross-polarized analyzer placed in the reflected/transmitted beam results in a TEM_{11} mode, ie. goes to zero at $\theta = n\pi/2$ for all values of r away from the beam center. Most importantly, the excitation polarization may be chosen such that the emitted QD scattering has a

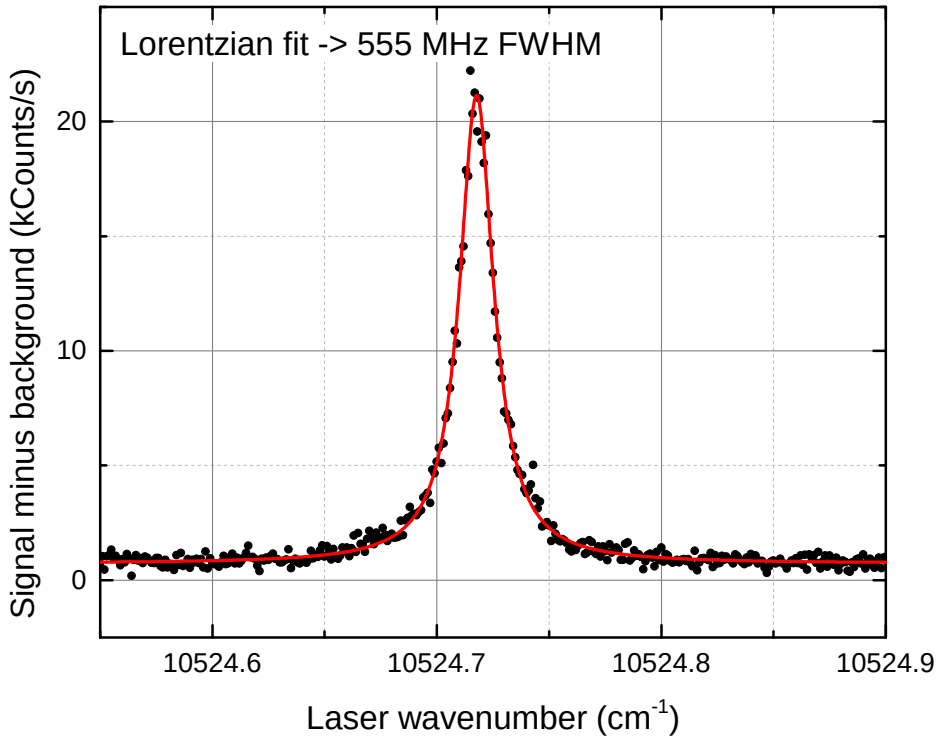

Figure 3.14: Resonance fluorescence laser frequency scan for a trion at zero magnetic field. The fluorescence lineshape is fit with a Lorentzian of FWHM = 555 MHz. The data is background subtracted by measuring the laser leak-through at each point by shifting the QD trion transition far off-resonance with the laser using the DC Stark shift.

significant component parallel to the polarization analyzer axis, allowing the QD scattering to pass while blocking the excitation beam. Single-mode filtering is then performed by coupling the scattering into a single mode fiber, which is coupled to single-photon detectors such as the QuantumOpus superconducting nanowire system, which is capable of 85% detection efficiency at 950 nm.

The excitation polarization is chosen at 45° CW from the vertical laboratory axis; the collection beam path first contains a quarter-wave plate which is rotated to compensate for wavelength-dependent birefringence in the cryostat windows due to strain. To maximize the beam rejection, high optical power at the wavenumber of interest is

reflected off the sample down the collection path. The polarizer transmission angle is fixed, since the rotation of most polarizers will result in spatial displacement of the beam which misaligns the beam from the single mode fiber. The half-wave plate is rotated to minimize the beam transmission through the polarizer, and the quarter wave plate is adjusted to further minimize the transmission. The rotation is iterated back and forth between the half and quarter wave plates, typically resulting in 10^5 extinction after single-mode filtering through the optical fiber. The resonance fluorescence spectrum is then measured by either scanning the laser across the transition (background subtracting at every laser point, measuring the laser leak-through by bias-shifting the QD transition far out of resonance), or by scanning the sample bias with the laser frequency fixed, bias-tuning the QD transition through the laser. The problem with the second method is that, as seen in the previous section, the QD transition energy shifts quadratically with the sample bias, distorting the RF lineshape without re-calibration. The problem with the first method is that scanning the laser over a frequency range larger than 30 GHz results laser leak-through which saturates the detector due to cryostat window birefringence. However, typical QD linewidths are less than 500 MHz, and therefore the wavelength-dependent leak-through is not typically an issue. This issue is dealt with more easily when measuring Raman scattering, since the scattering occurs at a different energy from the laser energy, and can be filtered using an etalon or monochromator.

Figure 3.14 shows the results of a resonance fluorescence laser scan of a trion at zero magnetic field under excitation of low optical power. A single even Lorentzian fits the spectrum exceptionally well, with a FWHM of 555 MHz, and no signs of distortion that were present in the differential reflectivity case due to homodyning interference effects. Thus, the QD trion at zero magnetic field is without much doubt an exceptional example of a two-level system with an optically-accessible dipole transition. Resonance fluorescence may be used to determine precisely the transition energies of the QD without needing to compensate for interference distortion, and provides single photons that may be utilized for quantum information protocols.

More formally, it is worthwhile to consider the scattering spectrum for resonance

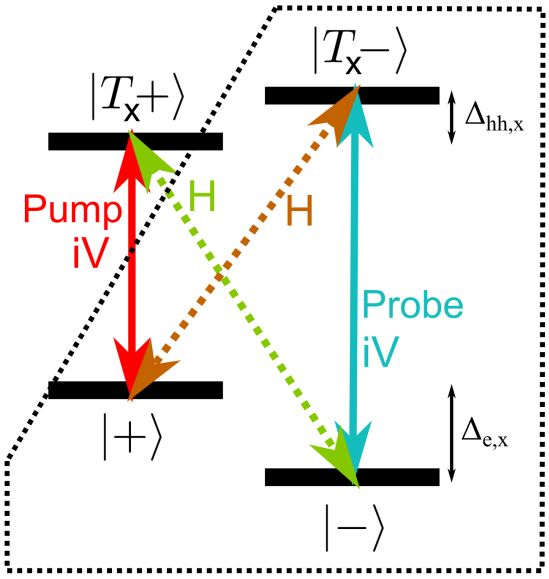

Figure 3.15: Lambda sub-system of the four-level electron-trion system in the Voigt geometry. Dashed black line indicates the subset lambda system considered here theoretically.

fluorescence and Raman scattering. The derivation of the spectrum is treated in detail in Appendix A. In the derivation, the full four-level system that arises in the presence of an in-plane magnetic field (Voigt geometry) (see Chapter 2) is treated perturbatively for weak pump and probe fields, and the probe is considered much weaker than the pump. The energy level and pump/probe field configuration is shown in Figure 3.15. In this configuration, the probe field drives the $|-\rangle \rightarrow |T_x-\rangle$ transition, and the pump field drives the $|+\rangle \rightarrow |T_x+\rangle$ transition. Spontaneous emission occurs on all four transitions, repopulating the ground states after excitation into the optically excited states. However, the pump is much stronger than the probe; therefore, in the perturbation limit adopted here, the population is effectively considered pumped into the $|-\rangle$ state entirely, resulting in $\rho_{11}^{(0)} = 1$. Two scattering channels are then derived, one corresponding to scattering on the $|+\rangle \rightarrow |T_x+\rangle$ transition and the other corresponding to the $|-\rangle \rightarrow |T_x-\rangle$ transition, given below:

$$\text{Scattering} \approx 2\text{Re}\left[\frac{g_1^2\chi^2\rho_{11}^{(0)}}{\left[\frac{1}{2}(\Gamma_e+\Gamma_r)-i\delta_1\right]\left[\frac{1}{2}\Gamma_e+i(\omega-\omega_a)\right]\left[-\frac{1}{2}\Gamma_r+i\delta_1^a\right]}\right] + 2\text{Re}\left[\frac{g_2^2\chi^2\rho_{11}^{(0)}}{\left[\frac{1}{2}(\Gamma_e+\Gamma_r)-i\delta_1\right]\left[-\frac{1}{2}\Gamma_e+i(\omega-\Delta_e-\omega_b)\right]\left[\frac{1}{2}\Gamma_r+i\delta_2^b\right]}\right] \tag{3.16}$$

where $g_i = -i\mu_i \sin\theta_i \left(\frac{\omega_i}{2\hbar\epsilon_0 V}\right)^{1/2}$, Γ_e is the electron spin state dephasing rate, Γ_r is the radiative relaxation rate, $\omega_{a/b}$ are the scattered photon modes, and the detunings are defined as $\delta_1 = (\omega_0 + \frac{\Delta}{2}) - \omega$, $\delta_1^a = (\omega_0 + \frac{\Delta}{2}) - \omega_a$, $\delta_2^b = (\omega_0 - \frac{\Delta}{2}) - \omega_b$. There are some very significant features observed in this result. The first scattering term is the product of three even Lorentzians (real part); the first one gives the overall scattering dependence which is measured in a laser scanning experiment and has the total width given by the radiative relaxation plus the electron spin state dephasing. The second Lorentzian in the product is peaked when $\omega_a = \omega$, or that the scattered photon mode has the same frequency as the excitation laser, with a width given by the *electron spin dephasing*, not the radiative relaxation rate. This result is especially important; it means that Rayleigh scattered photons have much higher indistinguishability than the photons produced via spontaneous emission, which are given by the third Lorentzian; that mode is centered at $\omega_a = \omega_0 + \Delta_e/2$, showing that the spontaneous emission always comes out at the natural frequency of the transition.

The second term contains the same first Lorentzian intensity dependence, but two new Lorentzian products. The second Lorentzian is the Raman scattering term, $\omega_b = \omega - \Delta_e$; in other words, the scattering always comes out at the laser frequency minus the electron spin state splitting, with a width that again is given by the electron spin state dephasing, which can be orders of magnitude slower than the spontaneous emission rate. The third term is another spontaneous emission term centered at the natural frequency of the $|-\rangle \rightarrow |T_x-\rangle$ transition. The advantages of using the Raman scattering as a spectrosopic tool become immediately apparent: first, on resonance, the Raman scattering channel is a factor of Γ_r/Γ_e brighter than the spontaneous emission channel. Second, so long as one can measure both the laser frequency and

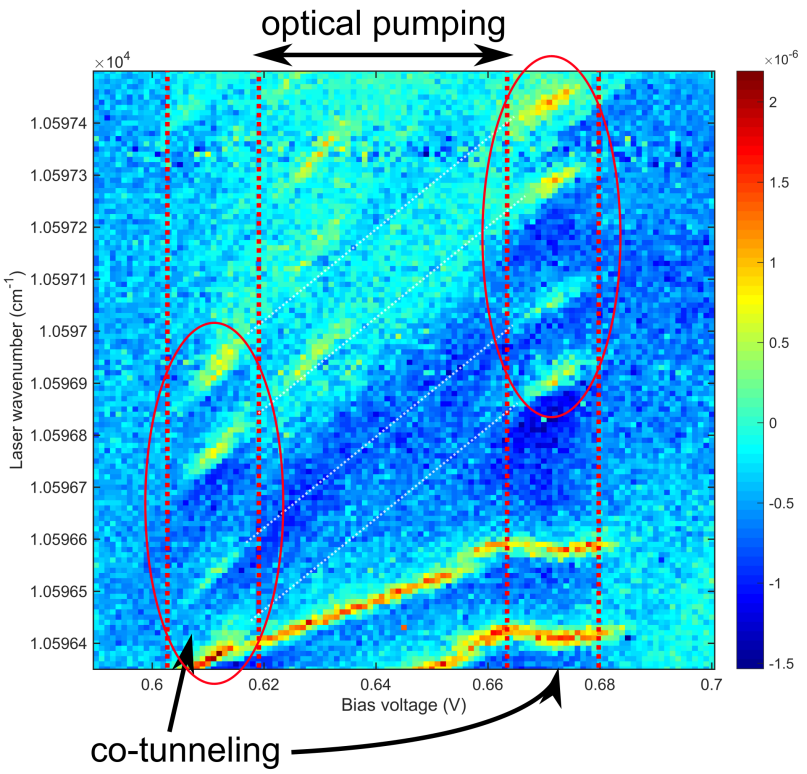

Figure 3.16: Demonstration of co-tunneling and optical pumping ranges using a single laser differential reflectivity bias-dependent map under the application of a 2 T Voigt geometry magnetic field. Co-tunneling is indicated by the presence of a dR/R signal under excitation from a single optical field between biases 0.6 and 0.62 for the 0e-1e transition, and ∼0.66-0.68 V for the 1e-2e transition, with the optical pumping region falling in between those bias ranges. dR/R signals from multiple QDs are observed in this map, but the spectra for the QD of interest are indicated circled in red and with faint dashed white lines in the optical pumping region.

the Raman scattering line with high precision, one can monitor the ground state splitting without having to ensure that the excitation laser is exactly on resonance with the transition. These properties are utilized in the experiments displayed in Chapter 5, where further experimental details are given regarding frequency filtering via a pressure-tuned etalon.

3.6 Two field experiments: optical pumping and coherent population trapping

In the trion stability range, it has been shown in this thesis that when an in-plane (Voigt geometry) magnetic field is turned on, the trion transition is split into four linearly-polarized transitions (Section 2.5). When the magnetic field strength is large enough to cause a splitting of the electron spin state greater than the trion optical linewidth, *optical pumping* of the electron spin may occur [58]. Xu et al. showed that the electron spin population could be optically pumped using a single pump field with a spin preparation efficiency of (98.9 ± 0.4)%. An important requirement for the optical pumping scheme is that the electric field structure (nip or Schottky diode) is fabricated with an appropriate thickness and doping such that the trion charge states are stable with minimal cotunneling to the Fermi reservoir on the optical pumping timescale (nanoseconds in the Voigt geometry, microseconds in the Faraday geometry).

Experimentally, the optical pumping bias range is determined first by the utilization of a single scanning laser. A bias-dependent differential reflectivity map is taken at high magnetic fields, in this case 2 T (Figure 3.16). At low biases between 0.6 and 0.62 V, a dR/R signal is measured (red circles), indicating that the electron spin tunnels between the Fermi reservoir and the QD on timescales faster than the optical pumping rate due to the single beam excitation (nanoseconds); this range corresponds to the 0e-1e co-tunneling range. Additionally, another co-tunneling range is observed between approximately 0.66 and 0.68 V, corresponding to rapid switching between the 1e-2e state due to reservoir-QD co-tunneling. However, in between these two bias ranges, the dR/R signal disappears (see white dashed lines in Figure 3.16). In this range, the dR/R signal rapidly decays (see Figure 7.17 in Section 7.5 for time-domain studies of optical pumping) when a single field resonantly excites one of the four QD trion transitions, leading to high-fidelity preparation of the electron spin in the undriven state (schematically illustrated in Figure 3.17).

Although signals from multiple QDs are present in Figure 3.16, optical pumping is verified by the introduction of another pump field brought into resonance with one of the two trion transitions coupled to the formerly undriven electron spin state. Taking for instance the optical pumping configuration illustrated in Figure 3.17, the

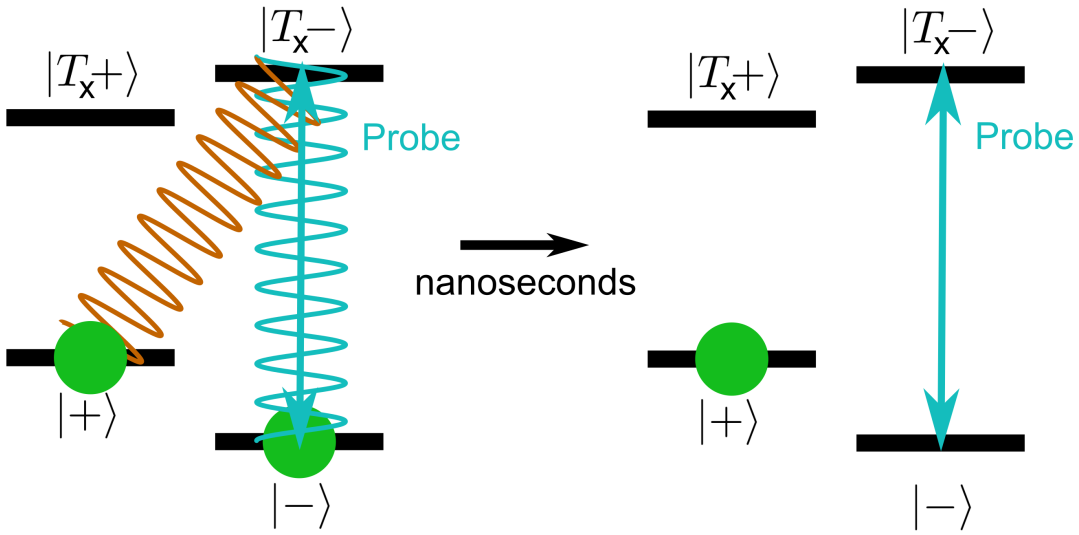

Figure 3.17: Schematic illustration of optical pumping phenomenon under single field excitation. Wavy curves indicate spontaneous emission from the excited state, repopulating the ground states, while the solid arrow indicates the probe field. Green circles indicate where the electron spin population is found.

probe drives the $|-\rangle \rightarrow |T_x-\rangle$ transition, with the electron spin population initially in a mixed state at thermal equilibrium. The population is driven up into the $|T_x-\rangle$ state, and spontaneous emission occurs, populating the $|+\rangle$ and $|-\rangle$ states. However, since the optical transitions associated with the $|+\rangle$ states are unpumped, the electron spin population is pumped into the $|+\rangle$ state. Thus, the probe no longer yields an optical signal since there is minimal population in the $|-\rangle$ state, neglecting ground state repopulation due to residual co-tunneling and off-resonant driving effects from the probe. The signal is recovered by driving either the $|+\rangle \rightarrow |T_x(+/-)\rangle$ transition, repumping the population partially back to the $|-\rangle$ state, with the steady-state populations dependent on the ratio of the pump and probe optical powers.

This recovery of the optical signal is demonstrated in Figure 3.18 in two plots, with the left (right) plot corresponding to pumping the $|-\rangle \rightarrow |T_x+\rangle (|-\rangle \rightarrow |T_x-\rangle)$ transition, while scanning the probe across the two $|+\rangle$ transitions. There are two optical transitions for each electron spin state which are linearly-polarized and orthogonal to each other; both the pump and probe field are set to 45° to the vertical

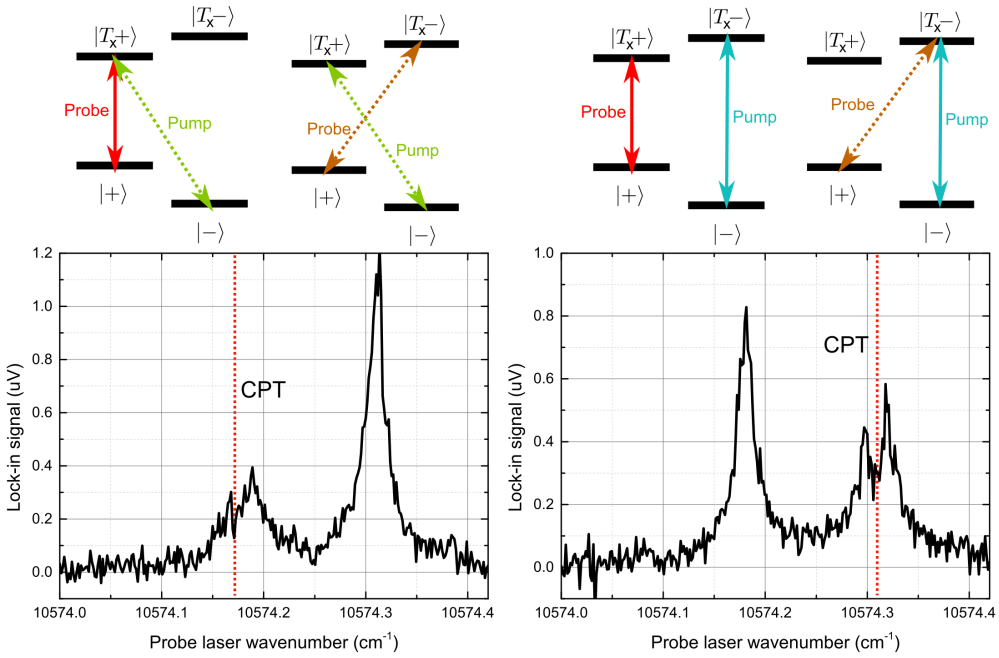

Figure 3.18: Two field optical pumping and coherent population trapping when probing the $|+\rangle$ electron spin state; each resonance in the spectra corresponds to the pump-probe configuration indicated in the energy level diagrams above the resonance. Left spectrum: pumping the $|-\rangle \rightarrow |T_x+\rangle$ transition, scanning the probe laser across both $|+\rangle$ transitions. Coherent population trapping is observed as a dip in reflectivity when the pump-probe detuning is equal to the electron spin state splitting, compared to the second transition which has approximately a Lorentzian response. Right spectrum: pumping the $|-\rangle \rightarrow |T_x-\rangle$ transition, scanning the probe laser across both $|+\rangle$ transitions.

lab frame, but the pump is orthogonal to the probe and rejected in the reflection collection geometry by polarization analyzers. When the two fields do not share an excited state resonantly, the optical response is approximately a Lorentzian, and the signal strength is comparable to the response in the co-tunneling regime, indicating that the electron spin state is prepared by the pump. The trion energy level structure is validated by checking the effect of the pump on the two trion transitions of the $|-\rangle$ state.

However, if the pump and probe share an excited state, when the probe is brought into resonance with the transition, the spectrum resembles a Lorentzian with a hole

driven into it at resonance; this phenomenon is known as electromagnetically-induced transparency (EIT) and is caused by coherent population trapping (CPT) of the electron spin state. This transparency effect has been demonstrated in countless experiments in a variety of systems including strontium, sodium and rubidium vapors [132–134], single QDs [85], quantum dot molecules [63, 135], and many others. When the difference between the pump and probe frequencies equals the ground state splitting, ie. $|\omega_{pu} - \omega_{pr}| = \Delta_e$, in the absence of ground state decoherence, the electron spin state is driven into a coherent superposition state given by

$$|\psi_{dark}\rangle = \frac{\Omega_{pu}|+\rangle - \Omega_{pr}|-\rangle}{\sqrt{\Omega_{pu}^2 + \Omega_{pr}^2}} \tag{3.17}$$

The superposition is referred to as a dark state because the interference between Rayleigh and Raman scattering between the pump and probe leads to a reduction in the reflectivity (or corresponding increase in transparency) [45]. A key point regarding CPT and EIT is that the coherent superposition state, and therefore optical transparency, requires that there is a long-lived coherence between the electron spin states (ground states); in fact, this optical spectrum in the vicinity of the CPT dip can be used as a powerful tool for studying the electron spin state coherence [85, 135, 136]. It can be shown that in the lowest order of the probe power that the probe absorption is given by [45]

$$\rho_{21} = -\chi_{pr}\mathrm{Im}\left[\frac{i\Gamma_{13} - (\delta_{pr} - \delta_{pu})}{i(\delta_{pr} - \delta_{pu})\gamma_{12} + \gamma_{12}\Gamma_{13} - \delta_{pr}(\delta_{pr} - \delta_{pu}) + i\Gamma_{13}\delta_{pr} + \chi_{pu}^2}\right] \tag{3.18}$$

where the lambda system states are defined as $|1\rangle = |+\rangle, |2\rangle = |T_x+\rangle, |3\rangle = |-\rangle$, $\Delta_{pr} = \omega_{21} - \omega_{pr}, \Delta_{pu} = \omega_{23} - \omega_{pu}$, Γ_{13} is the ground state decoherence rate, γ_{12} is the excited state decay rate, and χ is the Rabi frequency (divided by two) for each field. The transparency dip associated with EIT is observed when the two-photon condition is satisifed, ie. that $\delta_{pr} = \delta_{pu}$, but the depth of the dip is affected by both the pump power and the ground state decoherence time. The expected spectrum is plotted in Figure 3.19 for a fixed pump power and varying ground state decoherence times; the

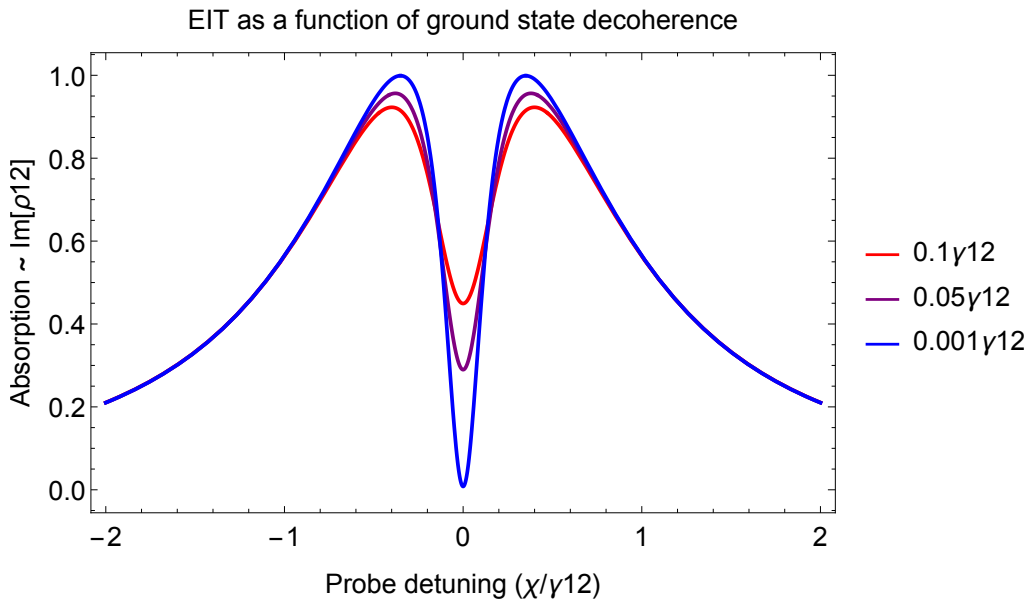

Figure 3.19: Perturbation theory result for the weak probe field absorption in the EIT configuration for the lambda system for varying ground state decoherence rates. The legend labels the ground state decoherence rate given as a fraction of the spontaneous emission rate.

depth of the EIT dip is observed to increase with decreasing ground state decoherence rates due to more complete interference between the two scattering pathways.

The EIT dip may be fit with the full expression for ρ_{21} without utilizing perturbation theory, which is required in order to recover effects such as the Autler-Townes splitting, which leads to a transparency that is related to a field dressing of the pumping transition. Since the depth of the dip has contributions related to the strength of the pumping field, precise measurements of the ground state decoherence time could be enhanced by utilizing time-correlated single-photon counting to determine the exact Rabi frequency for the pump and probe via time-resolved Rabi oscillations [108]. However, it is estimated here that the transparency dips observed in Figure 3.18 correspond to a ground state decoherence rate somewhere between 0.05-0.1 γ_{12}, or between in the vicinity of 40 MHz, or approximately a 25 ns electron spin decoherence time. It is notable that in this sample (the DBR sample utilized for the Raman scattering experiments presented in this thesis) that CPT and EIT are not often observed, and that the spectrum displayed above (Figure 3.18) is in fact exceptional. More often

than not, the probe scanning spectra measured in the optical pumping regime are distorted into broad lineshapes over a few GHz scanning range by dynamical nuclear spin polarization effects, as explored for the remainder of this thesis. CPT-locking of the nuclear spin ensemble was demonstrated by Xu et al. [85] and further examined by Sun et al. [136], where they showed that the dark state dip in the single QD system very similar to this system but with strong heavy-hole light-hole mixing could be enhanced by preparation via CPT narrowing. Comparisons between the two samples (the one studied here and Xu's sample) indicate that the effect of CPT on the nuclear spin ensemble is highly dependent not only on the sample structure but also varies from QD to QD within a single sample due to morphological differences. Nevertheless, the CPT narrowing technique is investigated in this thesis in Chapter 7 via time-domain techniques.

3.7 Chapter summary

In summary, this chapter gives the details for a variety of continuous wave spectroscopy techniques applied to single QDs utilized throughout this thesis for initial characterization and preparation for coherent control techniques. First, the physics of photoluminescence measurements was explained, introducing measurements of the DC Stark shift as measured via PL bias-dependent maps, including a discussion of InAs wetting layer physics. A PL magnification technique was introduced that allows for the spectroscopist to measure PL line centers with greater precision, demonstrating a precision increase of at least 16.6x compared to the standard optical configuration. Then, the density matrix formalism was introduced, and the optical response of a QD was derived in terms of the ground state - excited state coherence terms generated by the light-matter interaction, revealing the well-known complex Lorentzian dependence which yields absorption and dispersion for an optically-active two-level system. The workhorse of QD high-resolution spectroscopy, sample bias-modulation lock-in detected differential reflectivity was introduced. In combination with a broadband-scanning high-resolution TiSaph laser, the technique was used to perform a statis-

tical study on the DC Stark shift of negatively-charged trions in 97 different QDs, revealing a strong correlation between the trion permanent dipole moment and the polarizability of the trion charge wavefunctions. Scattering experiments, including Rayleigh and Raman scattering, were explained, along with a theoretical derivation using perturbation theory which reveals that for weak pump and probe fields that three quantum fields are produced in the scattering experiment: Rayleigh scattering at the laser frequency, Raman scattering at the laser frequency plus or minus the ground state splitting, and spontaneous emission in both channels of the lambda system. Measurement of the narrow linewidth Rayleigh and Raman channels allows one to determine the ground state splitting which much greater precision than absorption measurements. Finally, two field experiments in the optical pumping bias regime were detailed, and coherent population trapping of the ground state was demonstrated.

CHAPTER 4

Microscopic origins of dynamic nuclear spin polarization in quantum dots

4.1 Introduction

The primary electron and hole spin qubit dephasing mechanism in III-V semicondutor QD systems is due to the interaction between the electron/hole and the constituent half-integer nuclear spins of the QD [85, 89, 136–139]. The quantum confinement of the electron and hole in the QD due to the band-gap mismatch between the bulk and QD material leads to considerably higher hyperfine coupling strengths than in the bulk material [140], resulting in easily observable nuclear spin polarization effects that become non-linear with respect to laser frequency detuning, excitation power, and excitation polarization, during both non-resonant circularly-polarized excitation such as PL [141] and resonant laser excitation [85, 142].

In this chapter the microscopic mechanisms for the interaction between the quantum-confined electrons and holes and the nuclei are introduced. These mechanisms include the electron-nuclear hyperfine contact interaction, the quadrupole interaction, the dipole-dipole hole-nuclear interaction, and the nuclear spin diffusion terms. The morphology, in particular the strain fields and the anisotropy of the QD system must be considered carefully when determining the strengths and relevance of each of the aforementioned microsopic mechanisms.

4.2 Electron Fermi contact interaction

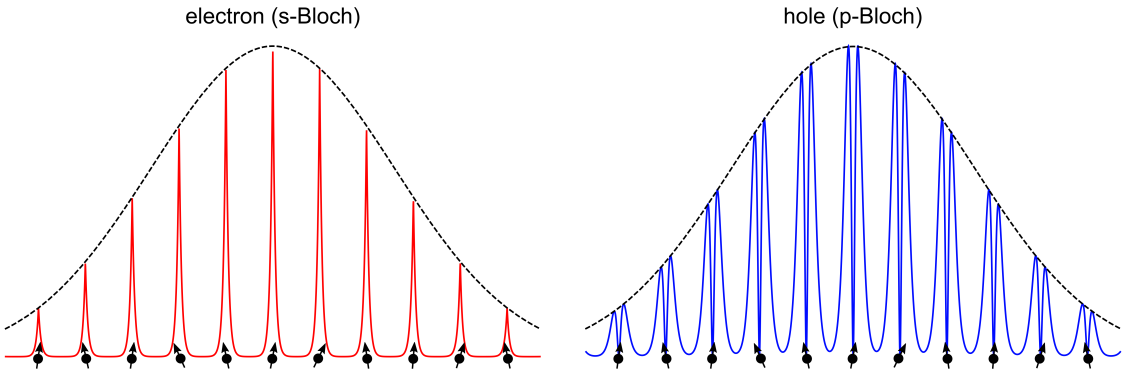

Figure 4.1: Electron (red solid line) and hole (blue solid line) probability density functions $|\psi|^2$ confined to the QD. Approximating the QD confinement potential as a finite square well (Chapter 2) results in a Gaussian envelope function for both the electron and hole wavefunctions (black dashed line). The periodic (Bloch) wavefunctions in III-V materials (InAs and GaAs) have s-symmetry for the electron (non-zero at the lattice site), and have p-symmetry for the hole (zero at the lattice site). The relative density of nuclear spin lattice sites (black circles with arrows) is lower than a realistic QD to emphasize the differences in the symmetry of the Bloch wavefunction for the electron and hole.

4.2.1 Formal derivation of Hamiltonian

The most important interaction term between the electron, which has an s-like periodic (Bloch) wavefunction in InAs, and nucleus is the Fermi contact interaction term, as opposed to the hole wavefunction which has p-like symmetry (Bloch) (Figure 4.1). This term can be derived in two ways [84]: first, as a non-relativistic correction to the dipole-dipole interaction when the finite spatial extent of the nuclear spin moments is accounted for, and second through a full relativistic approach using the Dirac equation. The resulting Hamiltonian is of the form

$$H_{e-n} = \frac{8\pi}{3}\gamma_e\gamma_n\hbar^2\hat{I}\cdot\hat{S}\delta(\vec{r}) = -\frac{8\pi}{3}\hat{\mu}_e\cdot\hat{\mu}_n\delta(\vec{r}) \tag{4.1}$$

where $\gamma_e, \gamma_n, \hat{I}, \hat{S}, \hat{\mu}_e, \hat{\mu}_n$ are the electronic and nuclear gyromagnetic ratios, the nuclear spin operator, the electron spin operator, the electron spin moment and the nuclear spin moment, respectively. Thus, the nuclear and electronic spin operators are coupled via this hyperfine contact interaction, which depends strongly on the overlap

of the electronic wavefunction at each crystal lattice site. When the Hamiltonian is summed up over the constituent nuclei of the QD and the expectation values are taken, the Hamiltonian can be written in the form

$$\begin{aligned} H_{e-n} &= \nu_0 \sum_j A_{e,j} |\psi_e(r_j)|^2 (I_{j,x} S_x + I_{j,y} S_y + I_{j,z} S_z) \\ &= \nu_0 \sum_j A_{e,j} |\psi_e(r_j)|^2 (I_{j,x} S_x + \frac{1}{2}(I_{j,+} S_- + I_{j,-} S_+)) \end{aligned} \tag{4.2}$$

where ν_0 is the two-atom unit cell volume for InAs and GaAs, and $\psi_e(r_j)$ is the electronic envelope wavefunction, and $A_{e,j} = \frac{8\pi}{3}\gamma_e \gamma_{n,j} \hbar^2 |u_e(r_j)|^2$, where $u_e(r_j)$ is the electronic Bloch (periodic) wavefunction evaluated at the nuclear site. The last line of the equation has been written in a form that separates the electron and nuclear spin projection along the external magnetic field $\vec{B}_x$ from the terms that are orthogonal, since the electronic and nuclear Zeeman Hamiltonians upon diagonalization lead to eigenstates with spin projection along $\hat{x}$.

The separation of the hyperfine contact interaction into two parts, a collinear and non-collinear term, is it at the heart of DNP phenomena. The first term $A_{e,j} I_{j,x} S_x$ results in the *Overhauser field* (OH field): an out-of-equilibrium non-zero nuclear spin polarization $\sum_j \langle I_j \rangle$, which exists in the QD either through direct RF excitation of the nuclei or through optical excitation, acts as an effective magnetic field of the form

$$\vec{B}_{OH} = \frac{\nu_0}{\mu_B g_e} \sum_j A_{e,j} |\psi_e(r_j)|^2 \langle \hat{I}_j \cdot \hat{n} \rangle \tag{4.3}$$

where $\hat{n}$ is a radial unit vector. The strength of the OH field is dependent on the hyperfine coupling constants, which in turn depend on the electronic Bloch wavefunction overlap at the nuclear site, and the electronic envelope wavefunction, which for the sake of simplicity can be considered to be uniform within the bounds of the InAs QD. More sophisticated treaments that study nuclear spin diffusion mediated by the electron take into consideration the non-uniform envelope wavefunction [140].

For all purposes in this thesis, the electron envelope wavefunction is taken to

be uniform over the interior of the InAs QD; this simplification is referred to as the "box model" [89]. The electron envelope wavefunction is taken to be equal to $\psi(r) = \sqrt{2/N\nu_0}$, where N is the number of nuclei present in the QD. The OH field then simplifies to

$$\vec{B}_{OH} = \frac{2\tilde{A}}{\mu_B g_e N} \sum_j \langle \hat{I}_j \rangle \tag{4.4}$$

where $\tilde{A}$ is taken to be the average of the In and As hyperfine constants.

The magnitude of the OH field can be expressed in terms of a nuclear spin polarization that ranges from -1 to +1. Working with the box model, the OH field can be expressed in terms of the hyperfine constants associated with each isotope

$$B_{OH} = \frac{2}{\mu_B g_e N} \sum_j A_j \langle I_j \rangle = \frac{1}{\mu_B g_e} \sum_j [3A_{Ga} n_{Ga} + 3A_{As} n_{As} + 9A_{In} n_{In}] \tag{4.5}$$

where n_α are the total fractional polarizations of each nuclear spin species. Assuming that the mechanism that polarizes the nuclei affects each isotope at the same rate, and that the QD is composed of In and As, the OH field can be expressed in terms of the uniform polarization s

$$B_{OH} = \frac{s}{2\mu_B g_e} [3A_{As} + 9A_{In}] = s \times (13.2 \text{ T}) \tag{4.6}$$

where s ranges from -1 to +1. Therefore, for InAs, the maximum OH field can be as large as 13.2 T.

The second term in the electron-nuclear hyperfine contact interaction, $I_{j,+}S_- + I_{j,-}S_+$, is the so-called flip-flop term [143], and describes an off-diagonal interaction in the Hamiltonian that simultaneously flips an electron spin while flipping (increasing or decreasing the spin projection by $\mp\hbar$) the state of the nuclear spin. The gyromagnetic ratio (before multiplying by the nuclear g-factor) of the nuclear spins is $31.52neVT^{-1}$, compared to that of the electron, which is equal to $57.88\mu eVT^{-1}$ [144]: thus, electron Zeeman energies are approximately 1800 times larger than the nuclear splittings for

equal magnetic fields. At zero external magnetic field and in the absence of the quadrupole splitting (Section 4.3), the flip-flop term is active, leading to electron spin and nuclear spin dephasing [89, 145], due to the degeneracy of the spin states. However, at magnetic fields which lead to an electron Zeeman splitting larger than any energy uncertainty present in the system due to dephasing from phonon scattering [146, 147], radiative recombination (2 μeV linewidth for InAs QDs) [108], or random fluctuations in lattice site occupation [145, 148], the nuclear Zeeman energy becomes negligible compared to the electron Zeeman energy. Electron spin flips are no longer matched in energy by the nuclear spin flip, and the interaction is effectively turned off. Nevertheless, the interaction may lead to nuclear spin diffusion mediated by a virtual electron spin flip to second order in the electron-nuclear hyperfine constant, as will be shown in Section 4.2.3.

It is important to consider the flip-flop portion of the Hamiltonian does not have to act in a dynamical fashion, but may contribute to the static energy shifts and mixing of the nuclear spin eigenstates. Recalling the first line of equation 4.2, without consideration of the external field, each of the three electron-nuclear coupled terms may correspond to an OH field pointing in the $\hat{x}, \hat{y}$, or $\hat{z}$ direction.

There are at least two possibilities for where these non-collinear terms may act in a static fashion: first, when a different interaction such as the quadrupole [147, 149] or heavy-hole-light-hole mediated DNP [88,138,150] generates an OH field perpendicular to the external magnetic field . A non-zero OH field along a direction different from the quantization axis (external magnetic field) will rotate the optical selection rules of the QD system [92]. Second, the uncertainty principle relates the variance in one spin component inversely to the uncertainty in an orthogonal spin component: $\sigma_{J_x}\sigma_{J_y} \geq \frac{\hbar^2}{4}$. Therefore, in an experiment in which one nuclear-spin component is well-known (or prepared with high fidelity), the variance in the orthogonal components is necessarily increased. This second effect has been understood to modify the fluctuations of the nuclear spin ensemble [63, 136, 142, 151–154] in directions orthogonal to the external field, leading to a fluctuation of optical selection rules which may be detrimentally mapped on to flying qubits (photons) [124–126].

It is important to recall that the more general interaction between the nuclei and a spin carrier in the solid state is given by

$$H = \int |\psi(r)|^2 dV [\frac{8\pi}{3}\gamma_e\gamma_n\hbar^2\hat{I}\cdot\hat{S}\delta(r) + \hbar^2\frac{\gamma_e\gamma_n}{r^3}(3\frac{(\hat{I}\cdot\vec{r})(\hat{S}\cdot\vec{r})}{r^2} - \hat{I}\cdot\hat{S})] \tag{4.7}$$

where the last term arises from the dipole-dipole interaction. While the last term is especially important when considering the interaction between the hole and the nucleus (Section 4.4), it is shown here that the interaction disappears for carriers with s-type Bloch wavefunctions, ie. the electron.

The Bloch wavefunctions in the vicinity of the nucleus at each lattice site can be approximated by the solutions to the hydrogen atom potential which are the product of a radial form R_{nl} and the usual spherical harmonics Y_l^m, with the first few eigenfunctions given by [155, 156]

$$\begin{aligned}
&\psi_{nlm} = R_{nl}(r)Y_l^m(\theta,\phi) \\
&R_{nl}(r) = \sqrt{\left(\frac{2Z}{na_\mu}\right)^3\frac{(n-l-1)!}{2n(n+l)!}}e^{-Zr/na_\mu}\left(\frac{2Zr}{na_\mu}\right)^l L_{n-l-1}^{2l+1}\left(\frac{2Zr}{na_\mu}\right) \Rightarrow \\
&\psi_{100} = \frac{1}{\sqrt{\pi}}\left(\frac{Z}{a_0}\right)^{3/2}e^{-Zr/a_0} \\
&\psi_{200} = \frac{1}{2\sqrt{2\pi}}\left(\frac{Z}{a_0}\right)^{5/2}(1-\frac{Zr}{2a_0})e^{-Zr/2a_0} \\
&\psi_{210} = \frac{1}{4\sqrt{2\pi}}\left(\frac{Z}{a_0}\right)^{5/2}re^{-Zr/2a_0}\cos\theta \\
&\psi_{21\pm1} = \frac{1}{8\sqrt{2\pi}}\left(\frac{Z}{a_0}\right)^{5/2}re^{-Zr/2a_0}\sin\theta e^{\pm i\phi}
\end{aligned} \tag{4.8}$$

where L_{n-l-1}^{2l+1} are the generalized Laguerre polynomials, $a_\mu = \frac{m_e a_0}{\mu}$, where μ is the reduced mass of the electron-nuclear system, Z is the atomic number, n,l and m are the principal, angular momentum and angular momentum projection quantum numbers, and r is the radial coordinate. The s-like states (electrons) have the symmetry of the ψ_{n00} states, ie. that they are non-zero at the lattice site. Taking $\psi_e = \psi_{100}$,

for example, the dipole-dipole Hamiltonian in Equation 4.7 involves terms of the following form:

$$\frac{(\hat{I}\cdot\vec{r})(\hat{S}\cdot\vec{r})}{r^2} = \frac{1}{r^2}\left(I_x S_x x^2 + I_x S_y xy + ...\right) \tag{4.9}$$

The expectation value of the result above is taken over the entire volume:

$$\begin{aligned}&\alpha I_x S_x \int \frac{1}{r^5} x^2 e^{-2Zr/a_0} r^2 \sin\theta dr d\theta d\phi + \alpha I_x S_y \int \frac{1}{r^5} xy e^{-2Zr/a_0} r^2 \sin\theta dr d\theta d\phi + ... \\ &= \alpha I_x S_x \int \frac{1}{r} e^{-2Zr/a_0} g(\theta,\phi) dr d\theta d\phi + \alpha I_x S_y \int \frac{1}{r} e^{-2Zr/a_0} h(\theta,\phi) dr d\theta d\phi = 0\end{aligned} \tag{4.10}$$

where the last line is equal to zero by using the method of an effective potential [155] that does not diverge at infinity and taking advantage of the odd parity of the integrand, using $g(\theta,\phi)$ and $h(\theta,\phi)$ as the lumped angular functions. Additionally, each term in Equation 4.9 has an even multiple of position coordinates, resulting in $\frac{1}{r}$ for all integrands. In the case of the $\hat{I}\cdot\hat{S}$ term in Equation 4.7, the final integrand also has a $\frac{1}{r}$ dependence, resulting in zero. Thus, it is shown that the dipole-dipole term between s-symmetry states and the nuclei goes exactly to zero. It is also important to note that the divergence of $\frac{1}{r}$ at the lattice site is the motivation for incorporating the hyperfine contact term. Deeper studies have been performed using optically-detected NMR (ODNMR) experiments revealing that the electron wavefunctions in InAs/GaAs systems must also incorporate higher principal number spatial wavefunctions such as d and f orbitals [157]; these effects are neglected here.

4.2.2 Review of OH field effects in the solid state

The OH field acting on the electron due to nuclear spin polarization is the crux of the dynamic nuclear spin polarization physics [1]. The phenomenon was first predicted by OH in 1953 [158]. In his seminal work, he showed that an out-of-equilibrium electron spin population would drive nuclear spin polarization in a metallic solid. Electron spin resonance techniques could be used to saturate an electron spin transition,

leading to equal populations in the spin-up and spin-down states; a saturated electron spin population differs from the temperature-dependent populations predicted by the Boltzmann equation. The competition between re-thermalization and electron spin saturation drives angular momentum transfer to the nuclear spin population, leading to a net nuclear spin polarization.

In fact, in the high temperature limit, Overhauser showed that the ratio of nuclear spin polarization after electron spin saturation to the thermal value I_0 is equal to [84]

$$\frac{\langle I_z \rangle}{I_0} = 1 - \frac{\gamma_e}{\gamma_n} \frac{(s_0 - \langle s_z \rangle)}{s_0} \xrightarrow[T \to \infty]{} \frac{\gamma_e}{\gamma_n} \tag{4.11}$$

The electron and, for example, ^1H nuclear magnetic moments are equal to $1.76 \times 10^{11} \frac{rad}{s \cdot T}$ and $268 \times 10^6 \frac{rad}{s \cdot T}$ respectively, resulting in a theoretical nuclear polarization enhancement of $\sim$660: the nuclei are polarized as though the nuclear magnetic moment is equal to the electron magnetic moment. Overhauser's incredible prediction was originally received with deep skepticism for supposedly violating the laws of thermodynamics [143] until experimentally demonstrated by Carver [159] during the same year. Carver and Slichter demonstrated a 100 fold increase in nuclear spin polarization by using electron spin double resonance techniques [84] on Lithium.

Lampel [160] later went on to demonstrate that the OH field effect could be generated using optical excitation. The principles of the experiments are nearly the same [1] when comparing the electron spin resonance and optical pumping techniques: an external excitation field drives an out-of-equilibrium electron spin polarization, which then drives the nuclear spin polarization via the hyperfine contact interaction between the electron and nucleus. The optical experiments, know as *optical orientation*, first utilized a high-intensity unpolarized light to excite n-type ^{29}Si, leading to electron spin saturation; this experiment demonstrated a small nuclear spin polarization enhancement factors of -5.6. A second experiment, more relevant to modern experimental studies of QDs, involved optical pumping of the ^{29}Si electron spin polarization using circularly polarized light, taking advantage of the orthogonal selection rules that can be used to selectively excite degenerate states [160]. The nuclear spin polarization

generated in that experiment corresponded to the equilibrium polarization predicted for a 2.8 T external magnetic field at 77 K, thereby demonstrating a deep cooling of the nuclear spin ensemble. This optical orientation technique laid the groundwork for optical DNP work performed in many other solid state systems [1], as well as the work demonstrated in this thesis.

OH field phenomena in QD systems have been examined in great detail for nearly twenty years, with initial groundbreaking studies performed by Brown [161] and Gammon [141] in interface-fluctuation GaAs QDs. These two works showed that nuclear spin polarization could be optically pumped in QDs at high external magnetic fields via excitation of the neutral exciton. OH fields as high as 1.5 T were measured, resulting from nearly 70% polarization of the constituent nuclear spin ensemble. The magnitude of the nuclear spin polarization was shown to be power dependent [161]; off-resonant excitation above the QD discrete energy levels saturates at high optical powers, leading to a saturation of the optically-created electron spin polarization. The connection to the OH field was directly corroborated by scanning a radio-frequency (RF) excitation across the Ga and As nuclear spin resonances, leading to a depolarization of the nuclear spin ensemble as measured in the PL splitting on the neutral exciton [141]. Additionally, it was shown that the direction of the OH field depended on the helicity of the circular polarization, with $\sigma_+(\sigma_-)$ leading to an increase (decrease) in the OH field. The hyperfine contact non-collinear terms found in equation 4.2 are energy forbidden at magnetic fields leading to a neutral exciton splitting larger than the exciton radiative linewidth; the authors therefore propose [161] a mechanism that involves the dark exciton, which possesses a much longer radiative lifetime (microseconds) [162,163] than the bright exciton (nanosecond). The experiment reported [141] a nuclear spin polarization resolution of around 6 % (5 μeV neutral exciton shift); for comparison, the resonant Raman scattering experiments reported in this thesis reach a resolution of 7.3×10^{-2} % nuclear spin polarization, corresponding to an absolute nuclear spin sensitivity of $\sim$40 spins.

4.2.3 Calculation of electron hyperfine contact mediated nuclear spin diffusion using the Schrieffer-Wolff transformation

The OH field portion of the electron-nuclear hyperfine contact interaction results in the direct energy shift of the electron Zeeman energy resulting from a net nuclear spin polarization. This section now turns to understanding the effects of the flip-flop term at high magnetic fields. As mentioned in the previous section, angular momentum transfer from the electron spin to the nuclei is energy forbidden when the external magnetic field exceeds optical linewidths due to dephasing and radiative recombination. This transition between the low and high magnetic fields for which the flip-flop processes become virtual rather than real occurs around

$$B_{\text{transition}} = \frac{h\nu_{\text{FWHM}}}{\mu_B g_e} = \frac{2\mu\text{eV}}{58\mu\text{eV}/T \times 0.42} \sim 80 \text{ mT} \tag{4.12}$$

depending on the exact electron g-factor and radiative linewidth for the QD. Experiments reported in this thesis substantially exceed the transition magnetic field calculated above, and therefore any process which requires an electron spin flip without an additional mechanism such as laser excitation will be neglected.

Nevertheless, second-order processes may occur involving the virtual flip of an electron spin, resulting in a nuclear flip-flop between two nuclei coupled to one another via the electronic envelope wavefunction. This nuclear spin flip-flop process can be diagrammed schematically in the following way, in which only the electron spin and two nuclear spins are isolated out of the nuclear spin ensemble:

$$\begin{aligned} |\psi_{\text{total}}\rangle = |\psi_e\rangle\,|\psi_n\rangle &= |+_e\rangle\,|I_j\rangle\,|I_k\rangle \bigotimes_{n\neq j,k} |I_n\rangle \\ &\xrightarrow[\text{e-n flip-flop}]{\text{virtual}} |-_e\rangle\,|I_j + m_j\rangle\,|I_k\rangle \bigotimes_{n\neq j,k} |I_n\rangle \\ &\xrightarrow[\text{e-n flip-flop}]{\text{virtual}} |+_e\rangle\,|I_j + m_j\rangle\,|I_k - m_k\rangle \bigotimes_{n\neq j,k} |I_n\rangle \end{aligned} \tag{4.13}$$

Overall, both nuclear spin and electron spin angular momentum are conserved in the process, but nuclear spin polarization may diffuse throughout the QD, where this diffusion length is only limited by the spatial extent of the electron envelope wavefunc-

tion [140] and the spatial inhomogeneity of nuclear energies due to the quadrupole interaction. This secondary process is not energy forbidden, considering that the nuclear gyromagnetic factors are equal to 38.8 and 30.3 neV/T for ^{115}In and ^{75}As, respectively [164]. Thus, nuclear spin flips can always be compensated for by phonon scattering up to extremely high external magnetic fields not typically achieved in the laboratory environment, although the preferential direction of nuclear spin polarization is affected by other parameters such as laser detuning, as will be shown in a later Chapter 6.

This second-order nuclear flip-flop can be treated more rigorously using the Schrieffer-Wolff perturbation theory method [165]. The purpose of the method is to eliminate the perturbation term of the Hamiltonian using a unitary transformation of the full Hamiltonian, leaving behind terms that are higher order in the perturbation expansion parameter. The transformation acts in the following way: $\tilde{H} = e^{\hat{s}}\hat{H}e^{-\hat{s}}$, where $\hat{s}$ is a unitary, anti-Hermitian operator, and $H = H_e^{Zee} + H_n^{Zee} + H_{OH} + H'_{e-n} = H_0 + H'_{e-n}$, where the terms are the electron and nuclear Zeeman splitting, the OH field term, and the electron-nuclear hyperfine contact interaction flip-flop terms from Equation 4.2. $\hat{s}$ is chosen in such a way that the appropriate cancellation of the perturbation Hamiltonian occurs.

Using the Baker-Haussdorff-Campbell theorem, the unitary transformation can be expanded in terms of commutators

$$\begin{aligned} \tilde{H} = e^{\hat{s}}\hat{H}e^{-\hat{s}} &= \hat{H} + [\hat{s}, \hat{H}] + \frac{1}{2!}[\hat{s}, [\hat{s}, \hat{H}]] + ... \\ &\equiv H_0 + [s, H_0] + H'_{e-n} + [s, H'_{e-n}] + ... \end{aligned} \tag{4.14}$$

The following choice for $\hat{s}$ is made such that $[\hat{s}, H_e^{Zee} + H_n^{Zee}] = -H'_{e-n}$, thereby producing the desired cancellation. It can be shown that the following choice for $\hat{s}$ results in a complete cancellation of the perturbation Hamiltonian:

$$\hat{s} = \frac{1}{B_x}\sum_j \frac{A_{e,j}}{2\hbar(\mu_B g_e + \mu_{n,j} g_{n,j})}\left(S_+ I_{j,-} - S_- I_{j,+}\right) \tag{4.15}$$

Now that $\hat{s}$ has been chosen appropriately, higher-order perturbation terms now

appear in the transformed Hamiltonian, ignoring the $[\hat{s}, H_{OH}]$ portion of the expansion since it results in $S_{\pm}$ operators:

$$H' = [\hat{s}, H'_{e-n}] = \sum_{i,j} \frac{A_{e,i}A_{e,j}}{B_x(\mu_B g_e + \mu_{n,j} g_{n,j})} \hat{S}_x [I_{i,-} I_{j,+} + I_{j,-} I_{i,+}] \tag{4.16}$$

The aforementioned electron-mediated second-order nuclear spin diffusion process (Equation 4.13) is clearly observed after the Schrieffer-Wolff transformation: no electron spin flip is required to exchange angular momentum between nuclear spins I_i and I_j. In fact, this diffusion process couples farther than the nearest neighbor on the lattice, with the coupling constant being proportional to the electron envelope wavefunction (incorporated into the hyperfine contact coupling constants $A_{e,i}$), slowing down at higher external magnetic fields. This mechanism is posited to allow for efficient transfer of nuclear spin polarization between vertically-stacked QDs forming a quantum dot molecule (QDM) [63]; in the two-electron bias regime of the QDM, electron probability density is comparably high in both QDs [166]. This process differs from the nuclear dipole-dipole interaction (see Section 4.5), in which diffusion between QDs separated by a GaAs/AlGaAs is prohibited due to high strain at the boundary between the QD and the bulk material barrier (see Section 4.3), resulting in inhomogeneities in the nuclear spin splittings between nearest neighbor sites [167].

The role that the electron plays in nuclear spin polarization and diffusion is not yet understood. One study examined the ODNMR of In and As nuclear spin polarization in InAs QDs, observing Rabi oscillations and spin echo as a function of RF excitation pulse duration [**?**]. The study observed that the spin echo times are orders of magnitude longer for QD even electron occupation states ($0e^{-1}$ and $2e^{-1}$) versus the $1e^{-1}$ state, with echo times of around 5 ms in the even case and 20 μs in the $1e^{-1}$ case. The spin echo experiments revealed that the nuclear spin ensemble loses its coherence much more rapidly in the presence of a confined electron, corroborating the role of the electron-mediated nuclear flip-flop mechanism.

In the limit of large strain fields isolating the QD from the surrounding host material, the electron-mediated diffusion term is expected to preserve nuclear spin

polarization, simply transferring nuclear spin polarization spatially throughout the QD. Nevertheless, one study [168] shows that under the application of a 220 mT external field along the sample growth direction that the nuclear spin polarization decays considerably faster in the presence of a confined electron as compared to an empty dot, 7.7 ms versus 60 s, respectively. Thus, the underlying assumption of a QD decoupled from the host environment does not seem to hold. However, an additional mechanism known as co-tunneling is likely at work in this system due to the coupling of the QD to the n-GaAs Fermi reservoir [169]. A fast virtual spin flip may occur that leads to a loss of nuclear spin polarization into the environment, depending on the strength of the coupling between the reservoir and QD [147]. In fact, this spin flip provided by strong coupling to the Fermi reservoir when the QD is bias-tuned into resonance may provide the energy necessary to flip-flop the electron and nuclei via the hyperfine contact flip-flop term. This spin flip rate, and related nuclear spin depolarization time, was shown [142] to depend inversely on the bias voltage across the sample, for a tunneling barrier of 25 nm. The details of co-tunneling are expounded upon further in Chapter 2.

The electron-mediated spin flip and co-tunneling-mediated nuclear spin depolarization effects are not always observed in QD samples, likely as a result of varying QD morphology and sample structure, especially as related to the biasing structure. Sun *et al* demonstrated that nuclear spin polarization and nuclear spin ensemble narrowing (NSN) could be prepared in around 7 ms and persisted in the absence of persistent laser excitation and in the presence of sample bias modulation into the co-tunneling region between the $0e^{-1}$ and $1e^{-1}$ states for at least 1.25 seconds [136]. The persistence of the NSN is attributed to the lack of optically excited hole, which drives the NSN via coherent population trapping (CPT). This result is remarkable in comparison to the aforementioned study [142], demonstrating that the nuclear spin ensemble coherence may not play a role in the NSN effect and that NSN may not necessarily depend on the electron spin orientation.

4.3 Electric quadrupole interaction

If the finite extent of the nuclear charge density that is centered at a site on the crystal lattice is considered, the nuclear charge moments (monopole, dipole, quadrupole) for nuclear spin $> 1/2$ [170] become significant for calculating the nuclear spin energy levels, even at zero magnetic field. For a non-spherical nuclear charge distribution (non-zero quadrupole), the orientation of the nuclear charge relative to the electric potential generated by the crystal lattice must be considered. In fact, in the presence of large strain fields found in Stranski-Krastanov grown QDs, the lowest energy nuclear charge configuration may be found with its major elliptical axis having deviated considerably from the growth direction [171]. The nuclear spin angular momentum projection eigenstates become coupled to the crystal lattice electrostatic potential when the diagonal elements of the quadrupole Hamiltonian are calculated using the Wigner-Eckart theorem [84, 143].

4.3.1 Formal derivation of the quadrupole interaction

One can expand the crystal lattice electric potential in a Taylor series expansion:

$$V(\vec{r}) = V(0) + \sum_{\alpha} x_{\alpha} \frac{\partial V}{\partial x_{\alpha}}\bigg|_{r=0} + \frac{1}{2!} \sum_{\alpha,\beta} x_{\alpha} x_{\beta} \frac{\partial^2 V}{\partial x_{\alpha} \partial x_{\beta}}\bigg|_{r=0} + ... \tag{4.17}$$

Then, taking the short-hand notation for the partial derivatives of the potential

$$V_{\alpha} = \frac{\partial V}{\partial x_{\alpha}}\bigg|_{r=0}, V_{\alpha\beta} = \frac{\partial^2 V}{\partial x_{\alpha} \partial x_{\beta}}\bigg|_{r=0} \tag{4.18}$$

one arrives at the mutual electrostatic energy due to the presence of the nuclear charge density in the crystal field is given by

$$\begin{aligned} E &= \int \rho(\vec{r}) V(\vec{r}) dV \\ &= V(0) \int \rho dV + \sum_{\alpha} V_{\alpha} \int x_{\alpha} \rho dV + \frac{1}{2!} V_{\alpha\beta} \sum_{\alpha,\beta} \int x_{\alpha,\beta} \rho dV + ... \end{aligned} \tag{4.19}$$

where the first term is the electrostatic energy of the nucleus treated as a point charge, and the final term is called the electric quadrupole term, related to the electric field gradient of the crystal field (the partial derivative of the electric field). The second term disappears due to the lack of nuclear permanent electric dipole moment [172]. The Wigner-Eckart theorem can be used to calculate the diagonal elements of the quadrupole interaction by representing the coordinates $x_{\alpha,\beta}$ and angular momentum operators in terms of their irreducible tensor operators, arriving at [84]

$$\begin{aligned} H_Q &= \frac{eQ}{6I(2I-1)} \sum_{\alpha,\beta} V_{\alpha\beta} \left[\frac{3}{2}(I_\alpha I_\beta + I_\beta I_\alpha) - \delta_{\alpha\beta} I(I+1) \right], \\ Q &= \langle II\eta | \sum_{k}^{protons} (3z_k^2 - r_k^2) \, |II\eta\rangle \end{aligned} \tag{4.20}$$

where Q is defined as the quadrupole moment of the nucleus and is the diagonal matrix element corresponding to the nuclear eigenstates $|JM_J\eta\rangle$, where J, M_J and η denote the quantum numbers for the total angular momentum, the z-component of angular momentum, and any other necessary quantum number used to denote the state, respectively. Physically, it is understood that the quadrupole energy arises from the difference in energies when the nuclear charge density is aligned along the z-axis versus the x and y axes; the energy difference may arise due to symmetry breaking from the electric field gradients in the crystal field. This symmetry breaking becomes especially pronounced at the QD-bulk boundary where the lattice mismatch between InAs and GaAs initially led to the self-assembly of the QD during the growth process, and is relaxed towards the center of the QD for larger height QDs [2].

Working under the assumption that no other charge is present within the spatial extent of the nuclear charge density, the quadrupole Hamiltonian can be simplified by using LaPlace's equation $\sum_\alpha V_{\alpha\alpha} = 0$:

$$H_Q = \frac{eQ}{6I(2I-1)} \left[V_{zz}(3I_z^2 - I(I+1)) + (V_{xx} - V_{yy})(I_x^2 - I_y^2) \right] \tag{4.21}$$

In the case of axial symmetry, one can choose a set of principal axes such that $V_{x'x'} = V_{y'y'}$, leading to the cancellation of the second term in the Hamiltonian. It is

important to note that in the QD system that the quadrupole Hamiltonian is a sum over all nuclei in the system: accordingly, each nuclear spin has local principal axes determined by the electric field gradients at that nucleus (Figure 4.2). Rewriting the Hamiltonian in the reference frame of the local principal axes

$$H_Q = \frac{eQ}{6I(2I-1)} V_{z'z'}(3I_{z'}^2 - I(I+1)) \tag{4.22}$$

where z' is direction along the uniaxial strain in the new principal axes frame. This Hamiltonian can be re-written in terms of the laboratory frame relative to the light propagation direction $\hat{z}$ and the external magnetic field along $\hat{x}$:

$$\begin{aligned} H_Q &= \frac{eQ}{6I(2I-1)} V_{z'z'}(3(I_z\cos\theta + I_x\sin\theta)^2 - I(I+1)) \\ &= \frac{eQ}{6I(2I-1)} V_{z'z'}(3I_z^2\cos^2\theta + 3(I_xI_z + I_zI_x)\cos\theta\sin\theta - I(I+1)) \end{aligned} \tag{4.23}$$

Thus, in the presence of axial strain along an axis that deviates from the z-axis, the nuclear spin projection eigenstates become mixed. This mixing is what opens up the possibility for nuclear spin polarization even when the electron is only coupled to the nuclei via the collinear OH field term $A_{e,n}\hat{S}_{e,x}\hat{I}_x$.

4.3.2 Calculation of quadrupole-mediated electron-nuclear coupling using the Schrieffer-Wolff transformation

It is not immediately evident from Equation 4.23 that the quadrupole Hamiltonian affects optically-driven DNP phenomena; as mentioned in the previous paragraph, the new Hamiltonian mixes nuclear spin states, but does not directly couple the nuclear spin states to the confined QD electron or hole.

The Schrieffer-Wolff transformation is used as a perturbation theory method, as applied in Section 4.2.3. The quadrupole interaction is treated as a perturbation relative to all other Hamiltonian terms in the system, especially the nuclear and electronic Zeeman energies. The exact strengths of the quadrupole mixing determined

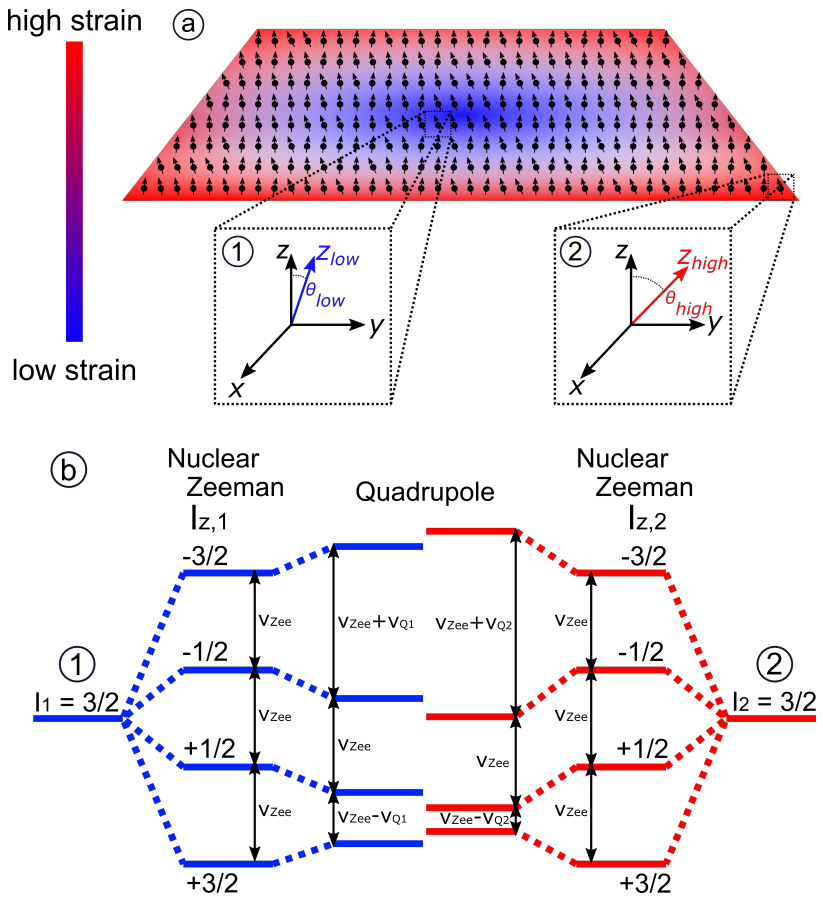

Figure 4.2: Quadrupole interaction effects in the QD. (a) The strain profile that originates from the lattice mismatch between InAs and the GaAs bulk material leads to high strain at the boundary of the QD (red), relative to the inner relaxed portion of the QD (blue). The local quantization axis of each nucleus depends on the direction of the strain at a given point, as indicated by the zoom boxes at the bottom of the figure. In the bottom left box of (a), a nucleus is fixed at a site of relatively low strain for which the principal axis is approximately aligned with the growth axis $\hat{z}$, compared to the bottom right box of (a) where the strain is considerably higher, causing the principal axis to deviate away from the growth axis more significantly. (b) Energy level diagram for the two nuclei (spin 3/2 in this case) examined in (a). Both nuclei are shifted by the external magnetic field due to the Zeeman interaction, leading to equal splittings for all nuclear spin transitions. When the quadrupole interaction is considered, the two satellite transitions (transitions involving a state with $|m_z| > 1/2$) shift with magnitude determined by the strength of the strain fields; the central transition is unshifted in first order. The energy levels of the two nuclei become non-degenerate due to the differing magnitude of the strain fields at different radial distances in the QD. $\nu_{Zee}, \nu_{Q,1}, \nu_{Q,2}$ are the nuclear Zeeman shift, and quadrupole shifts on nucleus 1 and 2, respectively.

experimentally will be considered in section 4.3.3. By performing an appropriate unitary transformation on the original Hamiltonian that includes the quadrupole term, the perturbation theory result leaves only the terms that couple the electron and nuclei and are not energy forbidden at high magnetic fields.

The transformation acts in the following way: $\tilde{H} = e^{\hat{S}}\hat{H}e^{-\hat{S}}$, where $\hat{S}$ is a unitary, anti-Hermitian operator, and $H = H_0 + H'_Q$, where the new quadrupole Hamiltonian contains only the nuclear mixing terms, and H_0 are the remaining terms including the electron and nuclear Zeeman energies and the OH field term; the diagonal terms of the quadrupole Hamiltonian are small compared to all other coupling constants in the system (Table 4.1).

Using the Baker-Haussdorff-Campbell theorem, the unitary transformation can be expanded in terms of commutators

$$\begin{aligned} \tilde{H} = e^{\hat{S}}\hat{H}e^{-\hat{S}} &= \hat{H} + [\hat{s}, \hat{H}] + \frac{1}{2!}[\hat{s}, [\hat{s}, \hat{H}]] + ... \\ &\equiv H_0 + [s, H_0] + H'_Q + [s, H'_Q] + ... \end{aligned} \tag{4.24}$$

The expansion becomes useful when $\hat{s}$ is chosen such that the commutator $[s, H_0^{subset}] = -H'_Q$, leading to a cancellation of the perturbation term. $[s, H'_Q]$ remains, in this case revealing a connection between the strong OH field interaction and the quadrupole interaction.

A form for $\hat{s}$ is chosen such that only nuclear spin operators are present. Thus, this term always commutes with H_e^{Zee} which only contains the electron spin operator. Additionally, the non-collinear hyperfine contact term with spin projection along the y and z directions is ignored due to energy mismatch between the nuclear and electron Zeeman energies under magnetic fields that lead to a splitting larger than the trion optical linewidth, ie. $\mu_B g_e B_x > \hbar\gamma_t$, or 80 mT. An operator $\hat{s}$ is sought such that $[\hat{s}, H_n^{Zee}] = -H'_Q$, thereby canceling out the perturbation term. Thus, one chooses $\hat{s}$ such that

$$\begin{aligned}\left[\hat{s}, H_n^{Zee}\right] &= -\mu_n g_n B_x[\hat{s}, I_x] = -H'_Q = -(I_z I_x + I_x I_z)\sin\theta\cos\theta B_Q \\ &\rightarrow [\hat{s}, I_x] = \frac{E_Q \sin 2\theta}{2B_x \mu_n g_n}(I_z I_x + I_x I_z)\end{aligned} \tag{4.25}$$

where $E_Q = \frac{eV_{z'z'}Q}{I(2I-1)}$. The following ansatz is made for the operator $\hat{s}$; this choice produces the desired cancellation:

$$\hat{s} = \frac{-E_Q \sin 2\theta}{\hbar B_x \mu_n g_n}\left[2(I_+ I_x - I_x I_-) + \hbar(I_+ - I_-)\right] \tag{4.26}$$

The operator algebra is detailed below, using the short-hand notation c_i for the constant out front of the operator $\hat{s}$. Additionally, the raising and lowering operators are defined in the following way, since the x-axis is chosen as the quantization axis: $I_\pm = (I_z \mp i I_y)$. The commutation relations are given by: $[I_x, I_y] = i\hbar I_z, [I_y, I_z] = i\hbar I_x, [I_z, I_x] = i\hbar I_y, [I_\pm, I_x] = \frac{i\hbar}{2}(I_y \pm i I_z)$. Thus,

$$\begin{aligned}[2(I_+ I_x - I_x I_-), I_x] &= 2([I_+ I_x, I_x] - [I_x I_-, I_x]) = 2([I_+, I_x]\, I_x - I_x\, [I_-, I_x]) \\ &= 2([I_z, I_x] - i[I_y, I_x])I_x - I_x([I_z, I_x] + i[I_y, I_x]) \\ &= 2i\hbar([I_y, I_x] + i(I_z I_x + I_x I_z))\end{aligned} \tag{4.27}$$

$$\begin{aligned}\hbar[I_+ - I_-, I_x] &= \hbar([I_z - iI_y, I_x] - [I_z + iI_y, I_x]) \\ &= -2i\hbar[I_y, I_x]\end{aligned} \tag{4.28}$$

Therefore,

$$[\hat{s}, I_x] = c_i(2(I_+ I_x - I_x I_-)I_x + \hbar[I_+ - I_-, I_x]) = \frac{E_Q \sin 2\theta}{B_x \mu_n g_n}(I_z I_x + I_x I_z) \tag{4.29}$$

leading to a cancellation of the H'_Q term. Now, this newly derived operator $\hat{s}$ is used to determine the perturbation theory result for the additional Hamiltonian term $[s, H_{e-n}^{OH}]$, where the second term in the commutator is the OH field electron-nuclear

hyperfine contact term. Working through the commutator below, the commutator is broken down into three parts:

$$\begin{aligned}\left[s^{(1)}, H_{e-n}^{OH}\right] &= [2c_i I_+ I_x, A_e S_x I_x] = 2c_i A_e (I_+ [I_x, S_x I_x] + [I_+, S_x I_x] I_x) \\ &= 2c_i A_e S_x [I_+, I_x] I_x = 2i\hbar c_i A_e S_x (I_y + iI_z) I_x\end{aligned} \tag{4.30}$$

$$\begin{aligned}\left[s^{(2)}, H_{e-n}^{OH}\right] &= [-2c_i I_x I_-, A_e S_x I_x] = -2c_i A_e (I_x [I_-, S_x I_x] + [I_x, S_x I_x] S_x) \\ &= -2c_i A_e S_x I_x [I_-, I_x] = -2i\hbar c_i A_e S_x I_x (I_y - iI_z)\end{aligned} \tag{4.31}$$

$$\begin{aligned}\left[s^{(3)}, H_{e-n}^{OH}\right] &= [\hbar c_i (I_+ - I_-), A_e S_x I_x] = \hbar c_i A_e S_x ([I_+, I_x] - [I_-, I_x]) \\ &= i\hbar^2 c_i A_e S_x (I_y + iI_z - I_y + iI_z) = -2\hbar^2 c_i A_e S_x I_z\end{aligned} \tag{4.32}$$

Resulting in the following new Hamiltonian term:

$$\begin{aligned}H' \equiv \left[s, H_{e-n}^{OH}\right] &= 2i\hbar c_i A_e (S_x I_y I_x + iS_x I_z I_x - S_x I_x I_y + iS_x I_x I_z + i\hbar S_x I_z) \\ &= 2i\hbar c_i A_e S_x (i(I_+ - I_-) I_x + i(I_+ + I_-) I_x \\ &\quad - 2iI_x (I_+ - I_-) + iI_x (I_+ + I_-) + i\hbar (I_+ + I_-)) \\ &= \frac{-E_Q A_e \sin 2\theta}{B_x \mu_n g_n} S_x (2I_+ I_x + 2I_x I_- + \hbar (I_+ + I_-))\end{aligned} \tag{4.33}$$

The Schrieffer-Wolff transformation has made evident that in the perturbation theory limit, ie. when the quadrupoplar interaction is weak compared to the hyperfine constants, there are still terms H' that drive nuclear spin polarization without requiring an electron spin flip. Thus, the terms will actively drive nuclear polarization without requiring additional energy input from the phonon bath or excitation lasers. No second order commutator terms are considered: each term involving higher powers of $\hat{s}$, and therefore higher order in the perturbation expansion parameter, are weak compared to the first order term.

The full Hamiltonian assuming electron-nuclear coupling is dominant with the quadrupole perturbation included is

$$\begin{aligned} H = H_{opt} + \mu_B g_e \hat{S}_{e,x} B_x - \mu_n \sum_j g_{n,j} \hat{I}_{j,x} B_x + \sum_j A_e S_x I_{j,x} \\ - \sum_j \frac{E_{Q,j} A_{e,j} \sin 2\theta_j}{B_x \mu_{n,j} g_{n,j}} \hat{S}_x (2I_{j,+} I_{j,x} + 2I_{j,x} I_{j,-} + \hbar(I_{j,+} + I_{j,-})) \end{aligned} \tag{4.34}$$

4.3.3 Relevance of the quadrupole interaction in QDs

The quadrupole interaction derived in the previous section is highly relevant to self-assembled QD systems. The formation of the QD as grown through the Stranski-Krastanov process is due entirely to the 7% lattice mismatch between InAs and GaAs [2]. Thus, strain is built in to the structure of the self-assembled QD, especially at the boundary between the QD and the bulk material [171]. Cross-sectional scanning tunneling microscopy experiments show that, as measured along the growth direction, the lattice constant of the QD compresses at the boundaries as measured relative to the bulk GaAs lattice constant, and expands internally as compared to the bulk InAs lattice constant [2, 80]. Taking this strain into consideration, the quadrupole shifts of the In, Ga and As nuclei are predicted via atomisitic calculations to range over as large as ± 18 MHz for a typical quantum dot with base diameter 25 nm and a height of 2.93 nm. These quadrupole shifts drop off around 3 nm away from the QD-bulk boundary [171].

The inhomogeneous strain present in the QD system has considerable implications on the nuclear-electron-hole coupling, as well as nuclear-nuclear coupling. In the presence of large strain, and therefore large electric field gradients, neighboring nuclear spin eigenstates can be detuned from one another considerably (Figure 4.2). Dzhioev *et al* measured the Hanle effect, or the measurement of the PL polarization relative to the excitation polarization in the Voigt geometry, in self-assembled InP/InGaP QDs, and revealed that the quadrupole interaction effectively decouples the nuclei from one

another [173]. This decoupling leads to an effective reduction in the nuclear dipole-dipole interaction, enhancing nuclear spin polarization even at zero external magnetic field. An important consideration is that the nuclear spin eigenvalues are shifted at first order in the quadrupole interaction strength only for values of $|m_z| > 1/2$ (satellite transitions).

Another important finding corroborating the significance of the quadrupole interaction in enhancing nuclear spin polarization was performed by Latta *et al* [139]. The authors report on experimental findings in which the QD nuclear spin polarization is measured to remain constant for at least 1000 seconds after generating a nuclear spin polarization via the excitation and laser frequency dragging of a neutral exciton (performed at 5 Tesla and 4 K). Furthermore, the injection of an electron during the waiting period shows that a temperature-independent nuclear spin polarization decay occurred on the order of 100 seconds. The authors show that this nuclear spin polarization time can be extended to 30 hours by cooling the sample down to 200 mK and decoupling the QD from the co-tunneling Fermi reservoir. The findings of these experiments indicate the presence of the quadrupole interaction: the MHz-level quadrupole shifts decouple the nuclei from one another, leading to exceedingly long depolarization times. In the presence of a confined electron, the nuclei are depolarized by an indirect term that can be derived by the Schrieffer-Wolff transformation in which the electron-nuclear off-diagonal contact terms are treated as a perturbation, resulting in a coupling Hamiltonian of the form $S_{e,x}I_i^+I_j^-$ [139] (details found in Section 4.2.3).

Pulsed NMR spectroscopy has been performed on both strained InAs/GaAs QDs and lattice-matched GaAs/AlGaAs interface-fluctuation QDs in order to further understand the role of the quadrupole interaction in DNP [167, 174]. The interface-fluctuation QDs consist of a single monolayer of GaAs embedded in 9 monolayers of $Al_{0.33}Ga_{0.67}As$. This class of QDs is nearly lattice-matched, and thus does not show signs of strong quadrupole shifts compared to Stranski-Krastanov-grown (SK) QDs. Chekhovich *et al* show that there are considerable differences in nuclear spin decoherence times between the two classes of dots: 4 ms for ^{115}In, 3 ms for ^{69}Ga for

the SK-grown QDs, and 1.27 ms for ^{115}In, 0.94 ms for ^{69}Ga in the lattice-matched QDs [167]. Although the nuclear spin decoherence time does not play a direct role in the nuclear spin depolarization time, it may possibly the electron spin decoherence time [63, 85, 136, 167, 175–177], although various reports are conflicting. This effect must be understood outside of the mean field theory typically used to explain OH field shifts; local nuclear spin fluctuations at each lattice site disturb the electronic wavefunction in a similar manner to collision-induced dephasing. Thus, the authors reveal that strain-induced quadrupole effects may considerably extend the coherence times of both nuclear spin quantum memories as well as electron spin qubits as compared to strain-free systems.

The detrimental effects of quadrupole-related DNP on the electron spin are investigated directly in a novel optical spin echo experiment performed by Stockill *et al* [149]. The experiment utilizes a modified Ramsey fringe technique using circularly-polarized, detuned two-photon Raman pulses to impart rotations on the electron spin qubit, with the initialized electron spin polarization alternating between each shot of the experiment. The authors claim that by generating no long term electron spin polarization averaged over the experiment that no net nuclear spin polarization is generated. This claim is supported by the absence of DNP-dragged Ramsey fringes, which are reported on in Chapter 7. Extending this technique to the optical spin echo reveals a complicated dependence of the spin echo visibility on both the magnetic field and the spin echo pulse delay time, with $T_{2,e}$ times extending out to 2.7 μs at 7 T. This complicated spin echo dependence is modeled by accounting for both the OH field components parallel and perpendicular to the applied magnetic field, where these perpendicular terms are generated by the quadrupole interaction. A key finding of the paper is that the electron spin coherence time is affected by the interplay of the quadrupole interaction and the nuclear Zeeman interaction, which has an external field dependence. In the intermediate regime in which the quadrupole and nuclear Zeeman energies are comparable, the nuclear spin angular momentum projection eigenstates are strongly mixed [147]. The relevant strengths of these interactions are investigated below.

A seminal theoretical paper by Huang and Hu [147] treats the interplay of the quadrupole interaction and nuclear Zeeman splitting rigorously. Their findings are that DNP in QDs operates in three qualitative regimes: low magnetic fields where the quadrupole dominates, high magnetic fields where the nuclear Zeeman splitting dominates, and the intermediate range where the eigenstates are mixed. Using constants found in that article, the external magnetic fields for which the system transitions into these different regimes are calculated below. Consider the quadrupolar energy defined in section 4.3.2:

$$E_Q = \frac{eV_{z'z'}Q}{I(2I-1)} = \frac{eQS_{11}\epsilon}{I(2I-1)} \tag{4.35}$$

where S_{11} is a constant determined by experiment for the principal axis strain and ϵ is the strain along the principal axis [178]. The constants used in the calculation, as well as the resulting quadrupole shifts calculated using equation 4.35 are listed in Table 4.1 [147, 171].

The magnetic fields reported in Table 4.1 are the fields for which the nuclear Zeeman energy becomes greater than the quadrupole energy for the two nuclear spin species. It is important to note that the Raman scattering (Chapter 5), Ramsey fringe, and EOM pulse experiments (Chapter 7) reported in this thesis are operated well above the transition magnetic fields determined here (experiments operate at 2 T). Nevertheless, the Hamiltonian terms listed in equation 4.23 may still account for the nuclear spin polarization observed in the experiments.

This section demonstrates that the quadrupole interaction arising from the coupling of the non-spherical nuclear charge density to the strained crystal lattice electric field gradients can contribute to DNP behavior in QD systems. The Hamiltonian term referenced in equation 4.23 will be used to explain DNP-broadening of Raman scattering lineshapes 5 and may additionally explain waiting time dependence behavior in experiments that do not involve continuous wave excitation of the trion (heavy-hole/light-hole) states.

Species	^{115}In	^{75}As
Nuclear spin I	9/2	3/2
Hyperfine constants (μeV)	56	46
Electric quadrupole moment Q ($10^{-24}cm^2$)	0.86	0.2
S_{11} (10^{15} statcoulombs/cm^3)	16.7	13
Gyromagnetic factor γ (neV/T)	39	30
ϵ (%)	9	8.6
$\theta_{z,Q}$	1.7°	12.9°
Results		
ν_Q (MHz) (using ϵ)	1.5	5.4
E_Q (neV)	6.2	22
$B_{\text{transition}}$ (mT)	150	740

Table 4.1: Quadrupole constants including results of energy calculations for ^{115}In and ^{75}As. $\theta_{z,Q}$ is the average deviation angle of the principal quadrupole axis from the z-axis, as found in equation 4.23.

4.4 Hole-nuclear interactions

The interactions of the valence band hole states with nuclei are frequently neglected in studies of DNP, but may act as the dominant mechanism for the generation of nuclear spin polarization and NSN under conditions where the electron spin mechanisms are inhibited [85, 88, 93–96, 136, 137, 150, 179–183]. Many studies to date have focused on investigating the coherence properties of the electron spin as a ground state qubit, thus utilizing the hole spin as an optically-excited state. If hole-nuclear interactions are present in a given QD system, the mechanism may be selectively turned off and on by optical excitation; many workers have developed theories incorporating the hole-trion probability into models of non-linear DNP phenomena [85, 175, 177, 184]. The modeling of DNP phenomena will be considered in more detail in Chapter 6.

The microscopic mechanisms for the hole-nuclear interactions, along with their associated Hamiltonians, are introduced below. The fundamental interaction between the hole and nuclei is the dipole-dipole interaction and the coupling of the orbital angular momentum of the hole to the nuclei, given by

$$H_{hh-n} = \hbar^2 \sum_j \frac{\gamma_h \gamma_{n,j}}{r_j^3} \left(3\frac{(\vec{r}_j \cdot \hat{S}_h)(\vec{r}_j \cdot \hat{I}_j) - \hat{S}_h \cdot \hat{I}_j}{r_j^2} - \hat{L}_h \cdot \hat{I}_j \right) \tag{4.36}$$

where γ_h is the gyromagnetic factor for the hole spin, and $\hat{L}_h$ is the hole orbital angular momentum [88]. The hyperfine contact interaction does not play a role due to the p-state symmetry of the Bloch wavefunctions for holes in InAs and GaAs [93]. Even in the absence of other symmetry breaking features such as heavy-hole light-hole mixing that will be discussed in further detail below, the hole-nuclear interaction contributes substantially [88].

This can be seen by expressing the electron and hole wavefunctions in terms of the hydrogenic eigenfunctions (Equation 4.8), assuming that the nuclei feel the effective charge distributions for In, Ga, and As associated with the $5s^2p^1$, $4s^2p^1$, and $4s^2p^3$ valence electrons. Specifically, the p-state orbitals are taken as having the form $\psi_{41\pm1}(r) = R_{41}(r)Y_1^{\pm1}(\theta,\phi)$. A theoretical study [88] evaluated the expectation value of the hole-nuclear Hamiltonian (Equation 4.36), arriving at an effective Hamiltonian $H_{hh-n} = \sum_j A_{hh-n,j} S_{hh,z} I_{j,z}$. The resulting Hamiltonian is of the same form as the OH field that couples the nuclear spin polarization to the electron spin splitting, although differing significantly in coupling strength. The ratio of the hole coupling to the electron coupling was calculated [88] using the effective screened nuclear charge distributions [185], with A_{hh-n}/A_e equal to 0.14 and 0.11 for Ga and As, respectively. It is important to note that the heavy-hole sub-band used for this calculation is derived by taking into account the valence band splitting between the heavy-hole and light-hole in the quasi-2D limit [186]; the Luttinger-Kohn parameters are calculated assuming the growth direction is along the crystal axis [001], defined here as the z-axis. Thus, the effective Hamiltonian coupling the hole and nuclei couples the z-projection components of the angular momentum operators even in the Voigt geometry. When

the external magnetic field is perpendicular to the growth direction of the QD, the Hamiltonian described here may contribute to an effective OH field acting on the hole spin that is orthogonal to the external field.

QDs which possess lower axial symmetry (growth axis), ie. are non-circular in shape, have valence bands (heavy hole, light hole and split-off hole states) which are mixed due to anisotropic strain [93, 179]. This mixing is referred to as heavy-hole light-hole (HHLH) mixing, and causes new hole-nuclear coupling terms to arise that act in competition with the electron-nuclear coupling terms. In the presence of HHLH mixing, the new hole wavefunctions are given by [93]

$$|\psi^{\pm}_{hole}\rangle \sim \chi_{hh}(r)\,|\pm\frac{3}{2}\rangle - \frac{\rho_s e^{\pm 2i\theta_s}}{\Delta_{lh}}\chi_{lh}(r)\,|\mp\frac{1}{2}\rangle \tag{4.37}$$

where $|\pm\frac{3}{2}\rangle$ are the heavy-hole states, $|\pm\frac{1}{2}\rangle$ are the light-hole states, Δ_{lh} is the energy separation between the heavy-hole and light-hole bands derived from the Luttinger-Kohn Hamiltonian [186], ρ_s is the strain coupling amplitude related to the anisotropy of the QD, θ_s is the angle of anisotropy in the QD, $\chi_{hh}(r)$ is the probability of the hole to be heavy, and $\chi_{lh}(r)$ is the probability of the hole to be light. The selection rules from the light-matter interaction coupling the hole to the electron become elliptically polarized [138, 179]. For example, the oscillator strength for the new transitions between the crystal ground state and the neutral exciton in the presence of HHLH mixing are given by

$$\Omega \sim |\,\langle\chi_h\psi_h|\,\langle\chi_e\psi_e|\,\vec{e}\cdot\vec{p}|0\rangle\,|^2 = 1 + A^2 + 2A\cos(2(\phi-\theta_s)), A = \frac{1}{\sqrt{3}}\frac{\rho_s}{\Delta_{lh}}\frac{\int\chi_e\chi_{lh}dr}{\int\chi_e\chi_{hh}dr} \tag{4.38}$$

where ϕ is the angle between a linear polarizer and an axis defined 45° clockwise from [110] crystal axis [179]. This change in oscillator strength can be measured directly in the laboratory through polarization-dependent resonant excitation (Chapter 5) or PL [94–96].

Using the HHLH-mixed hole states, an OH field-like term acting on the hole can be derived by plugging in these states into the Equation 4.36 [150]:

$$\vec{B}^h_{OH} = \frac{1}{\mu_B g_h} \sum_j \frac{C_j}{1+|\beta|^2} \left[\tilde{I}^j_z \vec{e}_z + \frac{2|\beta|}{\sqrt{3}} \left(\tilde{I}^j_x \vec{e}_x + \tilde{I}^j_y \vec{e}_y \right) \right] \tag{4.39}$$

where ν_0 is the unit cell volume, $\tilde{I}^j_x = I^j_x \cos\delta + I^j_y \sin\delta$, $\tilde{I}^j_y = -I^j_x \sin\delta + I^j_y \cos\delta$, $\tilde{I}^j_z = I^j_z$, $\psi_h(r_j)$ is the hole envelope wavefunction, $C_j = \frac{16}{5} \frac{\mu_B \mu_j}{I^j} \langle \frac{1}{r^3_j} \rangle \nu_0 |\psi_h(r_j)|^2$ is the dipole-dipole hyperfine constant associated with each lattice site averaged over the unit cell, $\delta = 2\theta_s$ and $\beta = \rho_s e^{\pm 2i\theta_s}/\Delta_{lh}$. The first term in Equation 4.39 is the same as described in the previous section derived by Leger *et al* [179]. The new additional terms are flip-flop type operators with coupling strength that depends on the amount of HHLH mixing β. These terms may contribute in the same manner that similar electron-nuclear hyperfine couplings (Section 4.2), including through nuclear spin polarization-induced shifts on the hole-splitting, or hole-mediated nuclear spin diffusion. Furthermore, the Hamiltonian (Equation 4.39) generates an OH field regardless of the direction of the external magnetic field.

A number of experimental studies indicate that the hole-nuclear interaction is non-trivial. Many experiments have focused on proving that the ground state hole qubit exhibits considerably slower dephasing times, showing initially that dephasing times are at least as long, if not longer than those of the electron [137]; dephasing was believed to be largely due to Rashba and Dresselhaus-type spin-orbit coupling. Multiple ultrafast coherent control experiments indicated that although the Ramsey fringe amplitude decay times of around 2.3 ns [180], which are given by T^*_2, are comparable to electron T^*_2 times, no non-linear effects such as hysteretic lineshapes are present as observed in the electron case. One study demonstrated exchange coupling between two hole qubits with no evidence for dephasing or non-linearities due to hole-nuclear coupling [187]. Another study showed that dynamical decoupling could be used to extend the hole T_2 time out to at least 4 μs.

However, there are a number of strong indications that the hole is indeed coupled to the nuclei in the QD system. Xu *et al* [85] demonstrated DNP lineshape non-linear broadening in a QD that exhibited strong HHLH mixing, and used coherent population trapping to significantly reduce the nuclear spin fluctuations. This DNP-related

behavior was attributed to trion, and hence the hole spin, population generated by laser excitation, and will be discussed in another chapter focused on modeling DNP phenomena (Chapter 6). Furthermore, another study following up on this work [136] showed that the NSN persisted in the dark, indicating that the effect is hole-trion related. Another ultrafast coherent control study performed on hole spin qubits [182] showed that the Ramsey fringe and spin echo time dependences are slowly modulated by a oscillation with 70 MHz frequency that nearly matches an integer multiple of the ^{115}In nuclear Zeeman splittings. This modulation is attributed to significant nuclear spin polarization generated when the pump-probe pulse delays match half-integer multiples of the same nuclear Zeeman splitting, with the behavior being accurately modeled by the OH field-like hole-nuclear coupling predicted by Fischer *et al* [88].

4.5 Nuclear dipole-dipole interactions

Another fundamental interaction in the QD nuclear system, and in the solid state generally, is the nuclear dipole-dipole interaction [84,143]. This interaction arises from the mutual interaction between the nuclear dipoles at each lattice site of the crystal, and exists independently of the other spin carriers in the QD or bulk. In this case of the bulk crystal, the nuclear dipole-dipole interaction leads generally to a broadening of magnetic resonance lines, and can typically be considered perturbatively [84]. The expression for the exact term is given by

$$H_n^{dipole} = \frac{\hbar^2}{2} \sum_{j,k} \gamma_j \gamma_k \left[\frac{\hat{I}_j \cdot \hat{I}_k}{r_{jk}^3} - 3 \frac{(\hat{I}_j \cdot \vec{r}_{jk})(\hat{I}_k \cdot \vec{r}_{jk})}{r_{jk}^5} \right] \tag{4.40}$$

The dipole-dipole expression contains combinations of nuclear spin operators that are non-secular, ie. they do not conserve energy without input from some external reservoir such as phonons. These terms can be neglected, and the approximate form of the expression can be written in terms of spherical coordinate angles [84]

$$H_n^{dipole} \sim \hbar^2 \sum_{j,k} \frac{\gamma_j \gamma_k}{r_{jk}^3}(1 - 3\cos^2\theta_{j,k})(I_{j,z}I_{k,z} - \frac{1}{4}(I_{j,+}I_{k,-} + I_{j,-}I_{k,+})) \tag{4.41}$$

This Hamiltonian therefore mixes the eigenstates of neighboring nuclear spins, with coupling strengths strongest at $\pi/2$ relative to the nuclear dipole moment, assuming that the moments have fixed orientation (not the case for precessing spins). In GaAs, the local magnetic fields due to this dipole-dipole interaction are approximately 0.1 mT for nearest neighbors, dropping off by $1/r^3$, providing a strong case for perturbative treatment compared to all other interactions in the system [1]. Rather than treating this interaction as a mixing term, it is used to describe nuclear spin diffusion in bulk solid state systems and QDs [1,140,166,167,188–191]. This nuclear spin diffusion phenomenon was observed using ODNMR in bulk GaAs doped with shallow donors [188]. In that experiment, nuclear magnetization generated by photoexcited electrons through optical orientation was shown to spatially diffuse in the absence of light excitation, thus attributed to nuclear dipole-dipole spin diffusion. This behavior is also present in QD systems, although the dipole-dipole diffusion must be considered along side other inhomogeneity effects that arise due to optically-generated carrier confinement and quadrupole effects [140, 189, 190].

One of the most important considerations in the QD system is the inhomogeneous Knight field shift on the nuclear spin ensemble [189,192]. The Knight field arises from the same Hamiltonian term as the OH field, but is the shift of the nuclear spin energy in the presence of the magnetic field produced by the electron via the electron-nuclear hyperfine interaction [84]. Moving beyond the box model [62] by considering the QD confinement potential realistically, the electron envelope wavefunction is found to be approximately Gaussian in the radial coordinate moving away from the center of the QD. Thus, the Knight field, which has the same spatial dependence given by the OH field term (Equation 4.3), results in inhomogeneous energy shifts of the nuclear spins throughout the QD [140, 189, 190], breaking the nuclear spin degeneracy and tuning the nuclei out of resonance with one another, inhibiting nuclear spin diffusion [167].

This reduction in nuclear spin diffusion leads to beneficial effects for QD nuclear spin polarization enhancement [140,189,190] and electron spin coherence [191]. The Knight field shifts are in competition with the electron-mediated nuclear spin diffusion term derived in Section 4.2.3; different magnetic field regimes exist for which the Knight shifts are dominant relative to the electron-mediated diffusion terms [140].

4.6 Conclusion

This chapter has introduced and expounded upon all of the known mechanisms for interactions between optically generated spin carriers, including the electron, heavy hole and light hole, and the constituent nuclei of the QD system. Rich physical phenomena arise due to the structural inhomogeneity both within a single QD and throughout an ensemble of QDs, leading to the strengthening of certain DNP mechanisms such as the quadrupole interaction or HHLH mixing, while inhibiting others such as the dipole-dipole nuclear spin diffusion. The relative strengths of each of these mechanisms must be taken into account rigorously when developing models for DNP: the coupled QD-nuclear-laser system is highly non-linear and there is a delicate balance between each competing mechanism, as will be discussed in more detail in Chapter 6.

Below is the full Hamiltonian for the electron-hole-nuclear coupling in the Voigt geometry, combining all terms discussed in the previous sections of this chapter:

$$
\begin{aligned}
H &= H_{opt} + H_e^{Zee} + H_n^{Zee} + H_{e-n} + H_{hh-n} + H_Q + H_{n-n} \\
&\sim H_{opt} + \mu_B g_e \hat{S}_{e,x} B_x - \sum_j \mu_{n,j} g_{n,j} I_{x,j} B_x + \sum_j A_{e,j} \hat{S}_{e,x} I_{j,x} \\
&+ \sum_{i,j} \frac{A_{e,i} A_{e,j}}{B_x(\mu_B g_e + \mu_{n,j} g_{n,j})} \hat{S}_x [I_{i,-} I_{j,+} + I_{j,-} I_{i,+}] \\
&- \sum_j \frac{E_{Q,j} A_{e,j} \sin 2\theta_j}{B_x \mu_{n,j} g_{n,j}} \hat{S}_x (2 I_{j,+} I_{j,x} + 2 I_{j,x} I_{j,-} + \hbar (I_{j,+} + I_{j,-})) \\
&+ \sum_j \frac{C_j}{1 + |\beta|^2} \hat{S}_h \cdot \left[\tilde{I}_z^j \vec{e}_z + \frac{2|\beta|}{\sqrt{3}} \left(\tilde{I}_x^j \vec{e}_x + \tilde{I}_y^j \vec{e}_y \right) \right] \\
&+ \hbar^2 \sum_{i,j} \frac{\gamma_i \gamma_j}{r_{ij}^3} (1 - 3\cos^2 \theta_{i,j}) (I_{i,z} I_{j,z} - \frac{1}{4} (I_{i,+} I_{j,-} + I_{i,-} I_{j,+}))
\end{aligned}
\tag{4.42}
$$

where the terms, in order, are the optical Hamiltonian coupling the electron ground state to the negative trion, the electron Zeeman Hamiltonian, the nuclear Zeeman Hamiltonian, the OH field acting on the electron, the electron-mediated nuclear spin diffusion term, the quadrupole-mediated electron-nuclear interaction, the dipole-mediated hole-nuclear interaction enabled by HHLH mixing, and the nuclear dipole-dipole diffusion terms, where all constants are defined in their associated sections in this chapter.

CHAPTER 5

Dynamic nuclear spin polarization in the electron-trion system measured using single-photon resonant Raman scattering and CW pump-probe spectroscopy

5.1 Introduction

There is an extensive body of previously reported spectroscopic and theoretical work providing evidence that the constituent nuclear spins in single self-assembled InAs QDs interact with the confined electron and heavy/light-hole in a highly non-linear manner with respect to experimental parameters that include the excitation laser frequency, power, pulse width/rate, and polarization [1, 57, 141, 158, 160]. This chapter details the implementation of high-resolution single-photon resonant Raman scattering to directly measure the Overhauser field (OH field) in the negatively-charged trion system in a single quantum dot (QD) subjected to an in-plane magnetic field as a function of resonant laser frequency in both the co-tunneling and optical pumping regimes. The data show two distinct nuclear spin ensemble configurations characterized by different OH field regimes that depend strongly on the excitation frequency and also exhibit hysteresis as a function of excitation frequency scan direction. The two distinct regimes qualitatively depend on which electron spin state is optically coupled to the scanning excitation laser. In one case the OH field tracks with the excitation frequency while in the other case the OH field shifts to avoid a forbidden range as the excitation laser is brought near the trion resonance. In the latter case, there is evidence for an increase in the fluctuations of the underlying OH

field distribution. The relative strengths of the electron-nuclear hyperfine contact interaction, hole-nuclear dipole interaction in the presence of heavy-hole light-hole mixing, and the electron-mediated quadrupolar interaction are carefully considered in conjunction with the steady-state electron spin OH field dependence and optical polarization-sensitive reflectivity measurements. The results appear consistent with the role of the electron-mediated quadrupolar interaction that transfers angular momentum from the laser to the electron to the nuclear spin ensemble; however, this conclusion is complicated by the possibility of DNP generated by hole-mediated mechanisms. A model is developed in the next chapter based off of the quadrupole interaction that is used to fit the resonant Raman spectra, further corroborating the role that in-built strain fields in the QD play in coupling the electron to the nuclear spin ensemble.

The electron spin qubit coherence times are affected detrimentally by the fluctuating Overhauser field [89]. Thus, many research groups have sought to understand, and in some cases control and reduce, the impact of this OH field. [63,85,136,149,154,176]. Various microscopic mechanisms have been proposed to account for DNP-induced effects related to nuclear spin polarization build-up and decay [168], ensemble narrowing, and fluctuation quieting [85,136]. These mechanisms include the electron-nuclear hyperfine contact interaction [1, 84, 143, 193], the hole-nuclear dipole interaction [96], and the electron-mediated quadrupolar interaction [62, 194], as well as additional depolarization terms [168], where each interaction's relevance depends on the external magnetic field strength, optical excitation conditions, and QD morphology [57]. All of these mechanisms are described in detail in Chapter 4.

To demonstrate the role of DNP on the electron-trion system, experiments are presented here that resolve the resonant Raman scattering in a single InAs quantum dot to directly determine the change in the OH field that affects the electron spin state splitting as a function of excitation frequency. Two dimensional maps of the Overhauser field distribution are generated as the excitation laser is scanned. The resulting OH field that reacts to the excitation laser scan depends clearly on which electron spin state is optically driven. Two-dimensional CW pump-probe maps are

also constructed for both the red and blue Zeeman transitions of the electron-trion system. Highly anomalous pump-probe dependences are observed that deviate considerably from the predicted Lorentzian lineshapes, and are accompanied by fast OH field dynamics (> 10 ms) and increased fluctuations in the red Zeeman case.

Two regimes are clearly evident: one for which the OH field shifts abruptly to bring the trion transition into resonance with the laser and tracks with the excitation laser detuning, and one where the OH field is rapidly pushed away from the laser in an anti-crossing-like fashion in the vicinity of the optical resonance; these two regimes are hereby referred to as the "tracking" and "avoiding" regimes, respectively. Quantitatively, the feedback in the tracking regime locks the trion transition with the laser frequency over a wide detuning range resulting in an OH field shift as large as 794 mT, compared to the avoiding regime in which the OH field shifts near the avoidance point in the center of the spectrum are on the order of $\sim$160 mT, measured from largest to smallest observed OH field for a given scan. Qualitatively, these nonlinear responses are common to both the optical pumping case with two lasers and the co-tunneling case in the presence of just a single laser. These two regimes are determined solely by which electron spin state is predominantly prepared by the repumping laser, or equivalently probed by the excitation laser scan. No discernible differences are observed when different heavy-hole states are probed by the excitation laser while keeping the initialized/probed electron spin state fixed.

The fluctuating nature of the OH field is also investigated by constructing two-dimensional excitation-detection maps with single data point acquisition times of less than 25 ms enabled by the utilization of high detection efficiency superconducting nanowire detectors as well as the cavity enhancement of the scattering/emission due to the on-chip distributed Bragg reflector (DBR) cavity. The data acquisition time scale has been successfully reduced down to the reported nuclear spin ensemble polarization/depolarization times [136, 168]. Abrupt jumps in Raman scattering energies are observed as the excitation laser is scanned that are indicative of rapid switching between nuclear spin ensemble states with upper bounds on switching times around 25 ms.

5.2 Indications of DNP phenomena in the electron-trion system

5.2.1 Review of observations of DNP in QD systems

Nuclear spin polarization effects were first observed in self-assembled GaAs/AlGaAs interface fluctuation dots by Brown *et al* via circularly-polarized PL excitation, in which the neutral exciton splitting was used as a probe of the OH field [141, 161]; OH fields as large as 1.3 T were reported. However, in these reports, no non-linear interactions between the optically excited carriers and the nuclear spin ensemble were observed; the OH field responded in a simple direct manner with respect to the optical excitation power. However, Merkulov *et al* [89] first pointed theoretically towards clues that the QD optical carriers may be strongly coupled to the nuclear environment. In that paper, the authors reported that the nuclear spin fluctuations present in the spin ensemble may detrimentally affect the electron spin coherence time due to time-dependent OH field shifts, but also that the back-action of the electron on the nuclear spin ensemble via the hyperfine contact interaction may modify these fluctuations.

The non-linear coupling between the QD exciton/trion and nuclear spin ensemble was first reported by Eble *et al* [195], in which circularly-polarized PL excitation was used to excite the neutral exciton and positively/negatively charged trions in a single QD. In the Faraday geometry (magnetic field parallel to QD growth direction) with a magnetic field strength of 200 mT, a non-linear dependence of the OH field with respect to the optically generated electron spin polarization was observed; the resulting OH field exhibited hysteresis with respect to the direction in which the electron spin polarization was increased or decreased. The authors adapted a model originally formulated by Abragam [143] to include a non-linearity in the nuclear spin pumping rate that depended on the nuclear spin pumping rate itself, and showed that this non-linearity limited the maximum achievable nuclear spin polarization to approximately 10%. This report was also the first indication that the quadrupole mechanism may be at play in the form of a nuclear spin depolarizing term. Braun *et al* also demonstrated

bistability in the resulting OH field as a function of the external magnetic field, optical excitation power, and optical polarization. A nuclear spin switching mechanism in the form of bistability was also demonstrated, and a dark exciton-mediated spin flip process was implicated for the non-linearity [196]. The microscopic mechanisms of the non-linear DNP process were investigated using temperature-dependent studies, ranging from 2 K to 55 K. At high temperature, achievable nuclear spin polarization reached as high as 50%; theoretical insights revealed that the energy level broadening of the electron and nuclear Zeeman levels at high temperature turns on the formerly energy-forbidden hyperfine contact interaction flip-flop terms.

The non-linearities associated with DNP became much more evident under resonant excitation (CW and pulsed, single dot and ensemble), as compared to previous studies that utilized polarized PL excitation. Very striking results were demonstrated in the pulsed excitation of an ensemble of negatively charged InAs/GaAs QDs [197]. In this study, the Faraday rotation technique was used to study the optical polarization rotation of picosecond pulses at a repetition rate of 76.5 MHz. These pulses were used to excite the electron-trion system; very strong Faraday rotations were observed to occur when a phase synchronization condition was satisified, specifically that the pulse separation time matched the electron spin precession period. From this, it was inferred that the nuclear spin ensemble OH fields were being focused by the repetitive pulsed excitation via the electron excitation, and nuclear spin memory was demonstrated to last for as long as 15 minutes. Under CW excitation, the "dragging" effect was reported by both Latta *et al* [142] and Xu *et al* [85]: trion absorption lines were broadened well beyond their expected linewidths, resulting in highly non-Lorentzian lineshapes. This dragging effect was investigated as a function of co-tunneling rate, and it was shown that the broadening widths increased as the inverse of the cotunneling rate [142]. Thorough studies of the nuclear spin decay times in the presence of resonant excitation were performed, revealing decay times ranging from 85-6000 seconds, and nearly complete suppression of nuclear spin diffusion out into the bulk environment [198]. Further observations of non-linear features were shown such as bistability and unstable points [194, 199]. Dragging lineshapes are even observed

in the resonant excitation of InAs quantum dot molecule structures, implying that DNP phenomena are not limited to single QDs [62]. An additional enlightening study showed that, when performing Ramsey fringe spectroscopy on the electron spin states using detuned Raman rotation pulses (Chapter 7), DNP non-linearities that distort Ramsey fringes are eliminated when the average electron spin polarization is maintained at zero by the usage of alternating optical pumping pulses on the $|\downarrow\rangle$ and $|\uparrow\rangle$ transitions, thus implicating the role of the electron spin polarization in the DNP effects present in some QDs [149].

5.2.2 DNP observations in the co-tunneling regime

In the absence of DNP effects, resonant excitation of the exciton/trion system in a single InAs QD at low temperature will result in a Lorentzian lineshape in absorption and resonance fluorescence [108], as demonstrated in Chapter 3. The optical response can be measured using sample modulation lock-in spectroscopy or direct detection of scattered single photons (Chapter 3). In a typical initial characterization experiment of a new QD, a high-resolution CW Ti:Saph tunable laser (Coherent MBR or MSquared Solstis) is frequency-scanned across the transition under investigation. The sample diode structure is bias-modulated with square wave modulation using a frequency of 517 Hz, with large voltage modulation of 100 mV peak-to-peak with offset voltages of around 600 mV, depending on whether the QD is operated in the co-tunneling or optical pumping regime (see Chapters 2 and 3 for details about DC Stark Shift bias modulation spectroscopy and more details about co-tunneling and optical pumping).

To identify the trion, an in-plane magnetic field (Voigt geometry) is applied, taking advantage of the Zeeman effect to split the trion into four linearly-polarized resonances (Chapter 2). For the QD under study in this chapter, the four absorption spectral lines are clearly resolved beyond their linewidths for magnetic fields greater than 1 T; the Raman scattering and pump-probe experiments are performed at 2 T (Figure 5.1). The sample is operated in the co-tunneling regime to allow for single beam

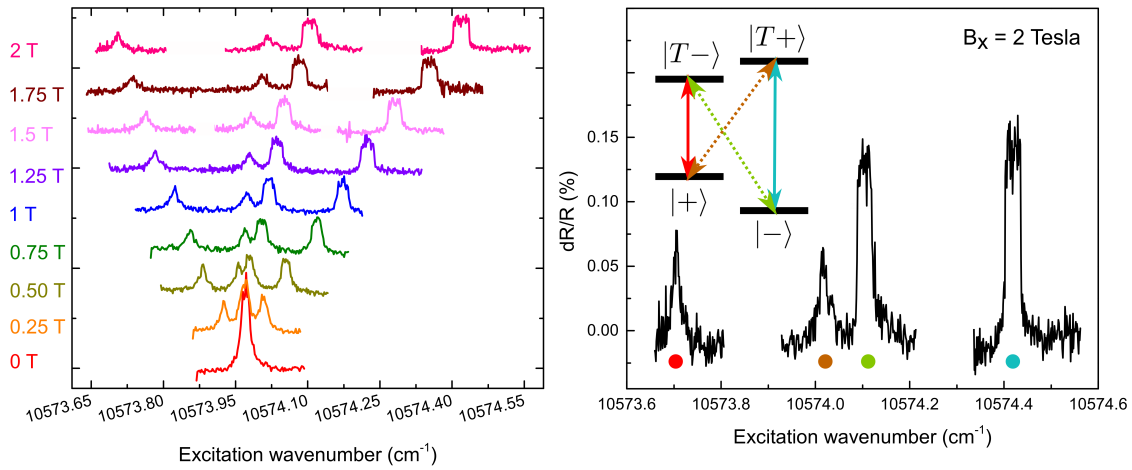

Figure 5.1: Fan diagram identifying electron-trion system. Left: Fan diagram: a resonant excitation laser is scanned across all four trion transitions and the modulated reflectivity is measured, where the magnetic field is increased in 250 mT steps for each trace. Right: Reflectivity scan at 2 T, with inset energy level diagram including selection rules and color-labelled transitions. Colored dots below each resonance match the corresponding color in the energy level diagram. Solid (dashed) lines in the energy level diagram correspond to horizontally (vertically) polarized selection rules.

excitation without optical pumping of the electron ground states.

As the magnetic field is ramped up in increments of 250 mT, the four lines clearly become split. However, the lineshapes deviate significantly from the expected Lorentzian lineshapes; the two red Zeeman transitions (two lowest energy transitions) which correspond to scanning the resonant laser over the $|+\rangle \rightarrow |T-\rangle$(red dot in Figure 5.1, right) and $|+\rangle \rightarrow |T+\rangle$(brown dot in Figure 5.1, right) transitions, have sharp cusps where a rounded Lorentzian is expected. The two blue Zeeman transitions, corresponding to the $|-\rangle \rightarrow |T-\rangle$(green dot in Figure 5.1, right) transition and $|-\rangle \rightarrow |T+\rangle$(blue dot in Figure 5.1, right) transition, are broadened significantly, with widths of around 4.3 μeV (0.035 cm^{-1}, 1.04 GHz) compared to the zero field linewidth of $\sim$500 MHz, with flat tops across the broadened range over which the reflectivity signal is approximately constant.

Broadened lineshapes with sharp edges have been observed before in single QDs, and are explained by DNP feedback processes [62, 85, 142, 177]. However, this DNP-

induced lineshape broadening is seldom observed in the co-tunneling regime. It has formerly been suggested that the rapid co-tunneling between the n-GaAs reservoir and the QD would lead to a fast averaging of the electron spin polarization to zero, therefore resulting in an unresponsive and decoupled nuclear spin ensemble as the laser is tuned across resonance [200]. Furthermore, another study reported DNP broadening widths inversely proportional to the bias-tunable co-tunneling rate for tunneling barriers on the order of 25 nm [142]. An additional study of the persistent narrowing of the nuclear spin ensemble, and consequential extension of the electron spin coherence time, revealed that bias modulation between neutral exciton and negatively-charged trion charging ranges does not necessarily depolarize the nuclear spins [136]. In light of these studies, the presence of the DNP effects in this sample is attributed to a relatively slow co-tunneling rate (< 1 MHz); the diode heterostructure is operated at the low bias range of the trion charging plateau, where the tunneling rate between n-GaAs reservoir and the QD is reduced compared to the higher bias co-tunneling region between the singly-charged and doubly-charged ranges (Chapter 2). Additionally, the quadrupole interaction DNP mechanism does not necessarily require a net electron spin polarization to drive nuclear spin polarization (Chapter 4) in the same manner that the hyperfine contact electron-nuclear flip-flop interaction does [143].

Thus, there is evidence for a strong interaction between the electron and the nuclear spin ensemble resulting in DNP. Broadened lineshapes are observed, and the qualitative nature of the broadening depends on which electron spin state is optically probed, pointing towards a mechanism that depends on spin projection.

The magnitude of the in-plane electron and heavy-hole g-factors is determined by fitting the fan diagram (Figure 5.1). Under these conditions, measurement of the g-factors assumes that *large* OH field shifts are eliminated by rapid depolarization due to tunneling electron spins between the QD and the reservoir, and the resonance center is determined as the centroid of the reflectivity peak [168]. Although there is DNP broadening present in the co-tunneling spectra that were used to measure the g-factors reported above, there is very little hysteresis (< 60 MHz) observed in these spectra, implying that the underlying bare (free of DNP) trion resonances sit

at the center of the co-tunneling resonances. The in-plane electron and heavy-hole g-factors are determined to be $|g_e^x| = 0.42$ and $|g_{hh}^x| = 0.31$, resulting in Zeeman shifts of 5.9 GHz/T and 4.3 GHz/T for the electron and heavy-hole, respectively. Error bars on the g-factors are chosen to be the standard errors of the linear fits of the electron and heavy-hole splittings as a function of magnetic field, and are equal to ± 0.004, or ± 50MHz/T. The g-factors are determined to have opposite signs based on their polarization selection rules; the electron spin g-factor has been to chosen to be positive. Determining the absolute sign of the g-factors goes beyond the scope of this work.

5.2.3 DNP observations in the optical pumping regime

Changing the bias to the middle of the charge stable range, where co-tunneling is minimal, optical pumping occurs, and the electron is trapped in the QD for at least 1 μsec (Chapter 7). A single excitation laser will rapidly optically pump the electron spin to opposite electron spin state, leading to a significant drop in the optical signal (absorption or scattering) (Chapter 7). The addition of strong pump laser driving the opposite electron spin state from that of the probe leads to a recovery of the optical signal, but significantly complicates the non-linearities associated with the coupled electron-nuclear system through DNP. Under these conditions, the effects of DNP are demonstrated to become more pronounced.

In the optical pumping regime, the DNP effects persist (Figure 5.7): in the dominantly initialized $|-\rangle$ case for which the re-pumping laser is resonant with the $|+\rangle \rightarrow |T+\rangle$ transition (Figure 5.7, right), the reflectivity is broadened and distorted over an excitation detuning range of 2.4 GHz, compared to 1.1 GHz for the co-tunneling case. In the dominantly initialized $|+\rangle$ case for which the re-pumping laser is resonant with the $|-\rangle \rightarrow |T-\rangle$ transition (Figure 5.7, left), the reflectivity peaks sharply in a non-Lorentzian manner. Additionally, both cases exhibit hysteresis with respect to the laser detuning direction, with the $|-\rangle$ initialized case abruptly shifting from a nearly zero reflectivity signal to a maximum in the forward scanning direction.

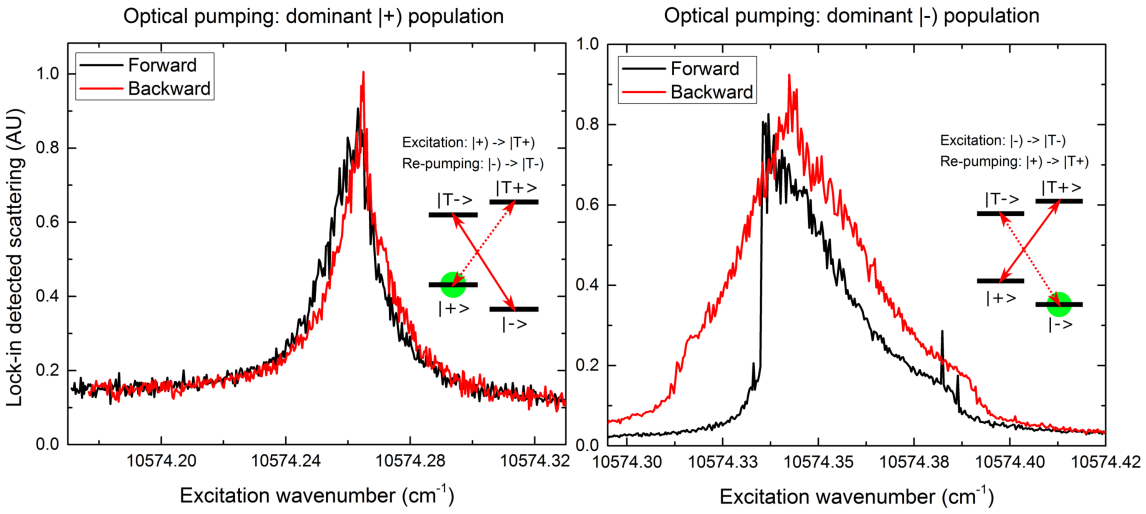

Figure 5.2: Optical pumping lock-in-detected photon scattering. Solid (dashed) arrowed lines in the energy level diagrams indicate re-pump (excitation) lasers, the green ball represents the prepared electron spin population. Left figure: Re-pump in resonance with $|-\rangle \rightarrow |T-\rangle$ transition and the excitation scans across the $|+\rangle \rightarrow |T+\rangle$ transition. Right figure: Re-pump in resonance with $|+\rangle \rightarrow |T+\rangle$ transition and the excitation scans across the $|-\rangle \rightarrow |T-\rangle$ transition. The excitation:repumping power ratio is equal to 1:5:10, and each data point is the average of 8 acquisitions integrated for 50 ms.

These abrupt drops in signal indicate that the OH field causes a shift in the optical resonance by at least the trion linewidth; this consideration shows that the OH field changes by at least 500 MHz/(5.9 GHz/Tesla) = $\sim$ 85 mT over a single laser step of 85 MHz.

The excitation and re-pumping transitions are carefully chosen to avoid the coherent population trapping (CPT) condition that occurs when two optically driven transitions share an optically-excited state, ie. that $|\omega_{repump} - \omega_{excite}| = \Delta_e$ [45]. This optical configuration is chosen to prevent the Rayleigh scattering from the probe from interfering with the Raman scattering of the pump, and vice versa, allowing for unique identification of the Rayleigh and Raman lines for each excitation field, and will be discussed in more detail in Section 5.3.

To investigate the effects of pump-probe excitation on the coupled electron-nuclear spin system, two dimensional pump-probe excitation maps were constructed using

high speed high-resolution sample bias modulation using single photon detecting nanowires. Using the resonance fluorescence technique described in Chapter 3, two co-polarized (45° CW relative to V) CW narrowband lasers (Coherent MBRs) are used in the pump-probe configuration that again avoids the CPT condition. For a given scan, the pump is held fixed, and the probe laser is scanned with an integration time of 10 ms. A 2D map is constructed by iterating the pump across the pumping resonance in question. The scattered single photons include both the Raman and Rayleigh scattering from both the pump and probe transitions; no energy discrimination occurs as in the Raman scattering experiments. The pump:probe power ratio is 10:1, with the pump and probe power well below the saturation regime.

In the first experiment (Figure 5.3), the pump is iterated across the $|-\rangle \rightarrow |T-\rangle$ transition while the probe is scanned rapidly across the $|+\rangle \rightarrow |T+\rangle$ transition. In the absence of any DNP effects, solving the density matrix equations for the four-level system indicates that the 2D maps for this configuration should be a simple 2D Lorentzian centered where both the pump and probe bare detunings are equal to zero, in this case with pump/probe wavenumbers approximately equal to 10574.335 cm^{-1} and 10574.275 cm^{-1}, respectively (Chapter 3). Instead, the 2D maps are highly anomalous: when the pump is red-detuned, a faint peak follows a diagonal line through the 2D map likely from the probe Raman scattering, and the signal drops off sharply after the probe is scanned across the diagonal. As the pump is brought closely into resonance with the $|-\rangle \rightarrow |T-\rangle$ transition, the signal brightens dramatically, and the peak brightness condition for each probe scan shifts dramatically in wavenumber at each consecutive pump wavenumber. For example (Figure 5.3, bottom), a small shift in the pump wavenumber (0.0011 cm^{-1}, 33 MHz) leads to a large shift in the peak brightness wavenumber in the probe scan (0.01 cm^{-1}, 300 MHz). In both cases, the overall signal plummets precipitously from the maximum signal to nearly the noise floor within a laser step of 0.0001 cm^{-1} (3 MHz) within 10 ms (experimental integration time). As the pump is moved farther into resonance, the slope of the peak shift in the 2D map becomes negative, indicating that the underlying OH field is shifting the underlying probe transition into the red. The red shift continues until

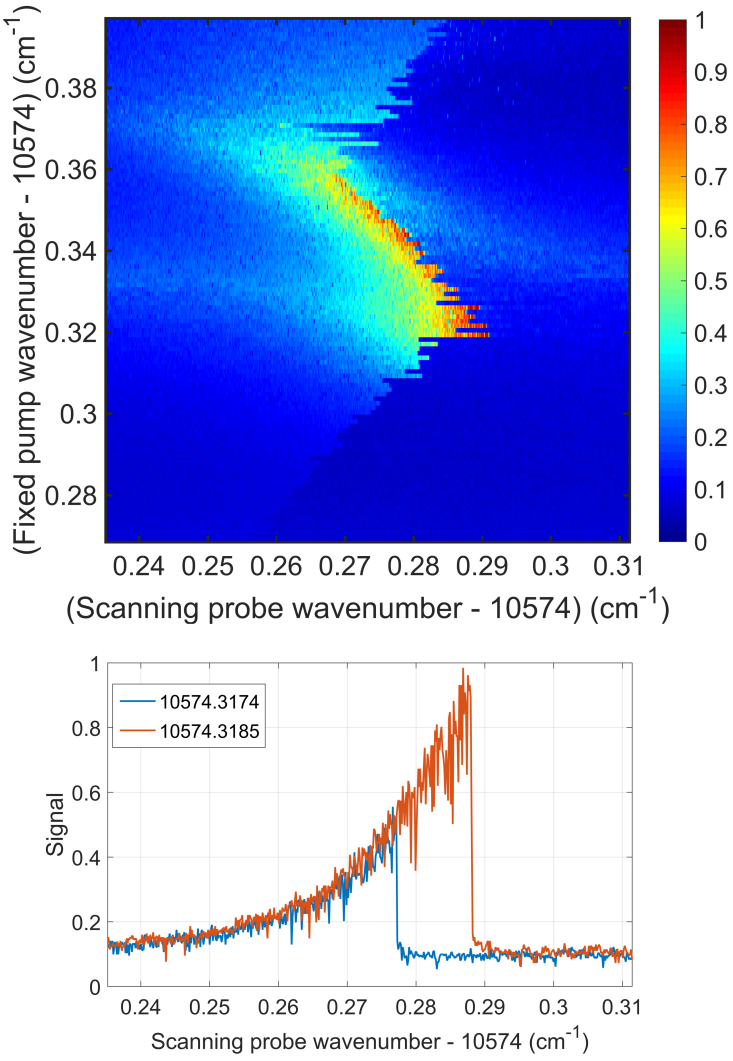

Figure 5.3: 2D pump-probe maps constructed using sample modulation lock-in detected single photon counting. The pump is iterated across the $|-\rangle \rightarrow |T-\rangle$ transition, and the probe is rapidly scanned across the $|+\rangle \rightarrow |T+\rangle$ transition with an acquisition time of 10 ms. Top: 2D pump-probe map. Bottom: probe scans taken from slices of the map at pump wavenumbers equal to 10574.3714 (blue) and 10574.3185 (orange) cm^{-1}.

the coupled electron-nuclear system abruptly moves way from this condition around the pump wavenumber 10574.37 cm^{-1}, and the total signal drops off and moves back towards the diagonal on the 2D map.

The main observations arising from the pump-probe experiment in which the probe is scanned across one of the red Zeeman transitions are the following:

1. There are forbidden regions where the optical transition is shifted far out of resonance with the pump and the probe (right-hand side of 2D map), and there are stable regions where the OH field apparently shifts into resonance with the pump and probe lasers (center of map). The transition from stability to instability occurs upon shifting the probe laser by a very small energy (3 MHz) compared to the trion linewidth.

2. The response time of the OH field acting on the electron is at least as fast as 10 ms, leading to OH field shifts at least as large as the magnetic field shift associated with the trion linewidth, or ∼85 mT.

3. The OH field fluctuates between adjacent probe scans (pump wavenumber difference of 0.0011 cm^{-1}, 33 MHz), indicating an unstable and fluctuating underlying OH field.

In the second pump-probe experiment (Figure 5.4), the pump is iterated across the $|+\rangle \rightarrow |T+\rangle$ transition while the probe is scanned rapidly across the $|-\rangle \rightarrow |T-\rangle$ transition. This 2D pump-probe map differs qualitatively from the previous configuration in a number of ways. There is a wide band of pump wavenumbers around the bare resonance condition (~ 10574.265 cm^{-1}) for which the signal is stable, bright, and does not drop off precipitously as in the red Zeeman probe case (Figure 5.3); one exemplary probe scan is displayed in the bottom plot of Figure 5.4 (orange curve). Nevertheless, even the relatively stable probe scans exhibit considerable lineshape broadening as distortion deviating significantly from the predicted Lorentzian with approximately 0.017 cm^{-1} (500 MHz) linewidth, comparing to the broadening width of approximately 0.07 cm^{-1} (2.10 GHz). Again, within the bright band centered around resonance, the OH field apparently shifts the transition red with increasing pump wavenumber. However, outside of this bright band, the system returns to instability observed in the red Zeeman probe case: the signal either snaps abruptly up to high signal when the pump laser is tuned blue or drops abruptly when the pump laser is tuned red. There are very clearly two regimes observed in this 2D map: a stable region near the center of the map that corresponds to where the bare

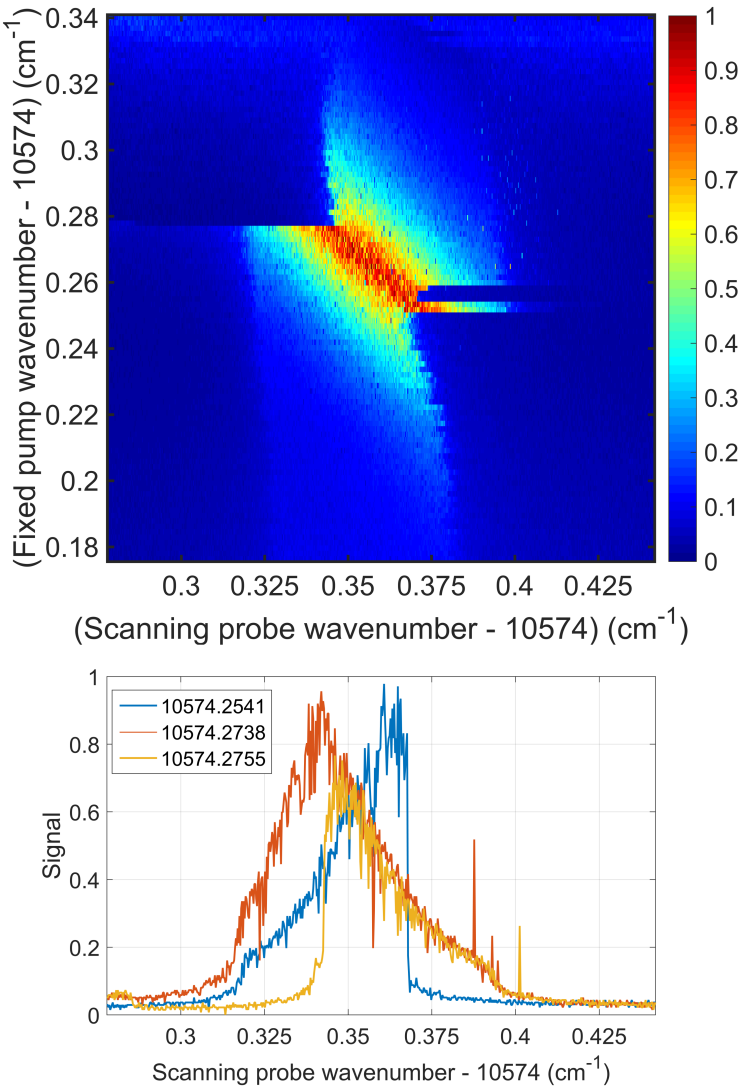

Figure 5.4: 2D pump-probe maps constructed using sample modulation lock-in detected single photon counting. The pump is iterated across the $|+\rangle \rightarrow |T+\rangle$ transition, and the probe is rapidly scanned across the $|-\rangle \rightarrow |T-\rangle$ transition with an acquisition time of 10 ms. Top: 2D pump-probe map. Bottom: probe scans taken from slices of the map at pump wavenumbers equal to 10574.2541 (blue), 10574.2738 (orange), and 10574.2755 (yellow) cm^{-1}.

resonance condition would lie, and a highly unstable region (deep blue portions of the map outside of the bright center) where the system is shifted far out of resonance, leading to very little signal from either the pump or probe.

In summary, the pump-probe experiments described above demonstrate that the electron-trion-nuclear system is highly non-linear with respect to the pump and probe

detunings, and that the qualitative nature of the DNP phenomena associated with this non-linearity depends on which Zeeman transitions are being optically probed (red or blue), at least in the limit of high pump:probe power ratio. Regions of stability and instability have been demonstrated, and the coupled system is shown to respond on time scales at least as fast as 10 ms.

5.3 DNP measured via single-photon Raman scattering

5.3.1 Introduction to single-photon Raman scattering measurements

Although the 2D pump-probe maps reveal that the OH field actively shifts the optical resonances non-linearly as a function of pump and probe detunings, the underlying OH fields are ambiguous and have not directly been measured. There are existing theoretical models [175,177] that predict how the OH field shifts under optical excitation, but the OH field has not been directly measured using resonant excitation without resorting to modeling efforts that extract an OH distribution from an absorption/fluorescence curve [85, 194].

To further understand the underlying OH field generating the non-Lorentzian optical response as the excitation laser is scanned across the trion resonances, the electron spin state splitting is directly measured as a function of the detuning. This measurement is achieved by using single-photon resonant Raman scattering which is frequency-resolved using a pressure-tuned etalon. The air-spaced etalon (SLS Optics) has a free-spectral range (FSR) of 45 GHz measured at 955 nm, and a FWHM of 400 MHz. To tune the optical resonance of the air-spaced etalon, the etalon is housed in a home-built pressure-tunable housing (Figure 5.5).

Pressure-tunable etalons have commonly been used to frequency resolve Brillouin scattering and to eliminate frequency drifts in diode lasers [201, 202]. Instead of using a mechanically adjustable bellows in a closed, vacuum-sealed system which requires high tolerances on vacuum leaks and is limited to slow resonance frequency adjustment, a voltage-controlled solenoid (MKS 640) is used to adjust the pressure,

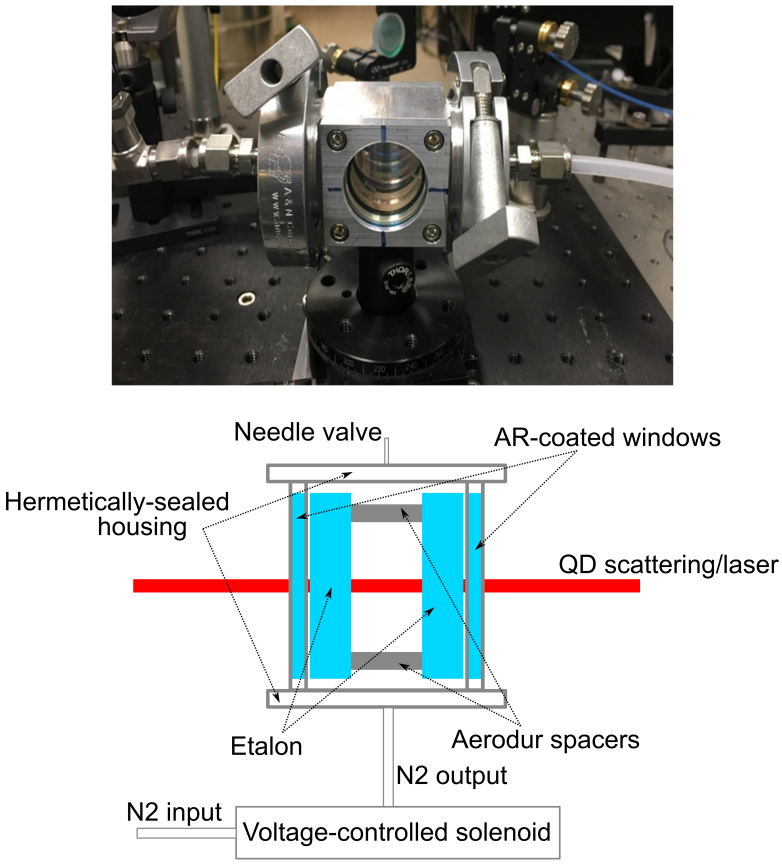

Figure 5.5: Pressure-tuned scanning Fabry Perot spectrometer. Top: photo of spectrometer in the lab. Bottom: schematic of spectrometer system. The QD scattering/laser light (red beam) is collimated from a fiber output and directed into the hermetically-sealed FP housing, with optical access through 1"-diameter AR-coated windows. Nitrogen gas (N_2) flows through the etalon housing, allowed to escape through a tuned needle valve output. The pressure of the N_2 gas is controlled by a servo-locked voltage-controlled solenoid, with a pressure-regulated N_2 tank attached.

and therefore the index of refraction, of the gas flowing through the etalon housing. Gas (nitrogen, in this case) is supplied by a tank with a static pressure regulator, which is allowed to flow through the cavity housing by the solenoid and leaked out by a needle valve. It can be shown that the change in wavelength for a given change in the density of a gas in a Fabry-Perot (FP) cavity is given by

$$\frac{\delta\lambda}{\lambda} = \frac{n-1}{n}\frac{\delta\rho}{\rho} \tag{5.1}$$

where n, ρ are the index of refraction of the flowing gas (nitrogen, in this case), and the density of the gas, respectively [202]. From the ideal gas law, it is known that the pressure, which is measured and regulated by the voltage-controlled solenoid, is directly proportional to the density of the gas. Thus, the shift in wavelength of the FP can be tuned by changing the pressure of the nitrogen gas flowing through the FP housing. The FP resonance can be scanned over at least one FSR for typical internal pressures ranging from 4 to 22 PSI. The tuning range could be extended by using a higher index of refraction gas or building a housing that can withstand higher pressures. The cavity has been designed such that the pressure of the gas inside and outside of the etalon is the same, preventing any deformation of the air-spaced etalon. The calibration curve relating the FP resonance to the pressure control bias is highly linear, with no observed deviations from linearity over at least one FSR.

Raman scattering techniques have previously been used to study single QDs. One study demonstrated high-quality single photons using Raman scattering, particularly in their tunability via the external magnetic field (in-plane) and laser detuning [203] over at least 2.5 GHz. Furthermore, the first-order coherence of the Raman and Rayleigh scattered photons from both an electron and heavy-hole was measured, allowing for a measurement of the ground state coherence time which is typically limited by the ground state lifetime [204], demonstrating an order of magnitude increase in ground state coherence time for the heavy-hole spin versus the electron spin. Another study investigated spin-cavity interactions for a QDM, and showed that the anti-Stokes Raman scattering could be enhanced considerably compared to the Stokes Raman pathway by resonant tuning of the high Q-factor photonic crystal cavity [205]. As far as the author of this thesis is aware, no studies have been performed which utilize Raman scattering to directly measure OH field shifts in single QDs.

For a fixed re-pump and excitation wavelength configuration, the pressure-tuned etalon is scanned slowly across one FSR in order to frequency-resolve the Rayleigh and Raman scattering; it is noted than an additional weak channel of spontaneous emission is expected that is enabled by a small amount of pure dephasing [124, 206]. For the four-level trion system, four scattering peaks are resolved: two Rayleigh

scattering peaks from the resonant re-pump and excitation, and two Raman scattering peaks. While the Rayleigh scattered photons will always scatter at the excitation laser energy and therefore do not reveal the trion transition energies, the difference between the Rayleigh and Raman peaks for a given laser is equal to the ground state splitting, here given by the electron spin state splitting due to the external magnetic field plus the OH field component along the external field direction:

$$E_{\text{Rayleigh}} - E_{\text{Raman}} = \pm\Delta_e = \pm(\Delta_e^{\text{ext}} + \Delta_{OH}) \tag{5.2}$$

At 2 Tesla, the electron splitting due to the combined external magnetic field and OH field is measured as 11.7 GHz. The linewidths of both the Rayleigh and Raman scattering are limited by the etalon linewidth of 400 MHz, which is smaller than the measured absorption reflectivity linewidth of the trion line at zero magnetic field (545 MHz), as expected for Rayleigh and Raman scattering in a system with minimal pure dephasing [206], (Appendix A and Chapter 3)

The QD spectrum is measured by resonantly exciting either one or two transitions of the QD, depending on whether the sample is operated in the co-tunneling or optical pumping charge bias range. The scattering of the laser by the QD and the emission are measured by slowly scanning the pressure on the etalon cavity, which scans the resonance condition of the cavity across the transitions under study. The filtered scattering/emission from the QD is then coupled into a single-mode fiber and detected by single photon counting nanowires (Quantum Opus). There is no further energy discrimination after the etalon; thus, the measurement consists of effectively integrating over the energy distribution of the filtered scattering. More explicitly, the scanning etalon spectrum of the QD is given by

$$\begin{aligned} I_{\text{spectrum}}(f_0^{FP}) &= \int I_{\text{QD}}(f, f_{FWHM}^{QD}, f_0^{QD}) T_{\text{FP}}(f, f_{FWHM}^{FP}, f_0^{FP}) df \\ T_{\text{FP}} &= \left[1 + F \sin^2\left(\pi \frac{(f - f_0^{FP})}{f_{FSR}}\right)\right]^{-1} \end{aligned} \tag{5.3}$$

where T_{FP} is the Airy function that describes the transmission of the FP cavity [207, 208], $F = (2r/(1-r)^2)^2$ is the *coefficient of finesse*, r is the amplitude

reflection coefficient for the etalon plates, and f_{FSR} is the free-spectral range of the etalon. The FWHM of the FP transmission can be derived to be equal to $f_{FWHM} = \frac{2f_{FSR}}{\pi}\sin^{-1}\left(1/\sqrt{F}\right)$. The QD spectrum may consist of spontaneous/stimulated emission, Rayleigh scattering, and Raman scattering (Chapter 3). For explanatory sake, the QD spectrum is here considered to consist of two contributions: spontaneous emission and Raman scattering, the first of which has a linewidth associated with radiative relaxation and the second which has a linewidth associated with the ground state dephasing time (Chapter 3). Both of these terms can be taken to be proportional to a Lorentzian:

$$I_{\mathrm{QD}} \propto \left[1 + \frac{4}{f_{FWHM}^2}(f - f_0^{QD})^2\right]^{-1} \tag{5.4}$$

where the typical power broadening term in the denominator has been neglected [45]. The resulting spectrum described above integrated over the emission/scattering energy by the single photon detector differs depending on the relative linewidths of the trion emission, Rayleigh/Raman scattering, and FP coefficient of finesse. A typical expected spectrum is displayed in Figure 5.6, where the parameters for the FP match those used in the experiment ($f_{FSR} = 45$ GHz, F = 5129.7 (FWHM of 400 MHz)). On the left, the Raman scattering case is displayed, where the raw Raman spectrum consists of a Lorentzian with negligible broadening (10 MHz) compared to the FP linewidth. In this case, the filtered spectrum after scanning the FP resonance shows very little difference from the FP transmission spectrum. Thus, without further deconvolution [209], an upper limit on the determined Raman linewidth is given by the FP linewidth. In the other case of the spontaneous emission dominated spectrum from the trion, where the QD linewidth has been chosen as slightly larger (550 MHz) than measured in this QD, the filtered spectrum is broadened beyond the FP linewidth, and the lineshape deviates from the Airy function.

An experimental FP scan of the trion resonance at zero magnetic field is displayed in Figure 5.7, along with the Airy function fit and residuals. The Airy function fits the filtered spectrum well, with a FWHM determined to be 425 MHz, compared to

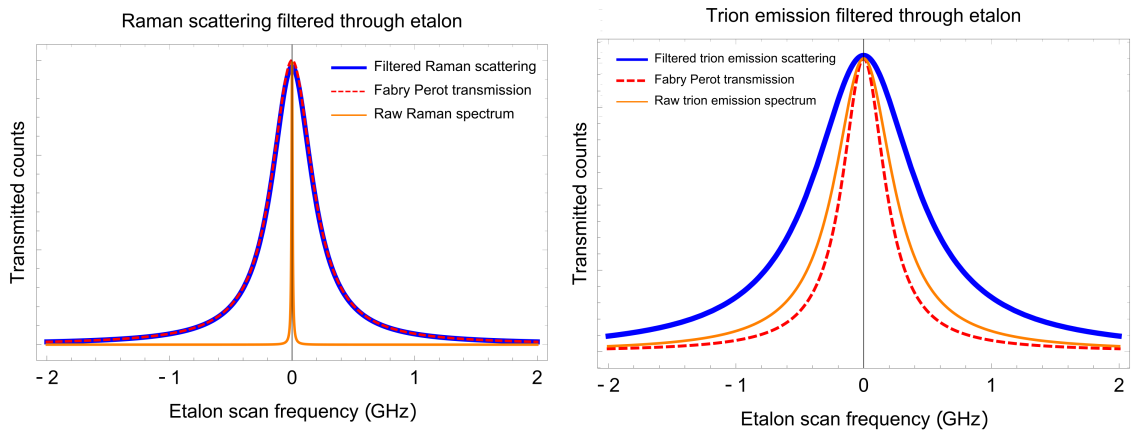

Figure 5.6: Scanning FP spectra for cases of Raman scattering and trion emission-dominated optical response. Left: Comparison of raw Raman spectrum from the QD (10 MHz linewidth)(yellow solid curve), FP transmission (45 GHz FSR, F = 5129.7) (red dashed), and the FP filtered Raman scattering (blue). Right: Comparison of the raw trion emission spectrum from the QD (550 MHz linewidth) (blue solid curve), FP transmision, and FP filtered trion emission spectrum (yellow).

the nominal 400 MHz FWHM of the FP. This small difference may possibly be due to slight de-collimation of the beam passing through the FP, leading to a slightly lower coefficient of finesse, since the lineshape is closer to an Airy function than the Lorentzian that would be expected if the QD spectrum linewidth exceeded that of the FP. Thus, it can be concluded that contribution from the spontaneous emission of the trion is relatively minimal and that the ground state dephasing of the electron spin state is small enough that it can not be resolved by the FP.

Additionally, the Raman scattering and Rayleigh scattering can easily be differentiated in the FP spectrum by holding the excitation laser in resonance with one of the trion transitions and scanning the FP resonance around $E_{laser} \pm \Delta_e$, depending on whether the $|+\rangle$ or $|-\rangle$ optical transitions are being probed. Furthermore, since the experiment is operated at low temperature (5 K), only one pathway of Raman scattering is observed for a given transition, as compared to typical room temperature Raman scattering experiments performed in molecules in which the ground state population is rapidly thermalized, leading to both Stokes and anti-Stokes Raman scattering [210]. As shown in Chapter 3, the Raman scattering intensity depends on

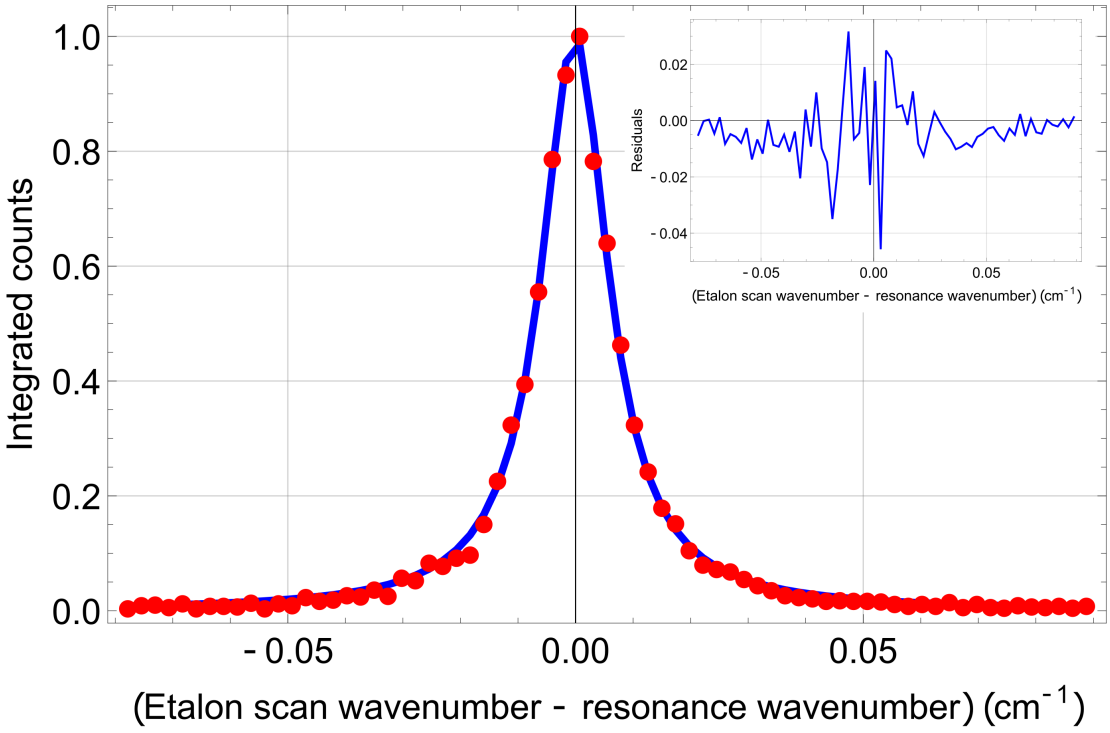

Figure 5.7: Scanning FP spectrum of zero magnetic field trion scattering from a single excitation field. The data (red dots) are fit with an Airy function (blue curve) with fit parameters F = 4544.67 ± 71.2, k_0 = 10574.1929 cm^{-1}, FSR = 45 GHz. Fit residuals are plotted in the inset.

the ground state population for the associated optical transition. A single excitation field experiment can be performed in the QD system when the sample bias fixes the system in the co-tunneling regime. Two scattering lines are observed (Figure 5.8): one associated with Rayleigh scattering from the $|-\rangle \rightarrow |T-\rangle$ transition centered around 10574.1187 cm^{-1}, and the Raman scattering line centered around 10573.7379 cm^{-1}. The difference in energy between these two scattering lines is exactly equal to the electron spin state (ground state) splitting, here equal to 11.42 GHz (in-plane magnetic field of 2 T), compared to the splitting predicted from the co-tunneling fan diagram of 11.8 GHz. Relatively small differences in the integrated counts for the Raman and Rayleigh scattering lines do not necessarily correspond to a difference in scattering rates due to the wavelength-dependent birefringence of the cryostat windows and collection optics (Chapter 3). The difference between the splitting measured in absorption and measured using Raman scattering indicates the possible presence

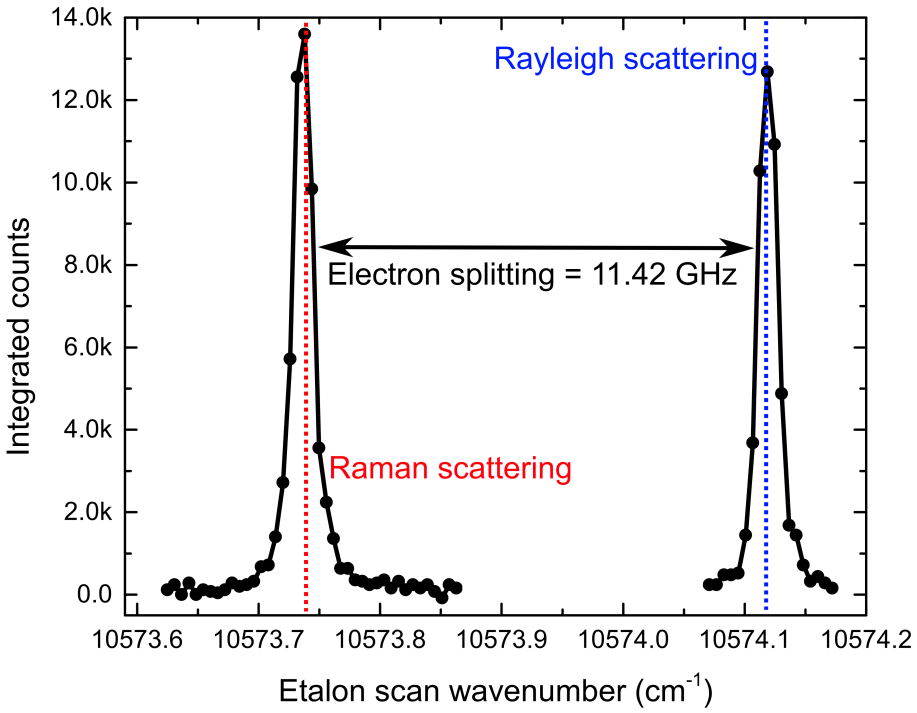

Figure 5.8: Rayleigh and Raman scattering for the single field excitation case in the co-tunneling regime. The excitation field is held in resonance with the $|-\rangle \rightarrow |T-\rangle$ transition. The separation between the Rayleigh and Raman scattering lines (lower energy line) is equal to the electron spin state splitting.

of OH field shifts due to resonant excitation; if the OH field is responsible for this shift, then the approximate magnitude of the field is (11.8-11.42)GHz/(5.9 GHz/T) = ∼60 mT.

The resonant Raman scattering technique is then extended to the optical pumping regime for which two excitation fields are required due to rapid decay of the optical signal in the presence of a single excitation field. The additional benefit of the use of two fields is that the electron spin state splitting can now be verified by comparing the pump and probe Rayleigh-Raman splitting, which should be identical. In one experiment, the probe excitation field is set in resonance with the $|+\rangle \rightarrow |T+\rangle$ transition, and the stronger repumping field is placed in resonance with the $|-\rangle \rightarrow |T-\rangle$ transition (Figure 5.9). Four scattering lines are resolved, two for each excitation field, where again the Rayleigh and Raman separation for a given excitation field is equal to the electron spin state (ground state) splitting. Thus, the electron-trion energy

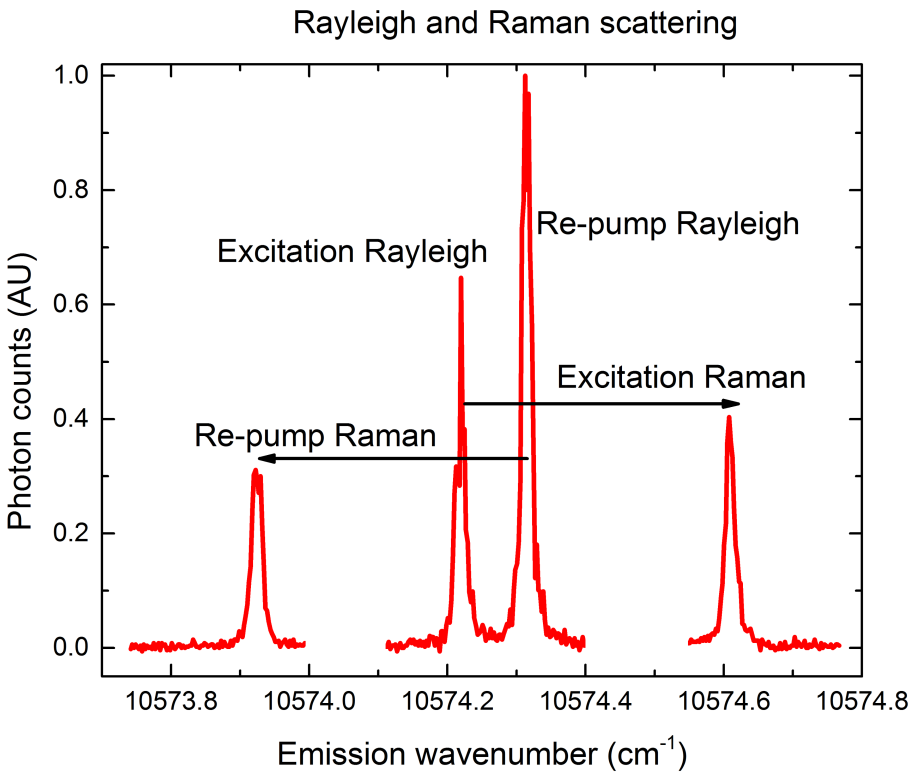

Figure 5.9: Rayleigh and Raman scattering in the re-pumping/excitation configuration at optical pumping. Excitation and re-pumping lasers are held on resonance with the $|+\rangle \rightarrow |T+\rangle$ and $|-\rangle \rightarrow |T-\rangle$ transitions, and the pressure-tuned etalon is scanned across all four Rayleigh and Raman scattering lines. The splitting between Rayleigh and Raman scattering lines for a given laser is equal to the ground (electron spin) state splitting.

level configuration is verified, consisting of two ground states and two excited states leading to the resulting Raman spectrum. The resulting electron spin state splitting is equal to 11.63 GHz for both the excitation and re-pump fields, in perfect agreement with one another, although still differing from the co-tunneling fan diagram fit. This class of two excitation field experiments lays the groundwork for the construction of 2D excitation-detection maps used to directly monitor the OH field shift as a function of excitation detuning.

5.3.2 Direct measurement of the OH field using resonant Raman scattering in the optical pumping regime

This Raman scattering technique is extended to construct two-dimensional excitation-emission energy maps to investigate the OH field as a function of excitation frequency. The two-dimensional map is obtained by measuring the scattering intensity while the etalon transmission frequency is fixed, and rapidly scanning the excitation laser across one of the trion transitions, iterating the etalon tuning to construct a 2D map. 25 ms integration time per data point is used, with an excitation laser frequency tuning time of < 5 ms. Maps were constructed for both the co-tunneling (Figure 5.10) and optical pumping (Figure 5.12) cases; the DNP responses are qualitatively similar for a given probed electron spin ground state, although the optical pumping cases generally show DNP responses with larger OH field shifts over wider excitation ranges and higher SNR (Tables 5.1 and 5.2). The main role of the re-pumping laser in these experiments seems to be a recovery of the scattering signal, rather than an overall change in the qualitative DNP response to a changing excitation laser frequency. This finding is corroborated by the striking similarities between the co-tunneling maps with a single excitation laser and the optical pumping maps with two lasers.

First, excitation-emission energy maps are presented for all four trion transitions in the co-tunneling bias range under single laser excitation (Figure 5.10), along with their corresponding extracted OH field shifts and dragging widths (Table 5.1). Line centers are extracted for a given excitation energy by fitting each detection energy slice with a single Lorentzian for the co-tunneling cases (Figure 5.11) and two Lorentzians for the optical pumping cases (Figure 5.13) if two Raman lines are observed from the re-pumping and excitation beams within the detection energy window. It is important to note that, as previously discussed in Section 5.3.1, there are two limits to the expected scanning FP spectral lineshapes: 1) when the QD spectrum is considerably narrower than the FP linewidth, the lineshape is expected to be an Airy function with the FP linewidth, 2) when the QD spectrum is a broad Lorentzian compared to the FP linewidth, the resulting lineshape is a broad Lorentzian. Nevertheless, a Lorentzian may be used in both cases: the only fit parameter of concern is the Raman scattering peak center, which does not depend on the determining lineshape fit choice (Lorentzian, Gaussian, Voigt, Airy). Four cases of re-pump and excitation

configurations in the optical pumping regime are then displayed (Figure 5.12, Table 5.2), examining all of the possible configurations in which the system is optically pumped by a strong optical field and the emitted radiation of interest reports on the electron spin splitting which yields a signal due to optical re-pumping without satisfying the CPT condition, and scan the excitation laser forward and backwards to examine hysteresis.

In the first cases under examination, the excitation laser is scanned across the $|+\rangle \rightarrow |T-\rangle$ transition (the lowest energy trion transition) (Figure 5.10, first panel). In the optical pumping case (Figure 5.12, first panel), two Raman lines are observed: the detection energy window now includes both the re-pump and excitation laser Raman scattering, allowing for independent corroboration of the OH field shift. In the absence of DNP, the Raman scattering due to the scanning excitation laser is anticipated to track diagonally (white dashed lines in maps) in the excitation-detection map as the laser is scanned, while the pump Raman line should be constant throughout. When optically pumping, the re-pumping beam (1.5:10 excitation:re-pump power ratio) is held fixed in resonance with the $|-\rangle \rightarrow |T+\rangle$ transition. The Raman scattering maps are highly anomalous: the Raman line red shifts to avoid an evidently forbidden energy range, abruptly shifts blue by 0.032 cm^{-1} (0.945 GHz, 157 mT, 1.19% nuclear spin polarization), and pulls back towards the expected diagonal line in the 2D map. The hysteresis between the forward and backward scans is particularly evident in the line center determination plots (Figure 5.11, first panel); there is considerable asymmetry in the region where the bare resonance would be expected, and the peak OH shifts are found at different locations for the two scan directions.

In the second case, the excitation laser is scanned across the $|+\rangle \rightarrow |T+\rangle$ transition, keeping the optically probed electron spin state the same as in the previous case. In the optical pumping case, a re-pumping beam is held fixed in resonance with the $|-\rangle \rightarrow |T-\rangle$ transition, pumping the electron spin to the $|+\rangle$ state to recover a scattering signal. In stark contrast to the expected diagonal Raman dependence, as the laser is brought within 0.02 cm^{-1} of the resonance, the Raman line brightens and red shifts away from the laser, abruptly shifting blue at the approximate line center,

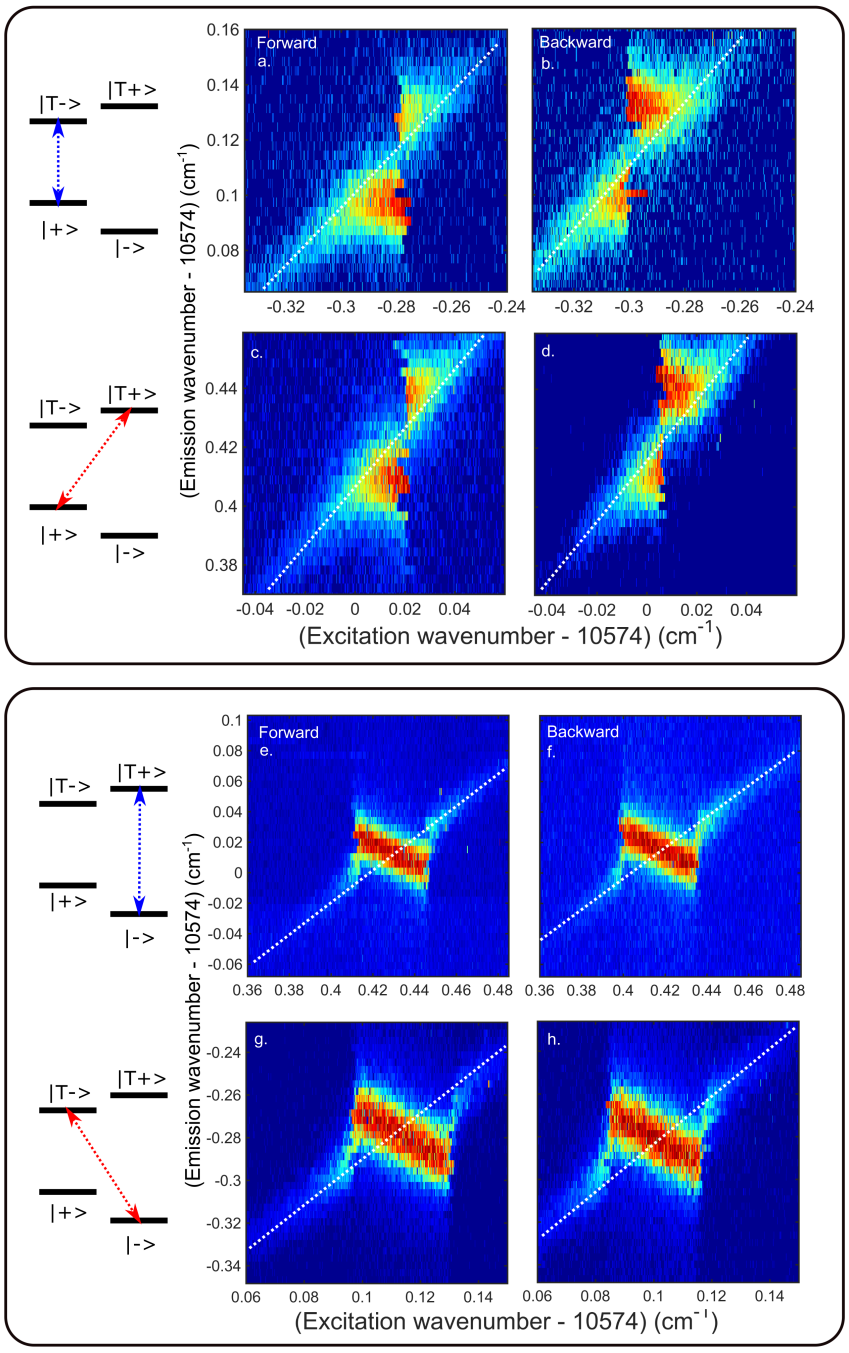

Figure 5.10: 2D Raman scattering excitation-emission energy maps for co-tunneling. Probe laser excitation of (first panel) $|+\rangle \rightarrow |T-\rangle$, (second panel) $|+\rangle \rightarrow |T+\rangle$, (third panel) $|-\rangle \rightarrow |T+\rangle$, and (fourth panel) $|-\rangle \rightarrow |T-\rangle$ transitions. Left (right) map in each panel is the corresponding forward (backward) probe laser scan. The probe excitation wavenumber is on the horizontal axis and the emission wavenumber (etalon detection wavenumber) is on the vertical axis. Dashed white lines in map indicate predicted Raman line in the absence of DNP.

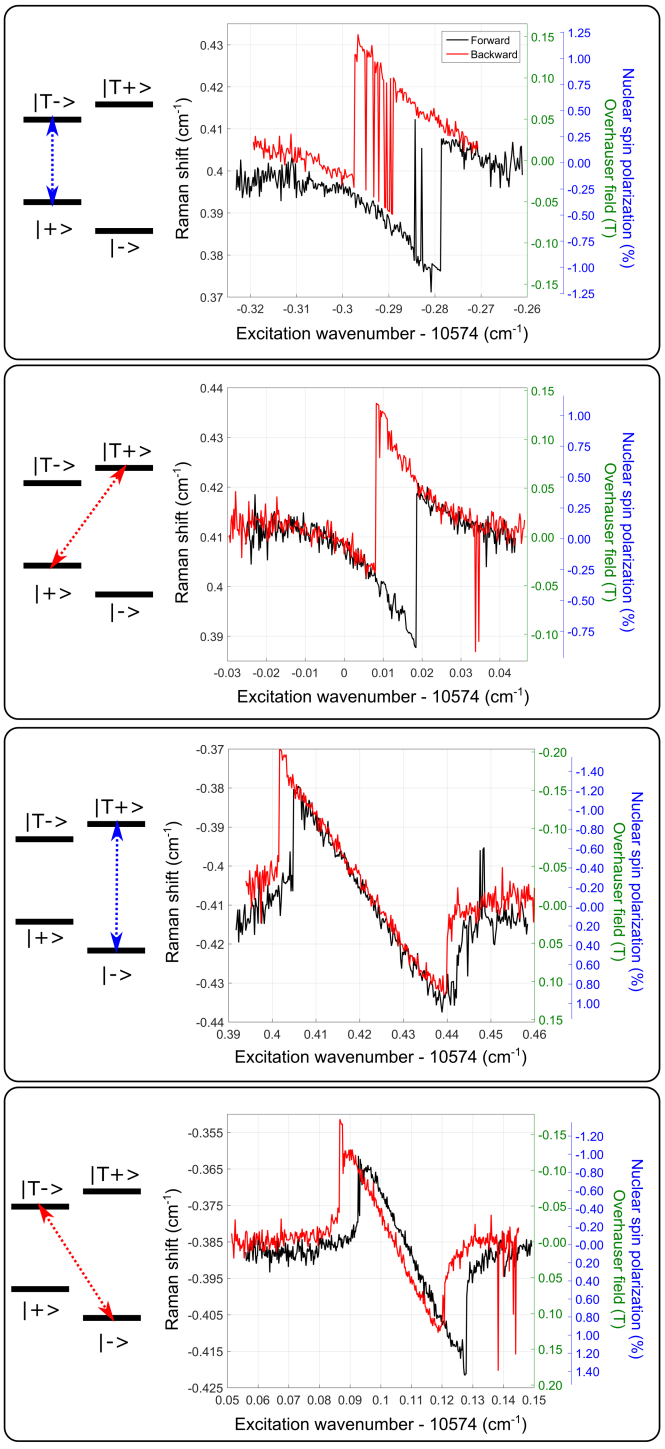

Figure 5.11: Determination of co-tunneling Raman line centers fit using Lorentzians. Probe laser excitation order is the same as in Figure 5.10. Left vertical axis is the difference between the probe laser excitation wavenumber and the Raman line center wavenumber, right green vertical axis is the OH field shift, and right blue axis is the nuclear spin polarization percentage. Black (red) curves are forward (backward) laser scans.

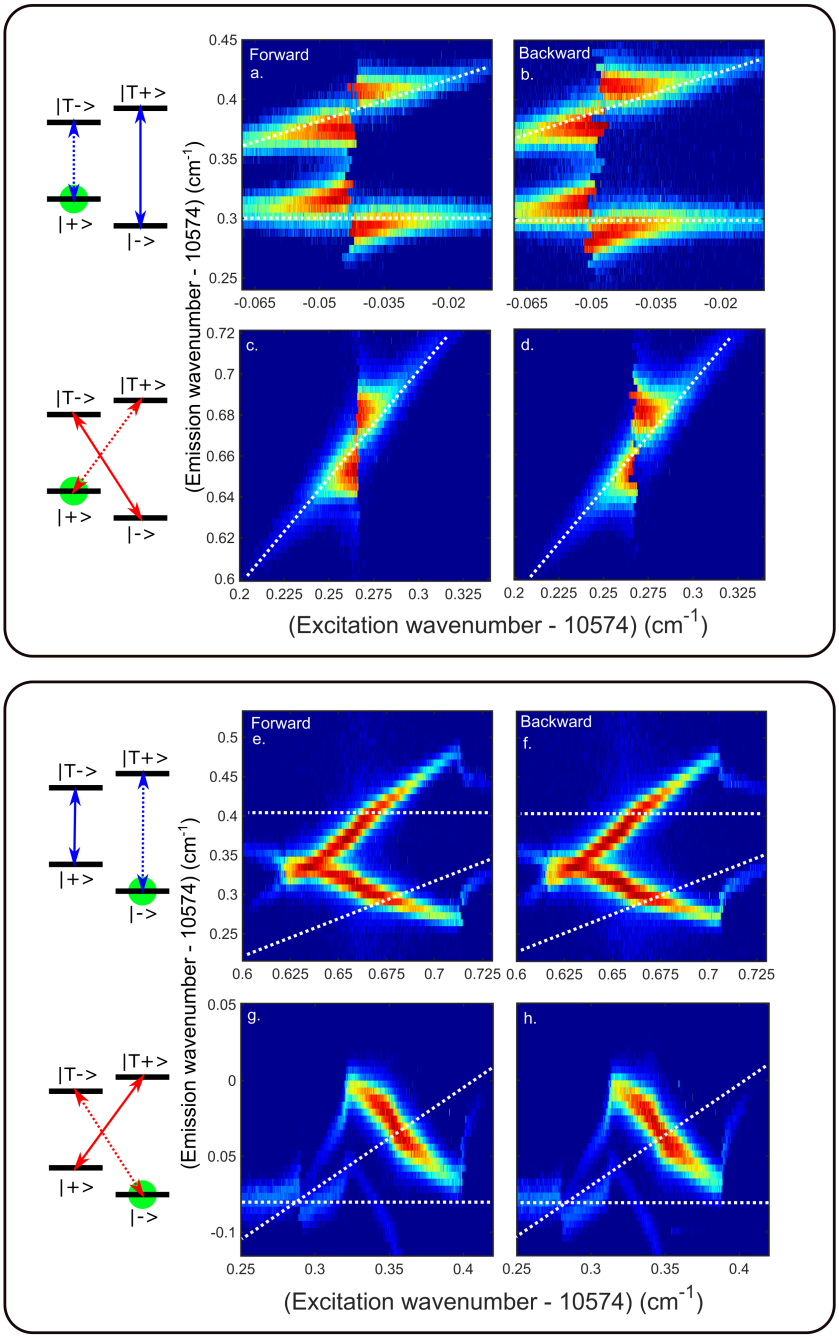

Figure 5.12: 2D Raman scattering excitation-emission energy maps for optical pumping. Probe/re-pumping laser excitation of (first panel) $|+\rangle \rightarrow |T-\rangle/|-\rangle \rightarrow |T+\rangle$, (second panel) $|+\rangle \rightarrow |T+\rangle/|-\rangle \rightarrow |T-\rangle$, (third panel) $|-\rangle \rightarrow |T+\rangle/|+\rangle \rightarrow |T-\rangle$, and (fourth panel) $|-\rangle \rightarrow |T-\rangle/|+\rangle \rightarrow |T+\rangle$ transitions. Probe(re-pump) indicated by dashed(solid) arrows in energy level diagrams. Left (right) map in each panel is the corresponding forward (backward) probe laser scan. The probe excitation wavenumber is on the horizontal axis and the emission wavenumber (etalon detection wavenumber) is on the vertical axis. Dashed white lines in map indicate predicted Raman line in the absence of DNP.

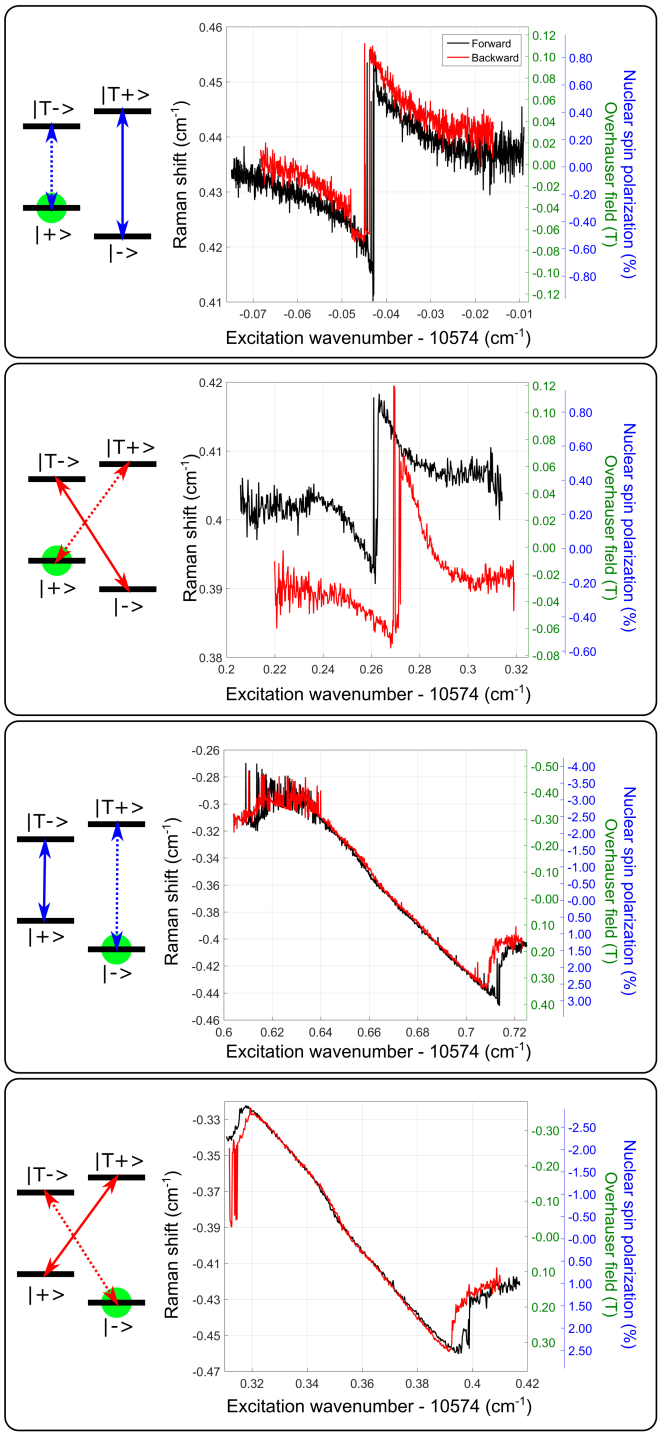

Figure 5.13: Determination of optical pumping Raman line centers fit using Lorentzians. Probe laser excitation order is the same as in Figure 5.12. Left vertical axis is the difference between the probe laser excitation wavenumber and the Raman line center wavenumber, right green vertical axis is the OH field shift, and right blue axis is the nuclear spin polarization percentage. Black (red) curves are forward (backward) laser scans. Green circles in the energy level diagrams indicate initialized the electron spin state due to high pump:probe power ratio.

Co-tunneling

Red Zeeman transitions				
Configuration:	(+;T-),F	(+;T-),B	(+;T+),F	(+;T+),B
Spectrum baseline (μeV,T)	49.6(1.99)	50.4(2.02)	50.8(2.04)	51.0(2.05)
OH_{max} (μeV)	0.979	3.26	1.12	3.20
OH_{min} (μeV)	-2.93	-1.26	-2.73	-0.978
Δ_{OH} (μeV,mT)	3.91(157)	4.53(182)	3.85(154)	4.17(167)
OH excess (μeV,mT)	-0.33(-13.2)	0.46(18.5)	0.70(28.1)	-0.712(28.6)
ΔE_{laser} (μeV)	0.025	0.108	0.026	0.027
Blue Zeeman transitions				
Configuration:	(-;T+),F	(-;T+),B	(-;T-),F	(-;T-),B
Spectrum baseline (μeV,T)	51.4(2.06)	50.4(2.02)	48.1(1.93)	47.6(1.91)
OH_{max} (μeV)	4.26	4.57	2.96	-3.24
OH_{min} (μeV)	-2.84	-3.25	-4.22	4.02
Δ_{OH} (μeV,mT)	7.1(285)	7.82(314)	7.18(288)	7.26(291)
OH excess (μeV,mT)	1.51(60.6)	0.53(21.3)	-1.84(-73.8)	-2.31(-92.7)
ΔE_{laser} (μeV)	4.38	4.65	4.18	3.97

Table 5.1: Overhauser field shifts measured for the co-tunneling single field excitation cases. The notation used to denote the optical excitation configuration is given by $(a;b),c$, where a is the ground state $|+/-\rangle$, b is the optically excited state $|T+/T-\rangle$, and c is the laser scan direction, which can have increasing(decreasing) frequency (F)(B). Spectrum baseline is the Raman shift determined far-off resonance at the edges of the scattering spectra, $OH_{max/min}$ are the maximum and minimum OH field shifts measured for a given spectrum, Δ_{OH} is the difference between the largest and smallest OH field shift in the spectrum, OH excess is defined as the difference between the measured spectrum baseline and the Raman shift predicted in the absence of OH field shifts (49.9 μeV, or 2 T), and ΔE_{laser} is the difference between the laser excitation energies at the maximum and minimum OH field shifts for each spectrum.

Optical pumping				
Red Zeeman transitions				
Configuration:	(+,T-, -,T+),F	(+,T-, -,T+),B	(+,T+, -,T-),F	(+,T+, -,T-),B
Spectrum baseline (μeV,T)	54.1(2.17)	54.4(2.18)	50.1(2.01)	48.4(1.94)
OH_{max} (μeV)	3.10	2.03	1.64	0.717
OH_{min} (μeV)	-2.33	-2.12	-1.79	-2.44
Δ_{OH} (μeV,mT)	5.44(218)	4.15(166)	3.43(138)	3.16(127)
OH excess (μeV,mT)	4.2(168)	4.55(183)	0.21(8.42)	-1.49(5.98)
ΔE_{laser} (μeV)	0.087	0.200	0.204	0.259
Blue Zeeman transitions				
Configuration:	(-,T+, +,T-),F	(-,T+, +,T-),B	(-,T-, +,T+),F	(-,T-, +,T+),B
Spectrum baseline (μeV,T)	44.8(1.80)	42.8(1.72)	44.2(1.77)	49.4(1.98)
OH_{max} (μeV)	10.8	11.5	9.80	7.54
OH_{min} (μeV)	-7.69	-8.36	-7.29	-9.28
Δ_{OH} (μeV,mT)	18.5(742)	19.8(794)	17.1(686)	16.8(674)
OH excess (μeV,mT)	-5.09(-204)	-7.15(-287)	-2.66(-107)	-0.52(-34.8)
ΔE_{laser} (μeV)	11.2	11.4	9.58	8.93

Table 5.2: Overhauser field shifts measured for the optical pumping two-field excitation cases. The notation used to denote the optical excitation configuration is given by $(a; b, c; d), e$, where a is the ground state $|+/-\rangle$ driven by the probe, b is the optically excited state $|T+/T-\rangle$ coupled to the probe, c is the ground state $|+/-\rangle$ driven by the pump, d is the optically excited state $|T+/T-\rangle$ coupled to the pump, and e is the probe laser scan direction, which can have increasing(decreasing) frequency (F)(B). Each measured shift is defined in Table 5.1.

and pulling back towards the expected behavior as the laser tunes off-resonance on the blue side. Each excitation energy scan consistently displays an abrupt drop in signal that occurs on the order of 25 ms, dropping from a maximum to effectively zero within one step of the excitation laser (0.0002 cm^{-1} = 6 MHz). During these jumps, the Raman energy hops by 0.028 cm^{-1} (827 MHz) in the optical pumping case, and 0.031 cm^{-1} (0.93 GHz) in the co-tunneling case, corresponding to a 138 mT (154 mT for co-tunneling) change in the internal OH field(1.05%, 1.17% nuclear spin polarization for optical pumping, co-tunneling, respectively). The two cases both exhibit

significant hysteresis with respect to the excitation laser scan direction: the abrupt energy shift around the expected line center is shifted in excitation energy between the forward and backward scans by 0.009 cm^{-1} and 0.011 cm^{-1} in the optical pumping and co-tunneling case, respectively (Figure 5.11, second panel). No discernible differences are observed between optically probing the $|T+\rangle$ and $|T-\rangle$ states, indicating that the underlying feedback mechanism does not qualitatively depend on the heavy-hole spin direction when the laser is scanned across the $|+\rangle$ transitions.

The DNP phenomenon described above observed when scanning the excitation laser across the $|+\rangle$ transitions is referred to as the "avoidance" regime: when the excitation laser is brought nearly into resonance with the trion transitions, where the resonance center is determined by the g-factors measured in co-tunneling, the electron spin state splitting shifts to avoid a range of forbidden energies.

For the next case, the excitation laser is scanned across the $|-\rangle \rightarrow |T+\rangle$ transition, and the optical pumping laser (when turned on) re-pumps the $|+\rangle \rightarrow |T-\rangle$ transition, resulting in a predominantly initialized $|-\rangle$ ground state. The Raman scattering energy deviates considerably from the expected diagonal response in the 2D map as far away from line center as 0.09 cm^{-1} (2.7 GHz). In this case, the Raman energy is blue shifted over a short excitation energy range (0.005 cm^{-1}, 150 MHz) into a state that tracks in a nearly linear fashion as the excitation laser is scanned across the transition. The scattering intensity remains bright over a wide excitation range, as large as 0.18 cm^{-1} (5.4 GHz) until abruptly shifting blue again, at which point the Raman energy asymptotically approaches the non-anomalous response far away from resonance. The OH field that reacts to the excitation laser is as large as 397 mT (3.00% nuclear spin polarization). The relatively narrow Raman spectrum is noted: here the widths of the scattering lines do not exceed the FP FWHM. Rather than being pushed away from resonance as in the $|+\rangle$ case, the DNP response tracks the excitation frequency tuning over a wide range of excitation energies.

In the final case, the excitation laser was scanned across the $|-\rangle \rightarrow |T-\rangle$ transition, while the re-pumping beam was held in resonance with the $|+\rangle \rightarrow |T+\rangle$ transition when necessary in the optical pumping bias range, thus switching the optically-

excited heavy-hole from the previous case. The overall qualitative response is the same as in the previous case, revealing no differences between the two heavy hole cases for the $|-\rangle$ initialization case. In the $|-\rangle$ excitation cases, the hysteresis occurs primarily at the edges far away from resonance in which the DNP response shifts back towards the asymptotic Raman dependence at large detunings, while the forward and backward scan directions show very little difference over the nearly-linear tracking regions of the spectra (Figure 5.11, fourth panel).

Additionally, although the qualitative tracking behavior is the same in the co-tunneling case, the quantitative response is quite different: the average Δ_{OH} as measured from the maximum to the minimum observed OH field shift, is 2.5 times larger for optical pumping than co-tunneling, and the dragging widths are 2.4 times larger larger for optical pumping (Tables 5.1, 5.2). This difference between co-tunneling and optical pumping is attributed to differences in QD occupation rates (referred to as the filling factor by some researchers [142]) between co-tunneling and optical pumping. In the co-tunneling regime, the electron spin actively tunnels between the QD and the Fermi reservoir. During this process, the QD may be unoccupied by an electron, and therefore the electron-mediated DNP processes are shut off. This is in comparison to the optical pumping regime for which the QD electron remains trapped and participating in DNP for considerably larger fraction of time [169].

It is important to note that for the $|-\rangle$ excitation case, the Raman scattering occurs at a lower energy than the excitation energy: $E_{Raman} - E_{excite} = -\Delta_{electron}$. Thus, dependence of the OH field on the laser detuning in the tracking case has a positive slope rather than a negative one (Figure 5.11). As the laser is scanned from much lower frequencies than where the trion transition is expected, the OH field shifts the trion resonance reactively towards the laser, maximizing the scattering intensity, and moves with the laser detuning until the system is unable to maintain this locking, at which point the anomalous response of the system due to the DNP non-linear feedback mechanism becomes energetically unfavorable.

Least-squares fitting of the detection energy spectrum for a given laser excitation energy allows for determination of the OH field shift with very high precision. The

spectra are fit with a Lorentzian and the line center is extracted. The 95% confidence interval for the line centers averaged with 8 fits for the case of re-pump/excitation resonant with the $|+\rangle \rightarrow |T+\rangle$ and $|-\rangle \rightarrow |T-\rangle$ transitions, respectively, (Figure 5.12, bottom panel) is $\pm 0.0009\ cm^{-1}$. Recalling from Chapter 4 that the OH field shift can be related to the nuclear spin polarization s by $B_{OH} = \frac{s}{\mu_B g_e}\left[\frac{9}{2}A_{In} + \frac{3}{2}A_{As}\right]$ one arrives at a nuclear spin polarization sensitivity of 7.26×10^{-4}. For an InAs QD with 5×10^4 atoms, this equates to a nuclear spin sensitivity of ~ 36 spins.

Another important figure of merit for the purposes of magnetometry and quantum metrology is the magnetic field sensitivity, which is defined as the smallest DC magnetic field detectable for an SNR of one if the noise is dominated by photon shot-noise [211]. The following calculation borrows considerably from the calculation performed in [211] for NV center magnetic field sensitivity. Although the calculation done there applies to electron spin resonance spectra, it can easily be adopted to the Raman scattering studies reported here.

The QD magnetometer in question is operated such that the etalon is held fixed at the highest sensitivity range of the Raman scattering peak, ie. the largest slope portion of the Raman lineshape. If the OH field (or external magnetic field) shifts by an infinitesimal variation δB, the Raman scattering changes by $(\partial I/\partial B)\,\delta B \Delta t$ where I, Δt are the scattering rate and integration time, respectively. Assuming that the noise is photon shot-noise limited, the noise is equal to $\sqrt{I\Delta t}$. One arrives at the magnetic field sensitivity equal to

$$\eta = \delta B\sqrt{\Delta t} = \frac{\sqrt{I}}{\partial I/\partial B} \approx \frac{h}{\mu_B g_e}\frac{\Delta\nu}{C\sqrt{I}} \tag{5.5}$$

where $h, \Delta\nu, C$ are Planck's constant, the Raman scattering linewidth as measured using the scanning Fabry-Perot, and the Raman scattering contrast, defined as $C = (I_{on} - I_{off})\,/\,(I_{on} + I_{off})$, where $I_{on/off}$ is the scattering rate with the etalon held on and off resonance.

The contrast for the data presented in Figure 5.9 is 98.2%, and the count rate for the lowest energy Raman scattering peak (for example) is 5.5 kcps. Plugging in the

numbers, one arrives at

$$\eta = \frac{(4.1357 \times 10^{-15} \text{ eV s})(400 \text{ MHz})}{(57.9\frac{\mu\text{eV}}{\text{T}})(0.42)(0.982)\sqrt{5.5 \text{ kcps}}}$$
$$= 1.0 \text{ mT } /\sqrt{\text{Hz}}$$

The magnetic field sensitivity can also be estimated in a cruder manner using dimensional analysis considerations. Considering the Raman energy confidence intervals calculated above, that energy uncertainty is converted to a magnetic field uncertainty and multiplied by the square root of the integration time

$$\eta = \delta B\sqrt{\Delta t} = \frac{0.0018 \ cm^{-1}}{(0.467\frac{\text{T}}{cm^{-1}})(0.42)}\sqrt{25 \times 10^{-3} s}$$
$$= 1.5 \text{ mT } /\sqrt{\text{Hz}}$$

which is in agreement with the earlier calculation.

Additionally, one can calculate the theoretical magnetic field sensitivity for this particular QD under the assumption that all scattered photons are collected and measured (100% detection efficiency) and that the Raman scattering is measured using a scanning Fabry-Perot with a FWHM smaller than the Raman linewidth. Assuming that the QD nuclear spin ensemble has been narrowed, leading to an extended electron spin coherence time of $T_{2e} = 1$ μsec [85], the Raman linewidth is equal to $\nu_{Raman} = 1/\left(2\pi 1 \times 10^{-6} s\right) = 160$ kHz. If the QD is driven in the saturation regime, the scattered photon counts approach $1/T_{1,optical} = 1/\left(400 \times 10^{-12}\right) = 2.5$ GHz, but only half of the photons are scattered/emitted into the measured Raman pathway. Thus, using Equation 5.5, one arrives at a theoretically achievable nuclear spin sensitivity for the QD system of

$$\eta = \frac{(4.1357 \times 10^{-15} \text{ eV s})(160 \text{ kHz})}{(57.9\frac{\mu\text{eV}}{\text{T}})(0.42)(1)\sqrt{2.5/2 \text{ GHz}}}$$
$$= 707 \text{ pT}/\sqrt{\text{Hz}}$$

In summary, the 2D excitation-emission energy maps of the Raman scattering directly reveal how the OH field reacts to a changing laser excitation detuning under

both optical pumping and co-tunneling conditions. The technique eliminates any ambiguities in the determination of the changes in the OH field that are present when one attempts to extract the OH field by modeling the absorption laser excitation scans [142, 194]. To the author's knowledge, this is the first report of a *direct* measurement of the OH field under conditions of resonant optical excitation, as opposed to above band-gap excitation measurements of PL [57]. Two qualitatively unique regimes are observed: when the excitation laser is scanned the optical transitions involving the $|-\rangle$ electron spin state, the OH field tracks with the excitation laser detuning over a wide range of frequencies, while in the $|+\rangle$ excitation case the OH field "avoids" a band of forbidden energies near the expected trion transition, shifts rapidly to higher energy on the timescale of no longer than 25 ms under these experimental conditions, and is pulled back to the non-anomalous response far away from resonance. A model is developed in Chapter 6 based off of the quadrupole interaction used to fit the Raman shifts (Figures 5.11 and 5.13) observed in this experiment.

The resonant Raman scattering exploits state-of-the-art high detection efficiency single photon detecting nanowires to reduce the integration time down to timescales relevant to nuclear spin polarization build-up, and increases the nuclear spin sensitivity down to the sub-hundred spin level. The utilization of a higher finesse Fabry-Perot may allow for a measurement of the electron spin coherence directly using the same technique demonstrated here, making the narrowing/broadening of the OH field distribution more obvious. Usage of a higher finesse Fabry-Perot combined with deconvolution has the potential to increase the sensitivity to the single spin level, allowing for the investigation of fundamental central spin and many-body theories. Further studies of the OH field distributions under CPT locking may reveal mesoscopic nuclear spin states that can be utilized for quantum memory applications.

5.4 Noise and dynamics of DNP

Throughout the discussion of the OH field shifts reported in this chapter, the dynamics associated with nuclear spin polarization and the fluctuations of the OH field

have so far been neglected. In fact, it is these fluctuations in the mean OH field that affect the electron spin coherence time most detrimentally, rather than the relatively slow ($\sim$10 ms) drift of the net nuclear spin polarization. In the absence of optical excitation, the fluctuations arise due to dipole-dipole interactions between neighboring nuclear spins, electron-mediated nuclear spin interactions, and fundamentally the quantum limits on the uncertainty of the measurement of orthogonal angular momentum spin projections [85,89,148,175,200,212,213]. However, in the presence of optical excitation, the coupled electron-trion-laser-nuclear system may exhibit entirely new dynamics and noise features, such as nuclear spin fluctuation quieting and nuclear spin ensemble narrowing [85,136,154], trapping of the nuclear spin ensemble in a stable, polarized state, or the driving of the system into instability leading to amplified fluctuations [212, 213]. These stable and unstable points have been revealed in the resonant Raman scattering experiments discussed above, and are discussed in detail in this section.

The data acquisition time scales have been successfully reduced down to reported nuclear spin ensemble polarization/depolarization times [136, 168]. Abrupt jumps in Raman scattering energies are observed in these experiments as the excitation laser is scanned that are indicative of rapid switching between nuclear spin ensemble states with upper bounds on switching times around 25 ms (Figure 5.11 and 5.13). Furthermore, the fluctuating nature of the underlying nuclear spin ensemble is evident by examining adjacent fixed detection energy slices: if the response of the OH field shifted smoothly with the excitation laser scan, one expects a smooth Raman spectrum due to the averaging along the detection energy axis limited by the FP FWHM. Instead, for detection energy step sizes as small as 0.003 cm^{-1} (90 MHz), abrupt shifts in the Raman line intensity are observed, indicating a large fluctuation in the OH field resulting in a Raman shift larger than the FP FWHM (Figure 5.10).

First, without the need for the use of the Raman scattering technique, the lock-in detected single-photon counting pump-probe maps presented in Section 5.2.3 reveal both the dynamics and fluctuations associated with the OH field. Examining Figure 5.3, around pump wavenumbers 10574.32 cm^{-1}, as the probe laser is scanned, the

scattering reaches a maximum and then drops off precipitously to the noise floor of the measurement. This signal drop, which is due to the OH field shift, occurs within 10 ms. It can be ascertained that the OH field causes a frequency shift of at least the trion linewidth, calculated to be at least 80 mT (nearly 1% nuclear spin polarization) within 10 ms. Thus, a large number of nuclear spins (approximately 500 in this example) can be flipped by a very small shift (85 MHz) in laser excitation frequency, likely due to a transition between different stability/instability points in the non-linearly coupled electron-trion-nuclear-laser-nuclear system. The fluctuations in the underlying OH field are apparent when adjacent probe laser scans are compared for a single pump wavenumber step. As shown in the bottom panel of Figure 5.3, the scattering peak has shifted significantly ($\sim$0.1 cm^{-1}), implying that the OH field has fluctuated over the course of the measurement without changing the optical excitation parameters considerably.

Similar dynamics and fluctuation phenomena are apparent in the Raman scattering maps. These 2D maps may also be interpreted as OH field probability distributions: for a given laser excitation frequency, if the OH field is assumed to have reached its steady-state mean value, the OH field distribution is described by a cut along the emission energy axis (vertically in the maps of Figure 5.12). This OH field distribution changes as the optical excitation frequency is changed. Strikingly, there are examples in the 2D maps where the OH field probability distribution transitions from relatively stable to a region of increased fluctuations.

For example, multiple OH field probability distributions are plotted in Figure 5.14 for the forward and backward scans with the probe/pump configuration exciting $|+\rangle \rightarrow |T+\rangle$ and $|-\rangle \rightarrow |T-\rangle$, respectively. In the top panel, when the excitation laser is detuned on the red or blue side of the central switching position of the Raman spectrum (Figure 5.12, second panel), the probability distributions are single-peaked (blue and purple curves of Figure 5.14). However, when the excitation laser is brought into the avoidance region (red and yellow curves of Figure 5.14), the distributions display multiple peaks, implying that the OH field distribution fluctuations have increased, but the rate of these fluctuations relative to the experimental acquisition

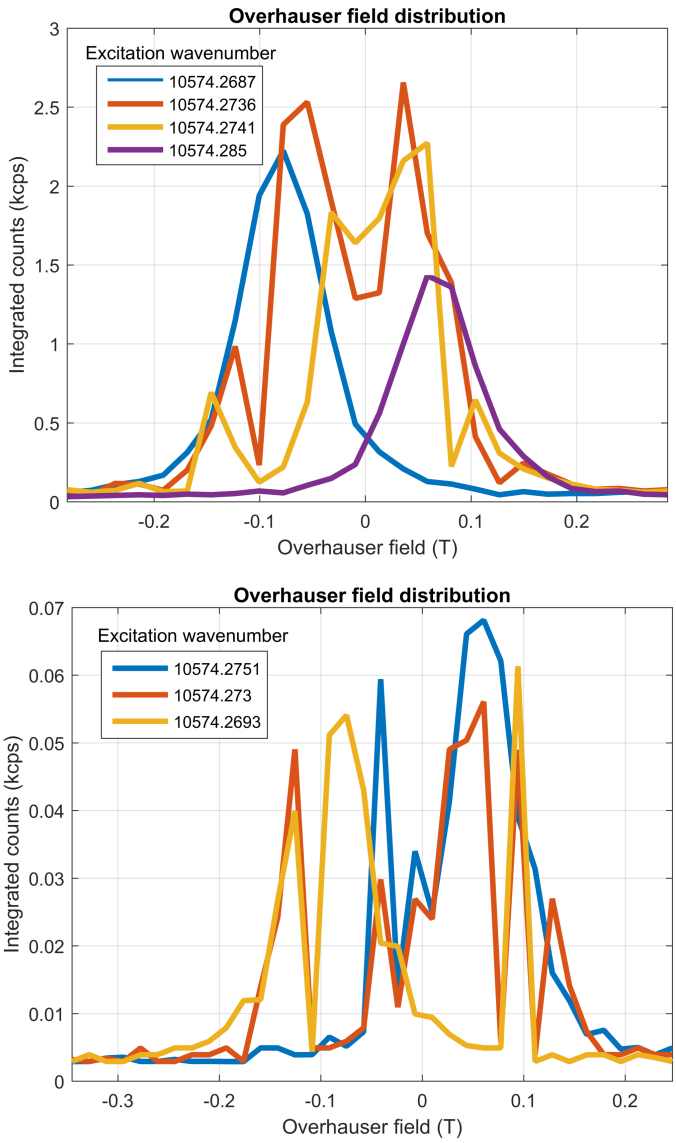

Figure 5.14: OH field distributions extracted from 2D excitation-emission maps. Distributions are constructed by cutting the map along a fixed wavenumber. Distributions for a given excitation wavenumber (see legends) for Figure 5.12, (second panel, forward scan for top figure; second panel, backward scan for bottom figure). Probe/re-pump configuration for this case is $|+\rangle \rightarrow |T+\rangle/|-\rangle \rightarrow |T-\rangle$.

time is not large enough to lead to a general broadening of the distribution. This increase in fluctuations around the avoidance region is also highly pronounced in the backward scan (Figure 5.14, bottom). Additionally, the FWHM of these individual peaks is sometimes smaller than the FP FWHM, implying that the OH field fluctuated between probe laser scans, recalling that the 2D maps are constructed by slowly

compiling fixed FP detection frequencies. It is noted that these unstable points with increased OH field fluctuations are not typically observed in the blue Zeeman cases under these experimental conditions, pointing towards a general difference in the feedback properties of optical excitation of the $|+\rangle$ and $|-\rangle$ states.

The dynamics associated with this drop in signal are in order of magnitude agreement with at least two previous measurements. One study measured the polarization build-up time using CPT in the negatively-charged trion system as 7 ± 1 ms at 5 K under the application of an in-plane magnetic field of 2.64 T [136]. Another study measured the build-up time using pump/probe spectroscopy under the application of an out-of-plane magnetic field of -220 mT, with a result that varied between 11.2 and 32.3 ms for excitation laser helicities of $\sigma-$ and $\sigma+$, respectively [168].

For longer integration time experiments, there are two distinct possibilities for the predicted OH field probability distributions. One possibility is that the fluctuations in general will average out, leading to smooth probability distributions, implying that the nuclear spin ensemble samples a range of values between $[\langle I_x^{min}\rangle, \langle I_x^{max}\rangle]$, which is discrete due to the finite size of the nuclear spin ensemble in the QD; this result may be expected in the absence of non-linear feedback [89]. Specifically, in the "frozen fluctuation model," (at zero magnetic field) the electron samples a random distribution of Overhauser fields given by [89]

$$\begin{aligned} W(B_{OH}) &= \frac{1}{\pi^{3/2}\Delta_B^3}\exp\left[-\frac{B_{OH}^2}{\Delta_B^2}\right] \\ \Delta_B^2 &= \frac{2}{3}\langle B_{OH}^2\rangle = \frac{2}{3}\sum_j I^j(I^j+1)(a_j)^2 \\ a_j &= \frac{\nu_0}{\mu_B g_e}A^j|\psi_e(R_j)|^2 \end{aligned} \tag{5.6}$$

where the last term is the hyperfine constant associated with the coupling between the electron and the j-th nucleus. Thus, in the absence of non-linear feedback, the OH field distribution is expected to be Gaussian; the role of nuclear spin narrowing via optical excitation could simply be to narrow this Gaussian distribution.

The second possibility is that this probability distribution is indeed multi-modal, and that the individual peaks observed here will remain. This result has been pre-

dicted theoretically in multiple studies. The first study [177] investigated the non-collinear hole-mediated DNP process and showed that a bi-stable OH field probability distribution could result under strong optical excitation when the nuclear Zeeman energy is negative. Additionally, this study showed that the nuclear spin fluctuations are amplified at the edges of what is referred to in this thesis as the "tracking" regime lineshapes, and the fluctuations are drastically reduced over the tracking range. In another study, Onur *et al* [176] predicted that when the QD is optically excited using CPT, holding both the pump and probe beam in the CPT condition ($|E_{pump} - E_{probe}| = \Delta_e$) but red-detuned from the lambda system results in a bi-modal OH field distribution as steady-state solutions for the non-linear system. Performing this experiment again and varying the integration times for each probe laser scan should reveal further information about the fluctuations of the OH field. A more ideal solution is to use a higher finesse FP etalon that can scan at a much higher rate, such a piezo-tunable FP, taking advantage of the high detection efficiency of the single photon detecting nanowires to compare repeated fast FP scans for a fixed laser excitation frequency. Additionally, sophisticated Ramsey fringe and spin echo studies of the coupled electron-nuclear spin system [149] have extracted complex power spectral densities of the nuclear spin noise, demonstrating that the OH field components parallel to the electron spin quantization axis (in-plane magnetic field) are highly non-Gaussian and are related strongly to the quadrupolar interaction.

5.5 Microscopic mechanisms leading to DNP in the electron-trion system

As has been described in the previous sections, the OH field operates as an internal magnetic field that shifts the electron spin state splitting due to the portion of the Fermi contact interaction Hamiltonian with spin components along the magnetic field direction [143]. The components of the OH field which are perpendicular to the external field rotate the electron spin quantization axis away from the external field, rotating the optical selection rules of the trion system [145]. In fact, optical pumping

of the electron ground state was first demonstrated in the Faraday geometry (magnetic field along growth direction) by exploiting this rotation of selection rules due to transverse OH fields; small transverse OH fields turn on previously forbidden cross transitions, leading to spontaneous emission channels coupling the electron ground states to one another via the optically excited trion [98, 169]. Although the relative oscillator strength of the optical transition driven by the re-pumping/excitation lasers may change due to the perpendicular components of the OH field, the experiment is insensitive to resolving the optical polarization of the scattering. The polarization analyzer system used to reject the co-polarized pump and probe excitation fields has a fixed polarization axis for a given experiment that is chosen to maximize the rejection of the beams (Chapter 3). Instead, the off-diagonal terms in the Fermi contact interaction can be treated as electron-nuclear spin flip terms of the form $H_{od} \propto (I_+S_- + I_-S_+)$, where $I_\pm$,$S_\pm$ are the spin flip operators for the nuclear and electron spins, respectively [143]. These terms open up the possibility of transfer of angular momentum from the electron to the nuclear spin ensemble, and their relative balance may be influenced by preferential optical excitation of one of the trion transitions, as well as the coupling of the electron-trion system to the phonon bath [193]. In fact, this term is implicated to be the main mechanism for nuclear spin polarization in some QD systems, especially at magnetic fields smaller than the OH field shift associated with the trion linewidth ($\sim$ 80 mT) [92, 145].

The relevance of the electron-nuclear Fermi contact interaction spin-flip terms is investigated by tuning the electron spin polarization via the re-pumping/excitation power ratio in the optical pumping regime. In principle, by changing the ratio of the optical pumping rates between $|\pm\rangle$ states, the electron spin polarization is adjusted, and therefore the rates of nuclear spin pumping are adjusted, resulting in a shift in the OH field in response [143, 214].

It can be shown [143] that an out-of-equilibrium electron spin polarization can lead to a nuclear spin polarization through the electron-nuclear Fermi contact interaction spin-flip terms. If the flip-flop term is written as

$$H_{e-n}^{ff} = \frac{\hbar}{2} A_{e,i}(t)(I_{i,+}S_{-} + I_{i,-}S_{+}) \tag{5.7}$$

where the hyperfine contact interaction term out front of the flip-flop terms is a time-dependent term that takes on values between 0 and $A_{e,i}$ when the QD is unoccupied/occupied by the electron. This occupation is affected both by the co-tunneling rates but also the optical excitation: in the electron-trion system, the trion state is effectively unoccupied by the electron since the two electrons $|T+\rangle = |\uparrow\downarrow\Uparrow\rangle$, for example, are in the spin-singlet form and do not interact with the nuclear spins. It can be shown that the differential equation governing the time dependence of the nuclear spin polarization is given by

$$\begin{aligned} \frac{d}{dt}\langle I_z\rangle &= -\frac{1}{T_1^n}\left[(\langle I_z\rangle - I_0) - \frac{I(I+1)}{S(S+1)}(\langle S_z\rangle - S_0)\right] \\ \frac{1}{T_1^n} &= \frac{S(S+1)}{3}\sum_i \int_{-\infty}^{\infty} e^{i(\omega_n-\omega_e)\tau} d\tau \overline{A_{e,i}(t)A_{e,i}(t+\tau)} \end{aligned} \tag{5.8}$$

where $\overline{A_{e,i}(t)A_{e,i}(t+\tau)}$ is the correlation function of the time-dependent flip-flop coupling, I_0, S_0 are the nuclear and electron equilibrium polarization, respectively, and ω_n, ω_e are the nuclear and electron Zeeman splittings [143]. Thus, in the absence of fast nuclear spin depolarization mechanisms as compared to the nuclear spin pumping rate, the steady state nuclear spin polarization is proportional to the electron spin polarization [195]. It was shown in Chapter 5 that the electron spin polarization can be tuned with high fidelity by adjusting the pump-probe ratio; if the hyperfine contact flip-flop term written above is relevant to the QD system under study, the pump-probe ratio should provide an easily tunable experimental parameter to adjust the nuclear spin polarization.

In the experiment, the re-pump is fixed on the $|+\rangle \rightarrow |T+\rangle$ transition and the excitation on the $|-\rangle \rightarrow |T-\rangle$ transition, and the excitation:re-pump power ratio is tuned between 1:2.5 to 22.5:2.5. Further, the intensity dependence of the Raman scattering is measured as a function of this ratio and it is verified that this dependence matches what is expected when the electron spin polarization tunes with the power

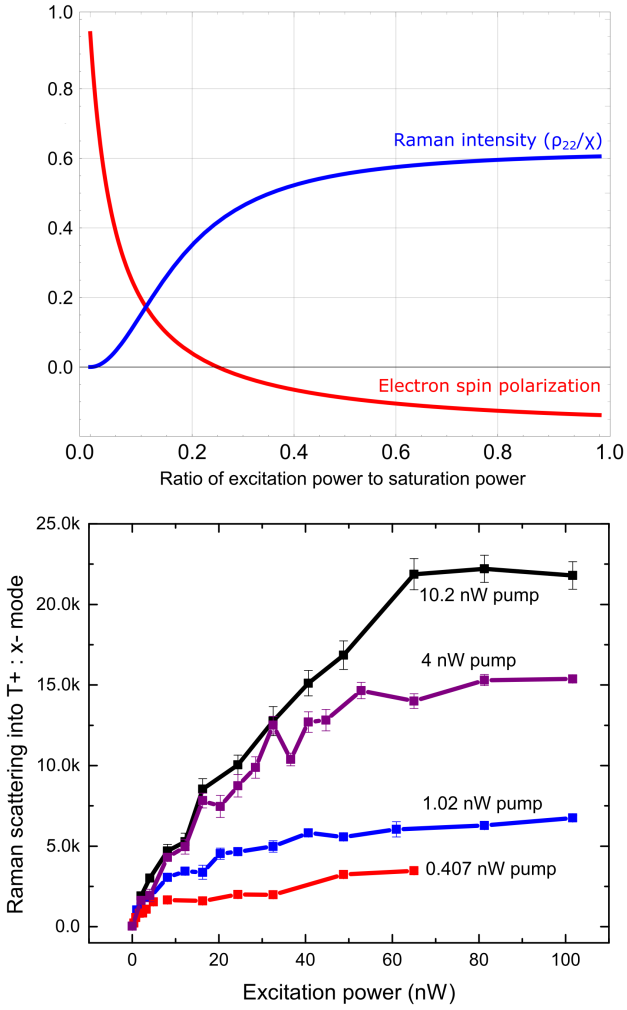

Figure 5.15: Numerical and experimental results of Raman scattering pump and probe power dependences. Top: Numerical results of the rate equations for the Raman scattering intensity (blue) proportional to ρ_{22} and the electron spin polarization (red) as a function of excitation power. Right: probe (excitation) power dependence at selected pump powers. The Raman scattering intensity is measured at the $|-\rangle \rightarrow |T+\rangle$ transition and the probe power ($|-\rangle \rightarrow |T-\rangle$) is scanned from 0-100 nW. Each point is the average of ten one second photon count integrations, and the error bars are standard deviations of each set of ten points.

ratio (in the absence of DNP). These results are supported by numerical density matrix calculations using the rate equation approach [45]. A plot of the numerical and experimental Raman scattering intensities is shown in Figure 5.15, proving that the electron spin polarization can be tuned from positive to negative by tuning the

pump-probe ratio.

The results of the power ratio dependence experiment are displayed in Figure 5.16. No discernible OH shift occurs as a function of the power ratio, and by extension the electron spin polarization. Additionally, no increase in the linewidth of the Raman/Rayleigh scattering lines is measured, indicating no measurable change in the nuclear spin fluctuations. In the absence of a more complex feedback mechanism that would lock the OH field as the electron spin polarization is tuned, it is asserted that this experiment rules out the electron-nuclear spin flip interaction as the primary mechanism for nuclear spin polarization observed in the 2D maps. This spin flip channel is likely inhibited by the large energy mismatch between electron and nuclear Zeeman energies, barring assisted electron-nuclear spin flip transitions resulting from interactions with the phonon bath, which are unlikely considering the 1LO phonon energy is on the order of 37 meV [57], energy-mismatched from the average electron splitting of 49 μeV. Additionally, the acoustic phonons are also unlikely to take part in this process: a previous study measured the ratio of the acoustic phonon side-band peak to the zero phonon line peak to be approximately 2×10^{-3} at 4.2 K [215], indicating that the acoustic phonons do not interact strongly with the QD at low temperature. A more complex scheme may involve a change in the rates of spin flip interactions as the excitation laser is detuned across the trion transitions; this mechanism would not have been revealed by the fixed detuning re-pump/excitation experiment described here. In fact, this experiment rules out any Hamiltonian term that leads to a direct coupling between the electron spin polarization and the nuclear spin polarization.

The next microscopic interaction under investigation, the heavy-hole light-hole mixing term, is strongest for anisotropic QDs (Chapters 2 and 4). In such QDs, the mixing of spatial wavefunctions of the optically excited holes in the valence band turns on the dipole interaction due to the fact that the envelope wavefunction develops significant projection along the growth axis [94, 150]. Even in the absence of HHLH mixing, the hole-nuclear dipole interaction is still relevant, although considerably weaker than the Fermi hyperfine contact interaction. These terms are discussed in

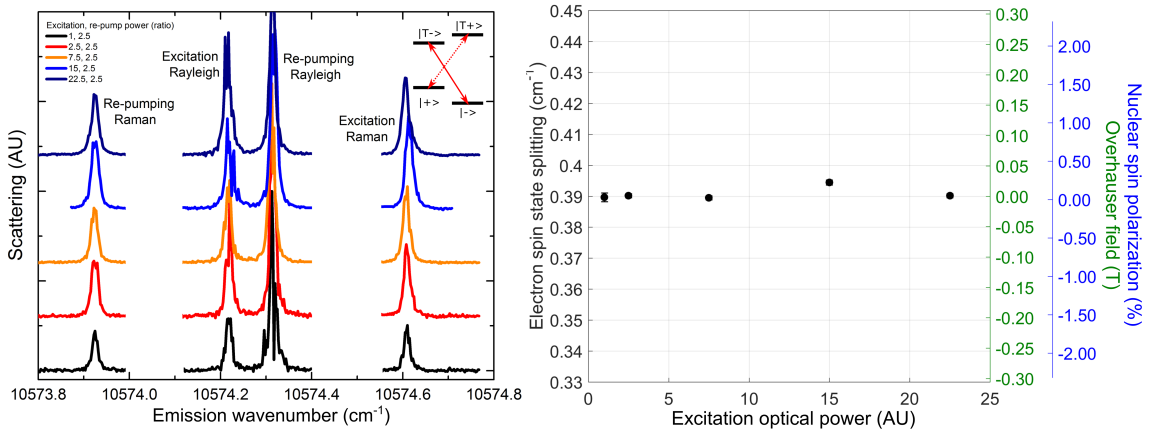

Figure 5.16: Excitation/re-pump power ratio Raman scattering experiment. The re-pump (excitation) is held on resonance with the $|+\rangle \rightarrow |T+\rangle$ ($|-\rangle \rightarrow |T-\rangle$) transition and the etalon detection energy is scanned across the four trion scattering lines (Rayleigh and Raman). The excitation power is changed while the pump power is held constant for a given spectrum, tuning the electron spin polarization across a wide range. Left: The two mid-energy lines correspond to the Rayleigh scattering of the excitation and re-pumping lasers. Poor polarization rejection of the two lasers results in background subtraction artifacts at these lines, but does not affect the overall lineshape. Right: The electron spin state splitting is extracted from the emission spectra (left figure) by lineshape fitting and measuring the Raman splitting, taking the average of the re-pumping and excitation Raman splitting. The energy axes for the figure on the right are chosen to match the axes of the emission-excitation energy maps of Figures 5.11 and 5.13 for easy comparison.

detail in the DNP microscopic theory Chapter 4.

The HHLH mixing in the sample was measured by performing bias modulated polarization sensitive reflectivity to measure the polarization selection rules (Figure 5.17). The linearly-polarized selection rules of the QD under investigation are rotated away from the external magnetic field axis by no more than 2°, which is within the error of the measurement due to sample mounting uncertainty. By comparison, in a previous study the HHLH mixing was measured to be 20°, and therefore the DNP and CPT nuclear spin narrowing phenomena observed there were reasonably attributed to the hole-nuclear dipole interaction [85]. Thus, it is concluded that the HHLH-mixing induced hole-nuclear dipole term is not relevant for the DNP-induced phenomena observed here. This conclusion is supported further by the absence of any qualitative

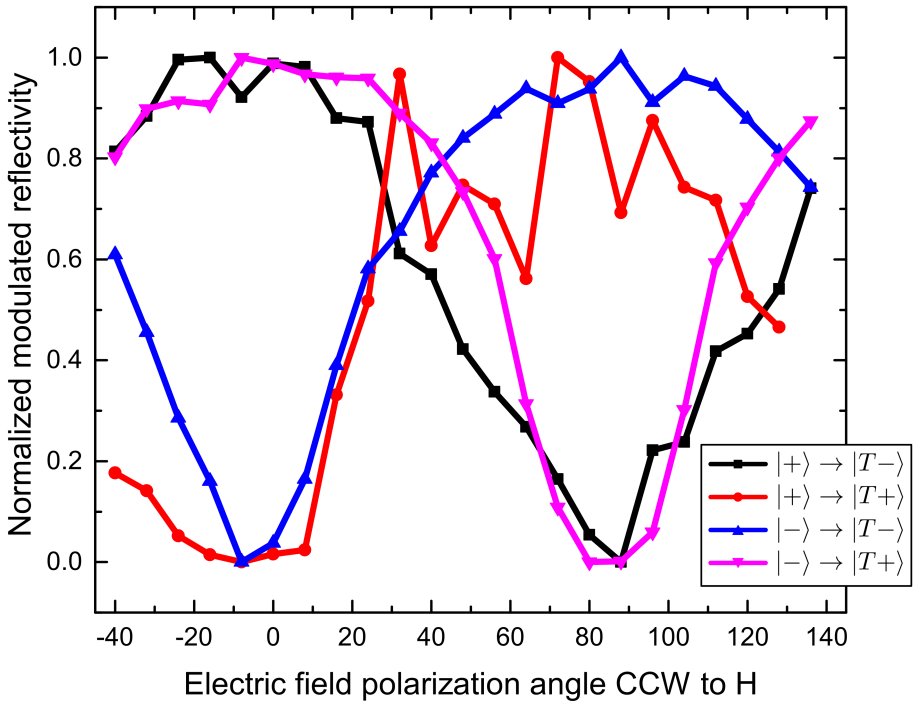

Figure 5.17: Polarization selection rules of the QD trion transitions measured by polarization-sensitive lock-in reflectivity spectroscopy. Each curve is color-coded corresponding to its resonant electron-trion transition.

differences in the DNP response measured in the 2D maps when different heavy hole states are probed for a given electron spin state. It is noted that the polarization-dependent absorption curves displayed in Figure 5.17 do deviate from the expected curve $L(\theta) = c(a^2 + b^2 - 2ab\cos 2(\theta + \phi))$, where θ, ϕ are the polarizer angle and HHLH mixing angle, and the other parameters are fit parameters related to the HHLH mixing terms [94]; the higher absorption portion of the curves is more rounded than expected, and the lower portion of the curve is sharper. It is possible that DNP is playing a role here; a number of studies have observed polarization-dependent DNP non-linearities [106]. It is also possible that the optical electric field polarization does not depend linearly on the half-wave plate angle. Nevertheless, the expected H and V selection rules line up within 2° with the expected directions in the absence of HHLH mixing.

One feasible mechanism for the generation of DNP in the QD system is the electron-mediated quadrupole interaction, which plays a role in highly strained QDs

fabricated using the Stranski-Krastanov growth technique [167]. As shown in Chapter 4, nuclear spin charge distributions that possess non-spherical symmetry (nuclear spin $> 1/2$), interact via their quadrupole moment with the non-zero electric field gradients present in the strained crystal lattice of the self-assembled QD [143]. Mixing terms between orthogonal nuclear spin projection operators are introduced, as well as small energy shifts [167], which were treated using perturbation theory in Chapter 4, leading to perturbation Hamiltonian terms of the form $H_{quad}^{elec} = \sum_i A_{nc} S_x^e \left[I_i^+ + I_i^- \right]$. Thus, nuclear spin polarization may be generated in the QD without flipping the electron spin, thereby opening up an energetically favorable polarizing channel compared to the electron-nuclear Fermi contact hyperfine interaction. Additionally, the lack of any dependence on the heavy-hole angular momentum projection of the qualitative and quantitative features of the DNP phenomena observed in this particular QD system point towards the role of an electron-mediated effect such as the quadrupole interaction. However, the quadrupole interaction is not directly manifested via an optically measurable quantity such as a selection rule polarization rotation in the HHLH mixing case. Without resorting to optically-detected NMR techniques used to examine the atomistic quadrupolar structure of the system [216], the other microscopic mechanisms discussed earlier are effectively ruled out as contributing significantly to the DNP phenomena observed here. A model is developed in the next Chapter based on the quadrupole Hamiltonian, proving that an electron-mediated DNP term may reasonably explain the observed Raman shifts observed in these experiments using physically appropriate model parameters.

5.6 Chapter summary

In summary, this chapter has presented observations of dynamic nuclear spin polarization in single QDs as measured using single-photon counting resonant excitation CW pump-probe spectroscopy and Raman scattering. The single QD system under study exhibits highly anomalous absorption/resonance fluorescence lineshapes, with lineshapes that depend on which electron spin ground state is being optically probed.

Two regimes are observed that are common to the co-tunneling and optical pumping cases, and are found in both sample modulated reflectivity/scattering experiments and are further investigated using a novel frequency-resolved Raman scattering technique: In one case the OH field tracks with the excitation frequency while in the other case the OH field shifts to avoid a forbidden range as the excitation laser is brought near the trion resonance. The dynamics of the observed DNP phenomena are found to occur on timescales faster than 25 ms in the Raman scattering experiments, and likely faster than 10 ms as inferred from the pump-probe scattering experiments. An increase in OH field fluctuations is observed in the red Zeeman cases both in co-tunneling and optical pumping. The electron-mediated quadrupole interaction is implicated to be the main DNP-generating mechanism leading to non-linear coupling between the electron-trion system and the nuclear spin ensemble.

CHAPTER 6

Modeling of DNP-induced Raman shifts

The two-dimensional excitation-detection energy maps, and their corresponding line center fits, along with an extensive body of literature, both experimental and theoretical work, discussed in Chapter 5 demonstrate that dynamic nuclear spin polarization (DNP) strongly perturbs the optically-coupled electron-trion system in a highly non-linear manner with respect to experimental parameters including optical excitation frequency, excitation power, laser frequency scan speed, laser polarization, and external magnetic field strength [1, 57, 141, 158, 160]. These experiments reveal directly the particular extent to which the laser detuning drives the electron spin ground state splitting away from the expected value determined by the electron Zeeman splitting in the external in-plane (Voigt geometry) magnetic field. Attempts at explaining the non-linear phenomena observed in single QDs must include not only the polarizing mechanism acting on the nuclei via the electron spin and the optical excitation, but also the effect of the nuclear spin polarization's back action on the electron spin resonance (Overhauser field). A model based on the quadrupole interaction discussed in Chapter 4 is developed below, and is shown to reproduce the observed Raman shifts when physically reasonable parameters are used.

6.1 Introduction to DNP non-linear feedback

Although nuclear spin polarization effects in the solid state have been observed starting with Lampel's foundational work on ^{29}Si in 1968, non-linear effects due to the back-action of the nuclear spin polarization on the optically-generated spin carriers

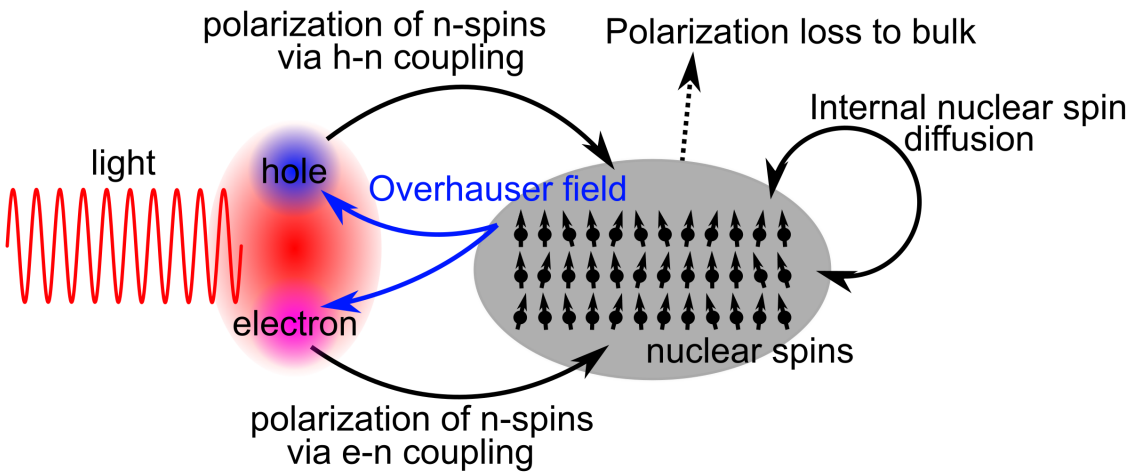

Figure 6.1: Schematic illustration of DNP non-linear feedback process in the QD system. Light generates polarized spin carriers (excitons) via both resonant and non-resonant excitation. The electron and hole polarize the nuclear spin ensemble, where the specific polarizing mechanism depends on the sample structure. In turn, the nuclear spin polarization acts back on the electron and hole spin splitting through the OH field. Additionally, nuclear spin-flip processes occur leading to both internal spin diffusion (spin-to-spin polarization transfer) and loss of polarization to the bulk environment.

were discussed and investigated in much greater detail AlGaAs crystals in the late 70s and early 80s [1, 217, 218]. These non-linear effects can be schematically represented (Figure 6.1) and understood in the following manner.

First, an out-of-equilibrium nuclear spin polarization is generated in the sample (bulk, quantum well, or QD) via a collection of optical orientation techniques, including polarized optical excitation of degenerate semiconductor electronic transitions via orthogonal selection rules, or the narrowband excitation of non-degenerate electronic transitions split by an external magnetic field via the Zeeman interaction (Chapter 2). The transfer of angular momentum from optically-generated spin carriers to the nuclei is fundamentally achieved by some form of the hyperfine interaction, although it may require the presence of quadrupole strain fields (Chapter 4) or spin-orbit coupling [219] to mix nuclear spin eigenstates. The amount of nuclear spin polarization generated in the sample is strongly dependent on the optical excitation parameters. It is noted that the process of the electron acting on the nuclei is sometimes referred

to as a Knight field [192]; this is the effective magnetic field that the nucleus feels due to the electron spin. One important feature of the Knight field in QDs is that it is *highly inhomogeneous* due to the strong quantum confinement of the envelope wavefunction of the electron. Thus, nuclei at the outer portions of the QD experience a different Knight field than those at the inner portions [140].

Consequently, the nuclear spin polarization acts back on the electron spin resonance via the Overhauser field, which arises from the hyperfine contact interaction. In some cases, the OH field may not be strong enough (insignificant amount of nuclear spin polarization generated due to fast nuclear spin relaxation, weak optical excitation, or weak hyperfine coupling in the bulk) to shift the optical resonance condition that is in turn driving the nuclear spin polarization. However, in the InAs QD system operating at low temperature, the electron-nuclear hyperfine interaction strength is large due to the strong confinement of spin carrier in the QD, and thus there exists high electron probability density function at each lattice site as compared to the bulk. Additionally, InAs QD optical resonances are narrow [108], and are easily shifted out of resonance with the excitation laser by the OH field. Thus, the back-action may act to decrease or increase the nuclear spin polarization rate. Non-linear phenomena result, and the interplay of the different polarization and back-action mechanisms depends very strongly on each mechanism's relative strength, as well as nuclear spin polarization decay that occurs due to thermalization and coupling to the bulk environment.

Common features that are indicative of non-linear optical phenomena related to DNP include

1. Hysteresis with respect to the scan direction of the laser [85, 142], external magnetic magnetic scan direction [195], and optical polarization helicity [106].

2. Broadening and distortion of absorption/resonance fluorescence lineshapes [85, 142].

3. Laser scan time dependence: resonant excitation lineshapes become more distorted as laser scan times increase [85, 142].

4. Stability/instability points: the coupled electron-nuclear system may display instabilities with respect to the laser detuning or optical excitation power [177].

6.2 DNP non-linear feedback modeling

Multiple groups have attempted to model the interaction between the confined electron-trion system in the QD, as well as exciton, and the constituent nuclear spins, working to explain the reported "dragging" and "anti-dragging" lineshapes measured in resonant absorption/fluorescence [85, 175, 177, 195, 220] as well as coherent population trapping nuclear spin narrowing [176, 212, 221]. The model developed in this thesis will be discussed in the context of previous modeling work.

The approach taken by Högele *et al* uses a stochastic numerical approach to model the electron-trion system where the quadrupole interaction is assumed to be the main DNP-generating mechanism [220]. The authors perform Schrieffer-Wolff transformations (quasi-degenerate perturbation theory) on both the Hamiltonian, which includes the optical coupling of the electron to the trion, and the Liouvillian superoperator [222], which describes the spontaneous emission channels, arriving at terms that result in nuclear spin polarization without the requisite electron spin flip that is energy-forbidden at high fields (Chapter 4). This modeling effort successfully reproduces the dragging lineshapes observed in the experiments presented in this thesis, but relies on multiple choices deemed arbitrary and without sufficient justification, including the addition of a spin-flip Raman scattering term that leads to asymmetric forward and backward laser scan spectra, and a detuning dependence that relies on the nuclear Zeeman energy E_n rather than the hyperfine coupling constant A_e [220]. Nevertheless, the approach demonstrates using the Schrieffer-Wolff transformation that a energy-conserving interaction leading to nuclear spin polarization via the electron can possibly explain the non-linear DNP phenomena. Additionally, that modeling approach relies on a change in the density of states of the final coupled electron-nuclear system, a principle that will be used in the model developed for this thesis.

Another approach was taken by Xu *et al* [85], and elaborated on by Ladd *et al* [184] to explain the dragging of the dark state dip in the coherent population trapping configuration (shared excited state between the pump and probe lasers) in a QD with a large amount of heavy-hole light-hole mixing (HHLH mixing). This model relies on the HHLH mixing to allow for coupling of the optically excited trion, and therefore the hole, to the nuclear spins, polarizing the nuclei without a simultaneous hole or electron spin flip [150]. This mechanism depends on the optical excitation of the trion/exciton state, and therefore can be turned off in the absence of laser excitation [136], allowing for versatile control of the nuclear spin polarization. This modeling effort also successfully reproduces the dragging of the dark state dip, and the characteristic hysteresis and laser scan speed dependence observed in the experiments. However, the authors' usage of Fermi's Golden Rule may not be valid, and will be discussed in detail futher below. Additionally, Yang and Sham [177] have taken issue with the inability of the theory to produce a preferential nuclear spin-flip direction which would establish a steady state nuclear field, leading to their assertion that most of the theoretical work performed by Xu *et al* [85] is invalid. Nevertheless, the model developed in this thesis adapts a similar approach using the Fermi's Golden Rule, relying more rigorously on a change in the density of states before and after a nuclear spin flip.

A model is developed below to explain and fit the anomalous Raman shifts that are posited to be caused by DNP discussed in the previous sections of this chapter. The Hamiltonian for the model is as follows

$$H = H_0 + H_{e-n} = H_{opt} + \mu_B g_e \hat{S}_{e,x} B_x + \sum_j A_{e,j} \hat{S}_{e,x} \hat{I}_{j,x} + \sum_j A_{Q,j} \hat{S}_{e,x} (\hat{I}_{j,+} + \hat{I}_{j,-}) \tag{6.1}$$

$$A_{Q,j} = \frac{E_{Q,j} A_{e,j} \sin 2\theta_j}{E_{n,j}} \tag{6.2}$$

where $H_{opt}, E_{Q,j}, A_{e,j}, \theta_j, E_{n,j}$ are the optical coupling Hamiltonian between the

electron and trion, the quadrupole interaction energy, the hyperfine contact interaction strength, the principal axis deviation angle from the growth axis $\hat{z}$, and the nuclear Zeeman interaction energy, respectively, where each term can be found discussed in more detail in Chapter 4. The nuclear Zeeman Hamiltonian has been left out this expression due to its small contribution relative to the other Hamiltonian terms (Table 6.1). The last term in the Hamiltonian is the electron-mediated quadrupole interaction that allows for nuclear spin polarization without a spontaneous electron spin flip, where the interaction strength constant $A_{Q,j}$ was derived using the Schrieffer-Wolff transformation in Chapter 4. This term is used as the perturbation term that drives transitions between coupled electron-nuclear spin states $|e\rangle \prod_j |I_j\rangle$, where the transition rates are evaluated below using Fermi's Golden Rule. Referencing the expression for this interaction strength, a few physical insights become clear. First, the interaction strength depends on the quadrupole strain present in the QD: stronger biaxial strain leads to a larger angle θ_j as well as a larger quadrupole interaction strength $E_{Q,j}$, while the overall interaction strength drops as the external magnetic field increases due to the nuclear Zeeman energy dependence in the denominator. As the magnetic field increases, nuclear spin flips eventually become energetically forbidden as they can not be compensated for thermally or by energy uncertainties due to spontaneous emission.

The quadrupole term induces transitions between states $|e\rangle \prod_j |I_j\rangle \rightarrow |e\rangle \prod_j |I_j \pm 1\rangle$; this change in nuclear spin polarization in turn changes the OH field acting on the electron spin, which leads to a non-linear feedback loop. The transition rates between these states are determined using Fermi's Golden Rule. Recall that the probability of a transition between eigenstates $|m\rangle \rightarrow |n\rangle$ of H_0 induced by the perturbation Hamiltonian $\hat{W}(t)$ is given by

$$w_{nm}(t) = |a_{nm}^{(1)}|^2 = \frac{1}{\hbar^2}\left| \int_0^\tau \langle n| \hat{W}(t) |m\rangle e^{i\omega_{nm}t} dt \right|^2 \tag{6.3}$$

where $a_{nm}^{(1)}$ is the first-order time-dependent perturbation theory result for the state amplitude of $|n\rangle$ and $\omega_{nm} = (E_n - E_m)/\hbar$ [155]. From this result, a transition

DNP modeling constants	
Hyperfine constant A_e	53 μeV
Quadrupole coupling E_q	41 neV
Average principal axis angle θ	35°
Nuclear Zeeman energy E_n	75 neV
Nuclear spin decay rate Γ_d	35 Hz
Radiative relaxation rate	1.4 μeV
Number of nuclear spins N	5 $\times 10^4$
Laser step time Δt	50 ms

Table 6.1: Dynamic nuclear spin polarization modeling constants. These constants are held fixed for all Raman shift fits, for both the co-tunneling and optical pumping datasets with one and two excitation fields.

rate between an initial state and a continuum of final states described by a density of states can be written down, assuming that the perturbation is constant in time:

$$\begin{aligned} P_{nm} &= \frac{2\pi}{\hbar} |\langle n| W |m\rangle|^2 \delta(E_n - E_m) \\ \Rightarrow \tilde{P}_{nm} &= \int P_{nm}\rho(E_n) dE_n = \frac{2\pi}{\hbar} |\langle n| W |m\rangle|^2 \rho(E_n) \end{aligned} \tag{6.4}$$

where $\rho(E_n)$ is the density of final states within a unit interval dE_n, and the density of states has units of inverse energy [155]. A key point to be made with respect to the Golden Rule described here is that the transition rate $\tilde{P}_{mn}$ describes transitions between eigenstates of H_0. However, in the theoretical work performed by Xu *et al* described above [85], the Golden Rule is used to calculate transition rates between state vectors that describe the *full wavefunction* rather than eigenstates, ie. between $|\psi_{i,f}\rangle = c_{+,(i,f)} |+\rangle + c_{-,(i,f)} |-\rangle + c_{t,(i,f)} |t\rangle$, where $|+\rangle, |-\rangle, |t\rangle$ are the eigenstates of H_0 describing the three-level lambda system of the electron and trion system. That approach is not taken here, and the Golden Rule is used rigorously.

The transition rates for flipping a nuclear spin up or down are then calculated. Plugging in the perturbation Hamiltonian to the Golden Rule results in (setting $\hbar = 1$, which means that all rates have units of inverse energy)

$$\begin{aligned} R_{\pm,j} &= 2\pi \left| \langle n| A_{Q,j} \hat{S}_{e,x} \hat{I}_{j,\pm} |+/-\rangle |I_j\rangle \prod_{k\neq j} |I_k\rangle \right|^2 \rho(E_{f,\pm}) \\ &= 2\pi A_{Q,j}^2 \left| \langle n| (\pm)\frac{1}{2}\sqrt{(J \pm m_j)(J \mp m_j + 1)}\, |I_j \pm 1\rangle \prod_{k\neq j} |I_k\rangle \right|^2 \rho(E_{f,\pm}) \\ &= \frac{\pi}{2} A_{Q,j}^2 (J \pm m_j)(J \mp m_j + 1)\rho(E_{f,\pm}) \end{aligned} \tag{6.5}$$

where J, m_j are the angular momentum and angular momentum projection quantum numbers associated with the j-th nucleus, and $\rho(E_{f,\pm})$ is the density of states of the coupled system after a nuclear spin has flipped up or down. The crux of the nuclear spin physics is found in two aspects of the result above, first in the coefficients out front of the density of states, and the density of states itself. The density of states contains the inherent optical non-linearity of the system. More explicitly, the final states of the system are $|+/-\rangle |I_j \pm 1\rangle \prod_{k\neq j} |I_k\rangle$; thus, the density of states can depend on the exact nature of how the nuclear spin flip affects the electron spin resonance. Neglecting thermal populations of the nuclear spin ensemble and assuming that the nuclear Zeeman energies are considerably smaller than the energy shift induced on the electron spin splitting by the OH field (Table 6.1), the density of final states can be written in terms of the electron spin population under laser excitation derived using the optical rate equations [45] with a new effective detuning determined by the OH field shift due to the nuclear spin flip. The density of final states will be defined using the rate equation result [45] for the two-level system, with the ground state equal to the electron spin state $|+/-\rangle$ and the excited state equal to one of the trion states which is not affected by the OH field shift, which is given by

$$\rho(E_{f,\pm}) = \frac{\rho_{elec}}{\gamma_2} = \frac{1}{\gamma_2} \frac{\gamma_2^2(1 + 4\beta^2) + 4\delta_\pm^2}{\gamma_2^2(1 + 8\beta^2) + 4\delta_\pm^2} \tag{6.6}$$

where $\delta = \omega_{laser} - (\omega_0 - \omega_e)$ is the laser detuning on the electron-trion transition, and $\beta = \Omega_0/\gamma_2$ is the Rabi frequency normalized by the radiative decay rate γ_2. The nuclear spin flip affects the density of states differently depending on whether the optical transition corresponding to the $|+\rangle$ state (red Zeeman transition) or the $|-\rangle$ state (blue Zeeman transition) is being driven. Specifically, the optical detunings for the red and blue Zeeman transitions are given by

$$\begin{aligned} \delta_{\pm}^{\mathrm{RED}} &= \omega_{laser} - (\omega_0 - (\Delta_e/2 + \frac{A_e}{N}(\langle I_x \rangle \pm 1))) \\ &= \delta_0^{\mathrm{RED}} + \frac{A_e}{N}(\langle I_x \rangle \pm 1) \\ \delta_{\pm}^{\mathrm{BLUE}} &= \omega_{laser} - (\omega_0 - (-\Delta_e/2 - \frac{A_e}{N}(\langle I_x \rangle \pm 1))) \\ &= \delta_0^{\mathrm{BLUE}} - \frac{A_e}{N}(\langle I_x \rangle \pm 1) \end{aligned} \tag{6.7}$$

where $\langle I_x \rangle \equiv \sum_j m_j$ is the net nuclear spin polarization, and the detuning takes into account the initial state OH field as well as the change in the OH field due to the single nuclear spin flip. Thus, it becomes clear that optical excitation of the blue and red Zeeman transitions may potentially lead to very different non-linear DNP behavior due to the difference in the sign of the new detuning term, as verified by the differences between the experimental Raman shifts of the red and blue transitions.

One can derive a non-linear differential equation by summing up the flip up and flip down rates over the entire nuclear spin ensemble (or summing up over the initial states) and using the definition of the nuclear spin polarization in terms of the angular momentum projection number defined in the previous paragraph, arriving at

$$\begin{aligned}
\frac{d\langle I_x\rangle}{dt} &= R_+ - R_- - \gamma_d \langle I_x\rangle \\
&= \frac{\pi}{2\gamma_2}\sum_j (J^2 - m_j^2 + J + m_j) A_{Q,j}^2 \rho_{elec}(m_j \to m_j + 1) \\
&- \frac{\pi}{2\gamma_2}\sum_j (J^2 - m_j^2 + J - m_j) A_{Q,j}^2 \rho_{elec}(m_j \to m_j - 1) - \gamma_d \langle I_x\rangle \\
&= \alpha b \tilde{A}_Q^2 (\rho_{elec}(m_j \to m_j + 1) - \rho_{elec}(m_j \to m_j - 1)) \\
&+ b\tilde{A}_Q^2 (\rho_{elec}(m_j \to m_j + 1) + \rho_{elec}(m_j \to m_j - 1)) \langle I_x\rangle - \gamma_d \langle I_x\rangle
\end{aligned} \tag{6.8}$$

where $\alpha = \sum_j (J^2 - m_j^2 + J)$, $b = \frac{\pi}{2\gamma_2}$, and $\tilde{A}_Q$ is the quadrupole interaction term avearged over the entire nuclear spin ensemble. Thus, there are three terms in the non-linear differential equation derived above. The first term in the last equality of Equation 6.8 is given by the difference in the density of states for a nuclear spin flip up versus down. The second term is related to the overall density of states since it is a sum of the spin flip up and down results, multiplied by the nuclear spin polarization. Since the nuclear spin polarizations measured experimentally are typically less than 10%, especially in this experiment, the second term will be neglected in this model. The third term is the nuclear spin polarization decay rate, whether related to simple nuclear spin relaxation or diffusion out into the environment.

The first term in the non-linear differential equation can be described as the primary feedback mechanism that introduces the non-linearity into the system. The density of states is itself a function of the nuclear spin polarization $\langle I_x\rangle$ as carried in the optical detuning. The feedback function is plotted in Figure 6.2, where the nuclear spin polarization has been taken to zero.

As the laser is scanned from red to blue, the feedback strength becomes strongly negative on the red side of the transition. This negative feedback term leads to a decreasing OH field, as opposed to the blue side of the transition for which the OH field is increasing in time until saturating at a constant value determined by the nuclear spin decay rate and optical excitation strength, as will be shown in more detail later. If the laser is held on resonance ($\delta = 0$), in the presence of nuclear spin fluctuations

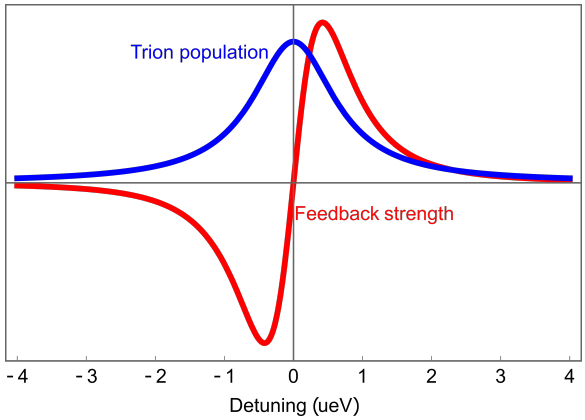

Figure 6.2: Feedback function from first term of Equation 6.8 given by the difference between the density of states for spin flip-up versus spin-down (red), imposed on the trion population dependence (blue). The feedback function has anti-symmetric dependence with respect to the detuning, resulting in locking of the resonance or pushing of the resonance depending on whether the optical resonance is part of the red or blue Zeeman transitions. Parameters are the same as given in Table 6.1, with $\beta = 0.1$.

that are a distinct phenomenon from the DNP shifts observed here, the feedback mechanism plotted here could act either as a restorative force, bringing the transition back into resonance with the laser, or as a destabilizing force, depending on whether the red or blue Zeeman transitions are being driven [85, 154, 176, 221]. If the laser is in resonance with the blue Zeeman transition, a nuclear spin flip $\langle I_x \rangle \rightarrow \langle I_x \rangle + 1$ leads to a larger OH field, which shifts the transition to a higher energy. Thus, the laser is now red-detuned, resulting in negative value of the feedback function, decreasing the OH field back to its original state. However, the opposite is true for the red Zeeman transitions: an increase in the OH field shifts the transition to a lower energy, resulting in a positive feedback function result, driving the OH field further out of resonance with the laser.

The non-linear differential equation can be used to effectively model the Raman shifts reported in this thesis which have been measured by scanning a laser across the electron-trion optical resonances. The results of these experiments depend strongly on the laser excitation power and laser scan time. The physics of these scan time dependences become more evident by examining the build-up times of the nuclear spin

polarization by solving the non-linear equation in Equation 6.8. Figure 6.3 displays the numerical solutions of the non-linear equation for the OH field as a function of time, with the initial nuclear spin polarization set to zero, for a fixed laser detuning of -0.1 μeV on the blue Zeeman transition, for varying excitation powers, with the nuclear spin polarization decay rate equal to 35 Hz (1/(35 Hz) = 29 ms).

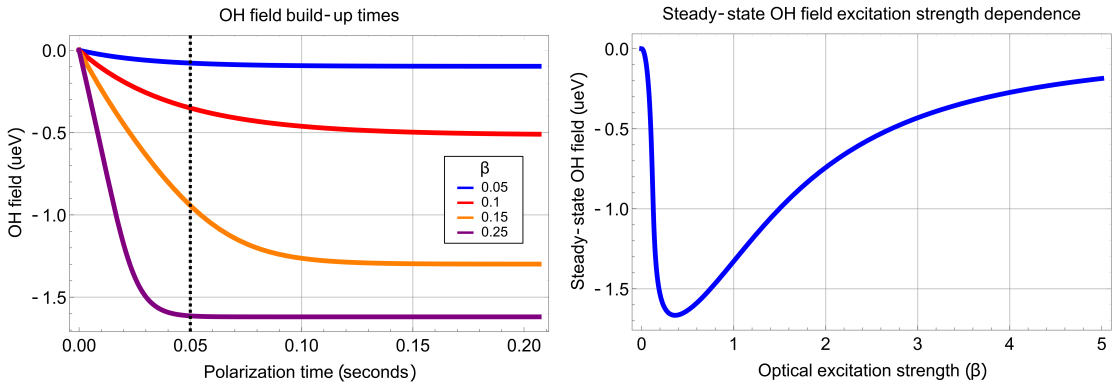

Figure 6.3: OH field build-up times and steady-state values. Left: The non-linear differential equation for the nuclear spin polarization is solved numerically for varying optical excitation strengths β(normalized by the radiative relaxation rate γ_2), using the parameters detailed in Table 6.1, for a laser detuning of -0.1 μeV, operating on the blue Zeeman transition. The dark dashed line at 0.05 seconds indicates the time at which the nuclear spin polarization is evaluated for the laser scan simulations performed later in the section. Right: Steady-state OH field as a function of the optical excitation strength.

Key features of the OH field build-up include:

1. The steady-state value of the OH field increases as the excitation strength increases, peaking at approximately $0.2\gamma_2$, and decaying to zero as the optical transition saturates.

2. The time required to evolve to the steady-state value for a given excitation strength decreases with increasing excitation strength.

Thus, a weaker excitation field is less likely to perturb the nuclear spin ensemble, leading to smaller Raman shifts and absorption lineshapes that deviate less from the DNP-free predicted lineshape. On the opposite end of the spectrum, scanning the

laser slowly and using an optical excitation strength leading to the maximal OH field build-up (Figure 6.3, right) will maximally distort the absorption lineshape and lead to considerable anomalous Raman shifts, as observed in the experiments reported in this thesis. Additionally, the OH field build-up time is in order of magnitude agreement with the nuclear spin polarization times of 7 ms and 12 ms measured by Sun *et al* [136].

The Raman shifts reported here are fit using the model described above. The procedure for numerical fitting is as follows: the initial OH field is set to zero. The initial laser detuning is set equal to the experimental value at the red or blue edge of the scan, depending on whether the laser scan frequency increased or decreased in time, respectively. The new OH field is determined by evaluating the non-linear differential equation (Equation 6.8) at the experimental laser step time (approximately 50 ms), not necessarily equal to the steady-state value as $t \to \infty$. The laser detuning is stepped by ΔE and the OH field result from the previous value is used as the initial condition for solving the differential equation at the new detuning. For the two excitation field case (optical pumping), the electron population term is replaced with the specific electron spin term ($|+\rangle \, or \, |-\rangle$) that the probe laser is scanned over, and the rate equations are solved for the pump/probe configuration in which the two fields do not share an excited state and off-resonant driving is not included. The details of pump/probe ratio effects on the DNP non-linearities are not discussed here, since the overall qualitative results are the same when comparing the one and two excitation field cases.

Highly distorted absorption lineshapes and Raman spectra that deviate considerably from the expected DNP-free behavior can be understood as the electron-nuclear system having approximately reached the steady-state within the laser frequency step time. Thus, nuclear spin polarization build-up times can be determined within an order of magnitude by a simple variation of the laser step time. Non-linearities such as hysteresis and broadening only become evident at long wait times relative to the build-up time, as seen in Figure 6.4 which displays the predicted absorption lineshapes for both the red and blue Zeeman transitions, comparing short and long

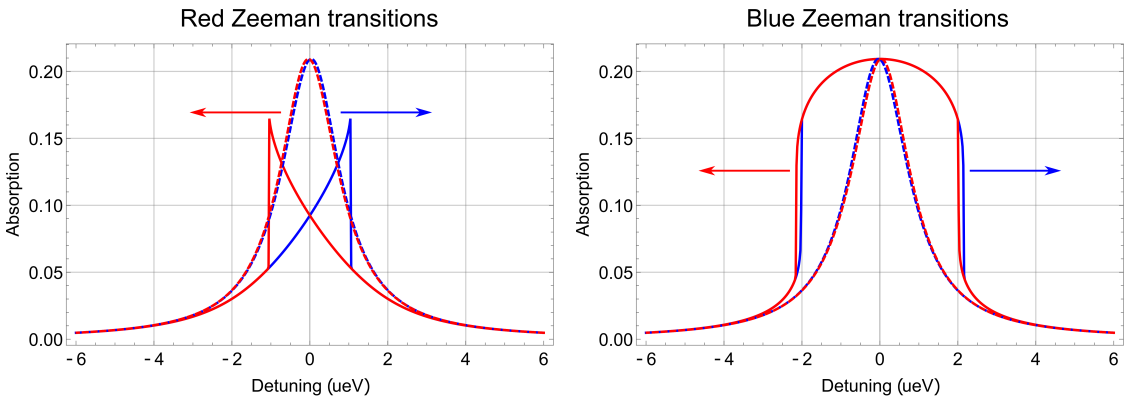

Figure 6.4: Absorption lineshapes comparing short and fast laser scan times. Solid (dashed) lines correspond to a laser step time of 400 ms (10 μs). Forward (backward) laser scans are denoted in blue (red). For the red Zeeman transitions (left), the scanning laser pushes the resonance away in the direction of the laser scan. For the blue Zeeman transitions (right), the tracking of the resonance with the laser in both directions becomes evident at long waiting times.

waiting times. Thus, for very fast laser scan times compared to the nuclear spin polarization build-up time, the optical resonance is effectively decoupled from the nuclear spin ensemble due to the lack of nuclear spin polarization build-up. In the case of the red Zeeman transitions, at long waiting times (400 ms), the absorption maximum is pushed away from the resonance in the absence of DNP in the direction of the laser scan by approximately 1 μeV before dropping off considerably. In the blue Zeeman transition case, the OH field brings the transition into resonance with the scanning laser, peaking the absorption over a wide range (4 μeV), exhibiting hysteresis at the edges of the broadened absorption range.

The Raman spectra fits are displayed in Figure 6.5 for the co-tunneling, single excitation field case with the resulting fit parameters in Table 6.2, along with the optical pumping fits in Figure 6.6 and the resulting fit parameters in Table 6.3. In the co-tunneling cases, the red Zeeman Raman spectra modeling matches the observed hysteresis centered around where the bare optical resonance would be observed. A key feature that is reproduced by the model is the "snapping" that occurs around the hysteresis range: the OH field increases abruptly from its lowest to highest value over a laser scanning range of $\sim$50 neV. The asymmetry of the Raman spectra are

also predicted with reasonably close fit parameters that match those measured during the experiment including the excitation power. Likewise, the blue Zeeman transition Raman spectra are reproduced, albeit by changing the feedback coefficient sign from positive to negative. The slope of the nearly-linear Raman spectra dependence in the tracking portion of the laser scan is reproduced very closely with the same fit parameters as in the red Zeeman case with slight changes in the excitation power that vary acceptably due to sample mis-alignment from day to day. Additionally, the tracking widths of the blue Zeeman transitions is reproduced in excellent agreement with the model.

However, the optical pumping fits, although reproducing the magnitude of OH field shifts in both the red and blue cases, do not model the blue Zeeman transitions as well. The OH fields measured experimentally exhibit only a small amount of hysteresis at the edges of the tracking range with large OH field shifts overall, compared to the modeling results which exhibit considerably more hysteresis while generally reproducing the overall OH field magnitude when both the forward and backward scans are considered together. Additionally, the red Zeeman models do not fit as well in the hysteretic range, again predicting hysteresis ranges (difference between forward and backward scans) larger than observed in the experiment. Nevertheless, the general qualitative features of the Raman spectrum are present in the optical pumping calculations, and the overall OH field magnitudes are reproduced within reasonable agreement.

It is very important to note that an arbitrary sign flip has been made between modeling the blue and red Zeeman transition scans in order to reproduce the proper qualitative response differences between the two cases, while keeping the magnitude of the fitting constants relatively the same (See Tables6.2 and 6.3). As far as the author is aware, this arbitrary sign flip has no known physical justification. Ideally the sign flip would arise naturally out of the Hamiltonian, and considerable effort was taken to accomplish this, with no success. The author also notes that this arbitrary sign flip is also taken in the published literature without much justification [177, 194]. In one case, the sign of the hyperfine constant is flipped, and in the other

case the sign of the nuclear Zeeman energy is flipped, and no justification is made in either case. Thus, the problem of non-linear feedback due to DNP in the QD system still needs theoretical clarification. Nevertheless, reasonable fit parameters are utilized in this thesis, implying that the quadrupolar mechanism (and likely other mechanisms including the HHLH-mixing mechanism depending on QD morphology) may be consistent with explaining the phenomena observed here.

There are multiple reasons for the deviation of the optical pumping models from the experimental results. First, the lineshape fits are performed manually by hand; the interplay of the nuclear spin decay rate, pump and probe excitation powers, and pump detuning in the non-linear differential equation lead to non-intuitive results for the Raman spectra fit and thus would better be performed by a fitting algorithm. However, there is not an analytical solution to the Raman spectra resulting from the non-linear differential equation, and therefore the numerical laser scanning process described above is not easily amenable to non-linear least-squares fitting.

Beyond the problems associated with fitting, there are two fundamental improvements that can be made to the model. First, in the two excitation field case, the effect of the pump on the DNP pumping rates as calculated for the probe using Fermi's Golden Rule has only been incorporated into the rate equation result for the electron spin population. In fact, the pump may also contribute directly to DNP pumping rates via optical excitation, and these terms should be incorporated into the non-linear differential equation via application of Fermi's Golden Rule. The incorporation of the additional pump DNP rate may explain why it is necessary to increase the DNP feedback constant α from 40 in the co-tunneling case to 60 and 90 in the red and blue Zeeman optical pumping cases, respectively. Additionally, the occupation (or filling) factor is often times considered in the DNP modeling process [57, 142, 143, 212]: this factor describes the percentage of experimental that the electron spends in the QD. In the limit of rapid tunneling between the Fermi reservoir and the QD, this filling factor function can contribute to electron Zeeman level broadening, significantly modifying the DNP response [169]. In this experiment, the electron is expected to spend a larger fraction of time undisturbed in the QD in the optical pumping regime versus

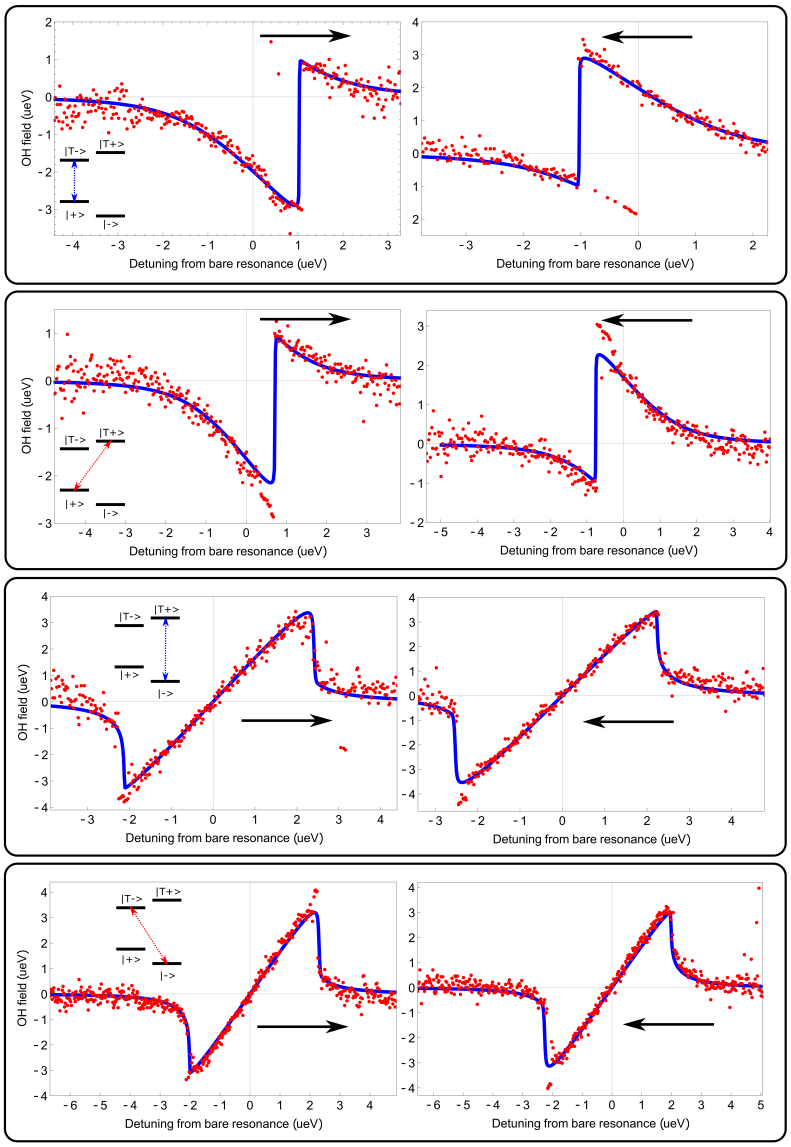

Figure 6.5: Modeling fits of the Raman spectra for the co-tunneling cases. Optical excitation of: (first panel) $|+\rangle \rightarrow |T-\rangle$, (second panel) $|+\rangle \rightarrow |T+\rangle$, (third panel) $|-\rangle \rightarrow |T+\rangle$, (fourth panel) $|-\rangle \rightarrow |T-\rangle$. The red dots are the measured Raman spectra data and the blue solid lines are the non-linear fits. The detuning is measured from where the optical resonance is expected in the absence of DNP. Fitting parameters are found in Table 6.2. Black arrows indicate direction of laser scan.

co-tunneling, possibly accounting for the increase in the feedback parameter α.

Second, no attempt at modeling the nuclear spin fluctuations and how they are affected by optical pumping of the nuclear spin polarization has been made here. It has been demonstrated both theoretically and experimentally that nuclear spin fluc-

Co-tunneling				
Red Zeeman transitions				
Configuration:	(+;T-),F	(+;T-),B	(+;T+),F	(+;T+),B
α	40	40	40	40
$\beta_1 = \Omega_1/\gamma_2$	0.28	0.28	0.21	0.22
k shift (cm^{-1})	10573.7125	10573.7111	10574.013	10574.014
Δ_{OH} shift (μeV)	-0.4	-0.9	-0.2	-0.4
Blue Zeeman transitions				
Configuration:	(-,T+),F	(-,T+),B	(-,T-),F	(-,T-),B
α	-40	-40	-40	-40
$\beta_1 = \Omega_1/\gamma_2$	0.35	0.39	0.32	0.31
k shift (cm^{-1})	10574.423	10574.4215	10574.1099	10574.1041
Δ_{OH} shift (μeV)	-0.7	0.1	0.2	0.25

Table 6.2: DNP modeling fit parameters for the co-tunneling single excitation field cases, separated into red and blue Zeeman transitions.α, β_1, k shift, and Δ_{OH} shift are the feedback strength, optical Rabi frequency (normalized by the radiative relaxation rate), the bare optical resonance wavenumber (cm^{-1}), and an offset used to shift the Raman spectra, where the offset is much smaller than the overall Overhauser field shift. The notation used to denote the optical excitation configuration is given by $(a; b), c$, where a is the ground state $|+/-\rangle$, b is the optically excited state $|T+/T-\rangle$, and c is the laser scan direction, which can have increasing(decreasing) frequency (F)(B).

tuations can be tamed via coherent population trapping (CPT), but the effects of resonant excitation outside of the CPT condition are not yet understood. Nevertheless, a significantly narrowed nuclear spin ensemble may drastically affect the extent to which the Raman spectra are distorted, possibly explaining the deviation of the simple model developed in this thesis from the experimental optical pumping results.

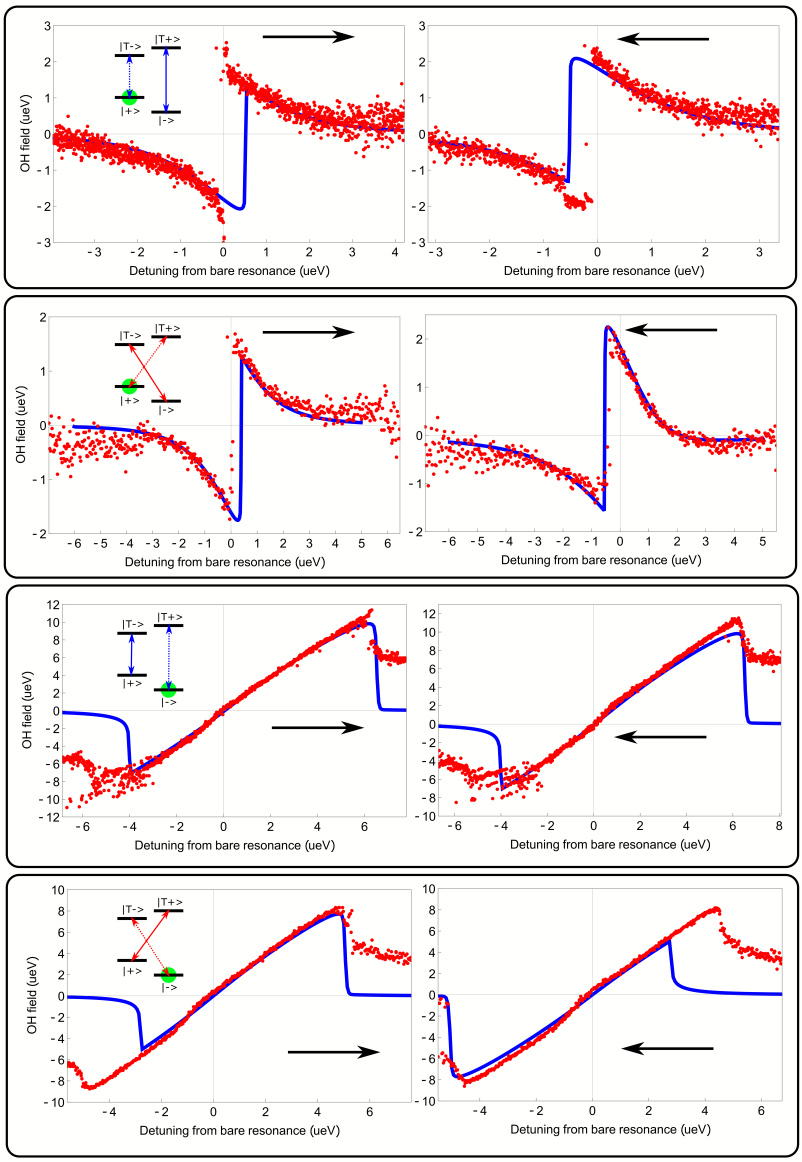

Figure 6.6: Modeling fits of the Raman spectra for the optical pumping cases. Pump-(probe) excitation of (first panel): $|-\rangle \rightarrow |T+\rangle(|+\rangle \rightarrow |T-\rangle)$, (second panel): $|-\rangle \rightarrow |T-\rangle(|+\rangle \rightarrow |T+\rangle)$, (third panel): $|+\rangle \rightarrow |T-\rangle(|-\rangle \rightarrow |T+\rangle)$, (fourth panel): $|+\rangle \rightarrow |T+\rangle(|-\rangle \rightarrow |T-\rangle)$. Raman spectra fits can be found in Table 6.3. Black arrows indicate direction of laser scan.

One particular theoretical framework [175, 177] utilizes the quantum Liouville equation and applies an adiabatic transformation, similar to that of the Schrieffer-Wolff method used by Issler *et al*, to derive a model that does predict the noise features of the non-linear trion-nuclear system. That model separates the density matrix elements

Optical pumping

Red Zeeman transitions				
Configuration:	(+;T-, -;T+),F	(+;T-, -;T+),B	(+;T+, -;T-),F	(+;T+, -;T-),B
α	40	40	40	40
$\beta_1 = \Omega_1/\gamma_2$	0.208	0.21	0.175	0.15
$\beta_2 = \Omega_2/\gamma_2$	0.541	0.546	0.455	0.39
δ_2	0	0	0	-1
k shift (cm^{-1})	10573.957	10573.957	10574.262	10574.275
Δ_{OH} shift (μeV)	0.435	0.25	-0.1	-0.3
Blue Zeeman transitions				
Configuration:	(-;T+, +;T-),F	(-;T+, +;T-),B	(-;T-, +;T+),F	(-;T-, +;T+),B
α	-90	-90	-60	-60
$\beta_1 = \Omega_1/\gamma_2$	0.333	0.333	0.243	0.243
$\beta_2 = \Omega_2/\gamma_2$	0.932	0.932	0.797	0.797
δ_2	-1/3	-1/3	0	0
k shift (cm^{-1})	10574.663	10574.658	10574.356	10574.356
Δ_{OH} shift (μeV)	-0.25	-1.5	0.21	0.21

Table 6.3: DNP modeling fit parameters for the optical pumping two-field excitation cases, separated into red and blue Zeeman transitions.$\alpha, \beta_1, \beta_2, \delta_2$, k shift, and Δ_{OH} shift are the feedback strength, optical Rabi frequencies for fields 1 and 2 (normalized by the radiative relaxation rate), the detuning of field 2 from the bare resonance, the bare optical resonance wavenumber (cm^{-1}), and an offset used to shift the Raman spectra, where the offset is much smaller than the overall Overhauser field shift. The notation used to denote the optical excitation configuration is given by $(a; b, c; d), e$, where a is the ground state $|+/-\rangle$ driven by the probe, b is the optically excited state $|T+/T-\rangle$ coupled to the probe, c is the ground state $|+/-\rangle$ driven by the pump, d is the optically excited state $|T+/T-\rangle$ coupled to the pump, and e is the probe laser scan direction, which can have increasing(decreasing) frequency (F)(B).

for the electron, trion, and nuclei based off of considerations of time scales: nuclear spin polarization and dephasing occur on much longer time scales than hole/electron

fluctuations caused by optical excitation and spontaneous emission. The model arrives at absorption lineshapes that are strikingly similar to those reported in this thesis. Additionally, the theory predicts increased nuclear spin fluctuations at the edges of the blue Zeeman transitions (verified in this thesis), but predicts a narrowed ensemble in the red Zeeman cases, which are in contradiction to the experimental evidence provided here. The theory arrives at these results by changing the sign of the nuclear Zeeman energy (without physical justification) between the two cases (blue and red Zeeman) and depends on virtual excitation of the hole state. It is possible that the quantum Liouville method approached in that report may be adapted to explain the Raman shifts and fluctuations observed in this QD system by application to the quadrupole Hamiltonian.

6.3 Chapter summary

This chapter describes modeling efforts taken to reproduce the DNP-induced Raman shifts reported in Chapter 5 using the quadrupole Hamiltonian. Previously developed models are discussed, and aspects of two specific models are adapted to explain the single QD data reported here. Reasonable parameters for quadrupolar shifts, hyperfine constants, nuclear Zeeman splittings, and optical excitation strengths result in acceptable fits for the Raman line center fits in the co-tunneling and optical pumping cases, although an arbitrary sign flip of the feedback strength is required when switching from the red to blue Zeeman transitions. Thus, it is argued that the electron-nuclear coupling brought about by the quadrupole interaction present in the strained QD system may viably explain the non-linear DNP phenomena observed in this QD system, especially in the absence of strong HHLH-mixing and spin-orbit coupling.

CHAPTER 7

Time-domain studies of dynamic nuclear spin polarization in single quantum dots

7.1 Introduction

While the previous chapters of this thesis have detailed experiments involving the continuous-wave (CW) excitation of the QD electron-trion system using pump-probe spectroscopy, this chapter will cover time-domain studies, or pulsed excitation of the QD system. The first section reviews previous literature on time-domain experiments, with a focus on pulsed optical pumping for the purposes of electron spin initialization, and ultrafast coherent control of the electron spin qubit. The theory behind detuned two-photon Raman rotation pulses is introduced. Two-pulse sequences known as Ramsey fringes which, in principle, allow for the determination of the electron spin inhomogeneous broadening (T_2^*) are introduced, along with the experimental setup used in the following experiments. The expected form of the Ramsey fringe pulse delay dependence in the presence of quasi-static environmental fluctuations is derived. Power-dependent Rabi oscillations of the probe scattering as a function of the Raman rotation pulse are demonstrated; in some cases, the probe scattering exhibits hysteresis with respect to the pulse power in the vicinity of the π pulse range, indicating DNP effects. Furthermore, Ramsey fringes are shown to be strongly distorted for external in-plane magnetic fields ranging from 2 to 5 Tesla, with a qualitative distortion that depends on which electron spin state is probed. The electron spin state splittings extracted from the Ramsey fringes are broadened beyond the result expected in the

presence of quasi-static OH field broadening with increasing broadening as a function of external magnetic field, and the measured state splitting deviates from the splitting measured at co-tunneling, implying the presence of baseline OH fields during pulsed excitation. Two EOM-pulsed narrowband fields are used in the coherent population trapping configuration to attempt to narrow the nuclear spin ensemble as measured using the Ramsey fringe technique. A reduction in the FWHM of the electron spin resonance analyzed using a Fourier transform of the Ramsey fringe signal for the 5 ms 70% duty cycle DNP pumping case is observed: the FWHM is reduced by (19.8 $\pm$ 2.0)%, indicating a narrowing of the OH field via CPT of the electron spin. This reduction in the OH field distribution is also correlated with a (561 $\pm$ 62) MHz blue shift of the electron spin resonance from the CPT-OFF to CPT-ON case, bringing the electron spin resonance frequency closer to the frequency measured at co-tunneling where the nuclear spin polarization is expected to be negligible. Thus, the effect of CPT pumping at timescales on the order of 5 ms is observed to be a narrowing of the OH field distribution accompanied by a depolarization of the net nuclear spin polarization.

An additional novel class of experiments is performed using EOM-pulsed pump-probe excitation. These experiments demonstrate that even under very weak probe excitation, where the electron spin population resides almost entirely in the $|+\rangle$ or $|-\rangle$ state during the experiment, the underlying OH field is unstable with respect to the probe laser frequency after sufficiently long pump-probe delays. Pump-probe experiments are performed for repetition periods ranging from 100 ns to 3 μs. A possible implication of these experiments is that the time-averaged electron spin polarization plays a significant role in DNP phenomena in the time-domain, as opposed to the absolute pump-probe delay at timescales less than 3 μs.

7.2 Review of coherent control

Quantum information and quantum computation applications require exquisite preparation and control of the quantum state of the qubit system and protection from

the environment [223]. The electron spin qubit has been examined extensively as a high performance qubit. Two major milestones have been achieved in the InAs/GaAs QD electron qubit system: high fidelity initialization of the electron spin qubit into a pure state via optical pumping [58, 98], and ultrafast control of the quantum superposition state of the two electron spin states [59, 60, 86, 149, 180–183, 224–226].

Initialization of the electron spin qubit to a pure state of either $|+\rangle$ or $|-\rangle$ is achieved via optical pumping of one of the electron-trion optical transitions, as detailed in Chapter 3. When the QD diode structure is configured to bias the QD into a region of charge stability in which the electron is confined to the QD for at least 1 μs, a single optical field brought into resonance with one of the trion transitions will rapidly optically pump the electron spin into the non-driven electron spin state [58]. The initialization fidelity of this scheme depends on a number of parameters, including the magnetic field strength, spin-orbit coupling leading to mixing of the ground states, the optical Rabi frequency, the spontaneous emission rate, and the co-tunneling rate which leads to electron spin state thermalization [58]. Nevertheless, in the in-plane magnetic field configuration, $(98.9 \pm 0.4)\%$ spin state preparation efficiency was achieved using CW excitation; in this thesis, at least 96.7% preparation efficiency is achieved under EOM pulsed excitation. High pumping efficiency can be achieved within less than 5 nanoseconds using reasonable optical Rabi frequencies and external magnetic fields. Additionally, preparation of the electron spin qubit state may be achieved in the out-of-plane magnetic field configuration in which the field is parallel to the growth direction of the QD by taking advantage of OH field fluctuations which enable forbidden cross transitions leading to optical pumping times on the order of microseconds [98]. Optical pumping of the electron spin qubit is now routinely performed before coherent control techniques are utilized in order to improve fringe contrast.

A coherent superposition of the electron spin states may be generated using pulsed excitation. Berezovsky *et al* first reported [224] on a π pulse rotation, or full population inversion, of a single electron spin qubit in a QD system measured using time-resolved Kerr rotation. This report was followed by higher fidelity schemes that

utilized ultrafast picosecond detuned two-photon Raman pulses (discussed in detail in Section 7.3.1), demonstrating coherent control of the electron spin qubit as a function of the detuned pulse rotation power [86]. This rotation pulse scheme was used to focus the electron spin precession frequencies of an ensemble of QD electron spins [181]; electron spin frequencies and the coupled nuclear spin ensemble were focused into specific frequencies that became synchronized with the repetition rate of the pulsed rotation laser. Interestingly, a *spin echo* [227] was observed in that experiment; at a delay time $2t_{12}$ where t_{12} is the delay time between a $\pi/2$ and π pulse, a revived echo is observed, at which time the inhomogeneities of the electron spin frequencies for different QDs in the ensemble are eliminated due to the π inversion pulse. The coherent control pulse sequences described above are used as high resolution spectroscopic tools; in one study [60], fast spin rotations were used to determine the electron and heavy-hole spin precession frequencies, as well as the trion spontaneous emission rate. It is also possible to impart fast geometric phases on the electron spin qubit via the resonant excitation of one of the electron-trion transitions using a quasi-CW beam [60]. Summary of these early coherent control experiments shows that dephasing times are on the order of 1-2 ns, and report on strong distortion of coherent oscillations due to electron-nuclear interactions.

Having demonstrated ultrafast (2-3 ps) rotation pulses acting on the electron spin qubit, more advanced pulsed schemes were developed to extract spectroscopic information about the QD electron-trion system. The spin echo was first observed on a single QD containing a confined electron [225], demonstrating a transverse decay time T_2 of 2.6 μs at high magnetic fields of 7 T, revealing that the electron spin qubit may prove to be a useful candidate for a high-performance qubit. Inexplicably, the particular QD electron system studied in that report did not demonstrate distortion of the fringes due to DNP electron-nuclear spin interactions. Relatedly, coherent control of the QD-confined hole spin qubit was demonstrated [180, 226] at around the same time, revealing a T_2 time of around 1.1 μs, achieving longer dephasing times more consistently than the electron spin qubit, which is typically dephased due to DNP effects. However, it was later demonstrated that the hole spin qubit does indeed

directly interact with the nuclear spin bath; DNP modulation of Ramsey fringe and spin echo fringes was demonstrated [182], revealing that the OH field does act directly on the hole spin, albeit with reduced interaction strength compared to the electron.

A very thorough study was performed on the electron spin qubit in which multiple coherent control techniques were combined with sophisticated optical pumping to reveal the intrinsic dephasing time T_2 of the electron spin in the presence of DNP effects [149]. In that report, an explicit attempt was made to ameliorate nuclear spin polarization build-up by the utilization of an alternating electron spin pumping technique; alternating experimental shots initialized the $|+\rangle$ and $|-\rangle$ states, leading to no net electron spin polarization, and therefore no net nuclear spin polarization build-up. DNP distortion of the Ramsey fringe, which typically leads to a total obfuscation of the fringes within 700 ps, was completely eliminated by this technique, revealing an T_2^* time due to inhomogeneous broadening of the single electron spin equal to 1.93 ns. From this study, an OH field distribution width of 33 mT was extracted. Furthermore, the study utilized this alternating optical pumping sequence in combination with spin echo as a very sensitive spectroscopic probe of the underlying quadrupole-strained nuclear bath, demonstrating dephasing of the electron spin qubit due to both parallel and transverse OH field components.

Coherent control techniques in the QD system are approaching a level of maturity paralleled by few other quantum systems. For instance, dynamical decoupling [228–230] was achieved [183] on the hole spin qubit, demonstrating that the coherence time of the qubit could be extended to 4 ± 0.2 μs using a 9 pulse dynamical decoupling pulse scheme. The dynamical decoupling pulse scheme consists of multiple π pulses, which can be shown using a window filter formalism [231] to eliminate higher frequency correlated noise with an increasing number of rotation pulses. Spin echo, being the most basic dynamical decoupling scheme, and higher-order dynamical decoupling pulse trains, suppress the effects of correlated (for example, non-Markovian) noise [230]. This study revealed that the hole qubit is indeed still affected by the nuclear spin environment, but that this noise is correlated; non-correlated noise due to electrical fluctuations in the diode structure and host environment continue to de-

phase the hole spin qubit with a large number of decoupling rotation pulses. There is great hope for further improvement of the coherent control techniques reported above through the usage of complex composite pulse sequences, promising that electron and hole spin qubits may be an integral part of future quantum computation architectures.

7.3 Ramsey fringes

7.3.1 Two-photon detuned Raman pulse rotation theory

Quantum information science depends on the high fidelity control of the wavefunction of the qubit system; in the single qubit QD electron system, this requirement amounts to precise control of the phase between the electron spin-up and spin-down state, ie. $|\psi_e\rangle = \frac{1}{\sqrt{2}}(|+\rangle + e^{i\phi}|-\rangle)$. The phase between the states may be controlled in a number of ways, for example through spin precession in an external magnetic field, geometric phase rotation under CW optical excitation, and two-photon detuned Raman pulses [61]. This section discusses the theoretical considerations behind the two-photon Raman pulse rotation of the electron spin, arriving at a theoretical result for the Ramsey fringe waveform.

The goal of operating with ultrafast optical pulses is to control the electron spin qubit coherently without the generation of the optically excited trion, which will lead to imperfect pulse rotations due to spontaneous emission. As discussed in Chapter 2, application of an external in-plane magnetic field leads to the mixing of the electron spin states with angular momentum spin projection along the growth axis ($\hat{z}$), resulting in the new diagonalized electron states $|\pm\rangle = (|z-\rangle \pm |z+\rangle)/\sqrt{2}$, and trion states $|T\pm\rangle = (|T-\rangle \pm |T+\rangle)/\sqrt{2}$, and linearly-polarized selection rules. Under broadband ultrafast (2 ps) optical excitation for which the pulse bandwidth is considerably broader than the electron spin state splitting, the pulse is considered to drive both the horizontally and vertically polarized transitions, resulting in the following Hamiltonian in the Schrodinger picture (Chapter 2)

$$H_{e-trion} = \begin{pmatrix} -\Delta_e/2 & 0 & \chi_H^* e^{i\omega t} & \chi_V^* e^{i\omega t} \\ 0 & +\Delta_e/2 & \chi_V^* e^{i\omega t} & \chi_H^* e^{i\omega t} \\ \chi_H e^{-i\omega t} & \chi_V e^{-i\omega t} & \omega_0 - \Delta_h/2 & 0 \\ \chi_V e^{-i\omega t} & \chi_H e^{-i\omega t} & 0 & \omega_0 + \Delta_h/2 \end{pmatrix} \tag{7.1}$$

where the rotating wave approximation has already been made, taking the optical pulse field as equal to $\vec{E} = \frac{1}{2}\left[(E_x(t)\hat{x} + E_y(t)\hat{y})\, e^{-i\omega t} + c.c.\right]$, and the Rabi frequencies are equal to $\chi_H = \mu E_x/\sqrt{2}\hbar, \chi_V = i\mu E_y/\sqrt{2}\hbar$, with $\mu = \langle T-|\,|\hat{\mu}|\,|x-\rangle$ being the reduced matrix element of the dipole moment (Chapter 2); the Hamiltonian basis has the ordering $\{|-\rangle, |+\rangle, |T-\rangle, |T+\rangle\}$. This Hamiltonian can be treated more conveniently using the field interaction picture, since a field with only one central frequency (although broadband, as incorporated into the envelope function $E_{x/y}(t)$) is operating on the system: the amplitude coefficients are first transformed with a unitary matrix:

$$\begin{aligned} \vec{a} &= \hat{U}\vec{c}, \\ \hat{U} &= diag\{1, 1, e^{-i\omega t}, e^{-i\omega t}\} \end{aligned} \tag{7.2}$$

Then, the amplitude vector $\vec{a}$ in the Schrodinger equation is replaced with the transformed amplitudes, resulting in the new transformed Schrodinger equation in the field interaction picture:

$$\begin{aligned} i\hbar\frac{d}{dt}\vec{a} &= \hat{H}\vec{a} \\ \rightarrow i\hbar\frac{d}{dt}(\hat{U}\vec{c}) &= i\hbar\left[(\frac{d}{dt}\hat{U})\vec{c} + \hat{U}(\frac{d}{dt}\vec{c})\right] = \hat{H}\hat{U}\vec{c} \\ \rightarrow i\hbar\frac{d}{dt}\vec{c} &= (\hat{U}^\dagger\hat{H}\hat{U} - i\hbar\hat{U}^\dagger(\frac{d}{dt}\hat{U}))\vec{c} \end{aligned} \tag{7.3}$$

where the matrix on the right-hand side of the last line is the newly transformed Hamiltonian. This newly transformed Hamiltonian is equal to

$$H_{FIP} = \begin{pmatrix} -\Delta_e/2 & 0 & \chi_H^* & \chi_V^* \\ 0 & +\Delta_e/2 & \chi_V^* & \chi_H^* \\ \chi_H & \chi_V & \delta - \Delta_h/2 & 0 \\ \chi_V & \chi_H & 0 & \delta + \Delta_h/2 \end{pmatrix} \tag{7.4}$$

where $\delta = \omega_0 - \omega$, thereby eliminating the fast oscillations at the optical frequency. The evolution of the electron-trion system under ultrafast pulsed excitation can now be examined. The pulse width (2-3 ps) is a very small fraction of the spontaneous decay time of the trion (∼500 ps), and therefore effects due to spontaneous emission during the pulsed excitation will be neglected. The goal is to determine the electron spin state amplitude coefficients c_+, c_- after the pulse interacts with the system. This calculation proceeds via adiabatic elimination of the trion [61, 87], assuming that the excited state population is very small compared to other parameters in the calculation, explained below.

First, the equations of motion for the excited states are written out explicitly

$$\begin{aligned} \dot{c}_{T-} &= -i\chi_H c_- - i\chi_V c_+ - i(\delta - \Delta_h/2)c_{T-} \\ \dot{c}_{T+} &= -i\chi_V c_- - i\chi_H c_+ - i(\delta + \Delta_h/2)c_{T+} \end{aligned} \tag{7.5}$$

where explicit time dependences of the amplitudes have been dropped for neatness. Then, a temporary substitution is made for the sake of integration by parts in the next step:

$$\begin{aligned} c_{T-} &= \tilde{c}_{T-} e^{-i(\delta - \Delta_h/2)t} \\ c_{T+} &= \tilde{c}_{T+} e^{-i(\delta + \Delta_h/2)t} \end{aligned} \tag{7.6}$$

Resulting in the following equations of motion in which the derivatives of the excited state amplitudes have been written only in terms of the ground state amplitudes:

$$\begin{aligned}\dot{\tilde{c}}_{T-} &= -ie^{i(\delta-\Delta_h/2)t}(\chi_H c_- + \chi_V c_+) \\ \dot{\tilde{c}}_{T+} &= -ie^{i(\delta+\Delta_h/2)t}(\chi_V c_- + \chi_H c_+)\end{aligned} \tag{7.7}$$

One can perform integration by parts to solve the equations of motion for the excited state amplitudes, resulting in

$$\begin{aligned}\tilde{c}_{T-} &= \frac{-1}{\delta-\Delta_h/2}(\chi_H c_- + \chi_V c_+)e^{i(\delta-\Delta_h/2)t} - i\int e^{i(\delta-\Delta_h/2)t}\frac{d}{dt}(\chi_H c_- + \chi_V c_+)dt \\ \tilde{c}_{T+} &= \frac{-1}{\delta+\Delta_h/2}(\chi_V c_- + \chi_H c_+)e^{i(\delta+\Delta_h/2)t} - i\int e^{i(\delta+\Delta_h/2)t}\frac{d}{dt}(\chi_V c_- + \chi_H c_+)dt\end{aligned} \tag{7.8}$$

At this point, the adiabatic approximation is made. First, it is assumed that the pulse detuning is considerably larger than both the electron and hole splittings, or that $\delta >> \Delta_h, \Delta_e$; physically this ensures that the detuning of the pulse relative to the H and V transitions is approximately equal. Next the derivative of the pulse envelope function and the ground state amplitudes are considered small compared to the pulse detuning, or that

$$\begin{aligned}\frac{d}{dt}\left(\frac{(\chi_H c_- + \chi_V c_+)}{\delta}\right) &<< (\chi_H c_- + \chi_V c_+) \\ \frac{d}{dt}\left(\frac{(\chi_V c_- + \chi_H c_+)}{\delta}\right) &<< (\chi_V c_- + \chi_H c_+)\end{aligned} \tag{7.9}$$

Thus, the integral term in both excited state amplitudes is small compared to the first term. The trion state amplitudes have now been expressed entirely in terms of the electron spin state amplitudes. The result above can now be plugged into the remaining equations of motion for the electron spin state amplitudes, and an effective two-level Hamiltonian can be derived that no longer involves the trion states; thus, the trion has been adiabatically eliminated. The resulting effective Hamiltonian is given by

$$H_{spin} = \begin{pmatrix} -\Delta_e/2 - \chi^2\left(\frac{\delta+\frac{\Delta_h}{2}\cos 2\theta}{\delta^2-\Delta_h^2/4}\right) & 0 \\ 0 & +\Delta_e/2 - \chi^2\left(\frac{\delta-\frac{\Delta_h}{2}\cos 2\theta}{\delta^2-\Delta_h^2/4}\right) \end{pmatrix} + \begin{pmatrix} 0 & \frac{-2\chi^2\cos\theta\sin\theta}{\delta^2+\Delta_h^2/4}\left(\delta\sin\phi + i\frac{\Delta_h}{2}\cos\phi\right) \\ \frac{-2\chi^2\cos\theta\sin\theta}{\delta^2+\Delta_h^2/4}\left(\delta\sin\phi - i\frac{\Delta_h}{2}\cos\phi\right) & 0 \end{pmatrix} \tag{7.10}$$

where the electric field has been written with arbitrary polarization: $\chi_H = \chi\cos\theta$,$\chi_V = i\chi\sin\theta e^{i\phi}$. There are a few important features to note about the resulting effective Hamiltonian. The first Hamiltonian which only includes diagonal terms consists of the electron spin splitting, as well as a light shift term. When the pulse is polarized such that both H and V transitions are driven equally, the $\cos 2\theta$ term goes to zero, and both the $|+\rangle$ and $|-\rangle$ states are shifted in the same direction and the effect is not measured on the electron spin after the pulse is completed. However, when the pulse polarization is not set perfectly to drive both polarization equally, whether due to experimental error or intrinsic HHLH mixing in the QD, a new energy level splitting develops between the two electron spin states; this splitting may contribute to an additional coherent phase imparted on to the electron spin wavefunction. In the second matrix, only off-diagonal coupling terms are written. These terms are maximized when $\theta = (2n+1)\frac{\pi}{2}$, or that the electric field coupling to both the H and V transitions is equal. However, when ϕ deviates from $(2n+1)\frac{\pi}{2}$, or the pulse is not perfectly circular polarized, the term proportional to the hole splitting introduces an additional rotation phase that may lead to imperfect pulse rotations. Nevertheless, even in the presence of imperfect polarization, both the light shift term on the diagonal and the additional coupling term are proportional to the heavy-hole splitting, which is considerably small than the pulse detuning δ.

More importantly, the term that is proportional to δ is the coherent rotation term

which can be used to impart a phase between the two electron spin states, which is hereby referred to as the *two-photon detuned Raman rotation pulse*. In the limit of large pulse detuning compared to the hole splitting and perfect circular polarization, the total effective Hamiltonian is of the form

$$H_{spin} = \begin{pmatrix} -\Delta_e/2 & -\frac{\chi^2}{\delta} \\ -\frac{\chi^2}{\delta} & +\Delta_e/2 \end{pmatrix} \tag{7.11}$$

Simply put, the adiabatic approximation leads to a coherent coupling between the electron spin states, allowing for the optical imparting of a coherent superposition state without exciting significant trion population. If the pulse is short compared to the electron spin precession time, then it has been shown that [61, 87] the pulse generates a rotation of the electron spin qubit given by

$$\hat{R}(\alpha) = \hbar \begin{pmatrix} \cos\alpha/2 & i\sin\alpha/2 \\ i\sin\alpha/2 & \cos\alpha/2 \end{pmatrix} \tag{7.12}$$

where α is equal to the integral of the effective Rabi frequency, or the pulse area. When the pulse area is equal to $\pi/2$, a pure initial electron state $|\psi_e\rangle = |-\rangle$ prepared by optical spin pumping is rotated to the state $|\psi_e^{after}\rangle = \frac{1}{\sqrt{2}}(|-\rangle + i\,|+\rangle)$, an equal superposition state of the two electron spin eigenstates. This pulse will be utilized to generate the Ramsey fringe sequence which may be used to measure the electron spin dephasing time T_2^*. When the pulse area is equal to π, the amplitude coefficients of the eigenstates are switched, ie. $c_-\,|-\rangle + c_+\,|+\rangle \rightarrow i(c_+\,|-\rangle + c_-\,|+\rangle)$. This pulse is utilized for the more complicated spin echo sequence, which eliminates the contribution of inhomogeneous broadening to the fringe decay, revealing the intrinsic transverse decay time T_2 [227].

The $\pi/2$ pulses derived above may be utilized for the Ramsey fringe sequence, which is a commonly used technique in the NMR community used to measure level

splittings and decoherence times of two-level systems [23]. The novelty of the Ramsey fringe technique in this system is that electron spin rotations may be generated optically on much faster timescales than achievable using microwave pulses that directly manipulate the electron spin via time-dependent magnetic fields, which requires the incorporation of complex microwave striplines or waveguides [**?**]. Another advantage in the QD system is that the electron spin may be prepared with very high fidelity of at least 95% [58]; pure state preparation leads to considerably higher SNR in the Ramsey fringe signal as will be shown below, and is difficult to achieve in a typical NMR experiment [23].

The Ramsey sequence proceeds as follows: first, the electron spin state is prepared in a pure state (or as close as possible due to imperfections in optical pumping due to off-resonant coupling and electron spin relaxation, see Chapter 3). For the sake of the calculation, it is assumed that the electron spin state after preparation is in a general superposition state $|\psi_e\rangle = c_- |-\rangle + c_+ |+\rangle$, which may have been prepared using coherent population trapping (CPT) pumping. After preparation, a $\pi/2$ rotation pulse interacts with the electron; if the spin was prepared in a pure state, the population is converted to a coherence. This coherence then precesses at the electron spin frequency [61], which is determined both by the external magnetic field as well as the OH field. After some time t_{12}, another $\pi/2$ pulse converts the coherence into a population which may be measured using the scattered counts from the next probe pulse. In NMR experiments and Ramsey fringe experiments performed on two-level systems with an optically-excited state, this second pulse is not required: the precession may be measured directly using pick-up coils or by measuring fluorescence. However, it is most convenient to measure the electron spin state using one of the trion transitions here.

The electron spin wavefunction at the end of the sequence may be determined using the rotation operator and the magnetic field precession operator:

$$
\begin{aligned}
|\psi_e^{after}\rangle &= \begin{bmatrix} 1 & i \\ i & 1 \end{bmatrix} \begin{bmatrix} e^{i\theta/2} & 0 \\ 0 & e^{-i\theta/2} \end{bmatrix} \begin{bmatrix} 1 & i \\ i & 1 \end{bmatrix} \begin{bmatrix} c_- \\ c_+ \end{bmatrix} \\
&= \frac{1}{2} \begin{bmatrix} (c_- + ic_+)e^{i\theta/2} - (c_- - ic_+)e^{-i\theta/2} \\ i(c_- + ic_+)e^{i\theta/2} + i(c_- - ic_+)e^{-i\theta/2} \end{bmatrix}
\end{aligned}
\tag{7.13}
$$

where $\theta = \Delta_e t_{12}$. The waiting time between the last rotation pulse and the beginning of the next experimental shot does not affect a population measurement of the $|-\rangle$ or $|+\rangle$ with the optical pumping/probe pulse, since the magnetic field precession phase accumulates on each amplitude coefficient separately and does not cause mixing. Measuring, for example, the $|-\rangle$ state, the probe scattering signal is proportional to

$$
|\langle -|\psi_e^{after}\rangle|^2 = 2\left[|c_-^2|\sin^2\frac{\theta}{2} + |c_+^2|\cos^2\frac{\theta}{2} + c_-c_+^*\sin\frac{\theta}{2}\cos\frac{\theta}{2} + c_-^*c_+\sin\frac{\theta}{2}\cos\frac{\theta}{2}\right] \tag{7.14}
$$

There are two limiting cases for the form of this signal: the pure state initialization case and the mixed state. For the mixed state case, the full statistical density matrix approach is not used; instead, it is assumed that at the beginning of the experiment the electron wavefunction is in the state $|\psi_e\rangle = \frac{1}{\sqrt{2}}(|-\rangle + e^{i\phi}|+\rangle)$, and that this phase fluctuates randomly over every shot of the experiment. Thus, in the "mixed state" case, the signal is equal to

$$
|\langle -|\psi_e^{mixed}\rangle|^2 = 2\left[1 + (e^{i\phi} + e^{-i\phi})\sin\frac{\theta}{2}\cos\frac{\theta}{2}\right] \to 2 \tag{7.15}
$$

where the last step is due to averaging over the random phase fluctuation. Thus, no Ramsey fringe signal is observed when the electron spin state is not initialized. Many NMR experiments rely on a small amount of spin population difference present

at a given temperature given by the Boltzmann distribution.

In the case of pure state initialization to the $|-\rangle$ state, the signal is given by

$$|\langle -|\psi_e^{pure}\rangle|^2 = 2\sin^2\frac{\theta}{2} = 1-\cos(\Delta_e t_{12}) \tag{7.16}$$

Thus, the Ramsey fringe, in the absence of any dephasing and spin relaxation, oscillates at the electron spin frequency as a function of the $\pi/2$-t_{12}-$\pi/2$ delay time, allowing for direct measurement of the electron spin splitting using detuned two-photon Raman pulses, and the SNR is enhanced considerably due to the high pure state initialization fidelity in the QD electron system.

The Ramsey fringe technique is not only used to measure electron spin splittings, but also to measure spin decoherence times [149]. The underlying decoherence mechanisms of the QD electron spin system are, of course, a rich topic of study. One regime of noise fluctuations are investigated here, the *quasi-static* fluctuation regime [89]. It was shown in the seminal work of Merkulov, Efros and Rosen [89] that, assuming the hyperfine interaction between the electron and nuclear spins cause fluctuations in the electron spin splitting, the decoherence and relaxation are determined by three processes: precession of the electron in the OH field of "frozen" fluctuations in the nuclear spin polarization, the precession of the nuclear spins in the Knight field generated by the electron spin, and dipole-dipole coupling between neighboring nuclear spins. The fastest of these mechanisms is the first one, the precession of the electron in the fluctuations of the OH field fluctuations, and will be examined here.

When the electron interacts with the nuclear spin ensemble constituents of the QD, the electron experiences a randomly fluctuating OH field, even in the absence of a net nuclear spin polarization. Absent any optical orientation mechanisms, the distribution of the magnitude and direction of the OH field are given by [89]

$$W(\vec{B}_N) = \frac{1}{\pi^{3/2}\Delta_B^3}\exp\left[-\frac{\vec{B}_N^2}{\Delta_B^2}\right]$$
$$\Delta_B^2 = \frac{2}{3}\sum I_j(I_j+1)a_j^2 \tag{7.17}$$
$$a_j = \frac{\nu_0}{\mu_B g_e}A_j|\psi_e(R_j)|^2$$

where ν_0, μ_B, g_e, A_j are the unit cell volume, Bohr magneton, electron g-factor, and hyperfine constant for the j-th nucleus, respectively. Thus, the OH field points isotropically in all directions with a variance given by Δ_B^2, which depends on the hyperfine coupling strength of the electron and nuclei. The OH field variation is typically measured to be between 15 and 45 mT, and varies due to QD size [63, 85, 149]. However, the distribution written above is simply a probability distribution of the OH field averaged over infinite time; there are no considerations of timescales over which the nuclear spin polarization fluctuates. This OH field fluctuation timescale is determined by the local dipole-dipole interactions between nuclear spins, with timescales posited to be around 100 μs in the QD system [89]; nuclear spin coherence times were recently measured using ODNMR experiments to be equal to 1.18 ms for ^{71}Ga and 4.27 ms for ^{75}As in a strained InGaAS/GaAs QD [167]. Thus, it is asserted here that, in the absence of other depolarizing/polarizing mechanisms such as optical polarization, the electron spin experiences a frozen OH field that varies on timescales between 100 μs and 5 ms.

This regime is referred to as the quasi-static fluctuation regime here; a large number of experimental shots ($\sim$ 1 ms/13 ns $\sim$ 77,000) are acquired before the OH field is expected to fluctuate. These slow fluctuations may in fact be observed directly in QDs without the need for the use of time-averaged experiments; measured photon count rates have easily exceeded 10 MHz (100 ns period), allowing for direct monitoring of the QD scattering counts which may be correlated with nuclear spin fluctuations [91,148]. However, the Ramsey fringe technique described in this chapter is averaged over timescales (2-5 seconds) longer than the expected OH field fluctuation time.

To determine the expected Ramsey fringe signal in the presence of these quasi-

static OH field fluctuations, it is assumed that the OH field is fixed over the course of most shots of an experiment. This is a reasonable assumption, considering the repetition period of the experiment is 12.70 ns. Thus, one can average the Ramsey fringe signal over the OH field distribution given by Equation 7.17, assuming that only the OH field fluctuations along the external magnetic field contribute to the dephasing of the electron spin coherence, and that the OH field does not cause a large enough fluctuation in the electron spin splitting to move the electron-trion transition out of resonance with the probe,

$$\text{Ramsey} = \int \left(1 - \cos(\Delta_e t)\right) W(\Delta_e) d\Delta_e \tag{7.18}$$

The constant term in the integral is ignored, and the electron spin splitting is expressed in terms of the OH field

$$\text{Ramsey} = \frac{1}{\pi^{3/2}\Delta_B^3} \int_{-\infty}^{+\infty} \cos\left(\Delta_e^{ext} t + \frac{\mu_B g_e B_{OH}}{\hbar} t\right) \exp\left[-\frac{B_{OH}^2}{\Delta_B^2}\right] dB_{OH} \tag{7.19}$$

Using the trig identity $\cos(\alpha+\beta) = \cos(\alpha)\cos(\beta) - \sin(\alpha)\sin(\beta)$, the cosine term is split up and the sine term can be shown to go to zero, being an odd function integrated from $-\infty$ to $+\infty$. The remaining integral is evaluated as follows

$$\begin{aligned} \text{Ramsey} &= \frac{1}{\pi^{3/2}\Delta_B^3} \cos\left(\Delta_e^{ext} t\right) \int_{-\infty}^{+\infty} \cos\left(\frac{\mu_B g_e B_{OH}}{\hbar} t\right) \exp\left[-\frac{B_{OH}^2}{\Delta_B^2}\right] dB_{OH} \\ &= \frac{1}{\pi\Delta_B^2} \cos\left(\Delta_e^{ext} t\right) \exp\left[-(\frac{\mu_B g_e \Delta_B}{2\hbar})^2 t^2\right] \\ &= \frac{1}{\pi\Delta_B^2} \cos\left(\Delta_e^{ext} t\right) \exp\left[-(\frac{t}{T_2^*})^2\right] \end{aligned} \tag{7.20}$$

where $T_2^* = 2\hbar/(\mu_B g_e \Delta_B)$. Thus, it has been shown that in the presence of quasi-static fluctuations of the electron spin splitting due to OH field fluctuations on timescales considerably longer than the experimental repetition period that the Ramsey fringe signal oscillates at the central electron spin frequency and has a Gaus-

sian amplitude decay, resulting in a measured T_2^* time that depends on the width of the OH field fluctuation distribution. Therefore, the Ramsey fringe technique is useful for measuring inhomogeneous broadening distributions when the fluctuations are assumed to be slow compared to rotation pulse delay times. One study measured Gaussian decay of the Ramsey fringes with a T_2^* time of 1.93 ns, corresponding to an OH field distribution width of 33 mT [149].

Furthermore, the technique can be extended to the spin echo [227], which eliminates the contribution of the "low-frequency" noise to the amplitude decay of the fringes, where the noise is referred to as low-frequency since the correlation time of the fluctuations is long compared to the electron spin manipulation time. The low frequency noise is eliminated by the introduction of a π pulse in the Ramsey fringe sequence: the pulse sequence becomes $\pi/2$-t-π-t-$\pi/2$. A spin echo appears at time 2t (or the $\pi/2$ pulse, in this case) at which time the Bloch vectors (or magnetization vector, in the case of Hahn's spin echo) with varying precession frequencies caused by the low-frequency fluctuations are averaged over a large number of experimental shots, and come back into phase, eliminating the contribution of the low-frequency noise [45, 231]. The intrinsic transverse decay time T_2 of the electron spin qubit is revealed by this experiment. Spin echo experiments performed in the QD electron system demonstrated a QD electron spin T_2 time equal to 2.6 μs [225]. However, these experiments are difficult to perform due to the presence of DNP non-linear effects that distort the Ramsey and spin echo fringes. No effort was made in the aforementioned study to discuss why the fringes observed in that experiment did not exhibit DNP effects. Therefore the question of the electron spin decoherence time in the QD system remained unsettled until explicit efforts were made to eliminate the average electron spin polarization during the course of the experiment, thereby eliminating DNP distortion; a T_2 time of 2.7 μs was measured in those experiments [149].

7.3.2 Ramsey fringe experimental results

The Ramsey fringes described theoretically in the previous section may be ob-

served experimentally in the QD electron-trion system using careful spectral and polarization rejection and time-correlated single-photon counting. The experiment is configured as follows (Figure 7.1). A Ti:Saph mode-locked laser (Coherent MIRA 900) is operated in picosecond mode, producing approximately 2 ps hyperbolic secant pulses at a repetition rate of 78.75 MHz (period of 12.70 ns). The pulses are sent to a Mach-Zehnder interferometer, which is not optically phase stabilized since the Ramsey fringe experiment does not require it. One arm of the interferometer is fixed while the other may be delayed over a pump-probe delay range of 2.4 ns using a Newport delay stage, having doubled the delay range from factory specifications by the introduction of a fixed retroreflector in front of the delay stage (Figure 7.1). For some experiments (proposed spin echo), each arm can be coupled into an EOM amplitude modulator (EOSpace) in order to produce more complex pulse sequences, or the arm before the first beamsplitter may contain an AOM to create a pulse picker. One must be careful about the maximum optical power allowed into the EOMs when coupling picosecond pulses: acceptable average powers for 12.7 ns repetition period from the MIRA is around 10 mW. The pulses are recombined on a 50/50 non-polarizing BS and sent to the cryostat to be combined on a 50/50 non-polarizing BS with the EOM optical pumping/readout pulses.

A reference photodiode signal from the MIRA is amplified and used as the synchronization trigger for the RF pulse generator (Picosecond Pulse Labs 12010), which is used to drive the RF input of the $LiNbO_3$ EOM amplitude modulators. The RF pulse generator is capable of operating with square pulse widths down to 125 ps; the optical pumping pulse width in the Ramsey fringe experiment described here is chosen to be approximately 6 ns to provide significant optical pumping. The EOM contrast ratio between pulse on and off is prone to drift due to temperature fluctuations and optically-generated charge fluctuations since the modulators are being operated outside of their ideal wavelengths (closer to 1.5 μm). This contrast drift is stabilized by picking off a small amount of light from the EOM output and sending it to a PID controller (YYLabs) that locks the drift using the EOM DC bias pins. Over the course of the experiment, the ON-OFF contrast ratio is typically around

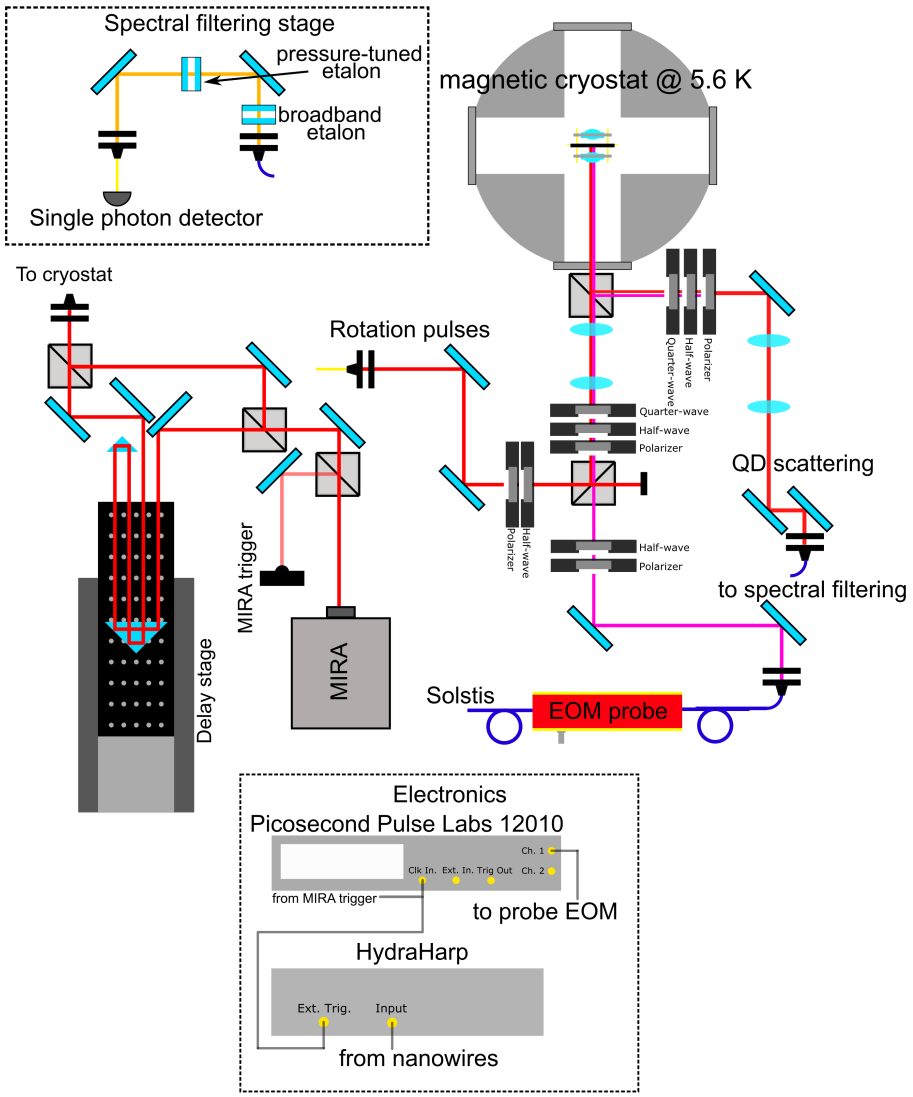

Figure 7.1: Schematic of experimental setup for observing Ramsey fringes in the single QD electron system. Exact details are contained in the text.

200, although this ratio varies from device to device. After the rotation pulses and optical pumping/readout pulses are combined, they are sent through a polarizer, half-wave plate and quarter-wave plate in order to circularly polarize the pulses. They are then transmitted through a 90R/10T BS to the cryostat, and focused down onto the sample by a 0.68 NA aspherical lens.

The reflected pulses and QD scattering are collected through the same lens in reflection, and reflected on the 90R/10T BS. The collected light is then transmitted through a quarter wave plate, half wave plate, and fixed axis nanoparticle-based

polarizer (Thorlabs LPNIR100-MP2). With the MIRA path blocked and the sample bias turned off to eliminate any scattering from the QD, the axes of the analyzer optics described in the previous sentence are adjusted to produce the maximum EOM pulse extinction, as high as 10^6. However, because of the broadband nature of the MIRA pulses, they are not rejected easily by polarization for a number of reasons, including the wavelength birefrigence of the analyzer optics and the cryostat windows. In order to successfully reject both the EOM optical pulse and the MIRA pulses, the remaining light is coupled into a single-mode fiber for mode cleaning, and is out-coupled to a spectral filtering stage. This stage consists first of broadband air-spaced etalon, which has a 37 GHz FWHM and FSR of $\sim$10 nm, providing an additional 35 dB of rejection (3×10^{-4}) of the MIRA pulses. The remaining light is filtered through the pressure-tuned etalon (see Chapter 5) with the transmission resonance held fixed with the probe resonance. The light is then fiber coupled into a single-mode fiber and sent to the single photon detectors (Quantum Opus), processed and time-tagged by time-correlated single-photon counting (TCSPC, HydraHarp 400), which is also synced with the rotation laser using the photodiode sync signal. The HydraHarp 400 is capable of achieving pulse arrival time resolution of 1 ps; typically the TCSPC signal is smoothed over 50 ps, which is approximately equal to the pulse jitter from the single-photon counting nanowire detectors. The signal is additionally processed by background subtraction, which is performed by collecting scattering with the sample bias on and off, and subtracting the scattering in the off case; because the experimental integration times are sometimes required to be rather long (ranging from 500 ms to 10 s per point, depending on the repetition period of the pulse picker), the background subtraction technique is highly susceptible to optical power drift, which must be accounted for carefully using AOM-based noise eaters.

First, the electron-trion level system is verified and the electron and heavy-hole splittings are determined using modulated reflectivity in the co-tunneling region (see Chapter 3 for experimental details). In the absence of trion population excitation via the pulsed excitation, the Ramsey fringe rotation pulse delay dependence should oscillate at the measured electron spin frequency at a given external magnetic field.

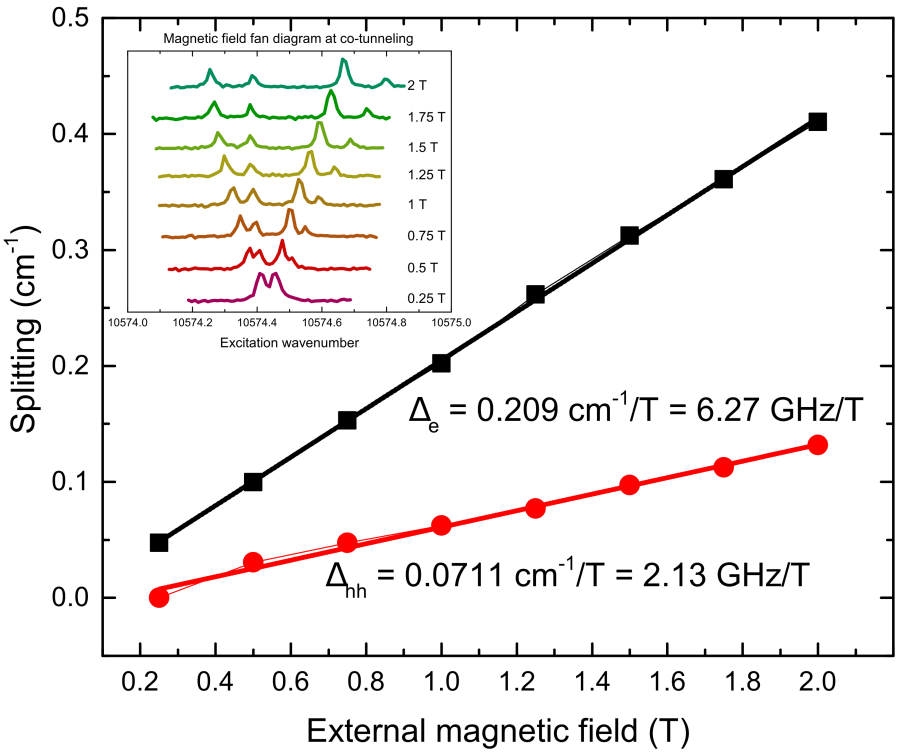

Figure 7.2: Electron and heavy-hole magnetic field splitting. Main figure: electron/heavy-hole splittings are determined at co-tunneling for QD #2 used bias-modulation reflectivity measurements in steps of 250 mT between 0 and 2 T. Inset: Raw probe laser reflectivity scans for each magnetic field. Splittings are plotted in units of wavenumbers (cm^{-1}).

The fan diagram, which measures the trion splittings at increasing magnetic fields, is reproduced in Figure 7.2 for QD #2, which is studied using the Ramsey fringe technique later in this section. The resulting electron and heavy-hole splittings at co-tunneling are equal to 6.27 GHz/T and 2.13 GHz/T, respectively. Recalling Chapter 5 that details the observations of DNP-shifted Raman scattering, the assumption is taken that DNP is minimal at co-tunneling due to rapid electron spin depolarization; the same assumption is made here for this particular QD (QD #2). In fact, less DNP distortion is observed in the modulated reflectivity of this QD (see inset of Figure 7.2) as compared to the QD studied using Raman scattering, implying effective nuclear spin depolarization via co-tunneling.

Once the electron and heavy-hole splittings are determined in co-tunneling, a

typical pulsed experiment is set up first by determining the required rotation pulse (MIRA) power necessary to perform the Ramsey fringe experiment, when the pulse area is equal to $\pi/2$. This pulse power is determined by using a two pulse sequence, one rotation pulse and one EOM probe pulse which is held in resonance with one of the four trion transitions. The rotation pulse power is varied; for each pulse power, a TCSPC time-series is acquired, and the probe pulse scattering is integrated over the entire pulse (Figure 7.3). In order to minimize the amount of trion population generated by the MIRA pulse to satisfy the adiabatic conditions described in Section 7.3.1, the pulses are typically red-detuned by at least 400 GHz relative to the trion transitions. The EOM pulse is delayed by approximately 4 ns from the rotation pulse, at which point a strong scattering signal is observed from the EOM probe at around 5 ns. The signal clearly exhibits strong Rabi oscillations when the Rabi frequency of the EOM probe field is comparable to the spontaneous emission rate of the trion system, leading to coherent oscillations between the driven electron spin state and the trion state under excitation [108]. Additionally, the probe scattering signal decays at the optical pumping rate [58] due to spontaneous emission from the trion down to the non-driven electron spin state. For the purposes of the Ramsey fringe experiment, the electron spin population is not typically pumped completely to the other electron state. The optical pumping rate depends on the optical Rabi frequency of the EOM probe as well as the pulse duration; pulse duty cycles beyond 40% are not typically achievable with the EOM system used in this experiment due to the limitations of the PID drift locking modules. However, this incomplete optical pumping does not affect the measurement of the rotation pulse dependence except to reduce the overall integrated signal count, since the experiment is averaged over many shots and the steady-state integrated counts do not depend on the EOM probe power.

When the rotation pulse area is much smaller than π, the probe scattering is expected to be small, since any residual electron spin population residing in the driven spin state is optically pumped within a few experimental shots. However, when the pulse area is close to π, the electron spin state population is inverted completely; thus, upon the next shot of the experiment, the probe scattering signal is recovered,

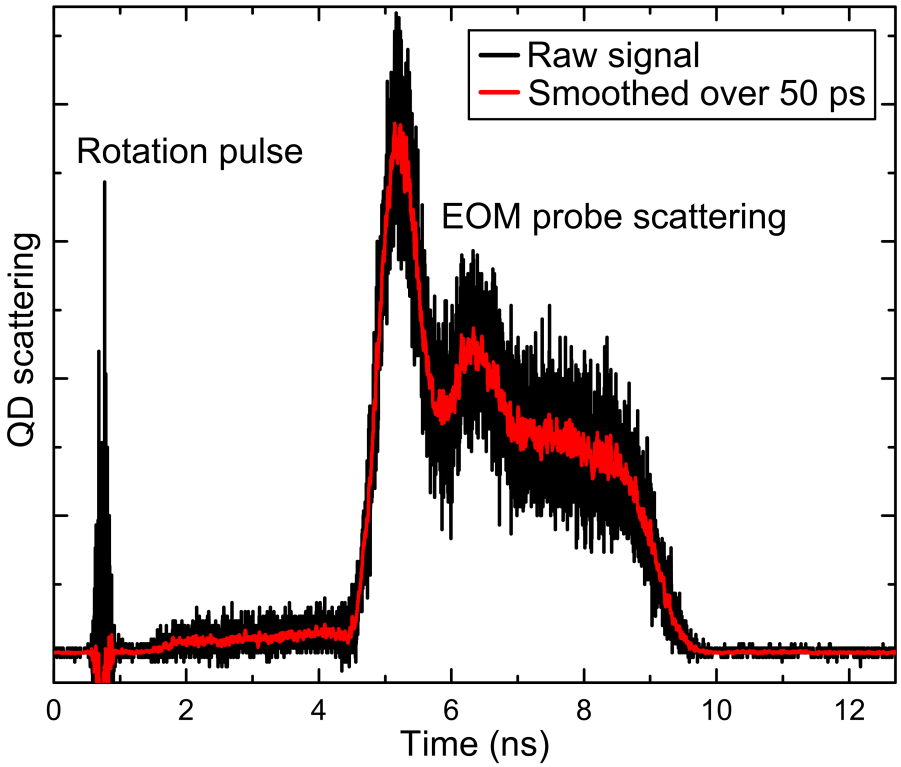

Figure 7.3: Time-correlated single-photon counting series for the rotation pulse power dependence experiment. The scattering from the QD due to the interaction of the QD electron-trion system with the MIRA rotation pulse and EOM probe pulse are time-correlated with synchronization pulses from the MIRA. The resulting signal is background subtracted by ejecting the electron from the QD using the biasing diode structure. The black curve is the raw integrated signal and the red curve is smoothed over 50 ps, or the timing jitter of the nanowire detectors. Clear Rabi oscillations and optical spin pumping are observed when the EOM pulse is turned on from ∼5 to 9 ns.

and the spin state is optically pumped once again. In the rotation pulse power dependence curve, the π pulse therefore corresponds to maximum probe scattering signal. The two plots in Figure 7.4 correspond to the rotation pulse power dependence for two different QDs, demonstrating a power-dependent Rabi oscillation of the probe scattering, which is indicative of coherent control of the electron spin wavefunction. Clear oscillations in the scattering signal are observed; however, the expected 2π pulse does not lead to an apparent full rotation of the electron spin around the optical axis; the contrast is reduced at higher powers. There are a number of possible explanations

for this, including unintentional elliptical polarization of the rotation pulse which would lead to $\chi_H \neq \chi_V$. Another fundamental reason is the presence of heavy-hole light-hole mixing, which also leads to a rotation the polarization selection rules and limits the achievable electron spin rotation fidelity [86]. The integrated probe counts have not been calibrated for this experiment to determine the absolute electron spin rotation [61], but could be established by the introduction of another EOM pumping pulse in place of the MIRA rotation pulse which completely pumps the electron spin population, leading to maximal achievable scattered probe counts.

Since the detuned Raman rotation pulses are acting on the electron spin state rather than the trion state, the effective Rabi frequency for the electron-pulse interaction was shown to be given by (Section 7.3.1) $\chi_{eff} = \chi^2/\delta$. Thus, higher optical excitation powers are required as the pulse detuning becomes larger, and larger pulse detunings are more ideal because less excited state population is generated. The pulse detuning dependence was measured for QD #2, as displayed in Figure 7.5. Both the π and 2π pulses are observed to shift to higher rotation pulse powers as the detuning is increased. Additionally, the contrast between the scattered probe signal increases as the detuning increases, as expected from the decreasing trion population generation. The form of the effective Rabi frequency described above implies that doubling the pulse detuning requires twice the optical pulse power ($\propto \chi^2$); this dependence is not observed in the experiment, implying a significant deviation away from either the adiabatic conditions or considerable polarization/selection rule imperfections. Nevertheless, electron spin population inversion is observed at the maximal probe scattering points; the $\pi/2$ area required for the Ramsey fringe is taken to be half of the optical power that corresponds to the maximum for a given pulse detuning.

The QD sample used in the experiments detailed in this chapter and the Raman scattering chapter incorporated a distributed Bragg reflector (DBR) cavity, differing from other samples typically investigated in this research group. The power-dependent probe scattering dependence discussed and displayed here provides an order-of-magnitude measure for the electric field enhancement factor in the DBR cavity compared to samples that do not incorporate a DBR cavity. One previous

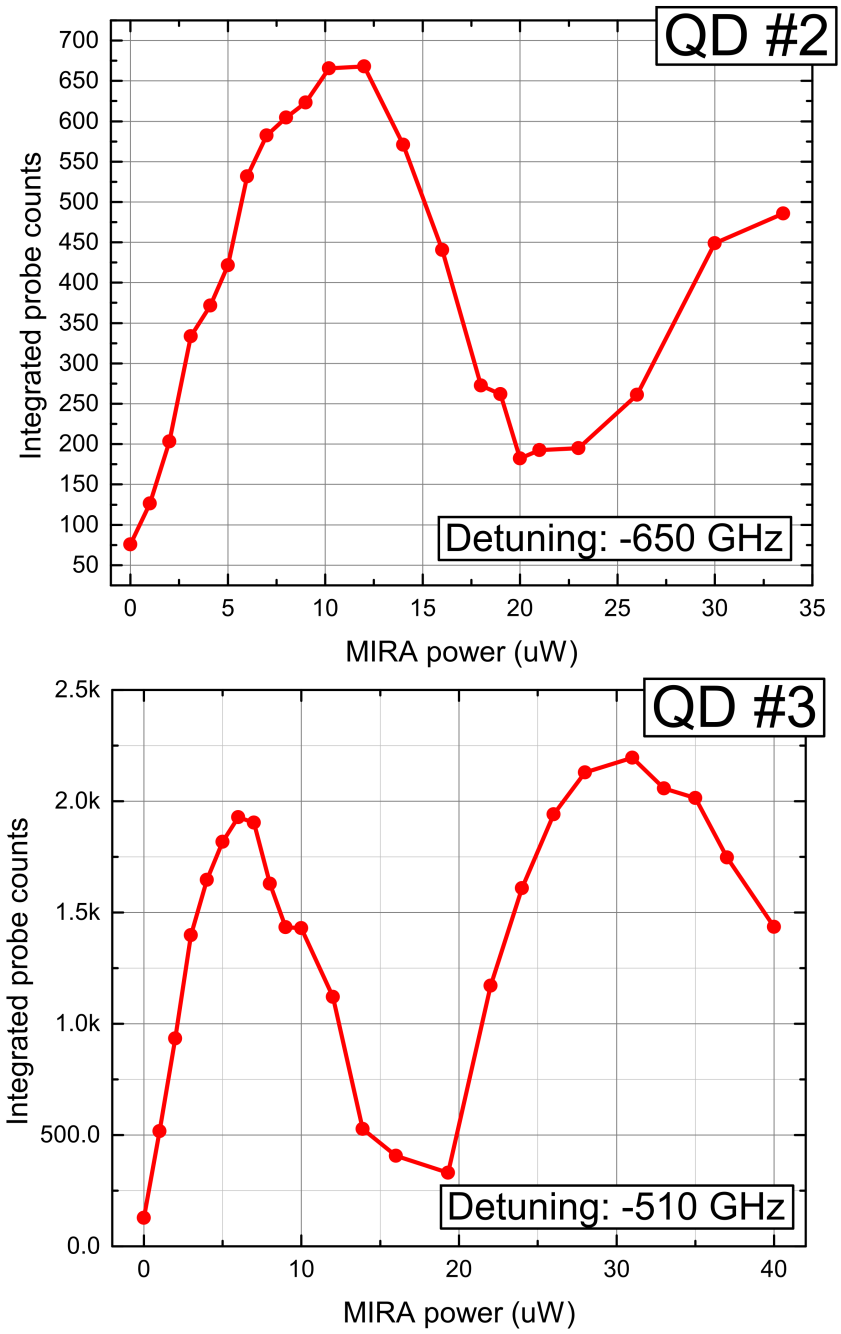

Figure 7.4: QD scattering dependence on the MIRA rotation pulse power. Both top and bottom plots are the QD scattering counts integrated from 4 ns to 10 ns using TCSPC (Figure 7.3) as a function of the MIRA rotation pulse power for two different QDs, and for two different MIRA pulse detunings.

study [232] utilized detuned Raman pulses for the purposes of spin-photon entanglement [124]. In that study, the π pulse power was determined to be 225 μW with

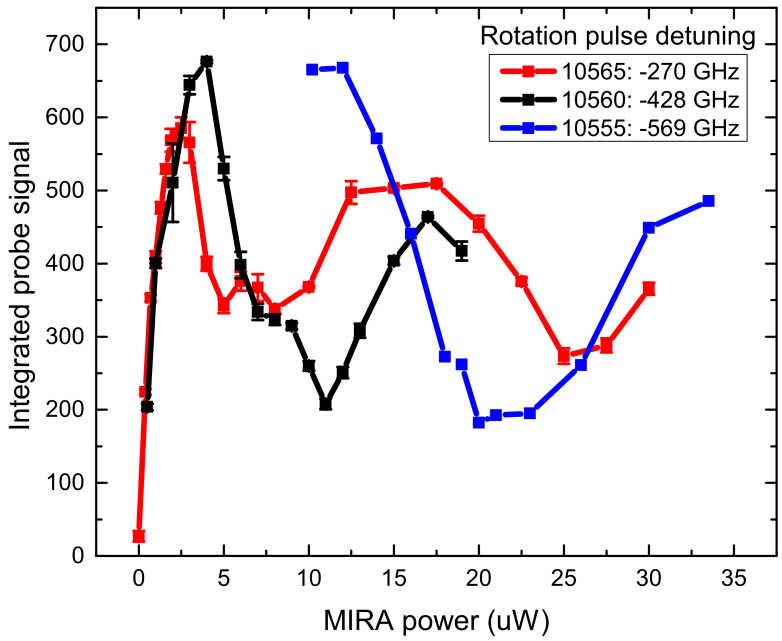

Figure 7.5: QD electron spin rotation dependence on MIRA detuning for QD #2. Red, black and blue curves correspond to MIRA detunings relative to the average electron-trion transition energy equal to -270, -428, and -569 GHz, respectively.

a pulse detuning of -240 GHz, compared to a typical π pulse power in the DBR sample under study here of 11 μW for a detuning of -510 GHz. If the electric field present at the QD in the DBR sample is written as $\alpha E_{in,1}$ where α is the electric field enhancement due to the cavity, then α is given by

$$\alpha = \sqrt{\frac{I_0 \delta_1}{I_1 \delta_0}} = \sqrt{\frac{225 \times 510}{11 \times 240}} = 8.9 \tag{7.21}$$

where I, δ are the incident pulse powers and the pulse detunings. Thus, the DBR cavity provides a considerable enhancement of the input optical power, which can provide very important advantages when rotation pulse power is limited due to losses incurred in the Mach-Zehnder interferometer and pulse picker EOMs.

However, the rotation pulse dependence may change dramatically depending on the morphology of the QD; in another instance of performing the single rotation pulse experiment, the power dependence deviates significantly from the expecting oscillatory power dependence (Figure 7.6). This third QD is the same one as investigated

in the Raman scattering chapter; therefore it is understood that DNP effects are possibly at play. Two experiments are performed: first, a CW probe is used rather than an EOM probe. In this instance, the scattered counts are measured by only integrating the scattered photon counts using the same integration window as used with the 4 ns EOM pulses. The probe scattering is observed to peak at approximately the same power as the previous power dependences, but seems to level off at higher powers before reaching the 2π pulse. Upon switching to the EOM probe scheme, the power is increased from low to high; when the pulse power reaches the peak of the CW scattering dependence, the measurement noise increases considerably and the signal jumps to maximum with a few uW. Upon scanning the power from high to low, the probe scattering response is hysteretic: the signal drops at a lower power (9 uW) in the decreasing power direction and jumps at a higher power (11 uW) in the increasing power direction. This measurement was repeated multiple times in the hysteretic region, hence multiple points measured in Figure 7.6, and the hysteresis is repeatable.

A possible explanation for the hysteretic switching between low and high probe scattering is DNP. Assuming that the optical pumping pulse (probe pulse) nearly completely pumps the electron spin during a single pulse (driving, for instance the $|+\rangle \rightarrow |T+\rangle$ transition), the electron spin remains in the $|-\rangle$ state for some time τ_-, at which point the rotation pulse acts. If the rotation pulse is equal to π, the electron spin polarization is inverted completely and the electron is now in the $|+\rangle$ state, remaining in that state until the next probe pulse for some time τ_+. Thus, the electron spin polarization averaged over the course of the experiment is equal to $(\tau_+ - \tau_-)/(\tau_+ + \tau_- + \tau_{pulse})$ (see Figure 7.7). In this experiment, the probe-rotation pulse delay is fixed, and thus the average electron spin polarization over each shot is affected by the rotation pulse power rather than the delay. The hysteretic region may correspond to the point at which the electron spin polarization crosses from positive to negative, or vice-versa. However, no attempts are made to rigorously model the possible DNP mechanism responsible for this switching in this thesis; in fact, it was shown in the DNP theory (Chapter 4) and Raman scattering (Chapter 5) chapters

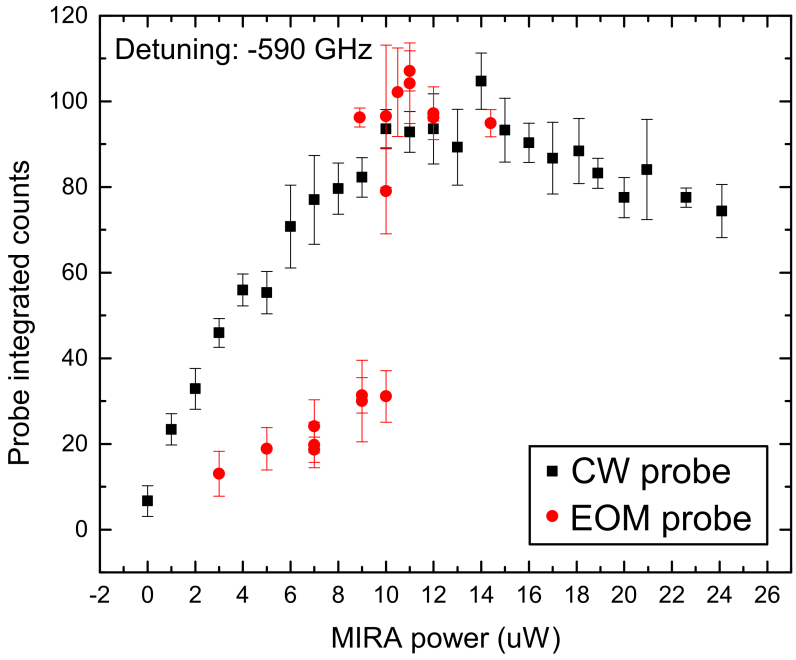

Figure 7.6: Demonstration of DNP-induced switching as a function of MIRA rotation pulse power for QD#2. Black (red) curves indicate integrated QD probe scattering counts for the CW (EOM probe) experiment. In the case of the EOM probe experiment (red curve), multiple points are measured in the range of 7 to 12 μW.

that electron spin polarization-dependent terms are unlikely to be at play in the electron-trion system at high magnetic fields. However, pulsed excitation may play the role of changing the correlation functions due to electron-spin level broadening that is not present in CW excitation [143], (Chapter 5).

The Ramsey fringe experiment is then performed in order to measure the inhomogeneous broadening of the electron spin splitting. The experiment is performed using three pulses: one EOM probe pulse and two rotation pulses with scanning delay time, and individual pulse areas set to $\pi/2$. As explained in section 7.3.1 of this chapter, the EOM pulse initializes the electron spin state to either the $|+\rangle$ or $|-\rangle$ state. Soon after initialization (within 3 ns), the first rotation pulse creates an equal coherent superposition state $|\psi_e\rangle = |+\rangle \pm i\,|-\rangle$ depending on the initialized state of the electron. The phase between the two eigenstates oscillates as a function of waiting time between the first and second rotation pulses at a frequency determined by the electron spin splitting. The second pulse converts the phase to a population, which

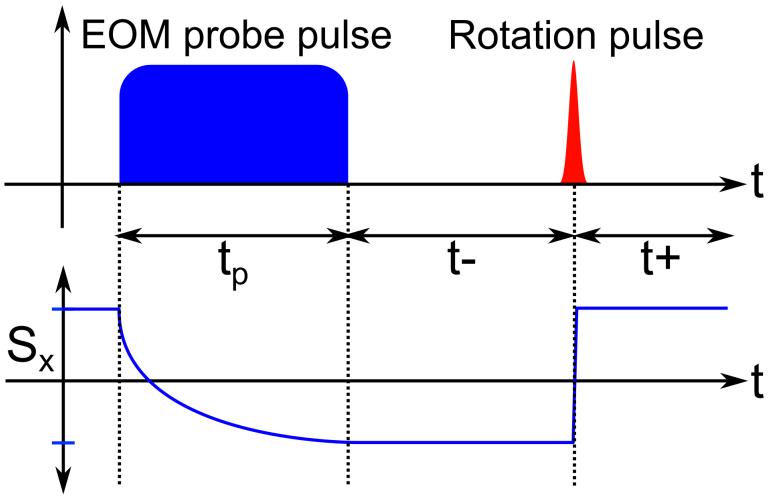

Figure 7.7: Schematic of single MIRA rotation pulse and EOM probe pulse experiment with electron spin polarization time-dependence. Top axis: optical excitation scheme. EOM probe pulse resonantly excites the $|+\rangle \rightarrow |T+\rangle$ transition with duration t_p. During that pulse, the electron spin polarization is pumped from positive to negative, assuming that the pulse duration is long compared to the optical pumping time. The electron spin polarization (bottom curve) remains negative for a time t_- until the rotation pulse (assumed to have pulse area π here) inverts the electron spin polarization, which remains positive until the optical pumping pulse.

is probed during the next experimental shot by the optical pumping/probe pulse.

The first experiment was performed on QD #3 (rotation pulse dependence in bottom plot of Figure 7.4) with an external in-plane magnetic field of 2 T. In one case, the highest energy electron-trion transition $|-\rangle \rightarrow |T-\rangle$ is probed with the EOM (blue curve, Figure 7.8), while in the other case the second lowest energy transition $|+\rangle \rightarrow |T-\rangle$ is probed (red curve, Figure 7.8). In both cases, clearly oscillatory behavior is observed as a function of rotation pulse delay, with an approximate oscillation frequency of 11.2 GHz and 11.9 GHz in the red and blue Zeeman transition cases, respectively. However, in the blue Zeeman case, the probe scattering counts drop off completely after a few periods of oscillation around 400 ps, while in the red Zeeman case the Ramsey fringe oscillations persist but become distorted into a sawtooth-like wave at around the same delay time. This sawtooth form requires the addition of higher harmonic frequencies present in the Fourier transform of the waveform as

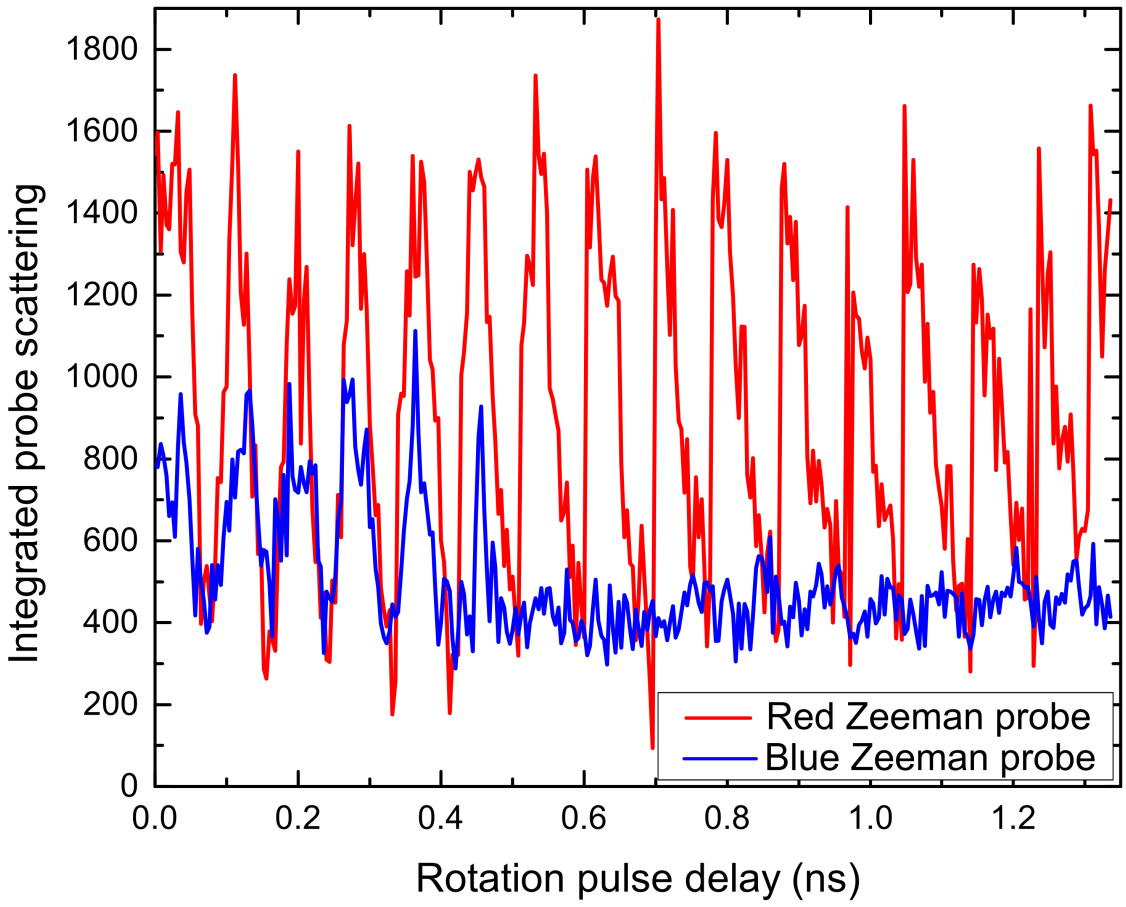

Figure 7.8: Ramsey fringe scans for two different EOM probe configurations. Red (blue) curves correspond to the EOM probe driving the $|+\rangle \rightarrow |T-\rangle$ ($|-\rangle \rightarrow |T-\rangle$) transitions, respectively.

the rotation pulse delay increases. Additionally, the overall signal strength of the red Zeeman case is nearly twice as large. Surprisingly, in the blue Zeeman probe case, the large amplitude of the Ramsey fringes persists for at least 1.3 nanoseconds, implying either relatively long dephasing time of the electron spin qubit or weak quasi-static broadening in this particular case.

The presence of an electron spin-dependent behavior in the Ramsey fringe scan is likely indicative of DNP effects. Recalling back to the Raman DNP chapter (Chapter 5), the non-linearities associated with laser frequency scans depended qualitatively on which electron spin state was optically probed. The same relationship is true for the Ramsey fringe scan, however with an inverted non-linear response: in the case

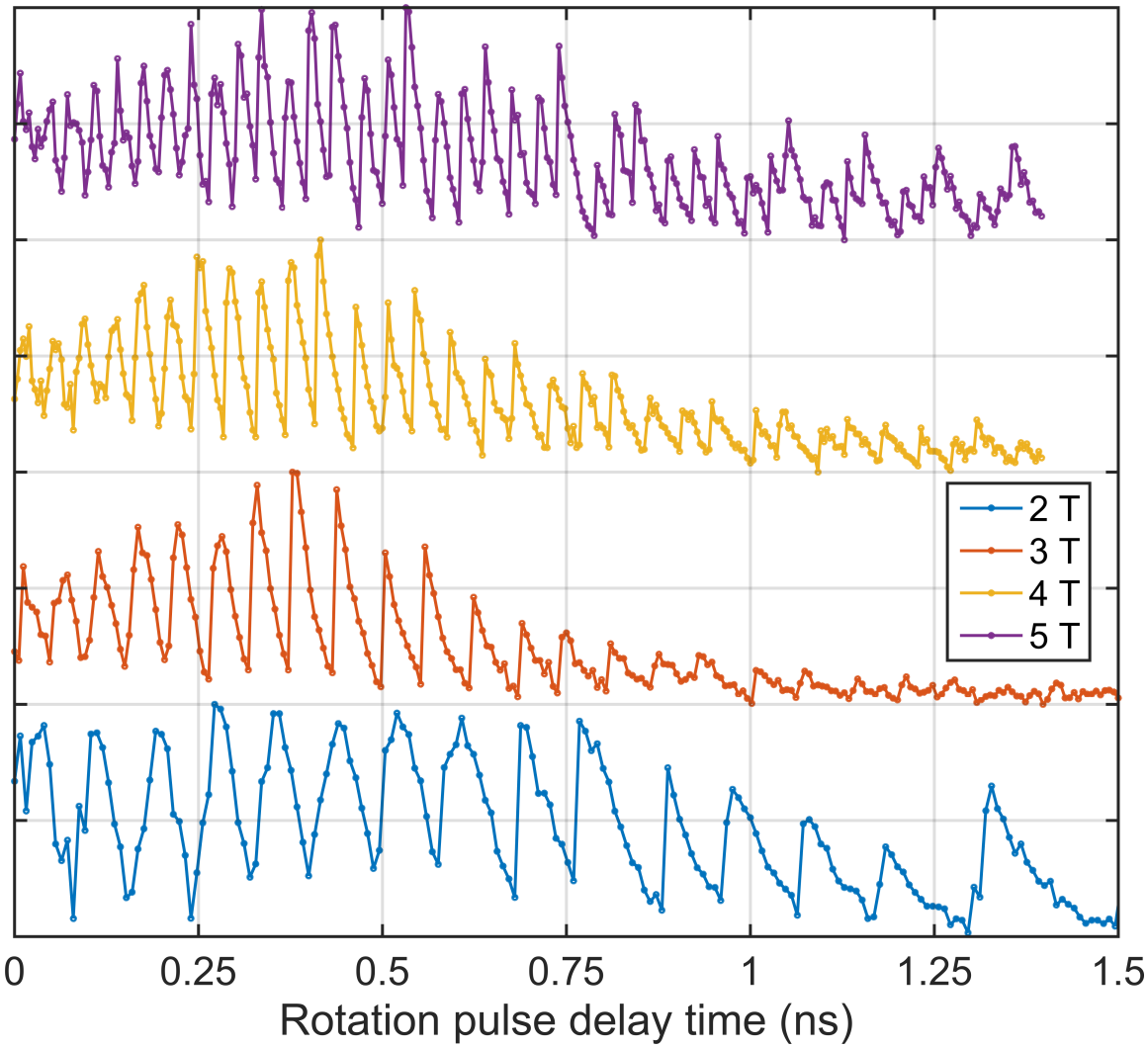

Figure 7.9: Ramsey fringe scans at magnetic fields ranging from 2 T to 5 T for QD #2. The EOM probe is brought into resonance with the $|+\rangle \rightarrow |T+\rangle$ transition after adjusting each magnetic field.

of the Ramsey fringe scan, the red Zeeman case seems to correspond to a relatively stable OH field regime, only acquiring higher frequency harmonics at longer delay times. This is in comparison to the highly unstable case of the blue Zeeman probe, in which the OH field apparently shifts by a magnitude large enough to push the $|-\rangle \rightarrow |T-\rangle$ transition completely out of resonance with the EOM probe. Since the EOM probe laser frequency and the MIRA pulse detuning are fixed for this experiment, the rotation pulse delay clearly has an effect on the nuclear spin polarization present in the QD.

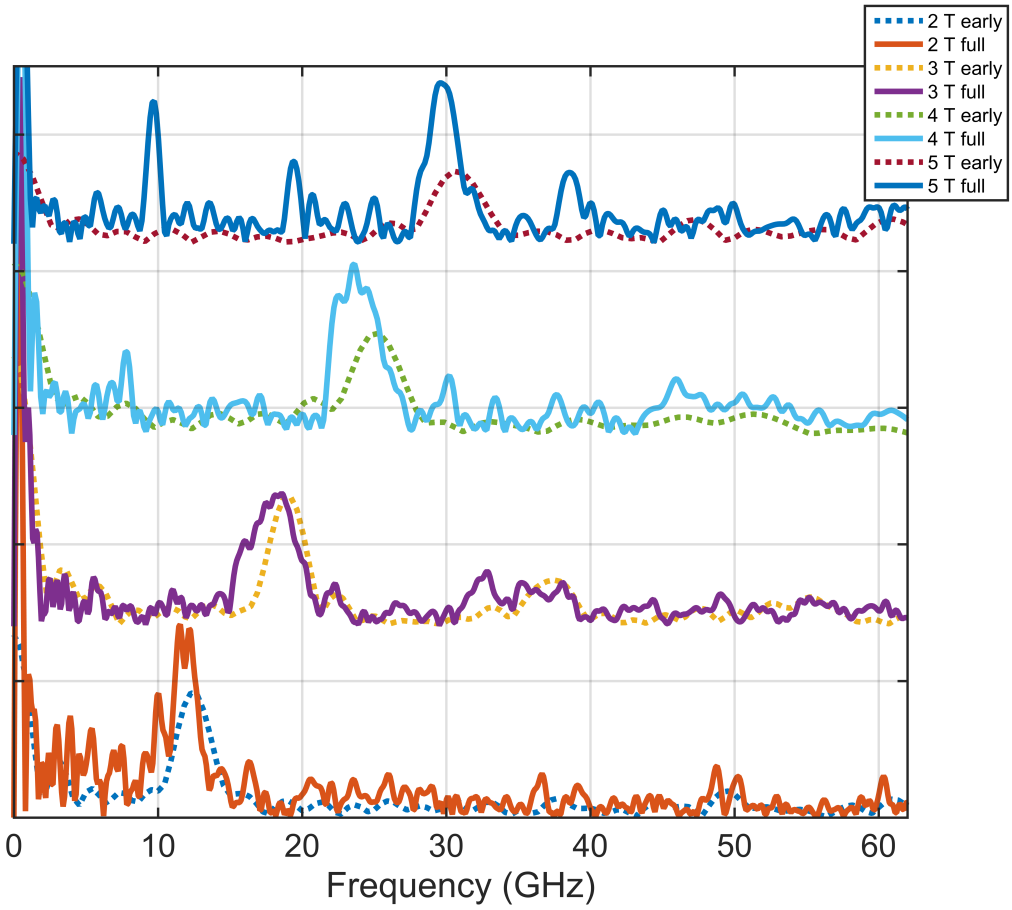

Figure 7.10: Absolute value of Fourier transforms for the Ramsey fringe scans displayed in Figure 7.9. Early (dashed) scans correspond to Fourier transforming the first 22% of a given scan, while full (solid lines) scans are the Fourier transforms of the entire scan.

Another set of Ramsey fringe experiments was performed on QD#2 (magnetic field splitting can be found in Figure 7.2) at external magnetic fields varying from 2 T to 5 T, using EOM probe excitation of the lowest energy red Zeeman transition $|+\rangle \rightarrow |T+\rangle$ (Figure 7.9). Again, Ramsey fringes are observed as a function of rotation pulse delay time, and the oscillation frequency is observed to increase as the magnetic field increases. However, the distortion attributed to DNP is immediately evident in each case of magnetic field. In each case, especially for lower magnetic fields, the amplitude of the Ramsey fringe is relatively constant for times less than 300 ps, and oscillates at what is apparently a single frequency. Once the rotation pulse delay time

exceeds 300 ps, higher harmonic effects start to play a major role in the Ramsey fringe waveform; the rising edge of each fringe is sharp at short times and falls off nearly linearly as the delay time is increased. The higher harmonic frequency components are more pronounced at higher magnetic fields (4 and 5 T). There is apparently a complex dependence of the amplitude decay rate as a function of magnetic field: at 2 T, the amplitude does not begin to decay until around 750 ps, compared to the 3 and 4 T cases which first increase in amplitude around 400 ps and then drop off rapidly by 800 ps.

This analysis can be made more concrete by the usage of a Fourier transform (Figure 7.10). Two Fourier transforms are taken for each Ramsey fringe scan, one for the first 22% of a given scan (dashed lines in Figure 7.10), and the second (solid lines) for the entire scan. The Ramsey fringes are padded with zeros on the end of the scan by a factor of 5 (5 times the length of the experimental data) to interpolate the Fourier transforms. This padding only acts to interpolate without shifting the Fourier transform peaks or broadening/narrowing peaks artificially. It is important to note that the Fourier transform of the Ramsey fringes observed here provide a distribution of electron spin state splittings over the course of the entire scan; at each Ramsey fringe rotation pulse delay time, the electron spin state splitting samples a distribution determined by the OH field distribution *at that point*. Thus, the Fourier transforms in Figure 7.10 should not be interpreted as OH probability distributions but simply as spectral decompositions of the Ramsey fringe waveform.

However, the transition from a regime of relative stability to one in which the non-linearities become more apparent can be illustrated by the short-time and full-time Fourier transforms. In Figure 7.10, the dashed lines indicate the short-time transforms taken over the first 22% of the scan, approximately the portion of the Ramsey fringe scan that is visually determined to lack strong DNP distortion effects. The full Fourier transforms (FT) of the Ramsey fringe scans are plotted in solid lines, and represent the entire spectral power density for the full Ramsey waveform. Immediately apparent are the higher-order harmonics present in the FT spectrum. Instead of a single frequency corresponding to the energy level splitting of a two-

level system which is undistorted by non-linear effects such as DNP, higher-order frequencies appear: in the 2 T scan, there are multiple repeatedly observed peaks around 37 GHz and 50 GHz, and at 5 T there is a higher frequency peak observed at around 38 GHz, along with a lower frequency peak observed around 19 GHz. In the 4 T FT, a weak and broad distribution is observed around 50 GHz, or approximately twice the main peak frequency. The peak centers, for both early time and full time FTs, along with the full-width half-maxima for each peak are extracted and recorded in Table 7.1.

B field (T)	Δ_e (GHz)		FWHM (GHz)		Δ_h(GHz)
	early	full	early	full	full
2	6.25	5.93	1.9	1.72	(N/A)
3	6.39	6.01	3.2	5.42	1.84
4	6.33	5.88	3.25	3.44	1.95
5	6.16	5.9	4.21	2.58	1.95

Table 7.1: Electron and hole splittings, and FWHM for the early and full Fourier transforms (Figure 7.10) of the Ramsey fringes plotted in Figure 7.9. The centers are determined by taking the centroid of a given range of the FT in the vicinity of a given peak.

It is noted that a lower frequency peak becomes apparent at fields greater than or equal to 3 T; the frequency of this peak (Table 7.1, right column) corresponds to the expected hole-splitting (Figure 7.2). Strict satisfaction of the adiabatic condition, perfect linear selection rules and pulse polarization restricts the population of the system to the electron spin states; however, the presence of the hole-splitting in the FT of each Ramsey fringe scan implies a violation of these conditions. Because the rotation pulses are detuned by a considerable amount ($\sim$ -570 GHz) compared to previous reports that did not demonstrate trion generation [232], the adiabatic condition is likely still satisfied; thus it is believed that QD exhibits considerable

HHLH mixing which will result in imperfect phase cancellation in the lambda system leading to excited state population generation. More intuitively, trion coherence, and hence hole coherence, is generated during the imperfect rotation pulse, and the coherence oscillates at the hole splitting frequency. A surprising result is the large weight of the hole frequency at 5 T, possibly contributing to the higher frequency peaks at ∼19 and 38 GHz, which are conspicuously observed at approximately $\Delta_e \pm \Delta_h$.

Another important observation is revealed by comparison of the early and full time FT is that the electron spin splittings, which are determined to be the main resonance frequency divided by the external magnetic field. The results of this comparison are that the early time splittings differ considerably from the full time splitting, on average by 350 MHz. By comparison, the expected electron spin state splitting determined at co-tunneling is equal to 6.27 GHz. Thus, the electron spin state splitting determined using the early FT is closer to the electron splitting in the absence of DNP, assuming that co-tunneling rapidly depolarizes the nuclear spins in this particular QD, as indicated by the lack of DNP dragging in the modulated reflectivity laser frequency scans (Figure 7.2 inset). By comparison, the full-time FT shifts towards a smaller electron spin state splitting, implying that a large and negative OH field approximately equal to -56 mT is generated in the QD as the rotation pulse delay increases, reducing the overall electron splitting. The overall frequency shift of the electron spin state splitting is as large as may be expected under the EOM narrow-band probe scheme: 350 MHz is comparable to the typical QD linewidth of approximately 500 MHz. The DNP cycle effectively turns off when the electron-trion resonance is pushed out of resonance with the EOM probe, but may drift back into resonance due to OH field diffusion at some later time (absolute experimental time, not necessarily rotation pulse delay time), initiating the DNP cycle anew [184].

Furthermore, although no attempts have been made here to fit the FT resonances due to lack of a phenomenological model for an electron spin splitting distribution, the FWHM of each resonance has been determined. The width of the FT resonance is related to the amplitude decay time of the frequency components centered at that

particular distribution, given by the T_2^* time as shown in the previous section. It is observed here that the FWHM of the early-time Ramsey fringe FTs of the main resonance increases with increasing magnetic field, and thus the T_2^* time decreases. However, the full-time FTs are much more complicated, with a relatively narrow distribution at 2 T that approximately matches the early time case, a maximum FWHM appearing at 3 T, and dropping off at higher magnetic fields. However, the simple analysis of the FWHM as a measure of the inhomogeneous dephasing is over-simplified; for instance, at 5 T, the frequency composition of the Ramsey fringe waveform becomes more distributed into harmonics of the electron and hole splittings, which may be considered a dephasing of the electron spin state coherence. If, in fact, the appearance of these peaks is coherent, ie. that it corresponds to a Hamiltonian term which can be accounted for by the electron and hole Zeeman splittings and rotation pulse (including hole spin generation), then it is possible that a more carefully constructed rotation pulse sequence may eliminate this coupling. The utilization of a spin echo experiment [225] would reveal if the broadening of the electron spin splitting is due to quasi-static OH field fluctuations which lead to an averaging of the Ramsey fringe signal over a large number of different experimental shots, or if a more complex non-linear mechanism is at play due to DNP non-linearities [182].

One possible explanation for the onset of DNP non-linearities as a function of rotation pulse delay time is related to the electron spin polarization averaged over a large number of experimental acquisitions. The shortest timescales typically accounted for related to the electron-nuclear coupling are given by the nuclear spin precession time in the external magnetic field, which is around 120 ns/T, taking the average of ^{115}In and ^{75}As gyromagnetic ratios (Chapter 4). Thus, all electron-nuclear timescales are longer than the experimental parameters relevant to the Ramsey fringe experiments demonstrated here, especially the rotation pulse delays which are shorter than the repetition period of the experiment (12.70 ns). Therefore, explanations of the DNP phenomena observed here must involve a rotation pulse delay-dependent quantity that remains constant over multiple shots of the experiment such as the average electron spin polarization. Building off of the discussion used to explain the

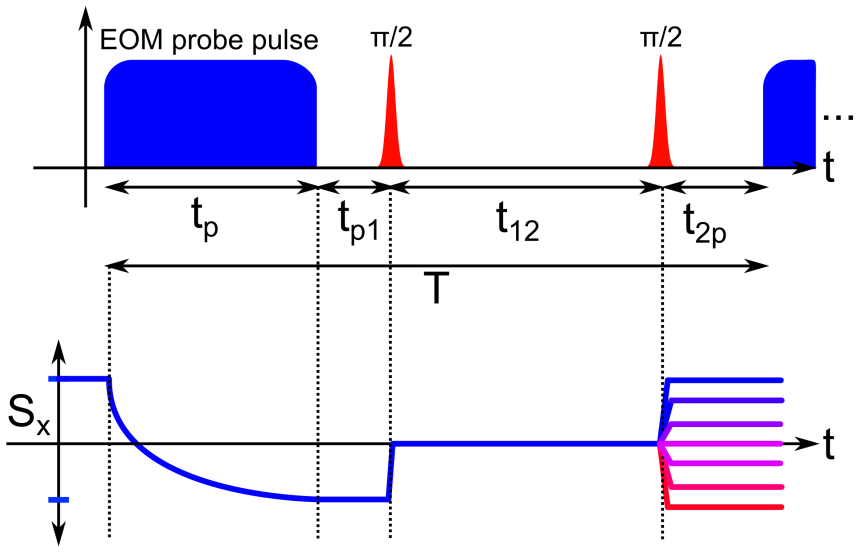

Figure 7.11: Schematic illustration of electron spin polarization build-up during the Ramsey fringe experiment. Top axis illustrates the optical pulse scheme, including the EOM probe pulse indicated in blue, and the rotation pulses in red, separated by the rotation pulse delay time t_{12}. The bottom axis illustrates how the electron spin polarization along the external magnetic field direction $\langle S_x \rangle$ changes over the course of a single shot of the experiment. At time $t_p + t_{p1} + t_{12}$, the resulting electron spin polarization depends on the waiting time t_{12}.

switching effect displayed in Figure 7.6, the electron spin polarization generated during the Ramsey fringe experiment is examined here (Figure 7.11). First, the EOM pulse, which is driving the $|+\rangle \rightarrow |T+\rangle$ transition, pumps the electron spin to $|-\rangle$ within a few nanoseconds. There are two possible ways to treat this optical pumping appoximately: if the pumping time is short compared to T, the experiment repetition period, then the optical pumping contribution to the average electron spin polarization is negligible. Otherwise, if the pulse is both strong and long compared to the pumping time, the electron spin polarization contribution is $-t_p/T$. After some short wait time t_{p1}, the $\pi/2$ pulse rotates the electron spin polarization; if the rotation pulse is perfect, the electron spin state is in a coherent superposition of the two spin states, leading to $\langle S_x \rangle = 0$. Thus, over the rotation pulse delay time t_{12}, the electron spin polarization is zero. After this wait time, the second $\pi/2$ pulse rotates the coherence into a population, which (as explained in Section 7.3.1) oscillates as the

electron spin splitting with respect to t_{12}, not in actual time; the electron spin polarization immediately after the pulse, absent any dephasing mechanisms, is equal to $\rho_{++} - \rho_{--} = \cos(\Delta_e t_{12})$. Thus, the electron spin polarization contribution for the t_{2p} period between the second rotation pulse and the next optical pumping pulse is equal to $\cos(\Delta_e t_{12}) t_{2p}/T$. All together, assuming that $t_{p1} << T$ (or that the time between the end of the initialization pulse and the first rotation pulse is short compared to the repetition period), the averaged electron spin polarization over a single shot of the experiment is equal to

$$\langle S_x \rangle = \frac{-t_p + t_{2p}\cos(\Delta_e t_{12})}{T} \sim \frac{-t_p}{T} + (1 - \frac{t_p}{T} - \frac{t_{12}}{T})\cos(\Delta_e t_{12}) \tag{7.22}$$

This average electron spin polarization, which is asserted to be the effective value that the nuclear spin ensemble interacts with, oscillates at the electron spin splitting with respect to the pulse rotation delay time t_{12}. The first term due to the EOM probe pulse time contributes an overall offset to the electron spin polarization, which is a major contribution when the pumping time is on the order of the repetition period; if the pumping time exceeds T/2, there will be no zero-crossings in the electron spin polarization. It is asserted here that DNP non-linearities may occur as a function of the pulse delay time when the electron spin polarization crosses over from positive to negative, or vice-versa. The electron spin polarization is plotted in Figure 7.12 for both 1 ns and 5 ns EOM probe pulse lengths, and an electron spin precession period of 10 ns. For both the short and longer EOM probe pulse lengths, zero crossings are observed at the electron spin precession frequency; however, the overall achievable electron spin polarization is offset for the longer probe length, and zero crossings no longer occur after approximately 3 ns (blue curve in Figure 7.12). Additionally, the overall swing between maximum and minimum electron spin polarization is larger for the short pulse at early times and dies off as the rotation pulse delay time increases.

Thus, there are a few possibilities for how the rotation pulse delay time, and therefore electron spin polarization, may determine the DNP non-linearities. If the nuclear spin polarization responds to the electron spin polarization on a time scale

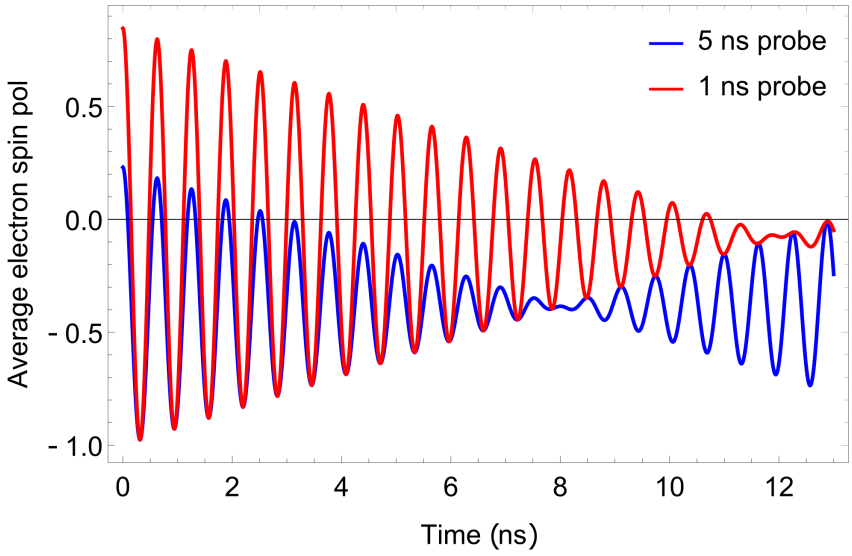

Figure 7.12: Plot of the average electron spin polarization over the course of a single shot of the Ramsey fringe experiment as a function of the rotation pulse delay time t_{12} (Equation 7.22). The red (blue) curves correspond to EOM probe lengths of 1 (5) ns, respectively, for an experimental repetition period of 12.7 ns. Note that the time on the x-axis is the rotation pulse delay time, not the experimental time throughout a single shot of the experiment.

short compared to a single Ramsey fringe delay time t_{12} acquisition, then the DNP non-linearity may be driven in a single Ramsey fringe oscillation after one zero crossing. However, if the DNP build-up times are comparable to the amount of time it takes to acquire a single Ramsey fringe, the nuclear spin effectively sees the electron spin polarization averaged over the fringe equal to $-t_p/T$, which is closer to zero for the short EOM pulse length (red curve in Figure 7.12), becoming more negative with increasing EOM pulse length. The acquisition time for a single point in the Ramsey fringe scans displayed in Figure 7.9 was equal to 2 seconds; for comparison, the DNP build-up physics reported in Chapter 5 were asserted to occur on timescales less than 25 ms. Thus, assuming that this QD has similar DNP build-up timescales to the QD studied in the Raman scattering chapter, it is more likely that the nuclear spin polarization is reaching a steady-state value within the acquisition time of a single Ramsey fringe delay time. This assumption may be flawed; systematic studies of multiple QDs have demonstrated dot-to-dot variations of DNP build-up timescales ranging 3 orders

of magnitude [198]. Additionally, DNP non-linearities seem to change characteristic at the maxima and minima of the Ramsey fringe signal; for instance, in the 3 T Ramsey fringe scan reported in Figure 7.9, the rising edge of the fringe jumps sharply within one or two delay points, whereas the signal falls off slowly on the falling edge of the fringe. This possibly implies that the DNP feedback mechanism takes the form of a derivative $\frac{d\langle S_x\rangle}{dt_{12}}$.

Nevertheless, the problem of the DNP distortion of the Ramsey fringe signal with respect to the rotation pulse delay remains unresolved in this thesis. The points discussed above that may explain the DNP non-linearities depend on the presence of an electron-nuclear coupling term that depends on the electron spin polarization. However, it was demonstrated in Chapter 4 that the electron-nuclear hyperfine contact flip-flop interaction which generates a nuclear spin polarization when an out-of-equilibrium electron spin polarization is present, is energetically forbidden at high magnetic fields. Thus, a more complicated term that likely depends on optical excitation of the trion may be required to explain the DNP phenomena reported here [175, 182, 184, 212].

7.4 Coherent population trapping combined with the Ramsey fringe technique

Numerous reports have indicated that the nuclear spin ensemble fluctuations can be reduced by the utilization of coherent population trapping (CPT) [63, 85, 92, 136, 151, 154, 175, 176, 212, 221]. Referring back to Chapter 3, in a lambda system, or in the four-level system neglecting one of the optically-decoupled trion states, two optical fields driving two transitions with a shared excited state may result in coherent population trapping of the electron spin ground state when the two-photon resonance condition is satisfied, that $|\omega_{pr} - \omega_{pu}| = \Delta_e$. When this condition is satisfied, the resulting electron spin wavefunction is of the form $|\psi_e\rangle \propto \Omega_1 |+\rangle + \Omega_2 |-\rangle$, where Ω_1 drives the $|-\rangle \rightarrow |t\rangle$ transition and Ω_2 drives the $|+\rangle \rightarrow |t\rangle$ transition [45]. An electromagnetically-induced transparency (EIT) dip is observed when this two-photon

condition is satisfied as a function of pump/probe laser detuning, with a depth that is related to the ground state coherence time [45]. It has been reported that the coherent control technique can narrow the nuclear spin fluctuations. In some cases, the laser detuning scans still result in dragged lineshapes [85, 136], but the EIT dips are considerably deeper in the presence of two fields satisfying the CPT condition, corresponding to an increase in the ground state coherence time attributed to fluctuation quieting/ensemble narrowing. In other cases, especially in the InAs QDM system, the addition of strong CPT beams eliminates any discernible dragging of the lineshape, additionally resulting in extension of the two-electron spin coherence time to at least 1 μs, with the measurement limited by experimental SNR [63].

This section reports on attempts to narrow the nuclear spin ensemble using AOM-gated CPT fields and to measure this narrowing via the Ramsey fringe technique described in the previous sections. The experimental apparatus (Figure 7.13) is a modified form of the setup used in the Ramsey fringe experiments from the previous section, with additional electronics complexity. Again, the MIRA photodiode is used to clock the Picosecond Pulse Labs 12010 RF pulse generator, which is used to drive the EOM probe pulse with 4 ns pulses; for this experiment, an MSquared Solstis Ti:Saph CW laser is used as the probe. The clock signal is also used to synchronize the HydraHarp TCSPC module. However, the Picosecond Pulse Labs generator is triggered by the synchronization signal from a Fluke 6060A RF generator, only producing EOM pulses when the Fluke generator trigger is on. The Fluke 6060A is used to produce square amplitude-modulated RF pulses with pulse lengths ranging from 200 μs to 5 ms for this experiment, driving an acousto-optic modulator (IntraAction AOM-402AF3), which has an optical rise time on the order of 200 ns. The Fluke 6060A is used in favor of the Keithley 3390 due to faster amplitude modulation, which is limited to 20 kHz for the Keithley 3990. Two CW Ti:Saph lasers (MBRs #1 and #2) are combined on a 50/50 beamsplitter and sent through the amplitude-modulated AOM, and the first-order diffracted beam is collected on to a single mode fiber. The trigger out signal from the Picosecond Pulse Labs RF pulse generator is sent to an HP8082A RF pulse generator, which is used to modulate a time-gating

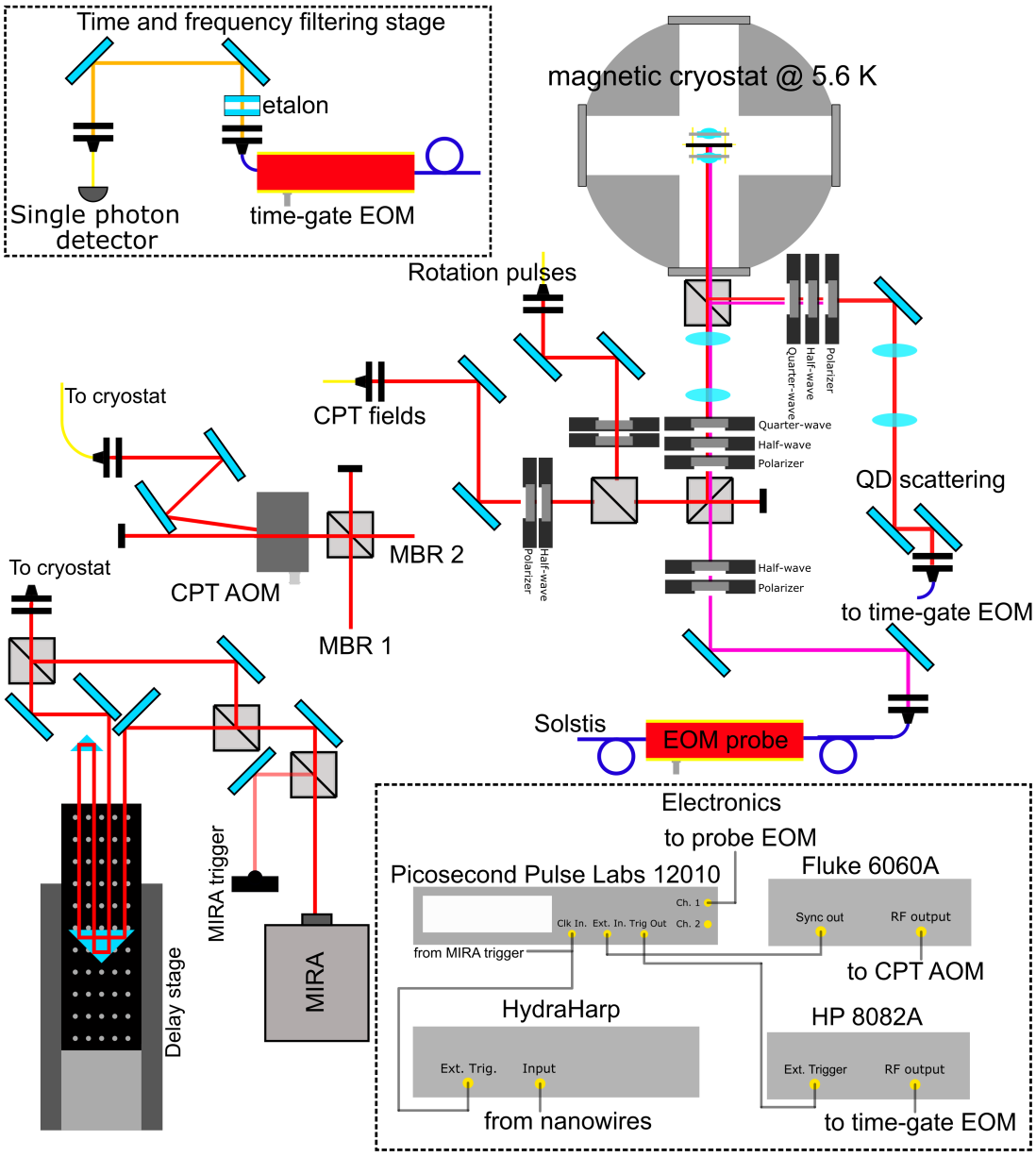

Figure 7.13: Experimental apparatus for Ramsey fringes measured in the presence of coherent population trapping of the electron spin. Details are found in the text.

EOM; the purpose of this device will be explained further below. The Ramsey fringe two pulse sequence is generated the same way as in the same experiment using a Mach-Zehnder interferometer.

The electronic and optical setup described in the previous paragraph results in a pulse sequence illustrated in Figure 7.14. The MIRA pulses are never blocked

during this sequence; the pulse sequence acts on the QD every 12.7 ns. However, the AOM-gated CPT beams are modulated on and off at either 200 μs or 5 ms repetition period, with a duty cycle of 70%. During the ON period of the CPT driving, the EOM probe pulse is turned off. Then, the AOM-CPT beams are turned off, and the EOM probe pulses are turned on. The QD scattering signal is separated from any emission occurring during the AOM-CPT driving phase by the usage of a time-gating EOM (EOSpace) placed in-line with the single-mode fiber which is routed to the single photon detecting nanowires. The time-gate EOM is driven with a 7 ns pulse, additionally isolating the EOM probe scattering from the rotation pulses leak-through. The time-gating EOM is required because the HydraHarp is synced with the MIRA photodiode signal, in order to retain the high timing resolution of the HydraHarp at 12.6 ns (1 ps); the HydraHarp is limited to $2^{16} = 65536$ bins, thus leading to poor time resolution when the HydraHarp is synced with the 5 ms amplitude-modulation of the CPT beams (76 μs bin size). Additionally, the time-gate EOM helps to reduce the leak-through of the AOM-CPT beams. These two fields are detuned from one another by the electron spin splitting, approximately 30 GHz, which leads to poor polarization rejection of the two beams together. It is noted that the time-gating EOM is highly susceptible to DC bias drift, leading to a slow drift in the measured QD scattering as a function of experimental time. The EOM can not be locked in the same manner as when used to amplitude modulate a CW beam; the CW beam leak-thru is used as a relatively bright servo in the CW case to lock the contrast. This problem could be solved by the introduction of a 1.55 μm laser coupled in with the QD scattering into the EOM. This laser would then be de-coupled from the QD scattering using a dichroic filter, and the locking PID system could be used to servo the transmission of the infrared laser to zero; such a scheme would result in possible leak-thru of the locking beam, as well as a loss of some signal due to insertion loss into the dichroic filter, although significantly improving stability which is highly necessary for Ramsey fringe contrast experiments.

The EOM probe is held in resonance with the $|+\rangle \rightarrow |T-\rangle$ transition and the two CPT beams are held in resonance with $|+\rangle \rightarrow |T-\rangle$ and $|-\rangle \rightarrow |T-\rangle$ transitions, with

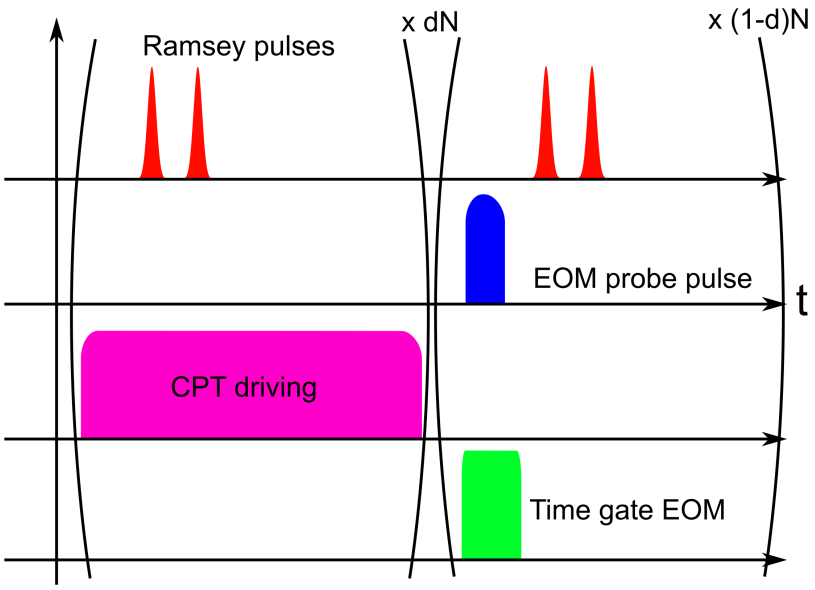

Figure 7.14: Pulse diagram for the CPT Ramsey fringe experiment produced via the experimental apparatus detailed in Figure 7.13. During the first phase of the experiment, which is dN experimental shots long, where d, N are the duty cycle of CPT pumping and total experimental shots of the pulsed laser, respectively, both the Ramsey pulses and AOM-CPT driving are interacting with the QD electron-trion system. The CPT driving field is always on during that period. During the second phase of the experiment, which is $(1-d)N$ shots long, the AOM-CPT driving is turned off, and the EOM probe pulses are turned on. The QD scattering is time-gated (green) using another amplitude-modulating EOM during the probe scattering period.

their relative detunings carefully chosen to equal the electron spin state splitting at co-tunneling using a Bristol wavemeter and more precisely using a Coherent scanning Fabry-Perot. This process of bringing the CPT beams into resonance could more reasonably be achieved by beating the two fields together on a fast photodiode and observing the beat frequency on a spectrum analyzer, eliminating the need to perturb the QD system with two lasers by bringing them into resonance and possibly shifting the resonances in the process. The spectrum analyzer technique would also allow for non-zero red and blue detuning of both CPT beams together while retaining the two-photon detuning equal to zero, which has been shown to lead to a considerable difference in the nuclear spin narrowing effect [154, 176, 221].

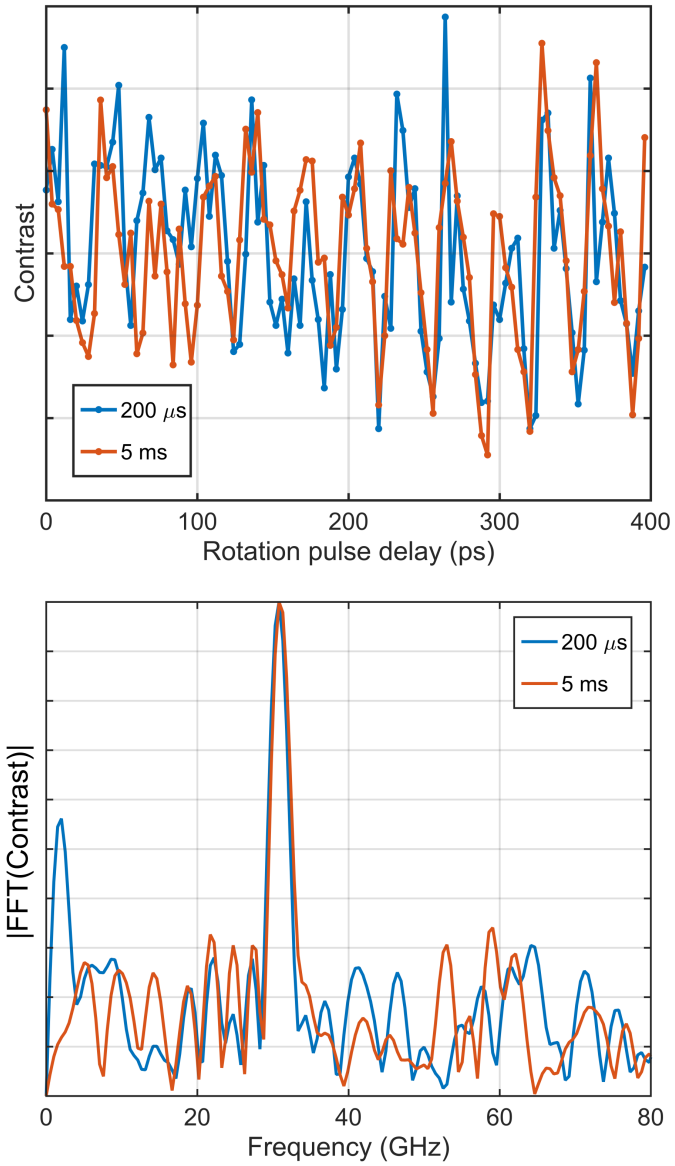

Figure 7.15: CPT Ramsey fringe results for short delay times out to 400 ps for CPT periods of 200 μs (blue) and 5 ms (orange), with duty cycles of 65%. Top: Ramsey fringe signal as a function of rotation pulse delay time in ps. Bottom: Absolute value of the Fourier transforms of the Ramsey fringe signals from the top plot. FT is performed using zero padding at five times the length of the original scan to interpolate the data.

In the first two experiments, the rotation pulse delay between $\pi/2$ pulses was scanned over a shorter range of 400 ps with delay steps of 4 ps, and CPT pumping periods of 200 μs and 5 ms were used, with 65% CPT-ON duty cycles; the scan results and FTs of both scans are displayed in Figure 7.15, and all experiments are performed at 5 T. No obvious differences are observed in the electron spin frequencies between the two cases, with a resulting electron spin splitting equal to 6.16 GHz/T. Additionally, fringes with sharp maxima and minima are observed, indicating that DNP phenomena are still in effect; however, the DNP distortion may be judged visually to be less severe than observed in the Ramsey fringes absent CPT pumping (Figure 7.9). There is also no measurable difference in the electron spin distribution FWHM for the 200 μs and 5 ms cases. Higher frequency resonances which are repeatable for both cases near 60 GHz shift to lower frequencies in the 5 ms case compared to 200 μs, and sidebands of the main electron spin frequency are observed in both cases; no attempts are made here to explain the presence of these signals and their shifts between the two pumping cases.

The Ramsey fringe scan is then extended out to 2 nanoseconds to study how the CPT pumping affects the overall amplitude decay of the fringes, using 5 μs CPT pumping with a duty cycle of 70% (Figure 7.16). The full signal without FT filtering is displayed in the yellow curve of Figure 7.16; this signal is compared to both the low-pass and high-pass signal, with a cutoff frequency of 8 GHz, chosen to be smaller than the predicted hole resonance. If the optical transition remains in resonance with the EOM probe field, but quasi-static fluctuations limit the T_2^* time to the length of the delay scan, then the Ramsey fringe amplitude falls off to zero but the overall optical signal reaches a value equal to half the initial amplitude. In these scans, there is a large amount of spectral power at frequencies lower than 8 GHz, which can be explained in two ways. First, the OH field may be shifting the optical resonance as a function of the rotation pulse delay time such that the optical probe signal drops and increases with an envelope period of around 1.5 ns. Second, it is possible that EOM probe power may be varying as a function of experimental time. Nevertheless, the high-pass signal above 8 GHz shows a Gaussian decay (dashed black curve) with a T_2^*

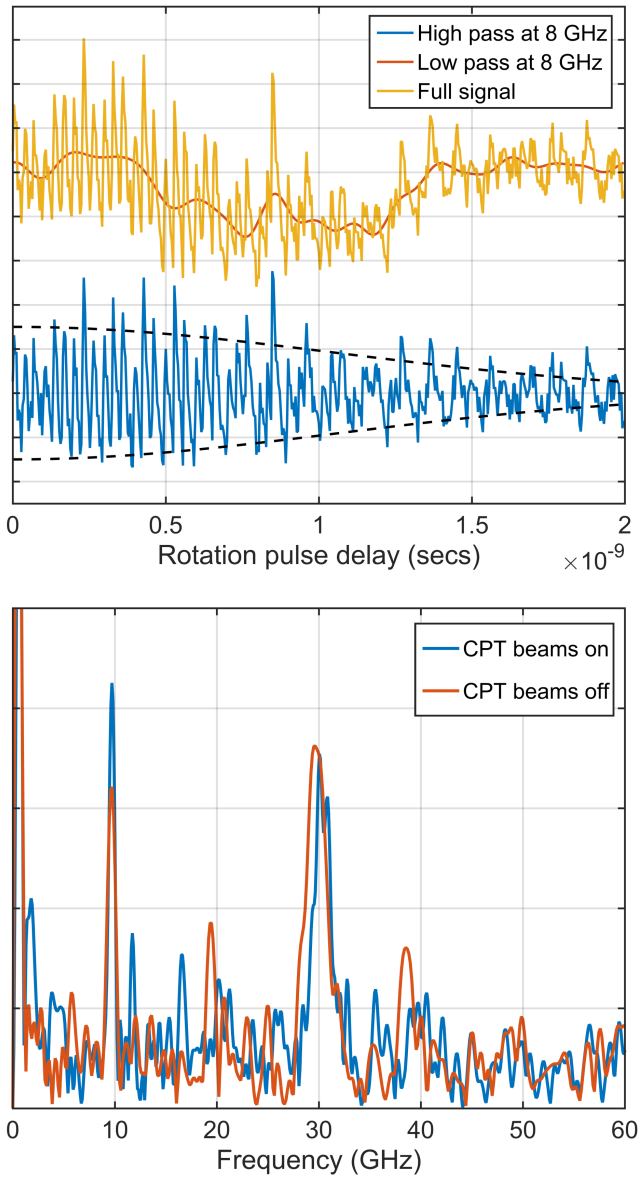

Figure 7.16: CPT Ramsey fringe results for 5 μs CPT pumping with a duty cycle of 70%. Top: Ramsey fringe signals, raw (yellow), low passed below 8 GHz (red), high passed above 8 GHz (blue), with Gaussian amplitude decay envelope with $T_2^* = 1.5$ ns (dashed black). Bottom: Absolute value of Fourier transform of full Ramsey fringe signal for the CPT pumping case in the top figure (blue) compared to the Ramsey fringe signal in the absence of CPT pumping (orange).

time equal to 1.5 ns, which is comparable to numerous other reports which measured the inhomogeneous broadening of the electron spin [86, 149, 154, 225]. DNP-induced

non-linearities are observed at rotation pulse delays greater than 600 ps: the electron spin frequency decreases as the delay time increases; this effect was also observed in the Ramsey fringe signals absent CPT pumping.

The FTs of the 5 T Ramsey fringes with and without CPT pumping are displayed for comparison in the bottom plot of Figure 7.16. The electron spin splitting and FWHM extracted from the CPT-ON Ramsey fringe is equal to 6.067 GHz/T and 1.91 GHz, respectively, compared to the CPT-OFF results of 5.955 GHz/T and 2.38 GHz, respectively. First, the electron spin splitting measured for the CPT-ON case is shifted less from co-tunneling splitting (6.29 GHz/T) than the CPT-OFF case. The difference between the CPT-ON and CPT-OFF FWHMs corresponds to a (19.8 $\pm$ 2.0)% reduction in the width of the electron spin resonance. This is a significant result, and indicates that CPT of the electron spin ground states results in a reduction of the OH field distribution width, even without the need for careful experimental balancing of the net electron spin polarization over multiple shots of the experiment [149]. Reductions in the OH field fluctuations is especially beneficial to the performance of quantum operations, allowing for a greater number of electron spin qubit gate operations. Additionally, the difference in electron spin frequency between the two cases is attributed to the coherent initialization of zero electron spin polarization in the CPT-ON case: the two CPT fields are equal in optical power, therefore when the two-photon condition is satisfied, the electron spin state wavefunction is in an equal coherent superposition $|\psi_e\rangle = |+\rangle + |-\rangle$. Thus, the electron spin remains unpolarized during the entire period the CPT pumping is on, or 70% of the experiment in this case. This implies that a DNP mechanism that depends on electron spin polarization may be in effect, since a shift is observed towards the DNP-free case (co-tunneling).

Other features of note are the prominent presence of the hole splitting, which is equal to 1.94 and 1.93 GHz/T in the CPT-ON and CPT-OFF cases, respectively, the appearances of beat frequencies in both CPT-ON and CPT-OFF cases, and the appearance of new frequencies observed around 12 and 17 GHz in the CPT-ON case. As shown in the theory chapter of this thesis (Chapter 4), the strength of the hole-nuclear coupling is around 10% of the electron-nuclear coupling resulting in the OH

field; thus, the levels of nuclear spin polarization present in this experiment are unlikely to be detected in the hole resonance. The peaks which were attributed to the beating of the electron and hole spin precession are shifted in the CPT-ON case by nearly the same amount as the electron spin splitting itself, corroborating that these peaks do indeed correspond to a beat signal. The appearance of new peaks at 12 and 17 GHz is unknown at this time, but their prominence should be noted.

An approximately Gaussian decay of the high-pass signal is observed, although higher frequency modes are present in the signal. The dashed black lines in Figure 7.16 indicate the Gaussian amplitude with a T_2^* time of 1.5 ns; this decoherence time can be related back to the OH field fluctuations (Section 7.3.1): $\Delta_{OH} = 2\hbar/(\mu_B g_e T_2^*) =$ 36 mT, a result that is comparable to other OH field fluctuation measurements in the QD electron system [85, 149].

One experimental feature worth noting in this experiment is that the Ramsey fringe $\pi/2$ pulses are present during the CPT pumping portion of the pulse scheme; these pulses can not be turned off without the introduction of a pulse picker in the Mach-Zehnder interferometer. Such a device was designed and constructed during the work leading up to this thesis. However, it was determined that insertion and coupling losses at the AOMs used for pulse picking were too high, and therefore the power required for the $\pi/2$ pulse could not be achieved. Furthermore, the effect of the pulsing is not yet understood; the effect is likely minimal since the pulses are only 2 ps long and the resulting electron spin wavefunction prepared by CPT does not depend on the initial state of the system before pumping.

By comparison, an experimental method was developed [154] to largely eliminate the time-averaged electron spin polarization present in the QD over the course of the CPT-Ramsey fringe experiment. This elimination is achieved by the usage of electron spin population inversion pulses; the electron spin pumping time, and the delay time between the first rotation pulse and the end of the optical pumping is minimized. Upon the next shot of the rotation pulses, rather than optically probing the blue Zeeman transition, the red Zeeman transition is probed. Thus, upon time-averaging over two shots of the experiment (with a repetition period much shorter

than the nuclear spin precession frequency), the electron spin polarization is zero. The authors report Ramsey fringes that are free of rotation pulse delay-dependent DNP effects, and are successful in measuring the nuclear spin narrowing effect via the Ramsey fringe technique. It is shown that the T_2^* time of the QD electron system can be extended from 3.2 ns to 39 ns after 840 μs of blue-detuned CPT pumping. That report is further evidence the time-averaged electron spin polarization does indeed drive DNP non-linear effects in the QD electron system, in both CW and time-domain studies.

The Ramsey fringe experiments described in this section, which measure the precession of an optically-prepared electron spin coherence, indicate that DNP effects play a strong role in the time-domain excitation of the QD electron-trion system, resulting in strong non-linear distortions of the Ramsey fringe waveform with respect to the rotation pulse delay time. The qualitative nature of the DNP non-linearities depends on which electron spin state is probed, a feature common to both CW and time-domain experiments. These DNP-induced non-linearities are measured at magnetic fields ranging from 2 to 5 Tesla; Fourier transforms of early and full time Ramsey fringe waveforms reveal that the magnitude of the OH field likely increases with increasing rotation pulse delay time. It may be possible to explain these effects through the influence of a time-averaged electron spin polarization for a given rotation pulse delay time. Surprisingly, attempts at narrowing the nuclear spin ensemble via CPT pumping lead not only to a shift in the electron spin frequency towards the unpolarized case, but also a significant reduction in the electron spin resonance FWHM, and correspondingly the OH field distribution width, of (19.8 $\pm$ 2.0)%. Future experiments should push this CPT technique further by utilizing longer CPT pumping times out at least hundreds of milliseconds, as well as the incorporation of more complex electron spin initialization schemes. Measurement of the underlying OH field fluctuations may be improved by incorporating a pulse scheme which results in a time-averaged electron spin polarization of nearly zero; the OH field fluctuations may then be more easily measured via the widths of the electron spin splitting peaks in the Fourier transform of the Ramsey fringes.

7.5 EOM pump-probe experiments

In the previous section it was demonstrated that ultrafast rotations of the electron spin state can result in DNP distortion of the Ramsey fringes that are typically used to measure the electron spin state splitting and inhomogeneous broadening. However, the exact origin of the DNP distortion has not yet been revealed. The experiments demonstrated in this section, which involve the optical pumping of the electron spin state over longer timescales, reveal that DNP distortion effects are present in the absence of the ultrafast rotation pulses as a function of optical pump-probe delay times. The onset of the distortion is a function of the pump-probe delay time over a wide range of experimental repetition periods. Thus, it is asserted again that the DNP distortion may arise from an average electron spin polarization effect that in turns polarizes the nuclear spin ensemble.

In these experiments, no ultrafast rotation pulses are utilized. The QD under investigation is the same QD that is studied in the Raman scattering chapter (Chapter 5). The experiment consists of two EOM amplitude-modulated optical fields, a pump and probe. The pump length is set to between 45 ns and 61 ns, and the probe length is set to 4 ns, and the probe peak power is set to at least 1/3 less than the pump. The QD electron spin is first driven with the pump field on the higher energy red Zeeman transition $|+\rangle \rightarrow |T+\rangle$, pumping the electron spin state into the nearly pure state $|-\rangle$. The pumping fidelity may be estimated by 1 minus the ratio of the minimum signal to the maximum signal measured during the pumping pulse. For instance, one example of a pump-probe time-correlated single photon counting (TCSPC) time trace is displayed in Figure 7.17. For the pumping pulse, the pumping fidelity is determined to be equal to 1-(1.85/55.6) = 96.7%. The second pulse probes the $|-\rangle \rightarrow |T-\rangle$ transition more weakly (E_{probe} = 0.75 E_{pump}) and for a shorter amount of time (4 ns compared to 45-61 ns) than the pumping pulse. The RF pulses used to drive the EOM amplitude modulators (EOSpace) are generated using two HP8082A RF generators, one of which determines the overall experimental repetition period and pump duration, syncing the second RF generator that drives that probe EOM, and the delay between the pump and probe may be set from 0 to T_{period} with

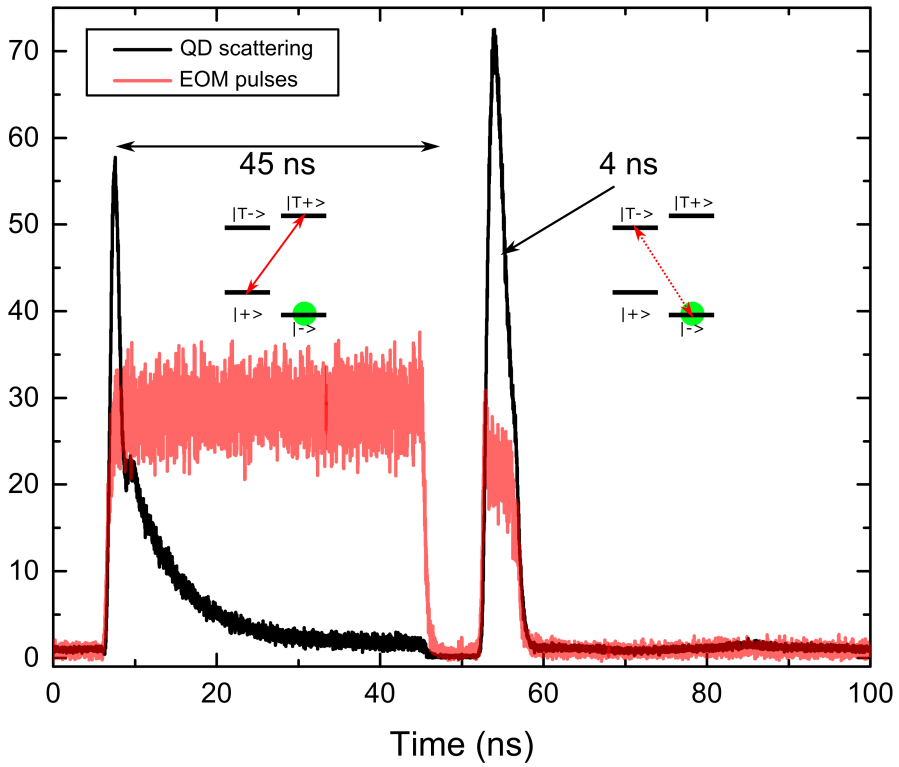

Figure 7.17: Time-correlated single-photon counting histogram of the EOM pump-probe experiment for 100 ns repetition period and approximately 9 ns pump-probe delay time. The histogram plotted in the figure is produced by time-tagging the detected photons with respect to the synchronization signal from the HP8082A pulse generator. The first pulse (the pump) drives the $|+\rangle \rightarrow |T+\rangle$ transition for 35 ns, while the probe is only incident on the QD for 4 ns on the $|-\rangle \rightarrow |T-\rangle$ transition. The QD scattering is isolated from the excitation fields by background subtraction between the QD bias ON and OFF (black histogram).

sub-nanosecond resolution. For a fixed pump-probe delay, the probe laser is scanned, and the pump and probe scattering response are separated in post-processing.

The goal of these experiments was to investigate the role that the pump-probe delay time has on the OH field shift under resonant excitation rather than ultrafast rotation pulses. Schematically, the electron spin state is prepared in the $|-\rangle$ state and remains fixed until the probe pulse interacts with the system. During the waiting period, it is possible that the polarized electron spin may interact with the nuclear spin ensemble. The relatively weak probe should detect relative changes in the nuclear spin ensemble via the OH field shift on the electron spin state splitting. Collecting

both the pump and probe scattering and separating them in post-processing allows for corroboration of these shifts; a change in the electron spin splitting shifts both the pump and probe transitions.

In the first set of experiments, the experimental repetition period is set to 100 ns. The timescale of the nuclear spin precession in a 2 T external magnetic field is equal to approximately 60 ns; as far as the current author is aware, this is the fastest relevant timescale related directly to nuclear spin physics in the QD system. The experimental results are displayed in Figure 7.18, with the probe(pump) scattering plotted in the top(bottom) plot. The probe laser is scanned across both the $|+\rangle \rightarrow |T+\rangle$ and $|-\rangle \rightarrow |T-\rangle$ transitions; a small amount of scattering is observed when the laser scans over the pump transition around 10574.42 cm^{-1}, which may be due to a higher rate of co-tunneling than expected. More importantly, as the probe is brought into resonance with the $|-\rangle \rightarrow |T-\rangle$ transition, the scattering brightens in both the pump and probe channels. For the first three delay times of 2.72, 5.3, and 21.75 ns, both the pump and probe scattering are observed to be relatively symmetric about their centers, with no indication of DNP-induced dragging. However, the FWHM of each peak (marked in the plot below each probe laser scan) is considerably larger than measured under CW excitation at zero magnetic field: the FWHMs are on average 0.0383 cm^{-1} (1.15 GHz), compared to a typical QD absorption/fluorescence linewidth of 450 MHz. This broadening may not be attributed to the time-domain excitation technique on its own: the shortest pulse width used in this experiment is 4 ns (250 MHz bandwidth), thereby not contributing significant broadening to the measured scattering lineshape.

Thus, it is evident that OH field fluctuations are already playing a role in this experiment for pump-probe delays ranging from 2.72 ns to 21.75 ns. The FWHM of the first three early scans can be used to determine the OH field fluctuation distribution width. The Gaussian OH field distribution (Equation 7.17) will be used as the broadening distribution for the Lorentzian optical response of the probe laser frequency scanned across the $|-\rangle \rightarrow |T-\rangle$ transition. The convolution of a Gaussian distribution with the Lorentzian is known as a *Voigt profile* [45], and is commonly

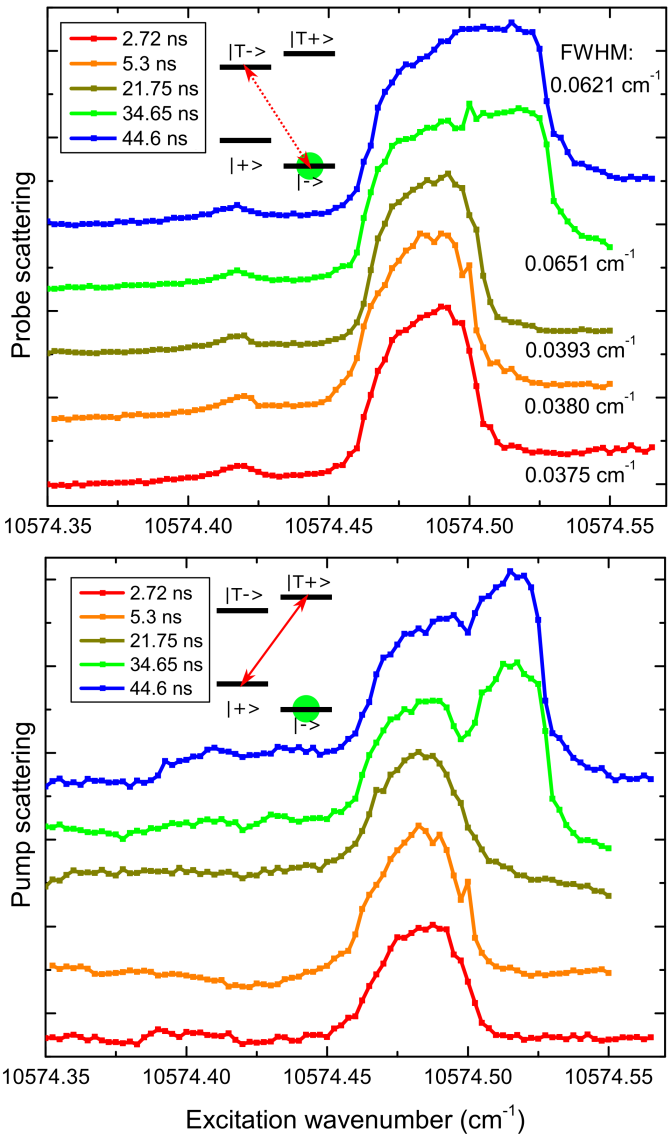

Figure 7.18: Probe and pump scattering for the 100 ns repetition period EOM pump-probe experiment. Top panel: probe scattering separated in post-processing of the TCSPC (Figure 7.17) by integrating the counts during the probe pulse only as a function of the probe excitation wavenumber. The probe laser is scanned and the scattering is collected for pump-probe delay times between 2.72 and 44.6 ns (legend), with FWHM for each scattering lineshape marked next to each curve. Bottom panel: pump scattering, same experiment. Pump scattering is isolated using the same post-processing technique except that only counts during the pump pulse are integrated.

observed in Doppler-broadened spectroscopy of thermal atomic vapors. The resulting expression is of the form

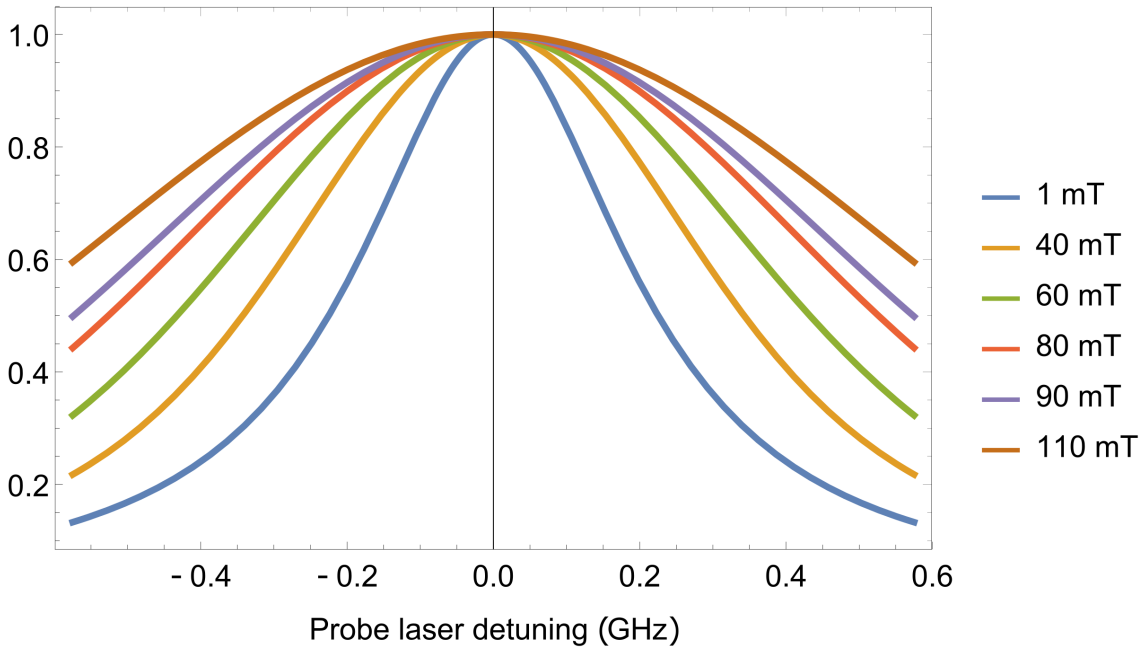

Figure 7.19: Probe scattering in the presence of quasi-static broadening (Gaussian) of a Lorentzian transition for different OH field distribution widths (Equation 7.23). Profiles are calculated numerically in Mathematica.

$$\text{Scattering}(\delta_0) = \frac{1}{\pi^{3/2}\Delta_{OH}^3}\int \frac{\gamma_2^2}{\gamma_2^2 + 4(\delta_0 - \frac{\mu_B g_e}{\hbar}B_{OH})^2}\exp\left[-\frac{B_{OH}^2}{\Delta_{OH}^2}\right] dB_{OH} \qquad (7.23)$$

where $\delta_0 = \omega - (\omega_0 + \frac{1}{2}\Delta_e^{ext})$. To extract an approximate OH field distribution width, a range of Voigt profiles are plotted in Figure 7.19 for OH field widths ranging from 1 mT (nearly absent of fluctuations), and 40-110 mT, for a Lorentzian with FWHM of 450 MHz. An OH field width of 90 mT matches the average FWHM of the 2.72 ns, 5.3 ns, and 21.75 ns delay time scans in Figure 7.18 most closely; no attempts are made at fitting the probe scans due to an increasing baseline at the blue edge of the laser scan, most likely due to either off-resonant coupling to the next blue Zeeman transition, or an increase in background scattering. The extracted OH field width is significantly larger than the measured width of 36 mT using the Ramsey fringe technique in Section 7.3, and outside of the typically measured range of 20-40 mT [57], indicating amplified fluctuations.

More strikingly, beyond pump-probe delays of 21.75 ns, the linewidth of the scattering lineshape nearly doubles to 0.0651 cm^{-1} (1.95 GHz) in the 34.65 ns delay case and 0.0621 cm^{-1} (1.86 GHz) in the 44.6 ns case. In these cases, the scattering lineshape is observed to be dragged with the scanning probe laser, remaining relatively flat in the probe case. No gradual broadening is observed as the pump-probe delay increases; rather, this abrupt change is observed between 21.75 ns and 34.65 ns pump-probe delay time. The DNP-induced non-linearities discussed thoroughly in Chapter 5 seem to turn on abruptly at this time delay, and are not observed at earlier times. Additionally, the same dragging behavior typically observed on the blue Zeeman transitions in absorption and resonance fluorescence is observed here in these pump-probe dependent laser frequency scanning experiments.

Although no quantitative model is developed in this thesis to explain this abrupt turn-on which is likely indicative of DNP-induced effects, the timescales for which the DNP distortion effects take effect match known nuclear spin precession frequencies. More specifically, the nuclear spin precession frequencies at 2 T are equal to 53 ns and 63 ns for ^{115}In and ^{75}As, respectively. The delay times referenced in the legends of Figure 7.18 refer to the time between the end of the pump pulse and the beginning of the probe pulse. However, a more physically relevant parameter may be the time at which the optically pumped electron spin polarization crosses over from positive to negative due to the pump pulse. Assuming that the electron spin state at the beginning of the pump pulse is in a pure state $|+\rangle$, a signal drop of 50% corresponds approximately to the electron spin polarization zero-crossing. This time is determined to be approximately 8.4 ns into the pulse. At this point, the electron spin polarization becomes increasingly negative until the pulse is turned off and remains constant (neglecting spin relaxation) until the probe pulse interacts with the system. DNP-induced effects are observed to turn on some time between 21.75 and 34.65 ns, or an average time of 28.2 ns after the pump pulse ends. Thus, under these conditions, the amount of time the electron spin polarization is negative is equal to (45 - 8.4)+28.2 ns = 64.8 ns, within 2.8% of the ^{75}As spin precession period. This correlation between the DNP turn-on pump-probe delay and the nuclear spin pre-

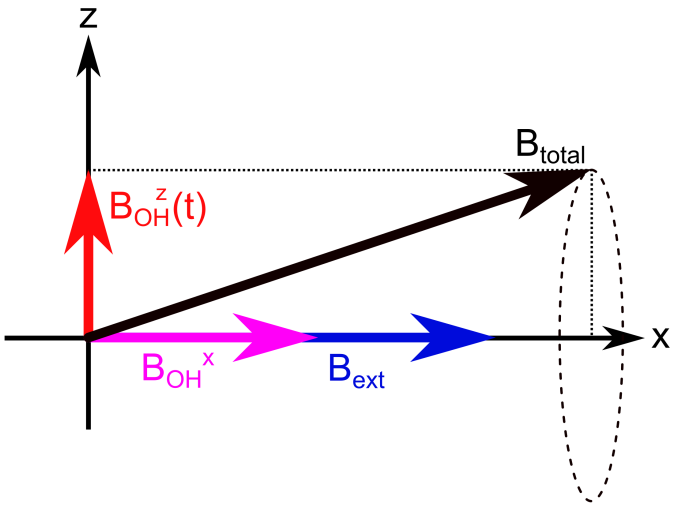

Figure 7.20: Vector diagram of the oscillating total magnetic field due to precession of the nuclear spins in the external magnetic field. The total magnetic field vector (black arrow) is the vector sum of the external magnetic field (blue) along $\hat{x}$, the OH field component along $\hat{x}$(purple), and the OH field component along $\hat{z}$ (red). However, the OH field is itself due to the average nuclear spin polarization, which is shown in the text to precess around the external magnetic field which has a non-zero cross-product.

cession period may be purely coincidental; however, it is physically feasible that the nuclear spin precession period may play a role in the DNP problem, as shown below.

The external magnetic field is pointed in the sample plane; the direction is defined as $\hat{x}$ (Figure 7.20). Even in the absence of any nuclear spin polarization mechanisms, an isotropic OH field exists pointing in all directions, with a probability distribution given by Equation 7.17. This OH field is due to a net nuclear spin polarization $\langle I_{x,y,z} \rangle$ which fluctuates with an autocorrelation time on the order of at least 100 μs, although likely slower. Consider the nuclear spin polarization that has non-zero angular momentum projections along $\hat{x}$ and $\hat{z}$, as predicted by the aforementioned probability distribution. For a given "frozen" fluctuation, or a single sample of the distribution, the total OH field consists of $\vec{B}_{OH} = B^x_{OH}\hat{x} + B^z_{OH}\hat{z}$. It is known [84] that, classically, the equation of motion of a magnetic moment $\vec{\mu}$ in a static magnetic field $\vec{B}$ is given by

$$\frac{d\vec{\mu}}{dt} = \gamma(\vec{\mu} \times \vec{B}) \tag{7.24}$$

where γ is the gyromagnetic ratio of the nuclear magnetic moment $\vec{\mu}$. Thus, the x-component of the OH field does not precess, but the z-component precesses around the external magnetic field along the $\hat{x}$ direction. Thus, the total magnetic field which is the vector sum of the external field and the two OH field components, precesses around the external magnetic field direction at a rate determined by the gyromagnetic ratio. For a given "frozen fluctuation," this time-dependent magnetic field may manifest itself on the measurement of the electron spin polarization in numerous ways. A total magnetic field that deviates from the $\hat{x}$ direction will cause a rotation of the polarization selection rules of the electron-trion system away from horizontal and vertical polarizations. This may lead to a reduction of the effective oscillator strength of a given transition being driven by the pump or probe. This time-dependent field must then be taken into account when developing a theory to explain the DNP-induced non-linearities as discussed in Chapters 4, 5, and 6. If this time-dependent field oscillates at the nuclear spin Zeeman frequency, the DNP non-linearities may become apparent when the pump-probe delay is in the vicinity of certain phase synchronization conditions with the nuclear spin precession, as observed in QD ensemble studies [197]. Even if the effect of this synchronization is relatively small over the course of a single shot of the experiment, a large number of shots are performed during a single experimental acquisition point for a given pump-probe delay time and probe laser detuning, possibly leading to a "nuclear mode-locking" type effect, as observed elsewhere [233].

The same experiment is then performed with a repetition period of 3 μs, with the same pump and probe pulse lengths and peak powers as in the previous experiment (Figure 7.21). Although the SNR is considerably lower due to the lower number of average integrated counts (factor of (100 ns/3 μs) = 3.3%), a similar phenomenon occurs in which strong DNP distortion of the scattering lineshape does not start to occur until beyond a certain pump-probe delay time. In the 3 μs case, the broadening

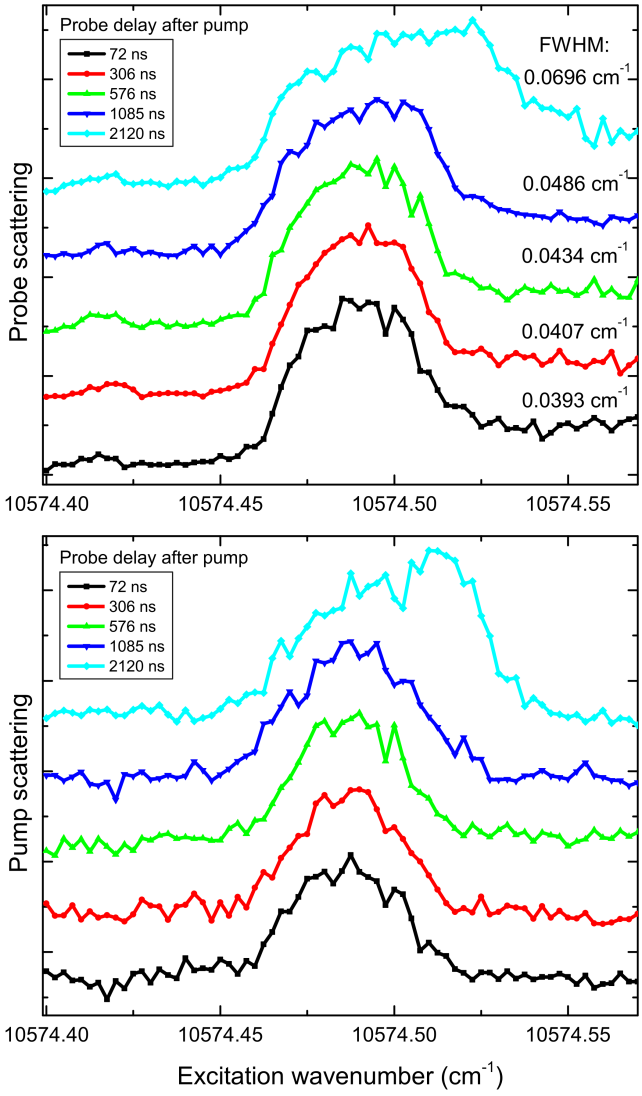

Figure 7.21: Probe and pump scattering for the 3 μs repetition period EOM pump-probe experiment. Top panel: Probe pulse scattering. Bottom panel: Pump pulse scattering. Delay times range from 72 to 2120 ns.

occurs gradually from 72 ns to 1085 ns, but jumps from 0.0486 cm^{-1} (1.46 GHz) to 0.0696 cm^{-1} (2.09 GHz) at 2120 ns delay. It is difficult to understand how the phase synchronization conditions used to explain the previous data set at 100 ns repetition period may come into play for this data set. In particular, the first pump-probe delay time is already on the order of the nuclear spin precession period at 2 T, but no DNP distortion is observed until 2120 ns pump-probe delay time. This longer timescale experiment implies that the average electron spin polarization acquired over a number

of experiment shots may be playing a large role in determining the response of the nuclear spin polarization in the presence of pulsed optical excitation. One common feature to both the 100 ns and 3 μs cases is that the switching effect due to DNP non-linearities turns on for negative electron spin polarization duty cycles greater than 50%: in the 100 ns, the electron spin polarization is negative for at least 65% of the time, and in the 3 μs that percentage of time is 54%. However, this calculation is in danger of over-simplification: the probe pulse does not necessarily drive the electron spin polarization back to positive due to it relative weak peak power and short pulse length compared to the required optical pumping time. A more detailed investigation would automate the pump-probe delay, scanning this delay time on timescales shorter than the nuclear spin precession frequency.

In the previous two experiments, although the probe peak power is smaller than the pump peak power, and considerably shorter than the pump pulse length, the probe may not be considered "perturbative." Evidence for the strong interaction of the probe with the QD electron-trion system is that the probe scattering (Figure 7.17) in the 100 ns repetition period case is high, and drops off by nearly 60% before the probe pulse is completed, indicating that the electron spin polarization may even have been pumped back to positive, reversing the effect of the pump. Thus, the pump-probe delay may then be predicted to have a strong effect on the response of the nuclear spin ensemble to the electron spin polarization, since the average electron spin polarization may be tuned from negative to positive by adjusting the delay. If instead one wishes to observe the system perturbatively as a function of waiting time after the pump pulse, the probe pulse peak power and delay must be reduced further.

An experiment was performed for which the repetition period was set to 993 ns, and the probe power was reduced considerably compared to the previous two experiments (Figure 7.22). The pump pulse length is set to 30 ns and the probe length to 1.8 ns, while the average pump power was set to at least four times the probe power. Setting the average probe power much lower than this causes the EOM DC offset locking modules to become unstable due to extremely small average powers off of which to servo the EOM contrast, making a true perturbatively small probe

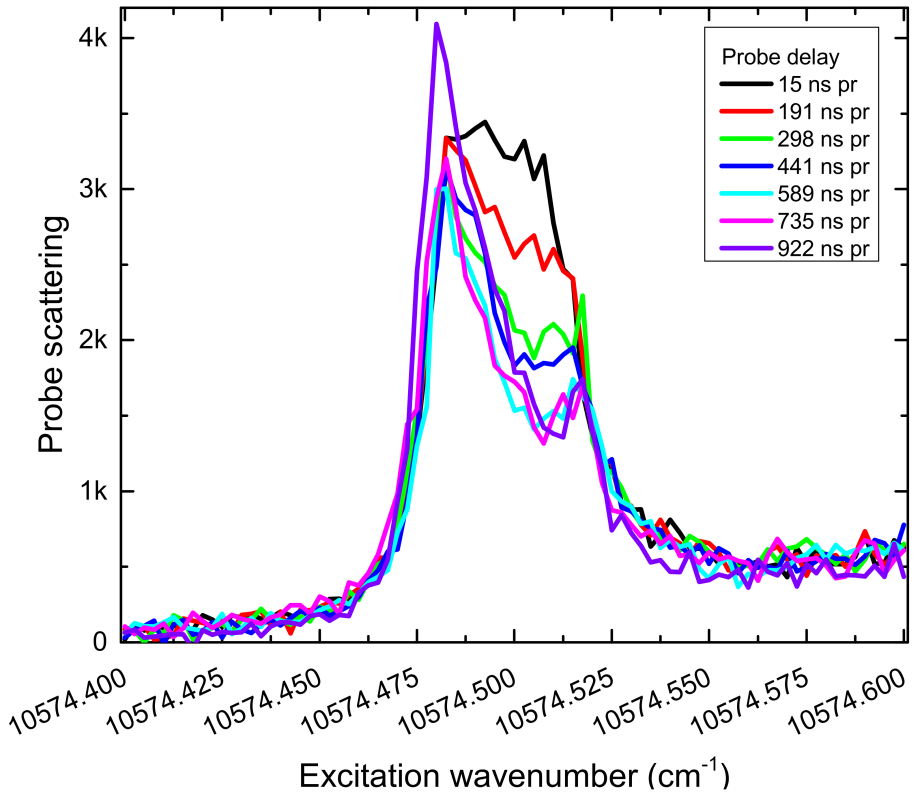

Figure 7.22: Probe and pump scattering for the 993 ns repetition period EOM pump-probe experiment with weak probe peak power. The EOM probe peak power is at least four times smaller than the pump power, and the probe pulse length is only 1.8 ns.

experiment difficult.

In stark contrast to the results of the previous two experiments for which the probe/pump peak power ratio was larger, the 993 ns repetition period experiment shows that DNP distortion of the probe scattering may occur at early pump-probe delay times, with the distortion becoming continuously more severe as the pump-probe delay is increased. For the shortest pump-probe delay, the probe scattering lineshape is symmetric (neglecting the baseline background scattering); as the delay is increased, the scattering becomes increasingly distorted towards the red side of the transition, implying a decrease in the OH field, bringing the transition into resonance with the laser. In fact, increasing the pump-probe delay all the way out to 922 ns, leaving only 39 ns remaining between the probe cut-off and the start of the next

experimental shot pump pulse, results in a very sharp scattering lineshape, with minimal distortion towards the blue end of the lineshape.

One of the implications of this experiment is that even in the limit of a perturbatively small probe, with probe peak power at least four times smaller than the pump and probe pulse length shorter than the typically required optical pumping length (at least 2 ns in this QD), DNP distortion effects are still demonstrated as a function of pump-probe delay. Thus, some change in the coupling between the electron/trion system and the nuclear spin ensemble must be tunable via the pump-probe delay. The first suspected mechanism is the one implicated for the previous experiments, or the coupling of the average electron spin polarization to the nuclear spin ensemble. In this scheme, a prepared electron spin polarization may precess in the orthogonal components of the OH field, which itself is oscillating due to the precession of the nuclear spin components $\langle I_z \rangle$ in the external magnetic field $\vec{B}_x$. This precessing electron spin polarization likely interacts with the nuclear spin polarization via the non-linear mechanisms outlined in Chapter 4; however, no attempt is made at outlining a theory to explain this non-linearity in this chapter. Nevertheless, it is made clear in these experiments that the probe does indeed affect the nuclear spin polarization as a function of pump-probe delay and laser excitation frequency, revealing that the DNP non-linearities resulting in the lineshape distortion are very sensitive to even perturbatively small probe excitation.

The experiments outlined in this section using EOM pump-probe excitation may be improved in a number of ways. First, DNP non-linear experiments are highly sensitive to initial starting conditions in cases where the system may not be allowed to reach a full steady-state. In the CW Raman scattering experiments detailed in Chapter 5 in which the laser frequency step time was inferred to be longer than the nuclear spin polarization time, the coupled electron-nuclear system was assumed to have reached its steady-state, which did not depend on the initial conditions of the nuclear spin polarization. However, the ideal time-domain experiment would initialize the full electron-nuclear system with the same initial conditions each shot of the experiment. It is possible to achieve this by using the co-tunneling regime to

attempt to bring the nuclear spin ensemble back into thermal equilibrium. This would require fast bias modulation of the sample [162]; current bias modulation bandwidths are limited by the high capacitance of the sample, limiting modulation bandwidths to the low kHz range. If this method were achieved, nuclear spin polarization would only develop over the course of a single shot of the experiment, and the electron spin and nuclear spin polarization would not have to be assumed to be averaged over a large number of experimental shots. A similar experiment was performed [168] using AOM modulators with a relatively weak external magnetic field (-220 mT along the growth direction) and non-resonant PL excitation/readout of the nuclear spin polarization. However, nuclear spin polarization effects are well understood to depend dramatically on whether the QD is excited resonantly versus non-resonantly.

7.6 Chapter summary

In this chapter, the non-linear interactions between the QD electron-trion system and the nuclear spin ensemble were investigated using ultrafast time-domain techniques and EOM-based pump-probe spectroscopy. A brief review of the current state of the art of coherent control of the electron spin qubit and trion system was presented. The theory of detuned two-photon Raman rotation pulses acting on the electron spin qubit was presented. The expected form of the Ramsey fringe rotation pulse delay time dependence was derived in the presence of quasi-static OH field fluctuations. Ramsey fringe experiments performed on the electron spin qubit showed that the fringes are strongly distorted by DNP effects, and that the qualitative nature of the DNP distortion depends on which electron spin state is initialized by the EOM optical pumping/probe pulse. The DNP distortion effect was shown to be in effect for magnetic fields ranging from 2 to 5 T in the plane of the sample. Attempts at narrowing the nuclear spin ensemble using coherent population trapping were successful for pumping periods of 5 ms with a duty cycle of 70%, resulting in a (19.8 $\pm$ 2.0)% narrowing of the electron spin resonance; this narrowing was correlated with a depolarization of the nuclear spin ensemble, pushing the electron spin central frequency

closer to the result measured in co-tunneling. The time-dependence of the OH field and related DNP distortion was further investigated through EOM pump-probe experiments, in which a 40-60 ns narrowband pump initialized the electron spin state, while a short (1-4 ns) probe laser was frequency scanned across the electron-trion transition. Even at short pump-probe delay times, broadening is observed, which is attributed to amplified nuclear spin fluctuations on the order of 90 mT. For the 100 ns and 3 μs repetition period experiments, an abrupt shift occurs at later pump-probe delay times in which the trion transition is likely dragged due to DNP non-linear effects. This dragging is shown to be continuous with respect to the pump-probe delay time when the probe/pump power ratio is reduced considerably at a repetition period of 993 ns. Although no rigorous or predictive model is developed in this thesis to explain the DNP phenomena, a non-linear mechanism that involves the precession of transverse OH field components due to the external magnetic field combined with one that depends on the average electron spin polarization accumulated over multiple experimental shots may explain the distortion behavior observed in the Ramsey fringe and EOM pump-probe experiments.

CHAPTER 8

Future directions and summary

8.1 Future directions

There are a number of future directions that should be investigated in order to understand the non-linearly coupled QD-electron-hole-nuclear system with greater certainty. The original discovery in this thesis of anomalous Overhauser field shifts as measured using resonant Raman scattering was an accident; the author was attempting to determine the trion transition resonant energies using the pressure-tuned etalon designed to optimize the transmitted photons scattered/emitted by the QD while rejecting the laser. While it is true that the etalon used for this thesis does in fact work ideally as an excitation laser filter, having a FWHM matched to the approximate linewidth of the trion absorption line, the etalon is not ideal for scanning etalon spectroscopy. The author proposes a different system which would allow for precise determination of the electron spin frequency and OH field distribution width: a two-etalon cascaded system which include the pressure-tuned etalon utilized in this thesis with an additional piezo-scanned etalon. The first etalon is used to resolve the Raman scattering from a single pathway from the Rayleigh/Raman and spontaneous emission from other pathways. The additional etalon, being piezo-scanned, would allow for rapid scanning across the QD transition. However, this etalon should have a much smaller FWHM, comparable to the inverse of the electron spin dephasing time (MHz level). This fast-scanning system would allow the spectroscopist to measure the coherence time of the electron spin directly by measuring the width of the Raman

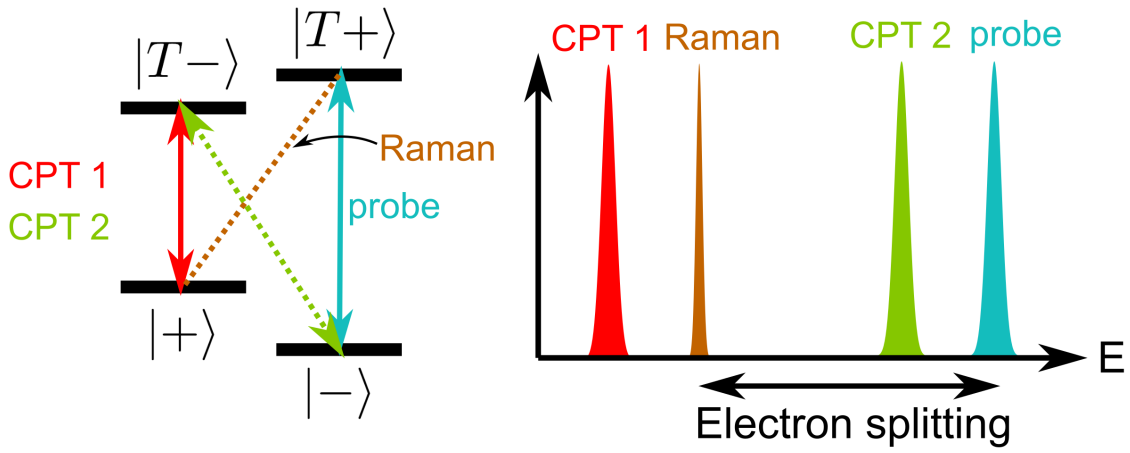

Figure 8.1: Energy level diagram for measuring narrowing of Raman scattering linewidth under coherent population trapping.

scattering, which was shown in Appendix A to be given by the ground state dephasing time. Additionally, the resolution of the Raman scattering experiment presented in this thesis was limited by the FP FWHM, and has already reached the approximately 50 spin level. A factor of 50 increase should bring the resolution of the experiment within single nuclear spin sensitivity, allowing for the optical spectroscopy of single nuclear spins in a self-assembled QD system, a feat that has never been achieved. The author notes that the development of a piezo-scanned etalon with these features is easily achievable; one caveat is that the etalon resonance will likely need to be stabilized with a narrow bandwidth laser which does not interact with the QD but is used to provide a servo lock. A similar system has already been developed elsewhere to resolve the "sub-natural linewidth" (smaller than the trion absorption linewidth) of the Rayleigh scattering in the trion system, utilizing a 29 MHz FWHM scanning etalon [123].

One particularly insightful experiment that would benefit from the utilization of this cascaded piezo-scanning system would involve coherent population trapping of the electron spin (Figure 8.1). It was already shown in the time-domain spectroscopy chapter (Chapter 7) that CPT can lead to narrowing of the OH field distribution as measured by the Fourier transform of the Ramsey fringes. The equivalent CW

experiment would involve three optical fields: two fields with two-photon detuning equal to zero, and one field exciting the transition involving the remaining uncoupled excited state. The probe field is required because in the presence of just the two CPT fields, the Raman scattering from one field overlaps with the Rayleigh scattering of the other field, and vice versa, which complicates the spectrosopic measurement. However, the introduction of a weak probe field results in Raman scattering at a frequency distinct from the other scattering pathways. One should study the effect of the CPT duration on the linewidth of the Raman scattering, as well as the electron spin frequency. In the CPT configuration, the hole (excited state) population is minimized, and the electron spin polarization can be chosen to be zero by carefully setting the two CPT fields equal to each other. Although there are a few existing time-domain studies of CPT, none of them have examined the electron spin coherence via the Raman scattering linewidth [136, 149]. Theoretical considerations predict that the CPT may lead to either narrowing or amplification or the nuclear spin fluctuations depending on the single-photon detuning from the optical transitions (keeping the two-photon detuning equal to zero); this could easily be examined using this technique.

The Raman scattered photons provide a very useful resource for quantum information, especially related to linear photon quantum computation. As described throughout the thesis, the linewidth of the distribution of Raman photons is very narrow, limited only by the ground state decoherence and the laser linewidth. In fact, the QD has been referred to as a converter of the weak coherent state generated by a CW laser to true single photons [123]. After spectral filtering of the Raman scattering from the Rayleigh scattering and spontaneous emission, the coherence properties of the Raman photons should be studied using standard quantum optical techniques including $g^{(2)}$ measurements of the second-order coherence, Michelson interferometry of the first-order coherence, and Hong-Ou-Mandel interference in order to measure the indistinguishability of the photons [47]. If the QD brightness is enhanced either by the DBR cavities with higher finesse or the inclusion of solid immersion lenses (SILs), the scattered photon budget should allow for CPT narrowing of the electron

spin qubit for a large duty cycle of the repetition rate of the experiment, resulting in higher indistinguishability. These scattered photons could be utilized for cluster state computation [234] or as single photon inputs to linear photonic systems. Furthermore, they could also be injected into electro-optic phase modulators and used as a frequency-qubit for frequency-domain quantum key distribution [47].

Equivalent measurements of the electron spin coherence can also be made in the time-domain. Recent experiments have reported on the effect of coherent population trapping on the Ramsey fringes of QD electrons using a sophisticated optical pumping technique which drives the average electron spin polarization to zero [154]. However, CPT has not yet been utilized to understand the intrinsic decoherence time T_2, which is revealed by the spin echo technique. Thus, it is proposed that future experiments first narrow the nuclear spin ensemble for at least milliseconds and then perform the spin echo technique to see if the T_2 time is affected at all.

Another important aspect of understanding the nuclear spin ensemble physics and its coupling to the electron-trion system in the single QD is for the sake of implementing quantum memory. Atomic vapors have been utilized for quantum memories, in which the vapor interacts strongly with an incoming photon or weak coherent source pulse; the quantum information from the photon is transferred on to the vapor via light-matter interactions, typically resulting in a matter wavefunction which looks like the coherent superposition of a single excitation distributed over all atoms in the vapor (similar to a Dicke state). In the QD electron-trion-nuclear system, it was shown in this thesis that there is a multistability in which when the laser is scanned across one of the red Zeeman transitions, that the Overhauser field (underlying nuclear spin polarization) changes by approximately 160 mT (or 550 spin flips). A proposed quantum memory may operate in the vicinity of the transition wavenumber between these two states, which differ by a large measurable number of nuclear spin flips. Single photon emission and scattering (say from a flying qubit scattered by a distant QD) may result in a superposition state of the nuclear spin ensemble, which is likely preserved for the nuclear spin depolarization time on the order of hundreds of microseconds out to a few milliseconds. Furthermore, the underlying physics of

the transition between low and high Overhauser field states is not yet understood; it is possible that the system settles into one of the ground states of a spin glass, which may lead to Dicke-like states in which the spin flips are distributed in a coherent superposition state throughout the nuclear spin ensemble in the QD. InAs QD systems may prove superior to other quantum memory systems in that the nuclear spin ensemble (memory) is easily accessible by the strong light-matter interactions of the QD.

8.2 Thesis summary

This thesis reveals experimentally new understandings of the interactions between the electron and hole confined to a self-assembled InAs quantum dot and its constituent nuclear spins. Chapter 2 introduced the structure of the QD sample, including the electric field biasing structure used to deterministically charge the QD with a single electron, and the selection rules which underlie optical excitation of the electron-trion transitions under the application of an external magnetic field. Chapter 3 introduces continuous wave spectroscopy techniques including photoluminescence, sample bias-modulated lock-in different reflectivity, and direct scattering measurements including resonance fluorescence and Raman scattering. One novel result described in that chapter is a strong correlation between the small permanent dipole of the trion and the polarizability of the electrons and holes in the quantum-confined Stark regime, which was revealed by the utilization of a broadband high-resolution scanning TiSaph laser to build up high statistical confidence. Chapter 4 gives an exposition of the microscopic origins of the interactions between the electron/hole and the QD nuclear spins, which is easily observable due to the strong quantum confinement of optically-excited carriers in the QD. These mechanisms included the electron-nuclear hyperfine contact interaction, the quadrupole interaction, the dipole-dipole hole-nuclear interaction, and the nuclear spin diffusion terms (dipole-dipole and electron-mediated). It was shown there that the quadrupolar interaction could lead to energetically-favorable nuclear spin polarization in the presence of a confined electron.

Chapter 5 presents the main experimental results of this thesis, studying the effects of a resonant excitation laser scanning across the electron-trion transitions under the application of a strong external in-plane magnetic field. Large Overhauser field shifts were measured in both the co-tunneling and optical pumping regime, with a qualitative non-linear feedback that depended on which Zeeman branch was being probed with a scanning laser. The absence of heavy-hole light-hole mixing strongly implicates the electron-mediated quadrupolar interaction as driving the nuclear spin polarization in the particular QD under study; this result could change significantly depending on changes in the QD morphology throughout the sample and between different samples. Chapter 6 introduces a phenomenological model used to understand and fit the Raman scattering dependences reported in Chapter 5 by utilizing the quadrupolar Hamiltonian. However, the qualitative differences between the two Zeeman branches (red and blue) are only recovered when an arbitrary sign flip is made in the feedback term; this arbitrary sign flip is common to many other theoretical studies. Chapter 7 details time-domain studies of the electron spin in the presence of DNP non-linearities. Time-domain studies included power-dependent Ramsey fringes using two-photon detuned Raman pulses to rotate the electron spin phase, and Ramsey fringes on the electron spin qubit, revealing DNP-induced non-linearities as a function of rotation pulse delay time. Nuclear spin narrowing was demonstrated by introducing coherent population trapping of the electron spin states for 5 ms with 70% cycle, resulting in a $(19.8 \pm 2.0)\%$ reduction in the FWHM of the electron spin resonance in the Fourier transform of the Ramsey fringe signal. Additionally, a novel class of EOM-pulsed pump-probe experiments explored the electron and nuclear spin dynamics for experimental repetition periods ranging from 100 ns to 3 μs, demonstrating DNP-induced non-linearities and amplified OH field fluctuations under certain regimes. This thesis presents a more comprehensive understanding of dynamic nuclear spin polarization and its effects on the QD electron-trion system, which will hopefully empower future researchers to continue to improve the system and utilize the observed non-linearities.

APPENDIX A

Derivation of Rayleigh and Raman scattering in the lambda system

In this appendix the scattering spectrum for the lambda system in the presence of a single classical field and the quantum vacuum field is derived. Rather than taking a quantum regression theorem approach, the perturbation theory approach is adopted [45]. The intent is to model the scattering spectrum for the four-level electron-trion system studied throughout this thesis when the pump and probe fields do not share an excited state, ie. that they drive different Zeeman-split trion states 3. Additionally, the pump is strong compared to the probe, but both fields are considered to be weak compared to the spontaneous emission rate of the transitions. The energy level diagram is illustrated in Figure A.1. The dashed black line indicates the sub-system of the electron-trion system in which the probe (blue arrow) drives the $|-\rangle \rightarrow |T_x-\rangle$ transition weakly, leading to repopulation of the $|+\rangle$ state. However, a much stronger pump field drives the $|+\rangle \rightarrow |T_x+\rangle$ transition; therefore, in the perturbation theory limit, all of the population is considered to be pumped into the $|-\rangle$ state, ie. $\rho^{(0)}_{1;0,1;0} = 1$, where the basis states are defined in the next paragraph.

The wavefunction basis states for the coupled atom-quantum field system only include states that are connected at most by two field interactions. Thus, the basis states are $[|1;0\rangle, |e;0\rangle, |1;a\rangle, |2;b\rangle]$, where $\hat{a}$ and $\hat{b}$ are the photon modes corresponding to the $|1\rangle \rightarrow |e\rangle$ and $|2\rangle \rightarrow |e\rangle$ transitions, respectively, which have different polarizations. The $|2;0\rangle$ state is not included in this calculation, since the probe field is weak and in the perturbation theory limit the system is considered to be initialized entirely to the $|1;0\rangle$ state.

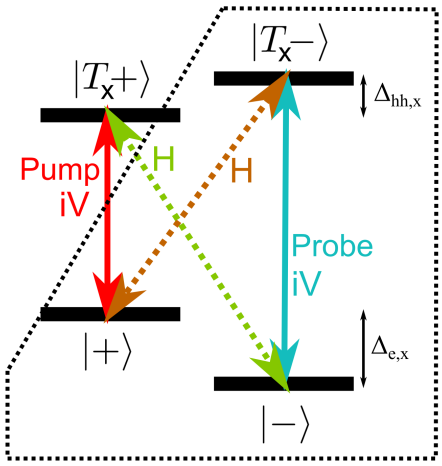

Figure A.1: Lambda sub-system of the four-level electron-trion system in the Voigt geometry. Dashed black line indicates the subset lambda system considered here theoretically.

The Hamiltonian for the combined atom-quantum field system can be written as follows: [45]

$$\begin{aligned} H = \hbar(-\frac{\Delta_e}{2}\sigma_{11} + \frac{\Delta_e}{2}\sigma_{22} + \omega_0\sigma_{ee}) + \hbar\omega_a a^\dagger a + \hbar\omega_b b^\dagger b \\ + \hbar\left(\chi_{1e}\sigma_{e1}e^{-i\omega t} + \chi_{1e}^*\sigma_{1e}e^{+i\omega t}\right) \\ + \hbar\left(g_1\sigma_{e1}a + g_1^*a^\dagger\sigma_{1e}\right) + \hbar\left(g_2\sigma_{e2}b + g_2^*b^\dagger\sigma_{2e}\right) \end{aligned} \tag{A.1}$$

where the first term is the fixed energies for the lambda system, the second and third terms are the field Hamiltonians for the quantum fields (photon modes), the fourth term is the classical field interaction term that drives population back and forth between states $|1\rangle$ and $|e\rangle$, and the fifth and sixth terms are the quantum atom-field couplings, and $g_i = -i\mu_i \sin\theta_i \left(\frac{\omega_i}{2\hbar\epsilon_0 V}\right)^{1/2}$ [45].

A more convenient picture is arrived at by utilizing a unitary transformation of the wavefunctions in order to get rid of the fast exponential oscillations at the laser frequency ω and ω_0. If the state amplitudes are transformed via $\vec{a}(t) = \hat{U}(t)\vec{c}(t)$, then the newly transformed Hamiltonian for the $\vec{c}$ amplitudes is equal to

$$H_{trans} = \hat{U}^\dagger\hat{H}\hat{U} - i\hbar\hat{U}^\dagger\frac{\partial\hat{U}}{\partial t} \tag{A.2}$$

Then, the following unitary transformation is utilized:

$$\hat{U} = \text{diag}\{e^{i\Delta_e t/2}, e^{-i\omega_0 t}, e^{i\Delta_e t/2}e^{-i\omega_a t}, e^{-i\Delta_e t/2}e^{-i\omega_b t}\} \tag{A.3}$$

arriving at a final transformed Hamiltonian given in matrix form by

$$H = \hbar \begin{array}{c} \begin{array}{cccc} |1;0\rangle & |e;0\rangle & |1;a\rangle & |2;b\rangle \end{array} \\ \begin{pmatrix} 0 & \chi e^{-i\delta_1 t} & 0 & 0 \\ \chi^* e^{+i\delta_1 t} & 0 & g_1 e^{+i\delta_1^a t} & g_2 e^{+i\delta_2^b t} \\ 0 & g_1^* e^{-i\delta_1^a t} & 0 & 0 \\ 0 & g_2^* e^{-i\delta_2^b t} & 0 & 0 \end{pmatrix} \end{array} \tag{A.4}$$

where $\delta_1 = (\omega_0 + \frac{\Delta}{2}) - \omega$, $\delta_1^a = (\omega_0 + \frac{\Delta}{2}) - \omega_a$, $\delta_2^b = (\omega_0 - \frac{\Delta}{2}) - \omega_b$. The density matrix formalism is then utilized, which allows for easy incorporation of phenomenological population decay and dephasing rates into the system [45]. The equations of motion for the density matrix elements are given by $\frac{d}{dt}\hat{\rho} = -\frac{i}{\hbar}[\hat{H}, \hat{\rho}] + \text{relaxation terms}$. Two relaxation terms are accounted for in this derivation, corresponding to spontaneous emission decay from the excited state at a rate Γ_r and electron spin pure dephasing at a rate Γ_e. The system investigated in this appendix is not considered closed; the population is not conserved to the basis states considered here, and thus population is lost over time due to the relaxation terms written below. However, this does not affect the overall quantitative results for the scattering terms, since the work is performed in the perturbation theory limit of a weak probe field compared to the pump which always re-initializes the system to the $|1\rangle$ state after a scattering event that causes a transition to the $|2\rangle$ state.

The Lindblad super-operator formalism may be used here to derive the relaxation terms for open quantum systems in the presence of non-unitary action. The new Lindblad relaxation terms are added to the density matrix equations of motion in the form

$$\mathcal{L} = \sum_j \left[2L_j \rho L_j^\dagger - \{L_j^\dagger L_j, \rho\} \right] \tag{A.5}$$

where $\{x, y\} = xy + yx$ and L_j are the Lindblad operators associated with the decay and dephasing processes [6]. The Lindblad operators used in this derivation are equal to

$$L = \begin{bmatrix} \sqrt{\Gamma_e} & 0 \\ 0 & 0 \end{bmatrix} + \begin{bmatrix} 0 & \sqrt{\Gamma_r} \\ 0 & 0 \end{bmatrix} \tag{A.6}$$

where the only non-zero elements occur in the $|1;0\rangle$ and $|e;0\rangle$ subspace. The resulting Lindblad relaxation terms are equal to

$$\mathcal{L} = \begin{bmatrix} \Gamma_r \rho_{1;0,1;0} & -\frac{1}{2}(\Gamma_e + \Gamma_r)\rho_{1;0,e;0} & -\frac{1}{2}\Gamma_e \rho_{1;0,1;a} & -\frac{1}{2}\Gamma_e \rho_{1;0,2,b} \\ -\frac{1}{2}(\Gamma_e + \Gamma_r)\rho_{e;0,1;0} & -\Gamma_r \rho_{e;0,e;0} & -\frac{1}{2}\Gamma_r \rho_{e;0,1;a} & -\frac{1}{2}\Gamma_r \rho_{e;0,2;b} \\ -\frac{1}{2}\Gamma_e \rho_{1;a,1;0} & -\frac{1}{2}\Gamma_r \rho_{1;a,e;0} & 0 & 0 \\ -\frac{1}{2}\Gamma_e \rho_{2;b,1;0} & -\frac{1}{2}\Gamma_r \rho_{2;b,e;0} & 0 & 0 \end{bmatrix} \tag{A.7}$$

Thus, population decay is observed due to spontaneous emission, dephasing of the optically-driven coherences occurs proportional to the spontaneous decay rate divided by two, and coherences involving the ground states decay due to the pure dephasing term proportional to Γ_e, where no T_1^e-type terms (longitudinal relaxation of the electron) have been included.

The scattering spectrum may now be determined using perturbation theory methods. First, the density matrix equations of motion are calculated for the entire system without further approximations being made. Reproducing all sixteen equations is cumbersome and will not be done here. However, two perturbation theory chains (corresponding to double-sided Feynman diagrams) may be written down as follows.

The scattering into the quantum fields $\hat{a}$ and $\hat{b}$ corresponds to the following terms

[45]:

$$\mathcal{I} = \frac{d}{dt}\left[\rho_{1;a,1;a} + \rho_{2;b,2;b}\right] \tag{A.8}$$

Starting from the 0th order assumption in perturbation theory that the density matrix is prepared via optical pumping to $\rho^{(0)}_{1;0,1,0} = 1$, the two lowest order chains can be written down as

$$\begin{aligned} &1.\ \rho_{1;0,1;0} \xrightarrow{\chi} \rho_{1;0,e;0} \xrightarrow{g_1} \rho_{1;0,1;a} \xrightarrow{\chi} \rho_{e;0,1;a} \xrightarrow{g_1} \dot{\rho}_{1;a,1;a} + c.c. \\ &2.\ \rho_{1;0,1;0} \xrightarrow{\chi} \rho_{1;0,e;0} \xrightarrow{g_2} \rho_{1;0,2;b} \xrightarrow{\chi} \rho_{e;0,2;b} \xrightarrow{g_2} \dot{\rho}_{2;b,2;b} + c.c. \end{aligned} \tag{A.9}$$

These chains are calculated below, starting with the first chain. Combining the unitary evolution from the Hamiltonian and the Lindblad terms, the equation of motion for $\rho_{1;0,e;0}$ is given by

$$\begin{aligned} &\frac{d}{dt}\rho_{1;0,e;0} = \\ &-\frac{\Gamma_e}{2}\rho_{1;0,e;0} - \frac{\Gamma_r}{2}\rho_{1;0,e;0} \quad + ig_1 e^{-i\delta_1^a t}\rho_{1;0,1;a} + ig_2 e^{-i\delta_2^b t}\rho_{1;0,2;b} + i\chi e^{-i\delta_1 t}(\rho_{1;0,1;0} - \rho_{e;0,e;0}) \\ &\qquad\qquad \approx -(\frac{\Gamma_e + \Gamma_r}{2})\rho_{1;0,e;0} + i\chi e^{-i\delta_1 t}\rho^{(0)}_{1;0,1;0} \end{aligned} \tag{A.10}$$

where the only terms kept in the last line are the 0th order initial population and the coherence between $|1;0\rangle$ and $|e;0\rangle$ generated by the classical field χ. Integrating formally [45], the resulting coherence term is given by

$$\rho_{1;0,e;0} = i\chi\rho^{(0)}_{1;0,1;0}\int_0^t e^{-1/2(\Gamma_e+\Gamma_r)(t-t')}e^{-i\delta_1 t'}dt' \approx \frac{i\chi\rho^{(0)}_{1;0,1;0}}{\left[\frac{1}{2}(\Gamma_e+\Gamma_r) - i\delta_1\right]}e^{-i\delta_1 t} \tag{A.11}$$

where the transient term proportional to $e^{-1/2(\Gamma_e+\Gamma_r)t}$ is thrown away since the scattering is typically measured in a CW experiment. This same formal integration process is carried out for the remaining terms in the perturbation chain, plugging in the result from the previous calculations into each consecutive step. The equations

of motions including only the relevant terms in the chain are written below

$$\begin{aligned}
\frac{d}{dt}\rho_{1;0,1;a} &\approx -\frac{\Gamma_e}{2}\rho_{1;0,1;a} + ig_1 e^{i\delta_1^a t}\rho_{1;0,e;0} \\
\frac{d}{dt}\rho_{e;0,1;a} &\approx -\frac{\Gamma_r}{2}\rho_{e;0,1;a} - i\chi e^{i\delta_1 t}\rho_{1;0,1;a} \\
\frac{d}{dt}\rho_{1;a,1;a} &\approx -ig_1 e^{-i\delta_1^a t}\rho_{e;0,1;a} + c.c.
\end{aligned} \tag{A.12}$$

The result of following the perturbation chain by solving each equation starting from the top gives the first scattering term

$$\mathcal{I}_a = \frac{d}{dt}\rho_{1;a,1;a} \approx 2\mathrm{Re}\left[\frac{g_1^2\chi^2\rho_{1;0,1;0}^{(0)}}{\left[\frac{1}{2}(\Gamma_e+\Gamma_r) - i\delta_1\right]\left[\frac{1}{2}\Gamma_e + i(\omega-\omega_a)\right]\left[-\frac{1}{2}\Gamma_r + i\delta_1^a\right]}\right] \tag{A.13}$$

which is the product of three Lorentzians. The first Lorentzian has the FWHM $\frac{1}{2}(\Gamma_e+\Gamma_r)$ and is maximized when $\delta_1 = 0$, or that the laser is brought into resonance with $|1\rangle \rightarrow |e\rangle$ transition; this Lorentzian determines the overall scattering strength into the two resulting modes. The next two Lorentzians give the two quantum field scattering modes. The first mode has a width $\frac{1}{2}\Gamma_e$ centered at the laser frequency; this is the *Rayleigh scattering* term. The second mode has the spontaneous emission width and is always found at the natural frequency of the $|1\rangle \rightarrow |e\rangle$ transition. The overall result is interesting because it proves that the Rayleigh scattering line has a width associated with the ground state dephasing/relaxation and *not* the linewidth associated with spontaneous emission, a result that is often times claimed in the literature without support.

The second perturbation chain is calculated using the same procedure. The first term in the chain is the same, given by Equation A.11. The next three equations are given by

$$\begin{aligned}
\frac{d}{dt}\rho_{1;0,2;b} &\approx -\frac{\Gamma_e}{2}\rho_{1;0,2;b} + ig_2 e^{i\delta_2^b t}\rho_{1;0,e;0} \\
\frac{d}{dt}\rho_{e;0,2;b} &\approx -\frac{\Gamma_r}{2}\rho_{e;0,2;b} - i\chi e^{i\delta_1 t}\rho_{1;0,2;b} \\
\frac{d}{dt}\rho_{2;b,2;b} &\approx -ig_2 e^{-i\delta_2^b t}\rho_{e;0,2;b} + c.c.
\end{aligned} \tag{A.14}$$

The result of the perturbation theory calculation gives the second scattering term

$$\mathcal{I}_b = \frac{d}{dt}\rho_{2;b,2;b} \approx 2\mathrm{Re}\left[\frac{g_2^2\chi^2\rho^{(0)}_{1;0,1;0}}{\left[\frac{1}{2}(\Gamma_e+\Gamma_r)-i\delta_1\right]\left[-\frac{1}{2}\Gamma_e+i(\omega-\Delta_e-\omega_b)\right]\left[\frac{1}{2}\Gamma_r+i\delta_2^b\right]}\right] \tag{A.15}$$

Again, the result is the product of three Lorentzians, with the first Lorentzian centered at the transition being driven by the classical field, giving the overall scattering intensity into the other two modes. However, the second Lorentzian has a width given by the ground state dephasing and is centered at $\omega_b = \omega - \Delta_e$, which is exactly the *Raman scattering* mode; this scattering mode always comes out at the laser frequency minus the ground state splitting, in the "Stokes" case. Switching the roles of the pump and probe will result in Raman scattering at a frequency given by $\omega+\Delta_e$, or the "anti-Stokes" mode. Additionally, there is a spontaneous emission term in the third Lorentzian which has the spontaneous emission width and is centered at the natural frequency of the $|2\rangle \rightarrow |e\rangle$ transition.

Thus, in the weak-field limits in which perturbation theory on the probe and pump fields is valid, the Raman scattering may be utilized as a high-resolution spectrosopic tool to examine the ground state splitting (electron spin state, in this case). First and foremost, if the ground state splitting is larger than the spontaneous emission width, then the Raman peak is spectrally separated from the spontaneous emission, unlike the Rayleigh scattering when the laser is near-resonant. Additionally, in the QD system, the ground state dephasing is very slow compared to the spontaneous emission width; thus the Raman channel is enhanced considerably compared to the spontaneous emission channel and is orders of magnitudes narrower than the spontaneous emission linewidth, allowing for precise determinations of ground state splittings via the utilization of high-finesse tunable etalons (Chapter 5).

BIBLIOGRAPHY

BIBLIOGRAPHY

[1] F. Meier, B.P. Zakharchenya, *Optical Orientation*, North-Holland, ISBN 9780444867414 (1984).

[2] D. M. Bruls, J. W. Vugs, P. M. Koenraad, H. W. Salemink, J. H. Wolter, M. Hopkinson, M. S. Skolnick, F. Long, S. P. Gill, "Determination of the shape and indium distribution of low-growth-rate InAs quantum dots by cross-sectional scanning tunneling microscopy", *Appl. Phys. Lett.* **81**, 1708 (2002).

[3] R. J. Warburton, "Single spins in self-assembled quantum dots", *Nat. Mater.* **12**, 483 (2013).

[4] R. P. Feynman, "Simulating physics with computers", *Int. J. Theor. Phys.* **21**, 467 (1982).

[5] R. P. Feynman, "Quantum mechanical computers", *Found. Phys.* **16**, 507 (1986).

[6] M. Nielsen, I. L. Chuang, *Quantum computation and quantum information*, Cambridge University Press, Cambridge (2010).

[7] J. Preskill, "Quantum computing and the entanglement frontier", 1–18 (2012).

[8] M.-H. Yung, "Quantum supremacy: some fundamental concepts", *Natl. Sci. Rev.* 1–2 (2018).

[9] P. Shor, "Algorithms for quantum computation: discrete logarithms and factoring", in "Proc. 35th Annu. Symp. Found. Comput. Sci.", 124–134, IEEE Comput. Soc. Press, ISBN 0-8186-6580-7 (1994).

[10] A. Aspuru-Guzik, "Simulated Quantum Computation of Molecular Energies", *Science* **309**, 1704 (2005).

[11] C. H. Bennett, G. Brassard, "WITHDRAWN: Quantum cryptography: Public key distribution and coin tossing", *Theor. Comput. Sci.* (2011).

[12] A. Huang, S. Barz, E. Andersson, V. Makarov, "Implementation vulnerabilities in general quantum cryptography", *New J. Phys.* **20**, 103016 (2018).

[13] E. Diamanti, H.-k. Lo, B. Qi, Z. Yuan, "Practical challenges in quantum key distribution", *Nat. Publ. Gr.* 1–12 (2016).

[14] L. Pezz, A. Smerzi, M. K. Oberthaler, "Quantum metrology with nonclassical states of atomic ensembles", **90** (2018).

[15] LIGO Collaboration, "Sensitivity of the Advanced LIGO detectors at the beginning of gravitational wave astronomy", *Phys. Rev. D* **93**, 112004 (2016).

[16] D. P. Divincenzo, "The Physical Implementation of Quantum Computation", **48**, 771 (2000).

[17] T. D. Ladd, F. Jelezko, R. Laflamme, Y. Nakamura, C. Monroe, J. L. O'Brien, "Quantum computers", *Nature* **464**, 45 (2010).

[18] N. Ofek, A. Petrenko, R. Heeres, P. Reinhold, Z. Leghtas, B. Vlastakis, Y. Liu, L. Frunzio, S. M. Girvin, L. Jiang, M. Mirrahimi, M. H. Devoret, R. J. Schoelkopf, "Extending the lifetime of a quantum bit with error correction in superconducting circuits", *Nature* **536**, 441 (2016).

[19] M. V. G. Dutt, L. Childress, L. Jiang, E. Togan, J. Maze, F. Jelezko, A. S. Zibrov, P. R. Hemmer, M. D. Lukin, "Quantum Register Based on Individual Electronic and Nuclear Spin Qubits in Diamond", *Science* **316**, 1312 (2007).

[20] G. Waldherr, Y. Wang, S. Zaiser, M. Jamali, T. Schulte-Herbrüggen, H. Abe, T. Ohshima, J. Isoya, J. F. Du, P. Neumann, J. Wrachtrup, "Quantum error correction in a solid-state hybrid spin register", *Nature* **506**, 204 (2014).

[21] T. E. Chupp, E. R. Oteiza, J. M. Richardson, T. R. White, "Precision frequency measurements with polarized He3, Ne21, and Xe129 atoms", *Phys. Rev. A* **38**, 3998 (1988).

[22] N. A. Gershenfeld, I. L. Chuang, N. A. Gershenfeld, I. L. Chuang, "Bulk Spin-Resonance Quantum Computation", **350** (2014).

[23] L. M. K. Vandersypen, I. L. Chuang, "NMR techniques for quantum control and computation", *Rev. Mod. Phys.* **76**, 1037 (2004).

[24] I. Chuang, L. M. K. Vandersypen, X. Zhou, D. Leung, S. Lloyd, "Experimental realization of a quantum algorithm", *Nature* 2 (1998).

[25] L. M. Vandersypen, M. Breyta, G. Steffen, C. S. Yannoni, M. H. Sherwood, I. L. Chuang, "Experimental realization of Shor's quantum factoring algorithm using nuclear magnetic resonance", *Nature* **414**, 883 (2001).

[26] J. I. Cirac, P. Zoller, "Quantum Computations with Cold Trapped Ions", *Phys. Rev. Lett.* **74**, 4091 (1995).

[27] J. Zhang, G. Pagano, P. W. Hess, A. Kyprianidis, P. Becker, H. Kaplan, A. V. Gorshkov, Z. X. Gong, C. Monroe, "Observation of a many-body dynamical phase transition with a 53-qubit quantum simulator", *Nature* **551**, 601 (2017).

[28] M. H. Devoret, R. J. Schoelkopf, "Superconducting Circuits for Quantum Information: An Outlook", *Science* **339**, 1169 (2013).

[29] Y. Nakamura, Y. A. Pashkin, J. S. Tsai, "Coherent control of macroscopic quantum states in a single-Cooper-pair box", *Nature* **398**, 786 (1999).

[30] D. G. Cory, M. D. Price, W. Maas, E. Knill, R. Laflamme, W. H. Zurek, T. F. Havel, S. S. Somaroo, "Experimental quantum error correction", *Phys. Rev. Lett.* **81**, 2152 (1998).

[31] J. Chiaverini, D. Leibfried, T. Schaetz, M. D. Barrett, R. B. Blakestad, J. Britton, W. M. Itano, J. D. Jost, E. Knill, C. Langer, R. Ozeri, D. J. Wineland, "Realization of quantum error correction", *Nature* **432**, 602 (2004).

[32] D. V. Averin, "Adiabatic quantum computation with Cooper pairs", *Solid State Commun.* **105**, 659 (1998).

[33] D. Aharonov, W. van Dam, J. Kempe, Z. Landau, S. Lloyd, O. Regev, "Adiabatic Quantum Computation is Equivalent to Standard Quantum Computation", **37**, 166 (2004).

[34] A. Mizel, D. A. Lidar, M. Mitchell, "Simple proof of equivalence between adiabatic quantum computation and the circuit model", *Phys. Rev. Lett.* **99**, 1 (2007).

[35] S. Boixo, T. F. Rønnow, S. V. Isakov, Z. Wang, D. Wecker, D. A. Lidar, J. M. Martinis, M. Troyer, "Evidence for quantum annealing with more than one hundred qubits", *Nat. Phys.* **10**, 218 (2014).

[36] R. Harris, Y. Sato, A. J. Berkley, M. Reis, F. Altomare, M. H. Amin, K. Boothby, P. Bunyk, C. Deng, C. Enderud, S. Huang, E. Hoskinson, M. W. Johnson, E. Ladizinsky, N. Ladizinsky, T. Lanting, R. Li, T. Medina, R. Molavi, R. Neufeld, T. Oh, I. Pavlov, I. Perminov, G. Poulin-Lamarre, C. Rich, A. Smirnov, L. Swenson, N. Tsai, M. Volkmann, J. Whittaker, J. Yao, "Phase transitions in a programmable quantum spin glass simulator", *Science* **361**, 162 (2018).

[37] W. M. Kaminsky, S. Lloyd, "Scalable Architecture for Adiabatic Quantum Computing of NP-Hard Problems", 1–10 (2002).

[38] E. Knill, R. Laflamme, G. J. Milburn, "A scheme for efficient quantum computation with linear optics", *Nature* **409**, 46 (2001).

[39] Y. Zhou, M. Mirhosseini, S. Oliver, J. Zhao, S. M. H. Rafsanjani, M. P. J. Lavery, A. E. Willner, R. W. Boyd, "High-dimensional free-space quantum key distribution using spin, azimuthal, and radial quantum numbers", 1–23 (2018).

[40] J. C. F. Matthews, A. Politi, A. Stefanov, J. L. O'Brien, "Manipulation of multiphoton entanglement in waveguide quantum circuits", *Nat. Photonics* **3**, 346 (2009).

[41] T. Rudolph, "Why I am optimistic about the silicon-photonic route to quantum computing", **030901** (2016).

[42] C. Roques-Carmes, Y. Shen, C. Zanoci, M. Prabhu, F. Atieh, L. Jing, T. Dubcek, V. Ceperic, A. Harrow, J. D. Joannopoulos, D. Englund, M. Soljacic, "Photonic Recurrent Ising Sampler", *Submitt. to Nat. Photonics - Manuscr. available upon Req.* 1–29 (2018).

[43] Y. Yamamoto, K. Aihara, T. Leleu, K.-i. Kawarabayashi, S. Kako, M. Fejer, K. Inoue, H. Takesue, "Coherent Ising machinesoptical neural networks operating at the quantum limit", *npj Quantum Inf.* **3**, 49 (2017).

[44] P. L. McMahon, A. Marandi, Y. Haribara, R. Hamerly, C. Langrock, S. Tamate, T. Inagaki, H. Takesue, S. Utsunomiya, K. Aihara, R. L. Byer, M. M. Fejer, H. Mabuchi, Y. Yamamoto, "A fully programmable 100-spin coherent Ising machine with all-to-all connections", *Science* **354**, 614 (2016).

[45] P. R. Berman, V. Malinovsky, *Principles of Laser Spectroscopy and Quantum Optics*, Princeton University Press, Princeton (2010).

[46] C. M. Gentry, J. M. Shainline, M. T. Wade, M. J. Stevens, S. D. Dyer, X. Zeng, F. Pavanello, T. Gerrits, S. W. Nam, R. P. Mirin, M. A. Popović, "Quantum-correlated photon pairs generated in a commercial 45nm complementary metal-oxide semiconductor microelectronic chip", *Optica* **2**, 1065 (2015).

[47] U. Paudel, *Mode Engineering of Single Photons from Cavity Spontaneous Parametric Down-Conversion Source and Quantum Dots*, Ph.D. thesis, University of Michigan (2017).

[48] N. Somaschi, V. Giesz, L. De Santis, J. C. Loredo, M. P. Almeida, G. Hornecker, S. L. Portalupi, T. Grange, C. Antón, J. Demory, C. Gómez, I. Sagnes, N. D. Lanzillotti-Kimura, A. Lemaítre, A. Auffeves, A. G. White, L. Lanco, P. Senellart, "Near-optimal single-photon sources in the solid state", *Nat. Photonics* **10**, 340 (2016).

[49] P. Senellart, G. Solomon, A. White, "High-performance semiconductor quantum-dot single-photon sources", *Nat. Nanotechnol.* **12**, 1026 (2017).

[50] X. Li, "An All-Optical Quantum Gate in a Semiconductor Quantum Dot", *Science* **301**, 809 (2003).

[51] J. Zhang, J. S. Wildmann, F. Ding, R. Trotta, Y. Huo, E. Zallo, D. Huber, A. Rastelli, O. G. Schmidt, "High yield and ultrafast sources of electrically triggered entangled-photon pairs based on strain-tunable quantum dots", *Nat. Commun.* **6**, 10067 (2015).

[52] Y. Chen, J. Zhang, M. Zopf, K. Jung, Y. Zhang, R. Keil, F. Ding, O. G. Schmidt, "Wavelength-tunable entangled photons from silicon-integrated IIIV quantum dots", *Nat. Commun.* **7**, 10387 (2016).

[53] R. Keil, M. Zopf, Y. Chen, B. Höfer, J. Zhang, F. Ding, O. G. Schmidt, "Solid-state ensemble of highly entangled photon sources at rubidium atomic transitions", *Nat. Commun.* **8** (2017).

[54] H. M. Meyer, R. Stockill, M. Steiner, C. Le Gall, C. Matthiesen, E. Clarke, A. Ludwig, J. Reichel, M. Atatüre, M. Köhl, "Direct Photonic Coupling of a Semiconductor Quantum Dot and a Trapped Ion", *Phys. Rev. Lett.* **114**, 123001 (2015).

[55] H. Huang, R. Trotta, Y. Huo, T. Lettner, J. S. Wildmann, J. Martín-Sánchez, D. Huber, M. Reindl, J. Zhang, E. Zallo, O. G. Schmidt, A. Rastelli, "Electrically-Pumped Wavelength-Tunable GaAs Quantum Dots Interfaced with Rubidium Atoms", *ACS Photonics* **4**, 868 (2017).

[56] D. Bouwmeester, J.-W. Pan, K. Mattle, M. Eibl, H. Weinfurter, A. Zeilinger, "Experimental quantum teleportation", *Nature* **390**, 575 (1997).

[57] B. Urbaszek, X. Marie, T. Amand, O. Krebs, P. Voisin, P. Maletinsky, A. Högele, A. Imamoglu, "Nuclear spin physics in quantum dots: An optical investigation", *Rev. Mod. Phys.* **85**, 79 (2013).

[58] X. Xu, Y. Wu, B. Sun, Q. Huang, J. Cheng, D. G. Steel, A. S. Bracker, D. Gammon, C. Emary, L. J. Sham, "Fast spin state initialization in a singly charged InAs-GaAs quantum dot by optical cooling", *Phys. Rev. Lett.* **99**, 097401 (2007).

[59] E. D. Kim, K. Truex, Y. Wu, a. Amo, X. Xu, D. Steel, a. S. Bracker, D. Gammon, L. J. Sham, "Picosecond optical spectroscopy of a single negatively charged self-assembled InAs quantum dot", *Appl. Phys. Lett.* **97**, 113110 (2010).

[60] E. D. Kim, K. Truex, X. Xu, B. Sun, D. G. Steel, A. S. Bracker, D. Gammon, L. J. Sham, "Fast spin rotations by optically controlled geometric phases in a charge-tunable InAs quantum Dot", *Phys. Rev. Lett.* **104**, 167401 (2010).

[61] E. Kim, *The coherent optical spectroscopy and control of an electron spin in a self-assembled quantum dot for quantum computing*, Ph.D. thesis, University of Michigan (2009).

[62] C. M. E. Chow, *Towards a Universal Two-Qubit Gate with Self-Assembled InAs Quantum Dot Molecules*, Ph.d. thesis, University of Michigan (2015).

[63] C. M. E. Chow, A. M. Ross, D. Kim, D. Gammon, a. S. Bracker, L. J. Sham, D. G. Steel, "Nonlocal Nuclear Spin Quieting in Quantum Dot Molecules: Optically Induced Extended Two-Electron Spin Coherence Time", *Phys. Rev. Lett.* **117**, 077403 (2016).

[64] D. Kim, S. G. Carter, A. Greilich, A. S. Bracker, D. Gammon, "Ultrafast optical control of entanglement between two quantum dot spins", *Nat. Phys.* **7**, 24 (2010).

[65] L. Webster, *Precursor to spin-photon entanglement in a single indium arsenide/gallium arsenide quantum dot*, Ph.D. thesis, University of Michigan (2012).

[66] D. J. Eaglesham, M. Cerullo, "Dislocation-free Stranski-Krastanow growth of Ge on Si(100)", *Phys. Rev. Lett.* **64**, 1943 (1990).

[67] O. Brandt, L. Tapfer, K. Ploog, R. Bierwolf, M. Hohenstein, F. Phillipp, H. Lage, A. Heberle, "InAs quantum dots in a single-crystal GaAs matrix", *Phys. Rev. B* **44**, 8043 (1991).

[68] U. Woggon, *Optical properties of semiconductor quantum dots*, Springer, Berlin (1997).

[69] Z. Wasilewski, S. Fafard, J. McCaffrey, "Size and shape engineering of vertically stacked self-assembled quantum dots", *J. Cryst. Growth* **201-202**, 1131 (1999).

[70] C. Kittel, *Introduction to solid state physics*, Wiley, New York, 4th edition (1971).

[71] P. Yu, M. Cardona, *Fundamentals of semiconductors : physics and materials properties*, Springer, Berlin (1996).

[72] G. Munschy, B. Stébé, "Nonadiabatic calculation of the binding energy of the excitonic molecule ion", *Phys. Status Solidi* **72**, 135 (1975).

[73] B. Stébé, A. Ainane, "Ground state energy and optical absorption of excitonic trions in two dimensional semiconductors", *Superlattices Microstruct.* **5**, 545 (1989).

[74] Y. Fu, K. A. Chao, "Exciton binding energy in GaAs/AlxGa1-xAs multiple quantum wells", *Phys. Rev. B* **43**, 12626 (1991).

[75] R. L. Greene, K. K. Bajaj, D. E. Phelps, "Energy levels of Wannier excitons in GaAs-Ga1-xAlxAs quantum-well structures", *Phys. Rev. B* **29**, 1807 (1984).

[76] M. Dutt, *Coherent optical manipulation of electron spin in charged semiconductor quantum dots*, Ph.D. thesis, University of Michigan (2004).

[77] J. Sakurai, *Advanced quantum mechanics*, Addison Wesley, Reading, Massachussetts (1967).

[78] M. E. Ware, E. A. Stinaff, D. Gammon, M. F. Doty, A. S. Bracker, D. Gershoni, V. L. Korenev, . C. Bdescu, Y. Lyanda-Geller, T. L. Reinecke, "Polarized fine structure in the photoluminescence excitation spectrum of a negatively charged quantum dot", *Phys. Rev. Lett.* **95**, 1 (2005).

[79] C. Nelson, *Coherent Nonlinear Optical Spectroscopy of InGaN Disks in GaN Nanowires*, Ph.D. thesis, University of Michigan (2016).

[80] P. Offermans, P. M. Koenraad, J. H. Wolter, K. Pierz, M. Roy, P. A. Maksym, "Atomic-scale structure and photoluminescence of InAs quantum dots in GaAs and AlAs", *Phys. Rev. B - Condens. Matter Mater. Phys.* **72**, 1 (2005).

[81] J. Singh, *Electronic and optoelectronic properties of semiconductor structures*, Cambridge University Press, Cambridge (2003).

[82] M. Bayer, G. Ortner, O. Stern, A. Kuther, A. A. Gorbunov, A. Forchel, P. Hawrylak, S. Fafard, K. Hinzer, T. L. Reinecke, S. N. Walck, J. P. Reithmaier, F. Klopf, F. Schäfer, "Fine structure of neutral and charged excitons in self-assembled In(Ga)As/(Al)GaAs quantum dots", *Phys. Rev. B* **65**, 195315 (2002).

[83] M. Bayer, O. Stern, A. Kuther, A. Forchel, "Spectroscopic study of dark excitons in In", **61**, 7273 (2000).

[84] C. P. Slichter, *Principles of Magnetic Resonance*, Springer-Verlag, New York, 3rd edition (1992).

[85] X. Xu, W. Yao, B. Sun, D. G. Steel, A. S. Bracker, D. Gammon, L. J. Sham, "Optically controlled locking of the nuclear field via coherent dark-state spectroscopy.", *Nature* **459**, 1105 (2009).

[86] D. Press, T. D. Ladd, B. Zhang, Y. Yamamoto, "Complete quantum control of a single quantum dot spin using ultrafast optical pulses.", *Nat. Phys.* **456**, 218 (2008).

[87] K. Truex, *Optical coherent control of a single charged indium arsenide quantum dot*, Ph.D. thesis, University of Michigan (2011).

[88] J. Fischer, W. A. Coish, D. V. Bulaev, D. Loss, "Spin decoherence of a heavy hole coupled to nuclear spins in a quantum dot", *Phys. Rev. B* **78**, 155329 (2008).

[89] I. A. Merkulov, A. L. Efros, M. Rosen, "Electron spin relaxation by nuclei in semiconductor quantum dots", *Phys. Rev. B* **65**, 205309 (2002).

[90] P. W. Shor, J. Preskill, "Simple proof of security of the BB84 quantum key distribution protocol", *Phys. Rev. Lett.* **85**, 441 (2000).

[91] C. Y. Lu, Y. Zhao, A. N. Vamivakas, C. Matthiesen, S. Fält, A. Badolato, M. Atatüre, "Direct measurement of spin dynamics in InAs/GaAs quantum dots using time-resolved resonance fluorescence", *Phys. Rev. B - Condens. Matter Mater. Phys.* **81**, 3 (2010).

[92] J. Hansom, C. H. H. Schulte, C. Le Gall, C. Matthiesen, E. Clarke, M. Hugues, J. M. Taylor, M. Atatüre, "Environment-assisted quantum control of a solid-state spin via coherent dark states", *Nat. Phys.* **10**, 725 (2014).

[93] G. E. Pikus, F. G. Pikus, "The mechanism of heavy and light hole mixing in GaAs/AlAs superlattices", *Solid State Commun.* **89**, 319 (1994).

[94] T. Belhadj, T. Amand, A. Kunold, C.-M. Simon, T. Kuroda, M. Abbarchi, T. Mano, K. Sakoda, S. Kunz, X. Marie, B. Urbaszek, D. F. Mexico, "Impact of heavy hole-light hole coupling on optical selection rules in GaAs quantum dots", *Appl. Phys. Lett* **97**, 051111 (2010).

[95] D. N. Krizhanovskii, A. Ebbens, A. I. Tartakovskii, F. Pulizzi, T. Wright, M. S. Skolnick, M. Hopkinson, "Individual neutral and charged InxGa1-xAs-GaAs quantum dots with strong in-plane optical anisotropy", *Phys. Rev. B - Condens. Matter Mater. Phys.* **72**, 8 (2005).

[96] A. V. Koudinov, I. A. Akimov, Y. G. Kusrayev, F. Henneberger, "Optical and magnetic anisotropies of the hole states in Stranski-Krastanov quantum dots", *Phys. Rev. B* **70**, 241305 (2004).

[97] E. L. Ivchenko, G. E. Pikus, *Superlattices and other heterostructures : symmetry and optical phenomena*, Springer-Verlag, Berlin (1995).

[98] M. Atatüre, J. Dreiser, A. Badolato, A. Högele, K. Karrai, A. Imamoglu, "Quantum-dot spin-state preparation with near-unity fidelity.", *Science* **312**, 551 (2006).

[99] H. Haus, *Waves and fields in optoelectronics*, Prentice-Hall, Englewood Cliffs, New Jersey (1984).

[100] A. Yariv, P. Yeh, *Optical waves in crystals : propagation and control of laser radiation*, Wiley, New York (1984).

[101] P. A. Dalgarno, J. M. Smith, J. McFarlane, B. D. Gerardot, K. Karrai, A. Badolato, P. M. Petroff, R. J. Warburton, "Coulomb interactions in single charged self-assembled quantum dots: Radiative lifetime and recombination energy", *Phys. Rev. B - Condens. Matter Mater. Phys.* **77**, 1 (2008).

[102] D. C. Reynolds, K. K. Bajaj, C. W. Litton, G. Peters, P. W. Yu, J. D. Parsons, "Refractive index, n , and dispersion, d n / d λ, of GaAs at 2 K determined from FabryPerot cavity oscillations", *J. Appl. Phys.* **61**, 342 (1987).

[103] G. Björk, S. Machida, Y. Yamamoto, K. Igeta, "Modification of spontaneous emission rate in planar dielectric microcavity structures", *Phys. Rev. A* **44**, 669 (1991).

[104] C. Klingshirn, *Semiconductor optics*, Springer, Berlin (1997).

[105] M. Grundmann, J. Christen, N. N. Ledentsov, J. Böhrer, D. Bimberg, S. S. Ruvimov, , P. Werner, U. Richter, U. Gösele, J. Heydenreich, V. M. Ustinov, A. Y. Egorov, A. E. Zhukov, P. S. Kop'ev, Z. I. Alferov, "Ultranarrow Luminescence Lines from Single Quantum Dots", *Phys. Rev. Lett.* **74**, 4043 (1995).

[106] P. F. Braun, B. Urbaszek, T. Amand, X. Marie, O. Krebs, B. Eble, A. Lemaître, P. Voisin, "Bistability of the nuclear polarization created through optical pumping in In1-x Gax As quantum dots", *Phys. Rev. B - Condens. Matter Mater. Phys.* **74**, 1 (2006).

[107] R. Heitz, M. Veit, N. N. Ledentsov, A. Hoffmann, D. Bimberg, V. M. Ustinov, P. S. Kop'ev, Z. I. Alferov, "Energy relaxation by multiphonon processes in InAs/GaAs quantum dots", *Phys. Rev. B* **56**, 10435 (1997).

[108] J. R. Schaibley, A. P. Burgers, G. A. McCracken, D. G. Steel, A. S. Bracker, D. Gammon, L. J. Sham, "Direct detection of time-resolved Rabi oscillations in a single quantum dot via resonance fluorescence", *Phys. Rev. B* **87**, 115311 (2013).

[109] E. B. Flagg, S. V. Polyakov, T. Thomay, G. S. Solomon, "Dynamics of nonclassical light from a single solid-state quantum emitter", *Phys. Rev. Lett.* **109**, 1 (2012).

[110] T. Huber, A. Predojević, D. Föger, G. Solomon, G. Weihs, "Optimal excitation conditions for indistinguishable photons from quantum dots", *New J. Phys.* **17** (2015).

[111] J. Puls, M. Rabe, H. J. Wünsche, F. Henneberger, "Magneto-optical study of the exciton fine structure in self-assembled CdSe quantum dots", *Phys. Rev. B - Condens. Matter Mater. Phys.* **60**, R16303 (1999).

[112] L. C. Andreani, F. Bassani, "Exchange interaction and polariton effects in quantum-well excitons", *Phys. Rev. B* **41**, 7536 (1990).

[113] H. W. Van Kesteren, E. C. Cosman, W. A. Van Der Poel, C. T. Foxon, "Fine structure of excitons in type-II GaAs/AlAs quantum wells", *Phys. Rev. B* **41**, 5283 (1990).

[114] B. Di Bartolo, *Collective Excitations in Solids*, volume 53, ISBN 978-1-4684-8880-7 (1983).

[115] Y. Onodera, Y. Toyozawa, "Excitons in Alkali Halides", *J. Phys. Soc. Japan* **22**, 833 (1967).

[116] E. Merzbacher, *Quantum mechanics*, Wiley, New York (1998).

[117] A. J. Bennett, R. B. Patel, J. Skiba-Szymanska, C. A. Nicoll, I. Farrer, D. A. Ritchie, A. J. Shields, "Giant Stark effect in the emission of single semiconductor quantum dots", *Appl. Phys. Lett.* **97**, 1 (2010).

[118] P. Jin, C. M. Li, Z. Y. Zhang, F. Q. Liu, Y. H. Chen, X. L. Ye, B. Xu, Z. G. Wang, "Quantum-confined Stark effect and built-in dipole moment in self-assembled InAs/GaAs quantum dots", *Appl. Phys. Lett.* **85**, 2791 (2004).

[119] W. Sheng, J. P. Leburton, "Anomalous Quantum-Confined Stark Effects in Stacked [Formula presented] Self-Assembled Quantum Dots", *Phys. Rev. Lett.* **88**, 4 (2002).

[120] W. Sheng, J.-P. Leburton, "Absence of correlation between built-in electric dipole moment and quantum Stark effect in single InAs/GaAs self-assembled quantum dots", *Phys. Rev. B* **67**, 125308 (2003).

[121] M. Kroner, A. O. Govorov, S. Remi, B. Biedermann, S. Seidl, A. Badolato, P. M. Petroff, W. Zhang, R. Barbour, B. D. Gerardot, R. J. Warburton, K. Karrai, "The nonlinear Fano effect", *Nature* **451**, 311 (2008).

[122] H. J. Kimble, L. Mandel, "Theory of resonance fluorescence", *Phys. Rev. A* **13**, 2123 (1976).

[123] C. Matthiesen, A. N. Vamivakas, M. Atatüre, "Subnatural Linewidth Single Photons from a Quantum Dot", *Phys. Rev. Lett.* **108**, 093602 (2012).

[124] J. R. Schaibley, A. P. Burgers, G. A. McCracken, L. M. Duan, P. R. Berman, D. G. Steel, A. S. Bracker, D. Gammon, L. J. Sham, "Demonstration of quantum entanglement between a single electron spin confined to an InAs quantum dot and a photon", *Phys. Rev. Lett.* **110**, 167401 (2013).

[125] W. B. Gao, P. Fallahi, E. Togan, J. Miguel-Sanchez, A. Imamoglu, "Observation of entanglement between a quantum dot spin and a single photon", *Nature* **491**, 426 (2012).

[126] K. De Greve, L. Yu, P. L. McMahon, J. S. Pelc, C. M. Natarajan, N. Y. Kim, E. Abe, S. Maier, C. Schneider, M. Kamp, S. Höfling, R. H. Hadfield, A. Forchel, M. M. Fejer, Y. Yamamoto, "Quantum-dot spinphoton entanglement via frequency downconversion to telecom wavelength", *Nature* **491**, 421 (2012).

[127] L. M. Duan, H. J. Kimble, "Scalable Photonic Quantum Computation through Cavity-Assisted Interactions", *Phys. Rev. Lett.* **92**, 127902 (2004).

[128] J. I. Cirac, P. Zoller, H. J. Kimble, H. Mabuchi, "Quantum state transfer and entanglement distribution among distant nodes in a quantum network", *Phys. Rev. Lett.* **78**, 4 (1996).

[129] H. J. Kimble, "The quantum internet", *Nature* **453**, 1023 (2008).

[130] P. Higdon, R. Juškaitis, T. Wilson, "The effect of detector size on the extinction coefficient in confocal polarization microscopes", *J. Microsc.* **187**, 8 (1997).

[131] M. Shribak, "Polarization aberrations caused by differential transmission and phase shift in high-numerical-aperture lenses: theory, measurement, and rectification", *Opt. Eng.* **41**, 943 (2002).

[132] M. Fleischhauer, A. Imamoglu, J. P. Marangos, "Electromagnetically induced transparency: Optics in coherent media", *Rev. Mod. Phys.* **77**, 633 (2005).

[133] K.-J. Boller, A. Imamolu, S. E. Harris, "Observation of electromagnetically induced transparency", *Phys. Rev. Lett.* **66**, 2593 (1991).

[134] A. S. Zibrov, M. D. Lukin, L. Hollberg, D. E. Nikonov, M. O. Scully, H. G. Robinson, V. L. Velichansky, "Experimental Demonstration of Enhanced Index of Refraction via Quantum Coherence in Rb", *Phys. Rev. Lett.* **76**, 3935 (1996).

[135] K. M. Weiss, J. M. Elzerman, Y. L. Delley, J. Miguel-Sanchez, A. Imamoglu, "Coherent Two-Electron Spin Qubits in an Optically Active Pair of Coupled InGaAs Quantum Dots", *Phys. Rev. Lett.* **109**, 107401 (2012).

[136] B. Sun, C. M. E. Chow, D. G. Steel, a. S. Bracker, D. Gammon, L. J. Sham, "Persistent Narrowing of Nuclear-Spin Fluctuations in InAs Quantum Dots Using Laser Excitation", *Phys. Rev. Lett.* **108**, 187401 (2012).

[137] D. V. Bulaev, D. Loss, "Spin relaxation and decoherence of holes in quantum dots", *Phys. Rev. Lett.* **95**, 1 (2005).

[138] C. Testelin, F. Bernardot, B. Eble, M. Chamarro, "Hole-spin dephasing time associated with hyperfine interaction in quantum dots", *Phys. Rev. B - Condens. Matter Mater. Phys.* **79**, 1 (2009).

[139] C. Latta, A. Srivastava, A. Imamoglu, "Hyperfine interaction-dominated dynamics of nuclear spins in self-assembled InGaAs quantum dots", *Phys. Rev. Lett.* **107**, 167401 (2011).

[140] Z. X. Gong, Z. Q. Yin, L. M. Duan, "Dynamics of the Overhauser field under nuclear spin diffusion in a quantum dot", *New J. Phys.* **13** (2011).

[141] D. Gammon, S. Brown, E. Snow, T. A. Kennedy, D. Katzer, D. Park, "Nuclear Spectroscopy in Single Quantum Dots: Nanoscopic Raman Scattering and Nuclear Magnetic Resonance", *Science* **277**, 85 (1997).

[142] C. Latta, A. Högele, Y. Zhao, A. N. Vamivakas, P. Maletinsky, M. Kroner, J. Dreiser, I. Carusotto, A. Badolato, D. Schuh, W. Wegscheider, M. Atatüre, A. Imamoglu, "Confluence of resonant laser excitation and bidirectional quantum-dot nuclear-spin polarization", *Nat. Phys.* **5**, 758 (2009).

[143] A. Abragam, *The Principles of Nuclear Magnetism*, Clarendon Press, Oxford (1961).

[144] E. R. Cohen, B. N. Taylor, "The 1986 CODATA Recommended Values of the Fundamental Physical Constants", *J. Phys. Chem. Ref. Data* **17**, 1795 (1988).

[145] M. J. Stanley, C. Matthiesen, J. Hansom, C. Le Gall, C. H. H. Schulte, E. Clarke, M. Atatüre, "Dynamics of a mesoscopic nuclear spin ensemble interacting with an optically driven electron spin", *Phys. Rev. B* **90**, 195305 (2014).

[146] P. Borri, W. Langbein, U. Woggon, V. Stavarache, D. Reuter, A. D. Wieck, "Exciton dephasing via phonon interactions in InAs quantum dots: Dependence on quantum confinement", *Phys. Rev. B* **71**, 115328 (2005).

[147] C.-W. Huang, X. Hu, "Theoretical study of nuclear spin polarization and depolarization in self-assembled quantum dots", *Phys. Rev. B* **81**, 205304 (2010).

[148] A. V. Kuhlmann, J. Houel, A. Ludwig, L. Greuter, D. Reuter, A. D. Wieck, M. Poggio, R. J. Warburton, "Charge noise and spin noise in a semiconductor quantum device", *Nat. Phys.* **9**, 570 (2013).

[149] R. Stockill, C. Le Gall, C. Matthiesen, L. Huthmacher, E. Clarke, M. Hugues, M. Atatüre, "Quantum dot spin coherence governed by a strained nuclear environment", *Nat. Commun.* **7**, 12745 (2016).

[150] B. Eble, C. Testelin, P. Desfonds, F. Bernardot, A. Balocchi, T. Amand, A. Miard, A. Lemaître, X. Marie, M. Chamarro, "HoleNuclear Spin Interaction in Quantum Dots", *Phys. Rev. Lett.* **102**, 146601 (2009).

[151] D. Stepanenko, G. Burkard, G. Giedke, A. Imamoglu, "Enhancement of electron spin coherence by optical preparation of nuclear spins", *Phys. Rev. Lett.* **96**, 3 (2006).

[152] J. Danon, Y. V. Nazarov, "Nuclear tuning and detuning of the electron spin resonance in a quantum dot: Theoretical consideration", *Phys. Rev. Lett.* **100**, 1 (2008).

[153] W. A. Coish, J. Fischer, D. Loss, "Free-induction decay and envelope modulations in a narrowed nuclear spin bath", *Phys. Rev. B - Condens. Matter Mater. Phys.* **81**, 1 (2010).

[154] G. Éthier-Majcher, D. Gangloff, R. Stockill, E. Clarke, M. Hugues, C. Le Gall, M. Atatüre, "Improving a Solid-State Qubit through an Engineered Mesoscopic Environment", *Phys. Rev. Lett.* **119**, 130503 (2017).

[155] A. Davydov, *Quantum Mechanics*, Elsevier, ISBN 9780080204383 (1965).

[156] G. B. Arfken, *Mathematical Methods for Physicists*, Elsevier, ISBN 9780120598151 (1995).

[157] E. A. Chekhovich, M. M. Glazov, A. B. Krysa, M. Hopkinson, P. Senellart, A. Lemaître, M. S. Skolnick, A. I. Tartakovskii, "Element-sensitive measurement of the hole-nuclear spin interaction in quantum dots", *Nat. Phys.* **9**, 74 (2013).

[158] A. W. Overhauser, "Polarization of Nuclei in Metals", *Phys. Rev.* **92**, 411 (1953).

[159] T. R. Carver, C. P. Slichter, "Polarization of Nuclear Spins in Metals", *Phys. Rev.* **92**, 212 (1953).

[160] G. Lampel, "Nuclear Dynamic Polarization by Optical Electronic Saturation and Optical Pumping in Semiconductors", *Phys. Rev. Lett.* **20**, 491 (1968).

[161] S. Brown, T. A. Kennedy, D. Gammon, E. Snow, "Spectrally resolved Overhauser shifts in single As quantum dots", *Phys. Rev. B - Condens. Matter Mater. Phys.* **54**, R17339 (1996).

[162] J. McFarlane, P. A. Dalgarno, B. D. Gerardot, R. H. Hadfield, R. J. Warburton, K. Karrai, A. Badolato, P. M. Petroff, "Gigahertz bandwidth electrical control over a dark exciton-based memory bit in a single quantum dot", *Appl. Phys. Lett.* **94**, 2007 (2009).

[163] I. Schwartz, E. R. Schmidgall, L. Gantz, D. Cogan, E. Bordo, Y. Don, M. Zielinski, D. Gershoni, "Deterministic writing and control of the dark exciton spin using single short optical pulses", *Phys. Rev. X* **5**, 1 (2015).

[164] R. K. Harris, E. D. Becker, S. M. Cabral de Menezes, R. Goodfellow, P. Granger, "NMR nomenclature: nuclear spin properties and conventions for chemical shifts. IUPAC Recommendations 2001. International Union of Pure and Applied Chemistry. Physical Chemistry Division. Commission on Molecular Structure and Spectroscopy", *Magn. Reson. Chem.* **40**, 489 (2002).

[165] J. R. Schrieffer, P. A. Wolff, "Relation between the Anderson and Kondo Hamiltonians", *Phys. Rev.* **149**, 491 (1966).

[166] D. J. Reilly, J. M. Taylor, J. R. Petta, C. M. Marcus, M. P. Hanson, A. C. Gossard, "Exchange control of nuclear spin diffusion in a double quantum dot", *Phys. Rev. Lett.* **104**, 1 (2010).

[167] E. A. Chekhovich, M. Hopkinson, M. Skolnick, A. Tartakovskii, "Suppression of nuclear spin bath fluctuations in self-assembled quantum dots induced by inhomogeneous strain", *Nat. Commun.* **6**, 6348 (2015).

[168] P. Maletinsky, A. Badolato, A. Imamoglu, "Dynamics of quantum dot nuclear spin polarization controlled by a single electron", *Phys. Rev. Lett.* **99**, 056804 (2007).

[169] J. Dreiser, M. Atatüre, C. Galland, T. Müller, A. Badolato, A. Imamoglu, "Optical investigations of quantum dot spin dynamics as a function of external electric and magnetic fields", *Phys. Rev. B - Condens. Matter Mater. Phys.* **77**, 1 (2008).

[170] R. V. Pound, "Nuclear Electric Quadrupole Interactions in Crystals", *Phys. Rev.* **79**, 685 (1950).

[171] C. Bulutay, "Quadrupolar spectra of nuclear spins in strained In x Ga 1x As quantum dots", *Phys. Rev. B* **85**, 115313 (2012).

[172] I. Stetcu, C. P. Liu, J. L. Friar, A. C. Hayes, P. Navrátil, "Nuclear electric dipole moment of3He", *Phys. Lett. Sect. B Nucl. Elem. Part. High-Energy Phys.* **665**, 168 (2008).

[173] R. I. Dzhioev, V. L. Korenev, "Stabilization of the electron-nuclear spin orientation in quantum dots by the nuclear quadrupole interaction", *Phys. Rev. Lett.* **99**, 1 (2007).

[174] M. N. Makhonin, K. V. Kavokin, P. Senellart, A. Lemaître, A. J. Ramsay, M. S. Skolnick, A. I. Tartakovskii, "Fast control of nuclear spin polarization in an optically pumped single quantum dot", *Nat. Mater.* **10**, 844 (2011).

[175] W. Yang, L. J. Sham, "General theory of feedback control of a nuclear spin ensemble in quantum dots", *Phys. Rev. B* **88**, 235304 (2013).

[176] A. R. Onur, J. P. De Jong, D. O'Shea, D. Reuter, A. D. Wieck, C. H. Van Der Wal, "Stabilizing nuclear spins around semiconductor electrons via the interplay of optical coherent population trapping and dynamic nuclear polarization", *Phys. Rev. B* **93**, 161204 (2016).

[177] W. Yang, L. J. Sham, "Collective nuclear stabilization in single quantum dots by noncollinear hyperfine interaction", (2012).

[178] R. K. Sundfors, "Experimental gradient-elastic tensors and chemical bonding in III-V semiconductors", *Phys. Rev. B* **10**, 4244 (1974).

[179] Y. Léger, L. Besombes, L. Maingault, H. Mariette, "Valence-band mixing in neutral, charged, and Mn-doped self-assembled quantum dots", *Phys. Rev. B - Condens. Matter Mater. Phys.* **76**, 1 (2007).

[180] K. De Greve, P. L. McMahon, D. Press, T. D. Ladd, D. Bisping, C. Schneider, M. Kamp, L. Worschech, S. Höfling, A. Forchel, Y. Yamamoto, "Ultrafast coherent control and suppressed nuclear feedback of a single quantum dot hole qubit", *Nat. Phys.* **7**, 872 (2011).

[181] A. Greilich, S. E. Economou, S. Spatzek, D. R. Yakovlev, D. Reuter, A. D. Wieck, T. L. Reinecke, M. Bayer, "Ultrafast optical rotations of electron spins in quantum dots", *Nat. Phys.* **5**, 262 (2009).

[182] S. G. Carter, S. E. Economou, A. Greilich, E. Barnes, T. Sweeney, A. S. Bracker, D. Gammon, "Strong hyperfine-induced modulation of an optically driven hole spin in an InAs quantum dot", *Phys. Rev. B - Condens. Matter Mater. Phys.* **89**, 1 (2014).

[183] L. Huthmacher, R. Stockill, E. Clarke, M. Hugues, C. Le Gall, M. Atatüre, "Coherence of a dynamically decoupled quantum-dot hole spin", *Phys. Rev. B* **97**, 1 (2018).

[184] T. D. Ladd, D. Press, K. De Greve, P. L. McMahon, B. Friess, C. Schneider, M. Kamp, S. Höfling, A. Forchel, Y. Yamamoto, "Pulsed Nuclear Pumping and Spin Diffusion in a Single Charged Quantum Dot", *Phys. Rev. Lett.* **105**, 107401 (2010).

[185] E. Clementi, D. L. Raimondi, "Atomic screening constants from SCF functions", *J. Chem. Phys.* **38**, 2686 (1963).

[186] P. Y. Yu, M. Cardona, *Fundamentals of Semiconductors*, Graduate Texts in Physics, Springer Berlin Heidelberg, Berlin, Heidelberg, ISBN 978-3-642-00709-5 (2010).

[187] A. Greilich, S. G. Carter, D. Kim, a. S. Bracker, D. Gammon, "Optical control of one and two hole spins in interacting quantum dots", *Nat. Photonics* **5**, 702 (2011).

[188] D. Paget, "Optical detection of NMR in high-purity GaAs: Direct study of the relaxation of nuclei close to shallow donors", *Phys. Rev. B* **25**, 4444 (1982).

[189] C. Deng, X. Hu, "Nuclear spin diffusion in quantum dots: Effects of inhomogeneous hyperfine interaction", *Phys. Rev. B* **72**, 165333 (2005).

[190] H. Christ, J. I. Cirac, G. Giedke, "Quantum description of nuclear spin cooling in a quantum dot", *Phys. Rev. B - Condens. Matter Mater. Phys.* **75**, 1 (2007).

[191] Ł. Cywiński, W. M. Witzel, S. Das Sarma, "Electron spin dephasing due to hyperfine interactions with a nuclear spin bath", *Phys. Rev. Lett.* **102**, 1 (2009).

[192] W. D. Knight, "Nuclear Magnetic Resonance Shift in Metals", *Phys. Rev.* **76**, 1259 (1949).

[193] D. Gammon, A. L. Efros, T. A. Kennedy, M. Rosen, D. S. Katzer, D. Park, S. W. Brown, V. L. Korenev, I. A. Merkulov, "Electron and Nuclear Spin Interactions in the Optical Spectra of Single GaAs Quantum Dots", *Phys. Rev. Lett.* **86**, 5176 (2001).

[194] A. Högele, M. Kroner, C. Latta, M. Claassen, I. Carusotto, C. Bulutay, A. Imamoglu, "Dynamic Nuclear Spin Polarization in the Resonant Laser Excitation of an InGaAs Quantum Dot", *Phys. Rev. Lett.* **108**, 197403 (2012).

[195] B. Eble, O. Krebs, A. Lemaître, K. Kowalik, A. Kudelski, P. Voisin, B. Urbaszek, X. Marie, T. Amand, "Dynamic nuclear polarization of a single charge-tunable InAs/ GaAs quantum dot", *Phys. Rev. B* **74**, 081306 (2006).

[196] A. I. Tartakovskii, T. Wright, A. Russell, V. I. Fal'ko, A. B. Van'Kov, J. Skiba-Szymanska, I. Drouzas, R. S. Kolodka, M. S. Skolnick, P. W. Fry, A. Tahraoui, H.-Y. Liu, M. Hopkinson, "Nuclear spin switch in semiconductor quantum dots", *Phys. Rev. Lett.* **98**, 1 (2007).

[197] A. Greilich, A. Shabaev, D. R. Yakovlev, A. L. Efros, I. A. Yugova, D. Reuter, A. D. Wieck, M. Bayer, "Nuclei-Induced Frequency Focusing of Electron Spin Coherence", *Science* **317**, 1896 (2007).

[198] E. A. Chekhovich, M. N. Makhonin, J. Skiba-Szymanska, A. B. Krysa, V. D. Kulakovskii, M. S. Skolnick, A. I. Tartakovskii, "Dynamics of optically induced nuclear spin polarization in individual InP/GaxIn1-xP quantum dots", *Phys. Rev. B - Condens. Matter Mater. Phys.* **81** (2010).

[199] C. Kloeffel, P. A. Dalgarno, B. Urbaszek, B. D. Gerardot, D. Brunner, P. M. Petroff, D. Loss, R. J. Warburton, "Controlling the interaction of electron and nuclear spins in a tunnel-coupled quantum dot", *Phys. Rev. Lett.* **106**, 1 (2011).

[200] G. Wüst, M. Munsch, F. Maier, A. V. Kuhlmann, A. Ludwig, A. D. Wieck, D. Loss, M. Poggio, R. J. Warburton, "Role of the electron spin in determining the coherence of the nuclear spins in a quantum dot", *Nat. Nanotechnol.* **11**, 885 (2016).

[201] W. Demtröder, *Laser spectroscopy : basic concepts and instrumentation*, Springer, New York (1996).

[202] E. Hansis, T. Cubel, J.-H. Choi, J. R. Guest, G. Raithel, "Simple pressure-tuned FabryPérot interferometer", *Rev. Sci. Instrum.* **76**, 033105 (2005).

[203] G. Fernandez, T. Volz, R. Desbuquois, A. Badolato, A. Imamoglu, "Optically Tunable Spontaneous Raman Fluorescence from a Single Self-Assembled InGaAs Quantum Dot", *Phys. Rev. Lett.* **103**, 087406 (2009).

[204] Z. Sun, A. Delteil, S. Faelt, A. Imamoglu, "Measurement of spin coherence using Raman scattering", *Phys. Rev. B* **93**, 241302(R) (2016).

[205] P. M. Vora, A. S. Bracker, S. G. Carter, T. M. Sweeney, M. Kim, C. S. Kim, L. Yang, P. G. Brereton, S. E. Economou, D. Gammon, "Spincavity interactions between a quantum dot molecule and a photonic crystal cavity", *Nat. Commun.* **6**, 7665 (2015).

[206] R. Loudon, *The Quantum Theory of Light*, Oxford Science Publications, 3rd edition, ISBN 9780198501763 (2000).

[207] E. Wolf, M. Born, *Principles of optics : electromagnetic theory of propagation, interference and diffraction of light*, Pergamon Press, Oxford (1983).

[208] E. Hecht, *Optics*, Addison Wesley, San Francisco (2002).

[209] G. Petrov, "A simple algorithm for spectral line deconvolution", *J. Quant. Spectrosc. Radiat. Transf.* **72**, 281 (2002).

[210] D. A. Long, *The Raman Effect*, John Wiley & Sons, Ltd, Chichester, UK, ISBN 0471490288 (2002).

[211] L. Rondin, J.-P. Tetienne, T. Hingant, J.-F. Roch, P. Maletinsky, V. Jacques, "Magnetometry with nitrogen-vacancy defects in diamond", *Reports Prog. Phys.* **77**, 056503 (2014).

[212] M. Issler, E. M. Kessler, G. Giedke, S. Yelin, J. I. Cirac, M. D. Lukin, A. Imamoglu, "Nuclear spin cooling using overhauser-field selective coherent population trapping", *Phys. Rev. Lett.* **105**, 1 (2010).

[213] W. Yao, R. B. Liu, L. J. Sham, "Theory of electron spin decoherence by interacting nuclear spins in a quantum dot", *Phys. Rev. B - Condens. Matter Mater. Phys.* **74**, 1 (2006).

[214] M. D'Yakonov, V. I. Perel', "Optical orientation in a system of electrons and lattice nuclei in semiconductors. Theory", *Sov. Phys. JETP* **38**, 177 (1974).

[215] J. Hansom, C. H. H. Schulte, C. Matthiesen, M. J. Stanley, M. Atatüre, "Frequency stabilization of the zero-phonon line of a quantum dot via phonon-assisted active feedback", *Appl. Phys. Lett.* **105**, 172107 (2014).

[216] E. A. Chekhovich, K. V. Kavokin, J. Puebla, A. B. Krysa, M. Hopkinson, A. D. Andreev, A. M. Sanchez, R. Beanland, M. S. Skolnick, A. I. Tartakovskii, "Structural analysis of strained quantum dots using nuclear magnetic resonance", *Nat. Nanotechnol.* **7**, 646 (2012).

[217] M. D'Yakonov, I. A. Merkulov, V. I. Perel', "Instabilities in the spin system of optically oriented electrons and nuclei in semiconductors", *Sov. J. Exp. Theor. Phys.* **51** (1980).

[218] V. A. Novikov, V. Fleisher, "Influence of local anisotropy on the states and resonant properties of an optically oriented system of electron and nuclear spins of semiconductors", *J. Exp. Theor. Phys.* **47**, 539 (1978).

[219] J. Cheng, *Coherent nonlinear optical spectroscopy of electron spin in charged semiconductor quantum dots*, Ph.D. thesis, University of Michigan (2006).

[220] A. Högele, M. Kroner, C. Latta, M. Claassen, I. Carusotto, C. Bulutay, A. Imamoglu, "Dynamic Nuclear Spin Polarization in the Resonant Laser Excitation of an InGaAs Quantum Dot", *Phys. Rev. Lett.* **108**, 197403 (2012).

[221] A. R. Onur, C. H. van der Wal, "Two-laser dynamic nuclear polarization with semiconductor electrons: Feedback, suppressed fluctuations, and bistability near two-photon resonance", *Phys. Rev. B* **98**, 165304 (2018).

[222] C. Gardiner, P. Zoller, *Quantum Noise*, Springer, ISBN 978-3-540-22301-6 (2004).

[223] M. A. Nielsen, I. L. Chuang, *Quantum computation and quantum information*, Cambridge University Press, Cambridge (2010).

[224] J. Berezovsky, M. H. Mikkelsen, N. G. Stoltz, L. A. Coldren, D. D. Awschalom, "Picosecond coherent optical manipulation of a single electron spin in a quantum dot", *Science* **320**, 349 (2008).

[225] D. Press, K. De Greve, P. L. McMahon, T. D. Ladd, B. Friess, C. Schneider, M. Kamp, S. Höfling, A. Forchel, Y. Yamamoto, "Ultrafast optical spin echo in a single quantum dot", *Nat. Photonics* **4**, 367 (2010).

[226] T. M. Godden, J. H. Quilter, A. J. Ramsay, Y. Wu, P. Brereton, S. J. Boyle, I. J. Luxmoore, J. Puebla-Nunez, A. M. Fox, M. S. Skolnick, "Coherent optical control of the spin of a single hole in an InAs/GaAs quantum dot", *Phys. Rev. Lett.* **108**, 1 (2012).

[227] E. Hahn, "Spin Echoes", *Phys. Rev.* **80**, 580 (1950).

[228] J. Du, X. Rong, N. Zhao, Y. Wang, J. Yang, R. B. Liu, "Preserving electron spin coherence in solids by optimal dynamical decoupling", *Nature* **461**, 1265 (2009).

[229] B. Martinac, S. Gilroy, T. Hirano, a. J. Hudspeth, D. B. Reichling, J. D. Levine, K. R. Spring, M. Crest, P. Delmas, J. N. Wood, P. Cesare, T. Suchyna, F. Sachs, B. J. Waldron, J. E. Brayden, G. R. Lewin, a. E. Dubin, M. J. Petrus, T. J. Earley, a. Patapoutian, S. B. House, H. Gainer, a. a. Harper, E. I. Harper, J. a. Garson, B. H. Anderton, P. W. Mccarthy, F. K. Pierau, M. R. Hanlon, B. a. Wallace, S. J. Tucker, F. M. Ashcroft, a. I. Basbaum, D. M. Bautista, G. Scherrer, D. Julius, R. Moshourab, N. Hong, "Universal Dynamical Decoupling of", 60–63 (2010).

[230] L. Viola, E. Knill, S. Lloyd, "Dynamical Decoupling of Open Quantum Systems", *Phys. Rev. Lett.* **82**, 2417 (1999).

[231] J. Preskill, *Lecture Notes for Physics 229: Quantum Information and Computation*, CreateSpace Independent Publishing Platform, ISBN 1506189911 (2015).

[232] J. R. Schaibley, *Spin-Photon Entanglement and Quantum Optics with Single Quantum Dots*, Ph.D. thesis, University of Michigan (2013).

[233] A. Greilich, D. R. Yakovlev, A. Shabaev, A. L. Efros, I. A. Yugova, R. Oulton, V. Stavarache, D. Reuter, A. Wieck, M. Bayer, "Mode Locking of Electron Spin Quantum Dots", *Science* **341**, 341 (2006).

[234] I. Schwartz, D. Cogan, E. R. Schmidgall, Y. Don, L. Gantz, O. Kenneth, N. H. Lindner, D. Gershoni, "Deterministic generation of a cluster state of entangled photons", *Science* **354**, 434 (2016).